

UC San Diego

UC San Diego Electronic Theses and Dissertations

Title

Elucidation of redox metabolism control points in highly proliferative cells

Permalink

<https://escholarship.org/uc/item/5p65m061>

Author

Badur, Mehmet

Publication Date

2018

Peer reviewed|Thesis/dissertation

UNIVERSITY OF CALIFORNIA SAN DIEGO

Elucidation of redox metabolism control points in highly proliferative cells

A dissertation submitted in partial satisfaction of the
requirements for the degree
Doctor of Philosophy

in

Bioengineering

by

Mehmet Gultekin Badur

Committee in charge:

Professor Christian Metallo, Chair
Professor Kun-Liang Guan
Professor Terence Hwa
Professor Prashant Mali
Professor Bernhard Palsson

2018

Copyright
Mehmet Gultekin Badur, 2018
All rights reserved.

The dissertation of Mehmet Gultekin Badur is approved, and it is acceptable in quality and form for publication on micro-film and electronically:

Chair

University of California San Diego

2018

DEDICATION

For my family, as none of this would be possible without their infinite patience
and unwavering support

TABLE OF CONTENTS

Signature Page	iii
Dedication	iv
Table of Contents	v
List of Figures	x
List of Tables	xii
Acknowledgements	xiii
Vita	xv
Abstract of the Dissertation	xvii
Chapter 1	Reverse engineering the cancer metabolic network using flux analysis to understand drivers of human disease	1
	1.1 Abstract	1
	1.2 Introduction	2
	1.2.1 Renewed interest in metabolism	2
	1.2.2 Thermodynamics and topology of metabolism	3
	1.3 Methods of quantifying fluxes	5
	1.3.1 Need of metabolic tracing	5
	1.3.2 Stable isotope tracing	6
	1.4 Cancer	11
	1.4.1 Renewed appreciation of metabolic dysregulation in cancer	11
	1.4.2 Glutamine metabolism	14
	1.4.3 Redox metabolism	18
	1.4.4 Serine biosynthesis and one carbon metabolism	20
	1.5 Emerging links between metabolism and epigenetics	23
	1.6 Observations from <i>in vivo</i> studies	24
	1.7 Conclusion	27
	1.8 Acknowledgements	28
	1.9 References	28
Chapter 2	Enzymatic passaging of human embryonic stem cells alters central carbon metabolism and glycan abundance	49
	2.1 Abstract	49
	2.2 Introduction	50
	2.3 Materials and Methods	51
	2.3.1 Cell culture	51

2.3.2	Enzymatic passaging experiments	52
2.3.3	Metabolite Extraction and GC-MS Analysis	53
2.3.4	Mass isotopomer distributions, isotopomer spectral analysis (ISA), and flux analysis	55
2.3.5	Statistical analyses	55
2.4	Results	56
2.4.1	Enzymatic passaging decreases glucose oxidation and fatty acid synthesis in hESCs	56
2.4.2	Rapid quantitation of total glycan pools and synthesis in hESCs	61
2.4.3	Glycan and carbohydrate pools are significantly depleted upon enzymatic passaging	65
2.4.4	Biosynthetic fluxes to nucleotides and glycans are similar in cultured hESCs	65
2.5	Discussion	68
2.5.1	Potential pitfalls in advanced hESC culture methods	68
2.5.2	Potential selective pressure of enzymatic passaging through altered metabolism	70
2.5.3	Glycocalyx is a significant biomass pool in cultured hESCs	70
2.5.4	Concluding thoughts	71
2.6	Acknowledgements	72
2.7	References	72

Chapter 3	Distinct metabolic states can support self-renewal and lipogenesis in human pluripotent stem cells under different culture conditions	78
3.1	Abstract	78
3.2	Introduction	79
3.3	Materials and Methods	81
3.3.1	Human pluripotent stem cell culture	81
3.3.2	Immunocytochemistry	81
3.3.3	Metabolite extraction and derivatization	82
3.3.4	Gas chromatography/mass spectrometry analysis	83
3.3.5	Metabolite quantification and isotopomer spectral analysis	83
3.3.6	Mole percent enrichment measurement	84
3.3.7	Extracellular flux and oxidative pentose phosphate pathway flux measurements	84
3.3.8	Cell dry weight measurements	85
3.3.9	ATP-linked oxygen consumption rate measurements	85
3.3.10	Gene expression analysis	85
3.3.11	Statistical analyses	85
3.4	Results	86
3.4.1	Medium choice influences hESC metabolic states	86
3.4.2	Media-dependent reprogramming of amino acid and NADPH metabolism	89

	3.4.3	Chemically defined medium dramatically increases lipogenesis	96
	3.4.4	Lipid supplementation mitigates hESC metabolic reprogramming	97
	3.5	Discussion	100
	3.6	Acknowledgements	103
	3.7	References	105
Chapter 4		Lipid availability influences the metabolic maturation of hPSC-derived cardiomyocytes	112
	4.1	Introduction	112
	4.2	Materials and Methods	114
	4.2.1	Human pluripotent stem cell (hPSC) culture	114
	4.2.2	Cardiomyocyte differentiation	114
	4.2.3	¹³ C metabolic tracing	115
	4.2.4	Metabolite extraction and derivatization	116
	4.2.5	GC/MS analysis	117
	4.2.6	Mole percent enrichment calculation	117
	4.2.7	Isotopomer spectral analysis (ISA)	118
	4.2.8	Oxygen Consumption Measurement	118
	4.2.9	Gene expression analysis	120
	4.2.10	Immunocytochemistry	121
	4.2.11	Statistical analyses	121
	4.3	Results	121
	4.3.1	Cardiac differentiation increases glucose oxidation of hPSCs	121
	4.3.2	Nutrient consumption of hPSC-derived cardiomyocytes	122
	4.3.3	Metabolic activation during hPSC cardiac differentiation	124
	4.3.4	Changes in lipid metabolism during hPSC cardiac differentiation	129
	4.3.5	Immature metabolic features of hPSC-derived cardiomyocytes cultured in lipid insufficient environment	131
	4.3.6	Nutrient lipids improve metabolic maturation of hPSC-derived cardiomyocytes	132
	4.4	Discussion	133
	4.5	Acknowledgements	136
	4.6	References	136
Chapter 5		Combinatorial CRISPR-Cas9 metabolic screens reveal critical redox control points dependent on the KEAP1-NRF2 regulatory axis	143
	5.1	Abstract	143
	5.2	Introduction	144
	5.3	Materials and Methods	145
	5.3.1	Cell lines and culture conditions	145

5.3.2	Dual-gRNA library design and cloning	146
5.3.3	Lentivirus production	146
5.3.4	CRISPR/Cas9 dual-gRNA screening	147
5.3.5	Quantification of dual gRNAs abundance	147
5.3.6	Computation of single and double gene knockout fitness and genetic interaction scores	148
5.3.7	Single-gRNA construct cloning	151
5.3.8	Competitive cell growth assay	151
5.3.9	RNA sequencing data analysis	153
5.3.10	Stable isotope tracing	153
5.3.11	Metabolite Extraction and GC-MS Analysis	154
5.3.12	Metabolite integration and isotopomer spectral analysis (ISA)	155
5.3.13	Immunoblotting	155
5.3.14	RT-PCR	156
5.3.15	Glutathione measurement	156
5.3.16	Statistical analyses	156
5.4	Results	157
5.4.1	Combinatorial CRISPR-Cas9 screening to probe metabolic networks	157
5.4.2	Mapping metabolic gene dependencies in glucose catabolism	160
5.4.3	Validation of significant SKO and DKO results on cellular fitness and metabolic fluxes	164
5.4.4	Comparison of metabolic liabilities across cell lines reveals key role of <i>KEAPI-NRF2</i>	167
5.5	Discussion	172
5.6	Acknowledgements	174
5.7	References	175

Chapter 6	Oncogenic R132 IDH1 mutations limit NADPH for <i>de novo</i> lipogenesis through (D)2-hydroxyglutarate production in fibrosarcoma cells	180
6.1	Abstract	180
6.2	Introduction	181
6.3	Materials and Methods	183
6.3.1	Cell culture and stable isotope tracing	183
6.3.2	Delipidation of FBS	183
6.3.3	Metabolite Extraction and GC-MS Analysis	184
6.3.4	Metabolite integration and isotopomer spectral analysis (ISA)	185
6.3.5	Measurement of extracellular and intracellular fluxes	185
6.3.6	NADPH consumption	187
6.3.7	RT-PCR	187
6.3.8	Quantification and Statistical Analysis	188
6.4	Results	188

6.4.1	Use of genetically-engineered HT1080 fibrosarcoma cell lines to dissect enzymatic functions of <i>IDH1</i> and mutant <i>IDH1</i> . . .	188
6.4.2	Cytosolic NADPH contributes to D2HG production from <i>IDH1</i> ^{+/<i>R132C</i>} cells	191
6.4.3	2HG production contributes significantly to cellular NADPH demands	193
6.4.4	<i>De novo</i> lipogenesis competes with D2HG production for NADPH	195
6.5	Discussion	198
6.6	Acknowledgements	199
6.7	References	200
Chapter 7	Conclusions	207
Chapter S1	Supplement to Chapter 1	211
	S1.1 Abbreviations	211
Chapter S2	Supplement to Chapter 2	212
	S2.1 Abbreviations	212
Chapter S3	Supplement to Chapter 3	215
	S3.1 Abbreviations	215
	S3.2 Supplemental Methods	215
	S3.2.1 Cell culture and media	215
	S3.2.2 Detection of 2-hydroxyglutarate isoforms	217
	S3.3 Supplemental Tables and Figures	217
	S3.4 Supplementary References	229
Chapter S5	Supplement to Chapter 5	231
	S5.1 Supplemental Figures	231
Chapter S6	Supplement to Chapter 6	240
	S6.1 Supplemental Tables and Figures	240

LIST OF FIGURES

Figure 1.1:	MFA applied to biological systems at different scales comes with a tradeoff in molecular resolution versus physiologic relevance	7
Figure 1.2:	Stable isotope tracing paradigm	8
Figure 1.3:	Tracing TCA metabolism using ¹³ C glucose and glutamine	12
Figure 1.4:	Metabolic pathways dysregulated in the context of disease	15
Figure 2.1:	Enzymatic passaging alters central carbon metabolism	58
Figure 2.2:	Quantitation of glycan residue abundance and labeling in cellular biomass	63
Figure 2.3:	Enzymatic passaging alters glycan abundance of hESCs	66
Figure 2.4:	Biosynthetic fluxes to glycans and nucleotides are similar in cultured hESCs	69
Figure 3.1:	Distinct metabolic states exist in hESCs adapted to MEF-CM versus chemically defined media	87
Figure 3.2:	Media choice influences glucose, glutamine, and NADPH metabolism	91
Figure 3.3:	HESCs adapted to chemically defined media upregulate lipid biosynthesis	94
Figure 3.4:	Lipid supplementation mitigates media-induced metabolic flux alterations	98
Figure 3.5:	Lipid supplementation mitigates media-induced metabolic enzyme expression and mitochondrial state alterations	101
Figure 3.6:	Nutrient availability reprograms intermediary metabolism in hPSCs	104
Figure 4.1:	hPSC-derived cardiomyocytes primarily oxidize glucose	123
Figure 4.2:	hPSC-derived cardiomyocytes are metabolically immature	125
Figure 4.3:	Day-by-day tracing reveals metabolic pathway activation and suppression during cardiac differentiation	127
Figure 4.4:	<i>De novo</i> lipogenesis is suppressed during cardiac differentiation	130
Figure 4.5:	Lipid supplementation activates mitochondrial activity	132
Figure 4.6:	Lipid supplementation increases intracellular fatty acid availability and β -oxidation	134
Figure 5.1:	Experimental design	158
Figure 5.2:	Combinatorial CRISPR screens reveal metabolic network dependencies	161
Figure 5.3:	Screening results validated through targeted fitness and metabolic flux measurements	165
Figure 5.4:	KEAP1 mutational status alters redox metabolism and impact of oxPPP gene knockouts on cellular fitness	170
Figure 6.1:	Metabolic characterization of isogenic IDH1-expressing HT1080 cell lines	190
Figure 6.2:	Tracing NAD(P)H regeneration and 2HG production in HT1080-IDH1 cell lines	192
Figure 6.3:	D2HG production and secretion increases NADPH demands in IDH1 ^{+R132C} cells	194
Figure 6.4:	D2HG production limits NADPH for DNL in lipid-deficient conditions	196

Figure S2.1: Polar metabolite labeling and abundances	213
Figure S2.2: Biomass metabolite abundances.	214
Figure S3.1: Atom transition maps of labeled glutamine species	219
Figure S3.2: Metabolic alterations in hESCs adapted to MEF-CM versus chemically defined media	221
Figure S3.3: Mass isotopomer distributions from [1,2- ¹³ C]glucose	223
Figure S3.4: Mass isotopomer distributions from [U- ¹³ C ₅]glutamine	225
Figure S3.5: HESCs adapted to chemically defined media upregulate lipid biosynthesis	227
Figure S3.6: Oxygen consumption traces of hPSCs in different culture conditions	230
Figure S5.1: Schematic of dual-gRNA-library construction and quality control of screens	232
Figure S5.2: CRISPR screening results reveal metabolic network dependencies	234
Figure S5.3: Screening results validated through metabolic flux measurements and fitness assays	236
Figure S5.4: <i>KEAP1</i> mutational status alters redox metabolism and impact of oxPPP gene knockouts on cellular fitness	238
Figure S6.1: Central carbon isotopologue distribution in mtIDH cells	242
Figure S6.2: Metabolic alterations induced by lipid deficiency	243

LIST OF TABLES

Table 2.1: Metabolite fragments used for GC/MS analysis	56
Table 4.1: Metabolite fragments used for GC/MS analysis	119
Table 4.2: RT-PCR primers	120
Table 4.3: Fatty acid concentrations in commonly used albumin media supplements . . .	131
Table S2.1: MIDs for unlabeled hydrosylate fragments	212
Table S2.2: MIDs for labeled hydrosylate fragments	214
Table S3.1: Metabolite fragments used for GC/MS analysis	218
Table S3.2: Primers used for gene expression analysis	218
Table S6.1: Metabolite fragments	241
Table S6.2: RT-PCR primers	241

ACKNOWLEDGEMENTS

Thank you to everyone who has supported me through this work. You've been instrumental in its completion and I'm incredibly grateful for the ways in which you've influenced my success. I thank my advisor, Christian M. Metallo, for all of his efforts in shaping my thesis and my development as a scientist. I could not have achieved so much without his mentorship and the opportunities he afforded me. I thank Martina Wallace for her guidance through the scientific and personal challenges of graduate school. I thank the current and former members of the Metallo lab for their camaraderie and helpful discussions throughout the years: Seth Parker, Nate Vacanti, Chris Ahn, Thekla Cordes, Le You, Selvam Muthusamy, Esther Lim, and Michal Handzlik. I thank my numerous collaborators throughout the years for expanding my knowledge of biology and metabolism, especially Dongxin Zhao and Prashant Mali.

I would also like to thank my friends and family that have provided constant support through my time in UCSD. I have been incredibly fortunate to befriend new people in San Diego and forge stronger bonds with old friends. Finally, I want to acknowledge Jessica Ungerleider for being the constant source of happiness in my life.

Chapter 1, in full, is a reprint of the material as it appears in "Reverse engineering the cancer metabolic network using flux analysis to understand drivers of human disease," *Metabolic Engineering*, vol. 45, 2018. Mehmet G. Badur is the primary author of this publication. Christian M. Metallo is the corresponding author of this publication.

Chapter 2, in full, is a reprint of the material as it appears in "Enzymatic passaging of human embryonic stem cells alters central carbon metabolism and glycan abundance," *Biotechnology Journal*, vol. 10, 2015. Mehmet G. Badur is the primary author of this publication. Hui Zhang is a co-author of this publication. Christian M. Metallo is the corresponding author of this publication.

Chapter 3, in full, is a reprint of the material as it appears in "Distinct metabolic states can support self-renewal and lipogenesis in human pluripotent stem cells under different culture

conditions,” *Cell Reports*, vol. 16, 2016. Mehmet G. Badur and Hui Zhang are the co-primary authors of this publication. Ajit S. Divakaruni, Seth J. Parker, Christian Jager, Karsten Hiller, and Anne N. Murphy are co-authors of this publication. Christian M. Metallo is the corresponding author of this publication.

Chapter 4 is currently being prepared for submission for publication. Mehmet G. Badur, Hui Zhang, Sean Spierling, Ajit Divakaruni, Noah E. Meurs, Anne N. Murphy, and Mark Mercola are co-authors of this material. Christian M. Metallo is the corresponding author of this publication.

Chapter 5, in full, is a reprint of the material as it appears in ”Combinatorial CRISPR-Cas9 Metabolic Screens Reveal Critical Redox Control Points Dependent on the KEAP1-NRF2 Regulatory Axis,” *Molecular Cell*, vol. 69, 2018. Mehmet G. Badur and Dongxin Zhao are the co-primary authors of this publication. Jens Luebeck, Jose H. Magana, Amanda Birmingham, Roman Sasik, Christopher S. Ahn, and Trey Ideker are co-authors of this publication. Christian M. Metallo and Prashant Mali are the co-corresponding authors of this publication.

Chapter 6, in full, has been submitted for publication of the material as it may appear in ”Oncogenic R132 IDH1 mutations limit NADPH for *de novo* lipogenesis through (D)2-hydroxyglutarate production in fibrosarcoma cells,” *Cell Reports*, 2018. Mehmet G. Badur is the primary author of this publication. Thangaselvam Muthusamy, Seth J. Parker, Shenghong Ma, Thekla Cordes, Jose H. Magana, Kun-Liang Guan are co-authors of this publication. Christian M. Metallo is the corresponding author of this publication.

VITA

- 2018 Ph.D. in Bioengineering, University of California San Diego
- 2013 B.S. in Chemical Engineering, University of Wisconsin-Madison

PUBLICATIONS

Zhao D*, Badur MG*, Luebeck J, Magana JH, Birmingham A, Sasik R, Ahn CS, Ideker T, Metallo CM, Mali P. (2018) Combinatorial CRISPR-Cas9 metabolic screens reveal critical redox control points dependent on the KEAP1-NRF2 regulatory axis. *Mol Cell* 69(4): 699-708.

Badur MG & Metallo CM. (2018) Reverse engineering the cancer metabolic network using flux analysis to understand drivers of human disease. *Met Eng* 45:95-108

Zhang H*, Badur MG*, Divakaruni AS, Parker SJ, Jager C, Hiller K, Murphy AN, Metallo CM. (2016) Distinct metabolic states can support self-renewal and lipogenesis in human pluripotent stem cells under different culture conditions. *Cell Rep* 16(6):1536-47

Badur MG, Zhang H, Metallo CM. (2015) Enzymatic passaging of human embryonic stem cells alters central carbon metabolism and glycan abundance. *Biotechnol J* 10(10):1600-11

Hazeltine LB, Badur MG, Lian X, Das A, Han W, Palecek SP. (2013) Temporal impact of substrate mechanics on differentiation of human embryonic stem cells to cardiomyocytes. *Acta Biomater* 10(2):604-12

Hazeltine LB, Simmons CS, Salick MR, Lian X, Badur MG, Han W, Delgado SM, Wakatsuki T, Crone WC, Pruitt BL, Palecek SP. (2012) Effects of substrate mechanics on contractility of cardiomyocytes generated from human pluripotent stem cells. *Int J Cell Biol* 2012:508294

CONFERENCE PRESENTATIONS

Badur MG*, Zhao D*, et al. (2018) Interrogation of critical metabolic pathways for compartment-specific redox homeostasis in cancer cells. American Chemical Society, New Orleans, LA. Oral.

Badur MG*, Zhao D*, et al. (2018) Interrogation of critical metabolic pathways for compartment-specific redox homeostasis in cancer cells. Keystone Symposium: Tumor Metabolism, Snowbird, UT. Poster.

Badur MG*, Zhang H*, et al. (2016) Distinct metabolic states in hPSC culture conditions. American Chemical Society, San Diego, CA. Oral.

Badur MG*, Zhang H*, et al. (2016) Distinct metabolic states support pluripotent stem cell self-renewal. Keystone Symposium: Tumor Metabolism, Banff, BC. Poster.

Badur MG, et al. (2013) Stiffness-dependent differentiation of human pluripotent stem cells to cardiomyocytes. American Chemical Society, New Orleans, LA. Oral.

ABSTRACT OF THE DISSERTATION

Elucidation of redox metabolism control points in highly proliferative cells

by

Mehmet Gultekin Badur

Doctor of Philosophy in Bioengineering

University of California San Diego, 2018

Professor Christian Metallo, Chair

Metabolism is essential for cellular homeostasis as cells import nutrients as substrates for biosynthetic reactions or as energy to power the cell. However, maintenance of this homeostasis in the face of environmental or genetic insults requires altering metabolic fluxes to achieve a desired behavior. Redox metabolism is a critical subsystem within the metabolic network and must be finely tuned to support growth in highly proliferative cells. The chapters of this dissertation are independent bodies of work that explore how redox metabolism is altered to support stem cell and cancer cell growth. Chapter 1, titled "Reverse engineering the cancer metabolic network using flux analysis to understand drivers of human disease," is a review on the utility of applying metabolic flux analysis (MFA) to study cancer biology. The chapter first introduces techniques

required for MFA and then highlights recent advances in cancer metabolism that required the application of MFA. Chapter 2, titled "Enzymatic passaging of human embryonic stem cells alters central carbon metabolism and glycan abundance," explores how routine enzymatic passage methods alters metabolism to support increased hexosamine biosynthesis after cleavage of the glycolayx. Chapter 3, titled "Distinct metabolic states can support self-renewal and lipogenesis in human pluripotent stem cells under different culture conditions," examines how disparate media conditions routinely used in stem cell culture maintain pluripotency in distinct metabolic states. Chemically-defined media forces the cell to reside in an increased biosynthetic state to support *de novo* lipogenesis that can be reversed with lipid supplementation. Chapter 4, titled "Lipid availability influences the metabolic maturation of hPSC-derived cardiomyocytes," describes how gold-standard culture conditions for cardiomyocyte differentiation present a roadblock for metabolic maturation. Chapter 5, titled "Combinatorial CRISPR-Cas9 metabolic screens reveal critical redox control points dependent on the KEAP1-NRF2 regulatory axis," describes using novel combinatorial CRISPR screening technology to understand glycolytic network topology and enzyme compensation in cancer cells. Examination of dispensability of redox genes across cell types revealed a counterintuitive regulation of redox metabolism function and essentiality controlled by KEAP1-NRF2. Chapter 6, titled "Oncogenic R132 IDH1 mutations limit NADPH for *de novo* lipogenesis through (D)2-hydroxyglutarate production in fibrosarcoma cells," describes how oncogenic mutations in *IDH1* reprogram NAD(P)H metabolism to support 2HG production. While the mutation is generally tolerated, 2HG production competes with *de novo* lipogenesis for NADPH when cells are placed in lipid-deficient conditions. Taken together, these collective studies demonstrate the importance of understanding redox-specific metabolic flux regulation in highly proliferative cells. These findings have impact on bioprocess development of stem cells and therapeutic targeting of cancer cells.

Chapter 1

Reverse engineering the cancer metabolic network using flux analysis to understand drivers of human disease

1.1 Abstract

Metabolic dysfunction has reemerged as an essential hallmark of tumorigenesis, and metabolic phenotypes are increasingly being integrated into pre-clinical models of disease. The complexity of these metabolic networks requires systems-level interrogation, and metabolic flux analysis (MFA) with stable isotope tracing present a suitable conceptual framework for such systems. Here we review efforts to elucidate mechanisms through which metabolism influences tumor growth and survival, with an emphasis on applications using stable isotope tracing and MFA. Through these approaches researchers can now quantify pathway fluxes in various *in vitro* and *in vivo* contexts to provide mechanistic insights at molecular and physiological scales respectively. Knowledge and discoveries in cancer models are paving the way toward applications in other biological contexts and disease models. In turn, MFA approaches will increasingly help

to uncover new therapeutic opportunities that enhance human health.

1.2 Introduction

1.2.1 Renewed interest in metabolism

A largely forgotten vestige of biochemistry coursework, metabolism is once again being appreciated as a driver of human disease rather than a downstream effect of some genetic or transcriptional changes. Since the advent of the genomics revolution, biomedical research has largely focused on the roles of DNA and RNA dysregulation in disease. This information has led to an international, multidisciplinary effort to catalog, sequence, and interpret large amounts of genomics data from various sources [1]. While these efforts have generated large amounts of publically-available, highly-curated data and new insights into a range of diseases, the next steps often require researchers to look beyond the mutational or allelic status of disease-associated genes and gain a more mechanistic understanding of these changes. As such, higher level activities of the cell are now coming into focus as drivers of pathological phenotype - e.g. transcriptional and translational regulation, epigenetic states, and systems-level metabolic activities.

Indeed, recent work in cancer, metabolic syndrome, and regenerative medicine has highlighted situations where metabolic alterations precede other canonical modes of biological control (e.g. transcriptional activation), demonstrating its importance in biomedicine. Metabolism, or the biochemical reactions executed by cells, is essential for the maintenance of cellular function and the response to extrinsic and intrinsic cues. To control such a complex network, mammalian metabolism has evolved a regulatory framework and interconnectivity that ensures robust functionality. Advanced methods are required (and are now becoming available) to decipher the regulation of these processes and their dysfunction in disease settings [2]. In this review, we will establish the critical need for studying metabolism at a systems-level, introduce methodological advances that have enabled interrogation of mammalian metabolism, and highlight

recent work that has utilized stable isotope tracing and MFA to better understand human disease.

1.2.2 Thermodynamics and topology of metabolism

Metabolic reactions can largely be broken down into three main components or functions - bioenergetics, biosynthesis, and redox balance - with each component having a unique network behavior requiring systems-level interrogation.

The thermodynamic reality of a cell is the constant need to generate energy that can be coupled to unfavorable reactions with a positive Gibbs free energy [3–5]. In practice, nutrients are imported into cells then catabolized to regenerate adenosine triphosphate (ATP), the metabolic currency of cells. Due to the high energy stored in its phosphoanhydride bonds, ATP hydrolysis is required to drive thermodynamically unfavorable reactions and allow them to proceed at sufficient rates. The use of ATP regeneration and hydrolysis in disparate metabolic pathways is a prime example of how metabolic interconnectivity facilitates life and highlights the importance of the first law of thermodynamics in understanding metabolic function [6–8].

This connection results in two axioms of bioenergetics: (1) If a cell is consuming large amounts of ATP, a concomitant production of ATP molecules is needed. A cell can turnover its ATP pool over six times per minute [9], and ATP levels are "nearly universally homeostatic" [10]. Therefore, the proper biological unit of measure is the ATP regeneration rate (flux) rather than a metabolite level or ratio (i.e. nucleotide pool ratios). (2) Cells have evolved enough production capacity and storage (e.g. glycolysis, oxidative phosphorylation, creatine kinase, adenylate cyclase) to meet this demand in the face of various insults (e.g. substrate deprivation, hypoxia). This results in a topological reality where many pathways are connected by ATP, resulting in highly interdependent nodes within the metabolic network. More complex cells like eukaryotes have evolved further to compartmentalize reactions to facilitate (and complicate) pathway function further.

In addition to maintenance of energetic homeostasis, an important role of metabolism is

to provide biosynthetic precursors. Highly proliferative cells - such as immune cells, tumor cells, and transit-amplifying stem cells - require a doubling of cellular biomass each time they divide. In addition, all somatic cells have established rates of lipid and protein turnover/nucleotide synthesis that require constant production of biosynthetic intermediates [11]. While unique mammalian auxotrophies exist that contribute to large portions of cellular biomass (i.e. essential amino acids for protein biosynthesis), cells can choose to either synthesize or uptake macronutrients for the remaining portion of needed biomass. While the "cheapest" route for a cell would be to uptake all macromolecules, network topology might dictate the need for flux through a pathway to provide substrates for a different pathway. This interdependency results in a coupling of catabolic and anabolic reactions. Biological (and electrical) energy flow is coordinated by the movement of electrons, and these transfers are mediated by oxidoreductases and reducing equivalents (e.g. nicotinamide adenine dinucleotide (NAD⁺), nicotinamide adenine dinucleotide phosphate (NADP⁺), and flavin adenine dinucleotide (FAD)). At a high level, cells extract electrons from reduced substrates (e.g. carbohydrates, fatty acids) and secrete oxidized byproducts (e.g. lactate, CO₂). Therefore, flux through oxidative pathways consumes electron carriers and produces reducing equivalents. Cells in turn must consume electrons and regenerate electron carriers to maintain proper redox balance. For example, to maintain glycolytic rates and/or tricarboxylic acid (TCA) cycle flux, cells must constantly consume electrons via lactate dehydrogenase (LDH) or respiration to regenerate NAD⁺ and FAD. This point highlights one potential reason why rapidly proliferating cells exhibit high glycolytic rates (i.e. the Warburg effect). For example, diversion of glycolytic intermediates for serine biosynthesis can cause redox fluctuations or imbalances such that NAD⁺ is not regenerated at sufficient rates by LDH to maintain glycolytic flux. Alternate NAD⁺ recycling pathways such as the malate-aspartate shuttle and glycerol-phosphate shunt are active in proliferating cells but may be similarly blunted as aspartate and glycerol-3-phosphate are used for biosynthesis. By maintaining high flux through glycolysis such redox fluctuations are minimized. Redox balance in cells also extends to environmental stresses

through the consumption of reducing equivalents to regenerate antioxidants (i.e. the cycling of reduced (GSH) and oxidized (GSSG) glutathione). This redox control in cells demonstrates how cells have evolved metabolic interconnections to maintain homeostasis.

1.3 Methods of quantifying fluxes

1.3.1 Need of metabolic tracing

The interconnectivity, redundancies, and cross-dependencies that exist within metabolic pathways manifest themselves in classic emergent network behavior, where changes in one node can result in far-reaching and unforeseen states. For example, altering one pathway by modulating substrate availability or through molecular and pharmacological interventions can lead to system-wide changes in metabolic pathway fluxes as cells attempt to maintain homeostasis [12]. Historically, technological limitations forced scientists to interrogate metabolism at the resolution of individual enzymes. While this approach led to the elucidation of fundamental metabolic pathways, like the TCA cycle, a critical need for systems-level analyses has now emerged.

With technological advances such as gas chromatography-coupled mass spectrometry (GC/MS), liquid chromatography-coupled mass spectrometry (LC/MS), and nuclear magnetic resonance spectroscopy (NMR), researchers now have the ability to rapidly and simultaneously quantify large numbers of metabolites in a given biological setting [13]. These developments have been essential in driving both the rapid growth in new information about metabolic control/function and the metabolic basis of human disease [14–16]. In addition to the inherent complexities of studying any network, mammalian metabolism has unique features and must be studied at multiple length scales (Figure 1.1) For example, many metabolic pathways have many redundant, compartment-specific forms that can be regulated independently (e.g. TCA cycle enzymes in the mitochondria, cytosol, and/or peroxisome), or cells can reside in local

cellular communities that interact to elicit a broader function (e.g. beta cells within islets or stromal-epithelial interactions). On the other hand, diseases manifest themselves throughout the body, where dysregulated insulin secretion by the pancreas in diabetes affects distal muscle microvascular, liver, adipose tissue, and neurological functions.

With these realities of network and length-scale complexity, recent work has focused on the use of systems biology to parse through and integrate all available "omics" data - genomics, transcriptomics, and metabolomics. However, sequencing data is better used for identification of novel mutations in metabolic disease [1, 17] and pathway activation [18], as germline mutations and transcript level changes do not always directly map to changes in a specific metabolic pathway. Additionally, metabolomics studies have been successfully used to identify metabolic shifts and implicate potentially altered metabolic pathways [19]. However, rapid metabolomics platforms serve as a hypothesis generating methodology because one cannot necessarily infer metabolic flux alterations a priori through metabolite level changes. Since the primary driver of metabolic phenotypes is alteration of flux, stable isotope tracing and metabolic flux analysis (MFA) have emerged as critically important tools for interrogating metabolism [20].

1.3.2 Stable isotope tracing

Modeling approaches have been applied to metabolic systems for some time and center around the need to conserve mass in the context of network stoichiometry and cellular needs [21]. These systems are often highly underdetermined, and fluxes are resolved to varying extents by the application of constraints, which may include uptake/secretion from media, transcriptomics or proteomics data, and/or isotopic labeling [22]. The most detailed information is often provided by the use of stable isotope tracing and metabolomics, whereby a given atom of interest is "tracked" throughout the metabolic network by culturing cells with a tracer (e.g. [1-¹³C]glutamine where ¹³C isotope is in the 1 position of the glutamine molecule). Analogous to a dye mixing through a continuously-stirred tank reactor, stable isotopes (e.g. ¹³C, ²H, and ¹⁵N) within a given substrate

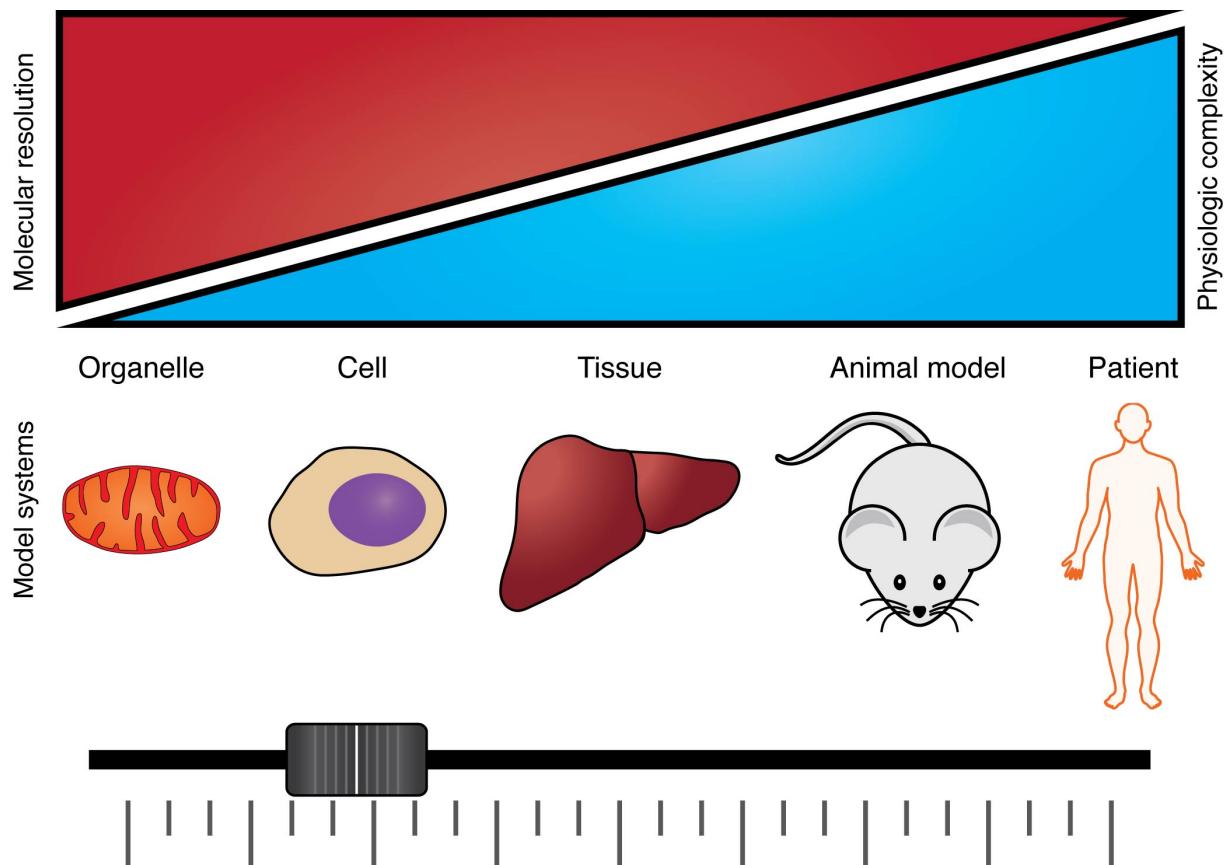


Figure 1.1: MFA applied to biological systems at different scales comes with a tradeoff in molecular resolution versus physiologic relevance. Use of metabolic flux analysis is technically feasible in many systems, but measurements in more physiologically complex systems come at a cost of molecular resolution. Integration of *in vivo* and *in vitro* MFA results will be important in the future as more therapeutic targets in metabolic pathways are identified.

are fed to cells, tissues, or animals which then consume the "heavy" metabolite of interest and metabolize it in various downstream reactions (Figure 1.2). By then measuring the presence of an isotopologue—a metabolite with a different molecular weight due to the presence of the stable isotope—the fraction of an individual molecule coming from a tracer can be quantified using knowledge of atom transitions throughout the metabolic network (Figure 1.2).

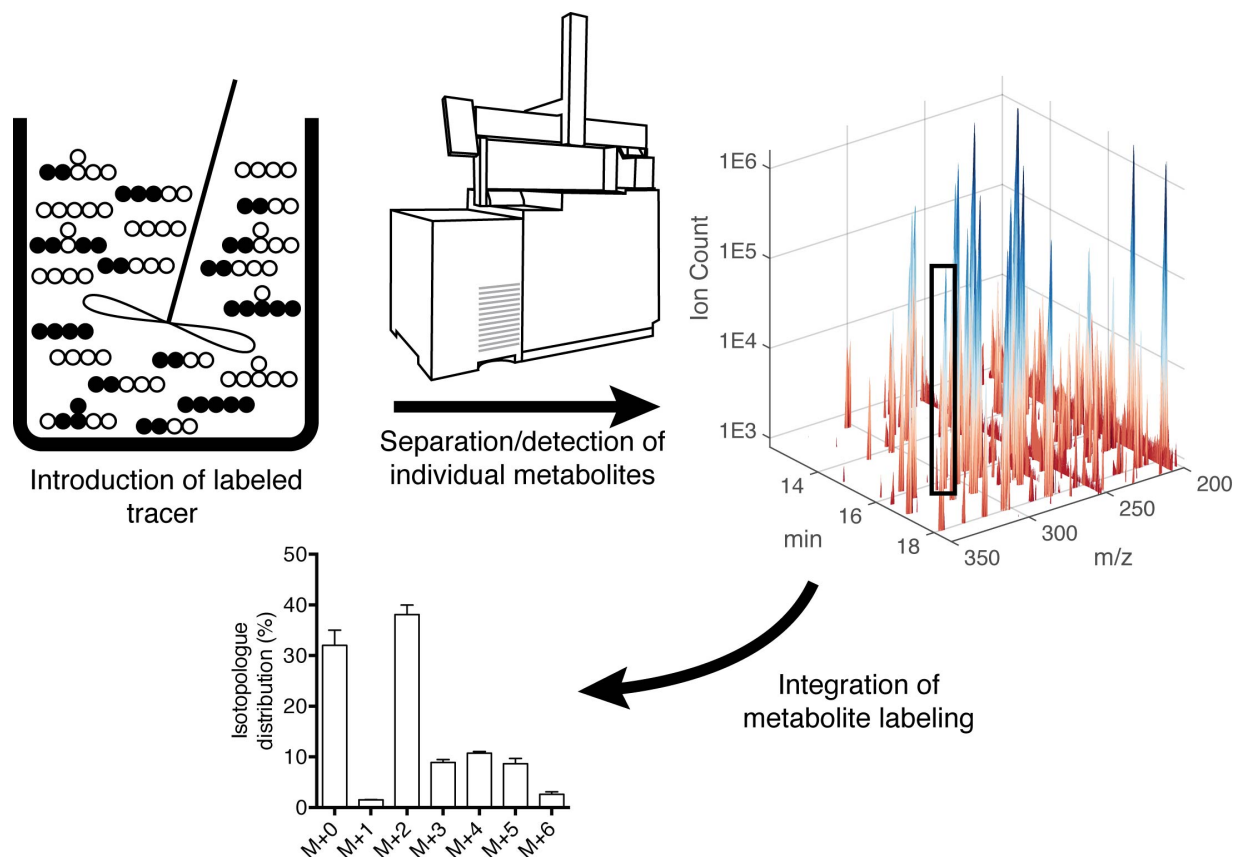


Figure 1.2: Stable isotope tracing paradigm. Isotopologue or mass isotopomer distributions (MIDs) are the central measurement in metabolic flux analysis. Stable isotope variants (i.e. ^{13}C , ^{15}N , ^2H) of carbohydrates, fatty acids, or amino acids are introduced into a biological system of interest. The labeled atoms of interest propagate throughout the metabolic network, and the biological matrix is sampled as needed. Mass spectrometry is used to measure isotope enrichment within individual metabolite pools to determine MIDs for all compounds of interest.

As an example, when cells metabolize $[\text{U-}^{13}\text{C}_6]\text{glucose}$ the fully-labeled pyruvate generated from glycolysis may be oxidized and/or carboxylated in mitochondria (Figure 1.3). When the cell oxidizes pyruvate, the ^{13}C carbon in the first position of pyruvate will be lost during the

decarboxylation step of pyruvate dehydrogenase (PDH), yielding an M+2 labeled AcCoA. When pyruvate is metabolized by pyruvate carboxylase (PC) all three ^{13}C atoms will be present on the resulting M+3 oxaloacetate. These metabolites condense to form citrate, resulting in a pool of labeled species with mass increments from 0 to 6, depending on the relative contribution of PC, PDH, and other pathways that produce or consume AcCoA, oxaloacetate, and citrate (Figure 1.3). This isotopologue or mass isotopomer distribution (MID) subsequently allows for inference of flux through certain metabolic reactions (Figure 1.2). In this simplified metabolite network, the ratio of the M+2 portion of the citrate pool vs the M+3 portion is a proxy of how many pyruvate molecules were catalyzed by PDH vs PC. However, data generated in real metabolic networks is more complex than that presented here due to TCA cycling and additional inputs into the citrate pool. Since many input and output fluxes influence labeling in well-connected metabolite pools, computational tools are often necessary to resolve information on fluxes for such systems [23].

MIDs therefore contain detailed information on relative fluxes, and these data are incorporated into models that estimate fluxes and associated confidence intervals within a given biological system [24]. The choice of tracer(s) will impact the specific pathways and fluxes to be resolved and should be considered carefully [25, 26]. Ultimately, MFA integrates extracellular flux measurements (e.g. glucose uptake and lactate secretion), biomass composition, growth rates, and intracellular steady state labeling data to estimate intracellular fluxes [27, 28]. By constraining potential flux measurements with physiological biomass demands and metabolite fluxes in and out of the system, MFA solves the inverse problem - where intracellular fluxes are estimated, theoretical labeling patterns calculated, error between theoretical and experimental data calculated, and estimated fluxes iterated through error minimization until a best fit is achieved [29]. Long applied to study microbial and prokaryote metabolic networks [24], advances in computational frameworks [30, 31] and software packages [32–36] have made mammalian applications far more tractable. Exchange fluxes (i.e. the minimum of the forward and reverse flux for a given reaction) can be the most difficult to resolve [37]. Compartmentation also complicates analyses

and interpretation of labeling data [29] and indeed MFA can help to resolve such information in certain settings [38–40]. Most MFA applications rely on the resolution of fluxes in a scaled-down, user-defined subset of the metabolic network, such as glycolysis, the oxPPP, and the TCA cycle [24]. Researchers have begun to apply genome-wide metabolic reaction networks in MFA studies of microbes more recently [41, 42].

Better resolution of intracellular fluxes can be achieved by incorporating dynamic labeling and pool size information into non-stationary MFA (NS-MFA) models. Steady-state labeling provides a relative measure of fluxes into and out of metabolic pools but requires the system to be at both metabolic and isotopic steady-state [43]. Such data are often not very informative for the analysis of linear pathways (e.g. glycolysis) or exchange fluxes. NS-MFA provides an alternative computational framework for integration of labeling data, extracellular fluxes, and biomass demands [44]. Unlike traditional MFA which relies on algebraic solutions, the transient labeling data and pool size data are incorporated into an ODE-based model [45]. While increased precision is achieved by incorporation of more experimental data, more care is needed on experimental design (e.g. sampling and quenching) and more data acquisition/analysis is required [44, 46]. This review will focus almost exclusively on steady-state MFA and basic tracing applications; however, use of NS-MFA has been reviewed extensively [47], and numerous protocols are available [44, 48, 49]. This approach is increasingly being applied to mammalian systems [50–52].

When applied in a coordinated fashion, stable isotope tracing, metabolomics, and computational modeling can effectively resolve metabolic flux alterations in the context of both microenvironmental cues and pathophysiological alterations. In short, stable isotopes can inform on aspects of metabolism that cannot be learned through other measurements. The remainder of this review will focus on recent examples in biomedicine of how stable isotope tracing and MFA have been used to understand the metabolic mechanisms driving human disease and associated pathologies. A primary (and still emerging) area of focus is applications to cancer biology, though

additional examples will be included to highlight the versatility of these approaches.

1.4 Cancer

1.4.1 Renewed appreciation of metabolic dysregulation in cancer

A desire to resolve the metabolic differences between normal tissue, tumors, and metastatic cells has re-invigorated interest in metabolic tracing and flux analysis over the last decade. Metabolism is tightly linked to the pathophysiology of a cancer cell, an observation first described by Otto Warburg in the early 20th century. He noted that rat tumors were susceptible to glucose deprivation (rather than oxygen deprivation) and exhibited higher than normal "fermentation" (glycolysis) to meet their ATP demands [53]. He later extended these observations to postulate mitochondrial dysfunction as the cause of neoplasia, since mitochondrial "poisons" are carcinogenic and cancer cells increased fermentation in response to irreversible low respiration rates [54]. Although at that time others (correctly) questioned whether mitochondrial dysfunction was a driver of neoplasia, in part due to radioactive isotope tracing indicating that mitochondria respiration was still active in cancer cells [55], the phenomenon that cancer cells are highly glycolytic was widely accepted [56]. Over time, however, the idea of metabolism as a driver of tumorigenesis largely fell to way side.

Cancer has now been reappreciated as a disease of metabolism [57, 58]. Recent work has succeeded in reinvigorating the study of metabolism as a means to both detect and study cancer growth [59, 60]. For example, since the late 1990s, accumulation of 2-deoxy-2- ^{18}F fluoro-D-glucose (FDG) and subsequent imaging through positron emission tomography (PET) has been an FDA-approved method (FDG-PET) for the noninvasive detection of tumors [61]. Related approaches now aim to study consumption of other nutrients or specific metabolic rates using novel tracer compounds or hyperpolarized NMR [62–65]. In addition to these diagnostic approaches, significant effort is now being applied to elucidate how metabolic pathways contribute to cancer

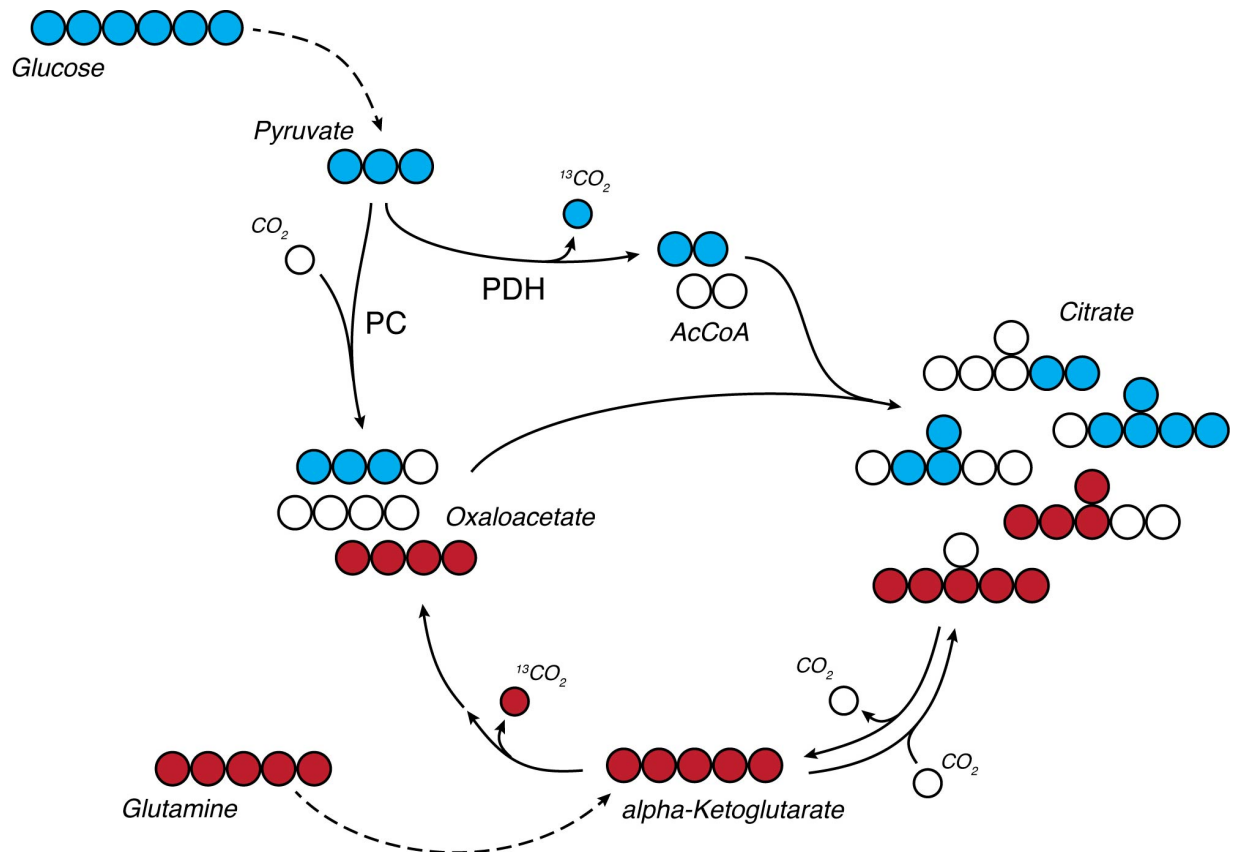


Figure 1.3: Tracing TCA metabolism using ^{13}C glucose and glutamine. In this example, labeling on citrate and other intermediates from fully labeled $[\text{U-}^{13}\text{C}_6]$ glucose changes depending on routes used for anaplerosis and AcCoA generation. Oxidation of glucose-derived pyruvate by PDH results in M+2 citrate. Carboxylation through PC results in M+3 or M+5 citrate. $[\text{U-}^{13}\text{C}_5]$ glutamine oxidation or reduction results in M+4 and M+5 citrate, respectively. Taken together, relative flux changes in well-connected nodes (e.g. TCA cycles) result in measurable differences in labeling. Open circles depict ^{12}C carbon atoms, filled circles depict ^{13}C carbon atoms.

initiation and progression [66].

Beyond the metabolic reprogramming required for proliferation, the discovery of mutations in genes encoding metabolic enzymes that directly impact tumorigenesis has been an important catalyst driving this resurgence in metabolic research [67, 68]. For example, the first widely characterized metabolic mutations were the loss of succinate dehydrogenase (SDH) and fumarate hydratase (FH), which are associated with development of paragangliomas and leiomyosarcomas, respectively [69]. These loss-of-function mutations lead to increases in succinate or fumarate levels within tumors, which are thought to inhibit aKG-dependent dioxygenases that impact HIF1 α stabilization and other biological processes [70–72]. Metabolic modeling was used to understand how a FH-null cancer cell could operate without a functional TCA cycle, elucidating a critical dependency on heme biosynthesis [73]. More generally, these findings highlighted critical links between metabolism and tumor formation while offering potential new avenues for therapeutic intervention.

Another critical demonstration of metabolic alterations in cancer is the discovery of mutant isocitrate dehydrogenase (mtIDH) tumors. First identified via exome sequencing of gliomas [74, 75], both IDH1 and IDH2 are now known to be mutated somewhat frequently in acute myeloid leukemia, low-grade gliomas, and chondrosarcomas [76]. These mutations are characterized by a gain-of-function, where D-2-hydroxyglutarate (2HG) is produced at millimolar concentrations intracellularly [77]. Mutant IDH1 and IDH2 reduce aKG to 2HG by consuming an NADPH reducing equivalent, either in the cytosol or mitochondria [78]. Similar to SDH and FH-null tumors, 2HG can disrupt aKG-dependent dioxygenase activity, in particular those regulating DNA and histone demethylation, and tumors often present with hypermethylation phenotype [79–83]. This mutation connects a fundamental node in the metabolic network with deep biological perturbations that are associated with tumor progression. Due to the highly compartment-specific and cofactor-dependent nature of this class of mutations, metabolic tracing is uniquely situated to understand the underlying metabolic features in these tumors [84]. However, cells harboring

such mutations exhibit only minor metabolic changes under normal physiological conditions, but under hypoxic or pharmacological redox stresses that impact mitochondrial function more tractable changes have emerged [85–87].

While these examples demonstrate how mutations in TCA cycle enzymes directly contribute to tumorigenesis, cancers in general hijack different metabolic pathways to fuel their proliferative needs (Figure 1.4). These pathways vary with environment, tissue of origin, and the genetic landscape of that cell. Therefore, a critical need exists to extend these MFA methods to understand how diverse cancers alter their metabolism to survive and what metabolic features can be therapeutically targeted.

1.4.2 Glutamine metabolism

Glutamine, the most abundant amino acid in plasma and culture media, is consumed by cancer cells *in vitro* at rates greater than any other amino acid. As such, glucose and glutamine are the most highly consumed carbon substrates in tumor cell cultures. Despite this fact, Hosios et al. recently applied ^{13}C and ^{14}C tracers to observe that glucose and glutamine only make up 25% of a cancer cell's total dry weight and only around 50% of its carbon [88]. The remaining carbon was found to come generally from amino acid uptake (both essential and non-essential amino acids), highlighting the large protein component of mammalian cells and contrasting lower organisms that can derive their biomass carbon entirely from glucose [88]. These data showcase the utility of flux-based studies that trace the fate of carbon atoms within cells, as more traditional "black box" approach (i.e. only looking at metabolite secretions and uptakes) would have suggested a smaller role for amino acid carbon.

These results also demonstrate the importance of protein synthesis for cancer cell growth, which requires both carbon and nitrogen. Indeed, glutamine is first and foremost a nitrogen donor (and/or carrier) within mammals. It is a precursor to glutamate, proline, and other amino acids; in addition, it is also an obligate nitrogen donor for asparagine, nucleotides, and hexosamines.

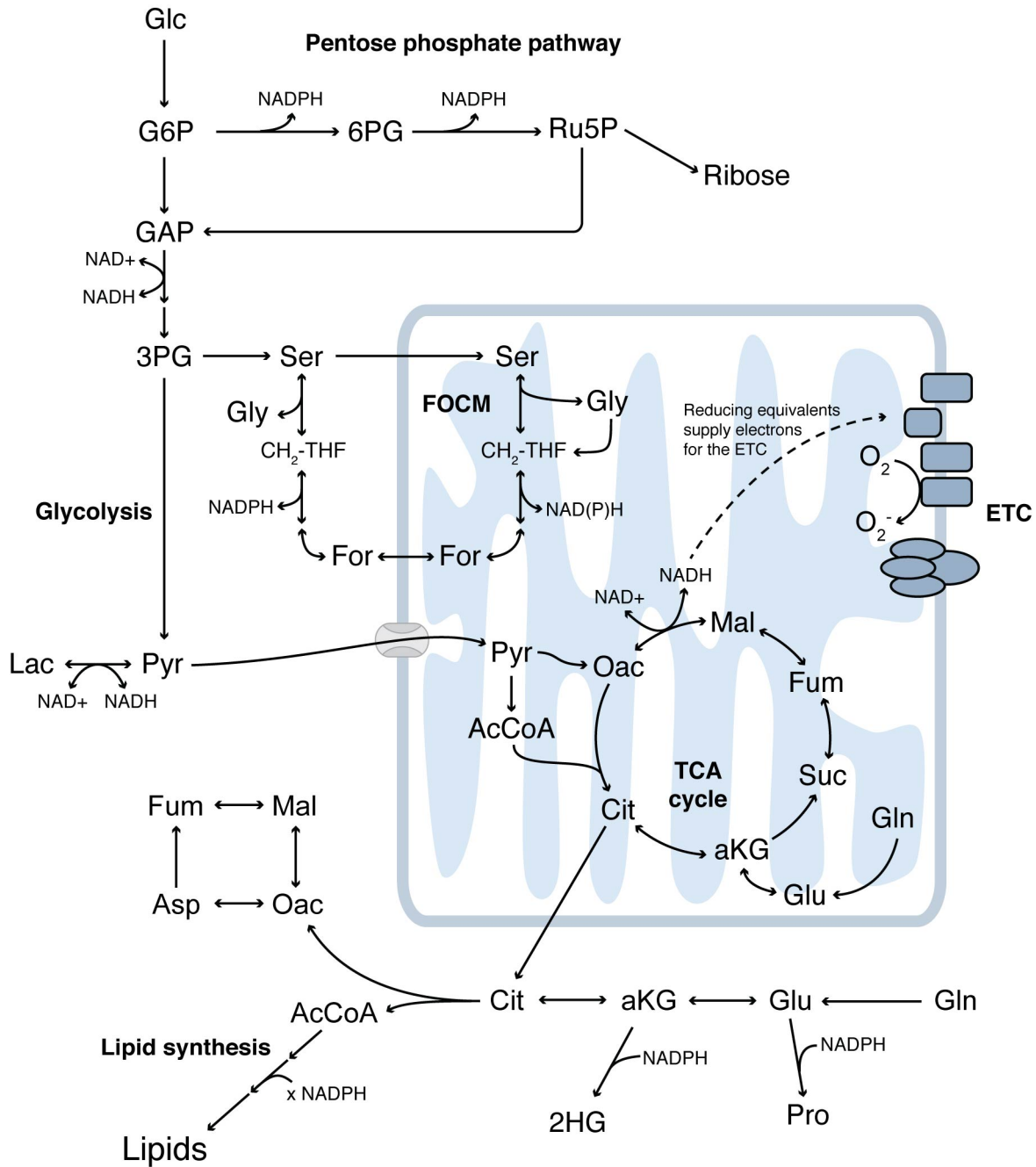


Figure 1.4: Metabolic pathways dysregulated in the context of disease. Glycolysis and the pentose phosphate pathway are fueled by glucose and generate biosynthetic intermediates, reducing equivalents, and ATP. Mitochondria are fueled by pyruvate, amino acids, and lipids, performing both anabolic and catabolic metabolism to generate energy. Serine, glycine, and folate-mediated one carbon metabolism are active in both cytosol and mitochondrial compartments. These pathways are connected orthogonally via cofactors and other disease- or tissue-specific pathways; as such, pathways beyond central carbon metabolism must be investigated in specific biological contexts.

Several studies have highlighted the importance of glutamine availability in driving these processes [89–91]. In fact, hexosamine biosynthetic fluxes in cultured cells are similar those measured for nucleotide (i.e., ribose) synthesis in proliferating stem cells [92]. Glutathione is an antioxidant present at high concentrations within cells, and recent studies have highlighted the role of glutaminase and the xCT transporter in coordinating glutamine uptake, glutamate secretion, and cystine consumption from culture medium in cancer cells [93, 94]. Indeed, the high rates of glutaminolysis that occur in cultured tumor cells is at least partially attributable to the need for cystine uptake.

In the absence of glutamine, cancer cells can become dependent on non-essential amino acid or protein uptake from stroma or the microenvironment, respectively. Tracer-based studies have described the importance of macropinocytosis and autophagy in allowing tumors to acquire proteinogenic amino acids under such nutrient-limiting conditions [95–97]. Alternatively, pancreatic tumor stroma use autophagy to provide alanine for cancer cell growth [98]. Yang et al. performed MFA modeling to delineate the role of cancer-associated fibroblasts (CAFs) in providing glutamine to ovarian cancer cells [99]. Although it remains challenging to deconvolute labeling results and decipher cell-specific fluxes [100], analysis of systems containing multiple cell types will continue to grow in importance as we gain a better understanding of tumor heterogeneity and immune cell interactions.

Some tumor cells rewire their mitochondria such that alternate substrates are used to fuel TCA metabolism. For example, the mitochondrial pyruvate carrier (MPC) is often expressed at lower levels in colorectal cancer and over-expression of MPC mitigates cell growth under anchorage-independence or as xenografts [101]. Notably, respiration is unchanged upon inhibition or knockdown of MPC [102], suggesting mitochondria remain functional and active. MFA studies on cells with reduced MPC activity or expression have highlighted how cells compensate when pyruvate flux into mitochondria is compromised [38, 103]. Under these conditions, glutaminolysis is significantly increased to maintain anaplerotic flux and biosynthesis of amino acids (e.g.

aspartate), nucleotides, and fatty acids. -oxidation of fatty acids was increased nearly 10-fold in *Mpc2* knockdown cells, and additional evidence indicated that BCAA catabolism was elevated upon MPC inhibition [38]. These studies highlight how mitochondria adapt to MPC inhibition. While this rewiring may benefit tumor growth, therapeutic benefits in diseases such as metabolic syndrome and neurodegeneration may also emerge [104–107].

Oxidative stress also causes rewiring of glutamine metabolism within mitochondria. Indeed, in response to hypoxic insult pyruvate oxidation is decreased [108] and cells rely on glutamine to support proliferation [109]. Glutaminolytic flux is increased to support oxidative TCA metabolism [85, 110, 111], since respiration remains active in low oxygen conditions. Thus, oxidation of aKG sustains respiration. However, NADP-dependent IDHs are reversible and have the capacity to reductively carboxylate aKG in mammals [112, 113], offering cells another pathway to generate AcCoA and reducing equivalents. Detailed tracer studies and MFA have more recently been applied to better understand how this pathway is controlled. Indeed, hypoxia reprograms TCA metabolism such that reductive carboxylation is the major route through which cells produce citrate and lipogenic AcCoA [114, 115]. Similar changes occur in "pseudohypoxic" renal carcinoma cells (RCC) that are deficient in the Von Hippel-Lindau tumor suppressor [114, 115]; tumors where this pathway may be therapeutically relevant. Indeed, evidence from *in vivo* tumor models and patient samples suggest this mode of TCA metabolism is active in VHL-deficient RCC downstream of HIFs [116, 117]. This pathway also seems critical for aspartate production upstream of the pyrimidine synthesis pathway [118].

At the same time, mitochondrial redox stress caused by mutations in mitochondrial Complex I or III induce cells to activate the reductive carboxylation pathway, with similar changes occurring using pharmacological inhibitors of the electron transport chain (ETC) [119]. Roles for the mitochondrial nicotinamide nucleotide transhydrogenase (NNT) enzyme in driving this metabolic state have also been established [120, 121]. These findings have all suggesting that the cellular redox state and pyridine nucleotides influence reductive carboxylation activity.

Indeed, modulation of NAD⁺/NADH ratio and citrate abundance are critical drivers of reductive carboxylation flux [122]. As such, activity in this pathway seems to be driven by redox stress caused by many different physiological conditions, including hypoxia, mitochondrial inhibitors, and lipid deficiency.

1.4.3 Redox metabolism

Reducing equivalents in the cell are transported between reactions using pyridine nucleotides, NAD⁺ and NADP⁺. These cofactors are essential for the various oxidoreductase reactions required for proper biosynthesis and redox control, with NADPH selectively required for cellular anabolism (i.e. fatty acid and proline synthesis) and antioxidant response (i.e. regeneration of GSH) [3]. A major contributor to cytosolic NADPH production is the oxPPP [123], extensively studied with a variety of ¹³C glucose tracers [25, 124]. However, these tracers cannot establish cofactor specificity and do not directly measure reducing equivalent pool.

Instead, because the transfer of electrons occurs through the transfer of a hydride anion, use of ³H (tritium) [125, 126] and ²H (deuterium) [127, 128] glucose tracers provides deep insight into cellular electron pools. Through the use of [1-²H] and [3-²H]glucose tracers, labeling of cytosolic NADPH was achieved through oxPPP enzymes, G6PD and PGD respectively [51, 129]. Total cellular NADPH production flux was estimated to be 10 nmol L⁻¹ hr⁻¹ (5-20% of glucose uptake rate) by estimation of oxPPP contribution to NADPH and measurement oxPPP flux [51]. Concomitant analysis of NADPH consumption (i.e. fatty acid, DNA, and proline synthesis) revealed that biosynthetic demands of NADPH was only 80% of production with the rest presumably used in redox defense [51]. Hydride transfer from NADPH to lipids can also be used as an indirect measure of cytosolic NADPH labeling, such that ISA-based modeling allows estimation of tracer contributions to this metabolic pool [129]. The importance of the oxidative pentose phosphate pathway in pluripotent stem cells (greater than many cancer cells) [130] and malic enzyme in adipocytes [130] have been elucidated using this approach.

Reducing equivalents cannot be directly transported across intracellular membranes (e.g. mitochondria) and these reactions are highly compartmentalized [123]. Instead, the cell relies on futile metabolic cycles to transport reducing equivalents into organelles (e.g. malate-aspartate shuttle) and maintain proper, compartmental redox homeostasis [131]. Use of [4-²H]glucose was able to label both cytosolic and mitochondrial NADH pools, through GAPDH and malate-aspartate shuttle respectively [129]. To better elucidate compartment-specific redox metabolism, an endogenous redox reporter system was developed through low-level, ecotopic expression of mtIDH in cytosol or mitochondria [129]. Examination of labeling on 2HG found that the oxPPP contributed significantly to cytosolic NADPH but the mitochondrial NADPH pool was mostly labeled by hydride anions from NADH [129]. Taken together, these results highlight the powerful application of positional deuterium labels as donors for compartment-specific electron pools.

Somatic cells have evolved their metabolism to reside within distinct niches. Normal cells reside in close contact with the extracellular matrix (ECM). For a cancerous cell to metastasize to a distant site, the cell must depart its ECM-rich niche and survive in atypical microenvironments. Cancer cells undergoing metastasis must therefore reprogram metabolic pathways to overcome such stresses. Previous studies have shown that ECM-detachment induces increased levels of cellular reactive oxygen species (ROS) and can lead to anoikis in non-transformed cells [132]. Activation of the PI(3)K pathway in this context led to higher glucose consumption and increased cell survival after ECM detachment, due to increased oxPPP flux and which maintains β -oxidation and ATP levels [132, 133]. More recently, Piskounova et al. observed that metastatic cells increased expression of enzymes in one carbon metabolism (discussed below) and more specifically the mitochondrial NADPH producing enzyme, *ALDH1L2* [134]. These enzymes increase survival of ECM-detached cancer cells and enhance metastatic potential of tumor cells *in vivo* [134].

Stable isotope tracing has recently been used to elucidate the specific directionality of how some cellular metabolic pathways are perturbed to enable NADPH production under anchorage

independent stress. Using both ^{13}C glucose and glutamine tracers, cells grown in anchorage-independent conditions were found to oxidize less glucose and exhibited increased reductive carboxylation activity [39]. However, unlike previous studies of reductive carboxylation, these effects were not due to any HIF-mediated changes to the cell, did not change the contribution of glutamine carbon to fatty acid synthesis, and could be reversed by simply re-attaching the cells to ECM [39]. Instead, reductive carboxylation flux coordinated metabolic shuttling of cytosolic NADPH into the mitochondrial matrix to enhance cell survival [39]. Furthermore, CRISPR knockouts of both *IDH1* and *IDH2* and $[3\text{-}^2\text{H}]$ glucose tracing confirmed that reductive carboxylation flux occurred in the cytosol but used to generate mitochondrial NADPH [39]. This leaves a model where cells protect against increased mitochondrial oxidative stress after detachment by using the futile cycle of *IDH1* and *IDH2* to transport NADPH into the mitochondria and regenerate mitochondrial GSH.

1.4.4 Serine biosynthesis and one carbon metabolism

Serine is a critically important metabolite for proliferating cells given its role in biosynthetic and redox-associated pathways [135]. Indeed, phosphoglycerate dehydrogenase (PHGDH) catalyzes one of the initial steps of serine synthesis and is amplified in some breast cancers and melanomas [136, 137]. Glycine lies immediately downstream of serine and is important for cell growth due to its use in purine metabolism and glutathione synthesis [138]. Serine also contributes to folate-mediated one carbon metabolism (FOCM), which lies at a critical biosynthetic node supporting nucleotide synthesis as well as methylation [139, 140]. Intriguingly, several enzymes within these pathways are expressed at higher levels in aggressive tumors, including the mitochondrial enzyme methylene tetrahydrofolate dehydrogenase 2 (*MTHFD2*) [141]. And this pathway is classically targeted in cancer and autoimmune diseases using the chemotherapeutics methotrexate or Pemetrexed [142]. However, even with the wealth of evidence demonstrating its importance, the specific mechanisms through which this pathway supports tumor growth and

survival is still not definitively clear.

Analysis of tumor cell responses to serine and glycine deprivation has identified specific susceptibilities in cells as a function of their genotype. In particular, loss of p53 sensitized colon cancer cells to serine/glycine starvation by arresting cells in the G1 phase of the cell cycle [143]. Additionally, p53 deficiency induced shunting of serine to glycine for glutathione synthesis to support antioxidant functions [143]. Various other stress (often associated with redox) can modulate sensitivity to serine and/or glycine deprivation as well as the serine synthesis pathway, including metformin and hypoxia [144, 145]. More recently, serine and glycine deprivation was shown to reduce tumor growth in several genetically-engineered mouse models of cancer [146]. These results highlight the importance of serine availability for tumor growth, though the metabolic driver of this sensitization downstream of serine is not fully clear. To this end, Jain et al. applied extracellular flux analysis of metabolites consumed and secreted by the NCI-60 panel of cell lines and observed that glycine uptake correlated most tightly with cell growth rate [138]. Tracing with [¹³C]glycine was then used to suggest that the glycine is directly used to support de novo purine synthesis rather supplying 1C units [138]. However, glycine alone does not rescue cell growth in serine-deprived conditions [143, 147]. Extensive tracing of serine and glycine conversion to nucleotides in HCT116 cells has indicated that glycine cannot replace serine due to the required consumption of 1C units and its impact on purine nucleotides [147], suggesting that cells selectively uptake serine to generate both glycine and 1C units.

Notably, removal of dietary serine and glycine was not effective in Kras mutant tumors, presumably due to the upregulation of serine biosynthesis in tumors of this genotype [146]. Other oncogenic pathways have also been associated with this metabolic pathway. For example, NRF2 is the master transcriptional regulator of the cellular antioxidant response and regulates expression of serine biosynthesis enzymes in non-small cell lung cancer [148]. Through a mechanism driven by the transcription factor ATF4, NRF2 expression was found to contribute to tumorigenesis by activating serine biosynthesis and supporting FOCM and transsulfuration

reactions (glutathione) [148]. Similar mechanisms mediated through mTORC1 have also been implicated to upregulate de novo purine biosynthesis [149]. Consistent with the amplification of PHGDH in breast cancers and activation by ATF4, these pathways are important for breast cancer cell in anchorage-independent conditions and as xenografts. Taken together, these results highlight an important role for serine metabolism in tumor growth, in particular downstream of cellular stresses.

Beyond nucleotide biosynthesis, serine has an established role in supplying mitochondrial glycine/1C units through FOCM, with the former contributing to heme biosynthesis. Importantly, FOCM can supply mitochondrial reducing equivalents through 1C oxidation enzymes (e.g. *MTHFD2*, *MTHFD2L*, *ALDH1L1*) [139, 140] or glycine cleavage [150], and flux balance analysis (FBA) modeling has suggested this pathway coordinates ATP regeneration along with glycolysis [151]. Experimental evidence has also recently supported a role for this pathway in generating reducing equivalents in proliferating cells. Indeed, only knockdown of oxPPP and FOCM enzymes perturbed cellular redox state [51]. Additionally, glycine oxidation measured with ¹⁴C tracers was found to be greater than purine synthesis rates, further suggesting a role in redox homeostasis [51]. Through the use of mutant IDH2 reporters and ²H serine tracers (section 3.3), FOCM was demonstrated to contribute significantly to mitochondrial reducing equivalent pools [129]. Importantly, minimal label from serine was observed in cytosolic reporters or on palmitate, suggesting mitochondrial oxidation of 1C units *MTHFD2* or *MTHFD2L* was the predominant route of NAD(P)H regeneration in this pathway [129]. In fact, as previously suggested by Herbig et al. [152], most cells were found to supply cytosolic 1C units through mitochondrial FOCM flux, even to the point of secreting excess formate [153, 154]. Loss of mitochondrial FOCM enzymes made cells dependent on extracellular serine/glycine and retarded growth of xenografts, but compensatory reversal of FOCM flux was observed both *in vitro* and *in vivo* [154]. Several studies have also connected these pathways to cancer through hypoxia and "stemness" [141, 145, 155], highlighting the need to study flux through this pathway in various microenvironments and

biological contexts.

1.5 Emerging links between metabolism and epigenetics

Finally, recent studies have established critical links between metabolic pathways and cellular epigenetics. Canonical epigenetic "marks" (e.g. methylation, acetylation) on DNA, RNA, and proteins are all metabolic intermediates and demonstrate a powerful relationship between metabolic pathway flux and epigenetic regulation [156]. In this manner, altered metabolic pathway activity can influence gene expression in the context of disease (reviewed extensively for cancer in [157]). Many metabolites (e.g. AcCoA, NAD⁺, aKG) also moonlight as substrates for the enzymatic addition and removal of epigenetic "marks" and other post-translational modifications [158]. In turn, numerous studies have elucidated how availability and/or localization of these metabolites can control histone acetylation [159, 160], enzyme acetylation [161, 162], and histone/nucleotide methylation (see section 3.1. discussion on aKG-dependent dioxygenases). For example, modulation of acetyl-CoA synthetase expression within the hippocampus decreased availability of AcCoA for histone acetylation and impaired long-term spatial memory [163]. While these studies have effectively demonstrated the causal link between metabolism and epigenetics, how dysregulation of distal metabolic pathways can modulate epigenetics remains poorly understood in many contexts. The widely studied epigenetic signature, methylation, connects amino acid metabolism (methionine and serine) to nucleotides through transfer of methyl groups [164] and provides one such example of distal metabolic reprogramming of epigenetics.

While methionine is considered the primary methylation donor through S-adenosyl methionine (SAM) pools [165], generation of 1C units from serine and remethylation of homocysteine provides an alternate source that links glycolytic flux to methylation [166]. Indeed *in vivo* tracer analysis of whole-body SAM pools confirmed that methionine was the primary donor of methyl

groups (70% of methyl group flux), though 1C units needed for re-methylation came solely from serine (estimated to be 3% of total serine flux) [167]. Loss of the nutrient sensor LKB1 increased serine biosynthesis and cycling that led to enhanced DNA methylation and retrotransposon silencing in a mouse-model of pancreatic cancer [168]. In addition, methionine deprivation reversibly altered histone methylation (e.g. H3K4me3) and expression of 1C-consuming enzymes to presumably reduce SAM consumption [169]. On the other hand, *in vitro* analysis of cellular DNA and RNA found that serine provided 1C units for methylation only under methionine starvation conditions [170]. Serine, however, was found to support methylation through purine synthesis (i.e. ATP) for SAM production [170]. These findings highlight yet another set of pathways and biological functions through which serine influences cancer biology.

1.6 Observations from *in vivo* studies

Many of the studies discussed above applied MFA and related approaches to cancer cells cultured *in vitro*. Clearly, *in vivo* models better recapitulate the physiologic conditions of human tumors; as such, increasing efforts have focused on *in vivo* tracing methods to characterize metabolism in these settings. However, the design, execution, and interpretation of such studies is complicated by a number of different factors: 1) administration of tracer may impact metabolism and downstream signaling, which is particularly important for glucose and insulin signaling, 2) labeling is quickly scrambled due to cross-tissue metabolic activity, and 3) multiple cell types exist within each tissue (e.g. epithelia, stroma). As such, comprehensive models that incorporate isotope labeling data from *in vivo* studies may have limited impact. On the other hand, analyses that focus on specific pathways/reactions have yielded insights into the metabolism of tumors *in vivo*.

As noted above, glutamine's role as a major substrate fueling TCA metabolism in cancer cells is well documented [171]. The concept of decreased glucose oxidation and increased

glutamine anaplerosis has largely been studied using *in vitro* models [91, 114, 116]. More recently, *in vivo* studies have challenged the concept that glutamine rather than glucose is the predominant supporting the TCA cycle in tumors. While some early studies highlighted a potential role for glutamine synthase (GS) in supporting breast cancer growth [172], more definitive evidence of GS supporting tumor growth has come from *in vivo* tracing studies. Using ¹⁵N tracing, Tardito et al. observed that glioblastoma cell lines sustained growth in physiological and glutamine-free conditions through the amination of glutamate to provide glutamine for purine synthesis [173]. Subsequently, infusion of mice (or human patients) with either ¹³C glucose or ¹³C glutamine followed by enrichment analysis demonstrated that both GBM xenografts and contralateral primary brain tissues synthesized glutamine *de novo* from glucose, with little evidence of high glutaminolysis activity [173].

If glutamine is not required for anaplerosis, what pathways take its place *in vivo*? To this end, early studies on the mitochondrial metabolism of non-small-cell lung cancer (NSCLC) tumors noted increased PC activity in human tumor biopsies that were infused with ¹³C glucose prior to surgery and analyzed by NMR [174]. These results and additional studies with tumor slices incubated with ¹³C glucose and glutamine tracers demonstrated that pyruvate carboxylase (PC) was an important anaplerotic path used by tumor cells to support mitochondrial metabolism [174]. Subsequently, knockdown of PC in lung cancer cell lines severely limited biosynthesis and growth of these cells as xenografts [174]. Similar results were previously noted in cell-based tracer studies using glutamine-free conditions [175]. Indeed, PC may emerge as a more critical enzyme in tumors with defective TCA metabolism. For example, PC flux is critical for supporting aspartate synthesis in cultured SDH-null cells [176, 177]. However how these rare tumors metabolize glucose and glutamine *in vivo* is not well characterized.

Detailed tracer studies in genetically engineered mouse models (GEMMs) of lung cancer as well as human patients have further supported the importance of glucose oxidation and anaplerosis in tumors [174, 178, 179]. Infusion of glucose tracers and enrichment analysis in

three independent NSCLC GEMMs demonstrated that all tumor types exhibited increased glucose oxidation through PDH and PC as compared to adjacent normal lung tissue [178]. However, when cells derived from the GEMMs are placed *in vitro*, there is an increased reliance on glutamine, and Glis1 knockout cell lines could not be expanded in culture [178]. Conversely, knockout cell lines of both *Pdh1a* and *Pcx* in GEMM cells were successfully isolated *in vitro* but could not form xenografts [178]. The importance of mitochondrial glucose metabolism has also been demonstrated in human lung tumors [179]. After first examining tumor characteristics such as grade, stage, stromal fraction, mutation status, and perfusion, Hensley et al. infused ^{13}C glucose before quantifying isotope enrichment within tumor biopsies and normal lung tissue [179]. Interestingly, lactate labeling suggested catabolism of lactate itself contributed significantly more to tumors, and this was confirmed using a ^{13}C lactate tracer in syngenic mouse xenograft models [179]. Finally, by correlating enrichment results with tumor perfusion data, a model where highly perfused tumors consumed more alternative fuels from the circulation (e.g. lactate) and less perfused tumors more exclusively used glucose as a primary fuel source was constructed [179]. These findings challenge Warburg's notion of defective mitochondria and the concept that tumors preferentially use glycolysis which pervades the literature.

Beyond mitochondrial metabolism, the routes through which tumors acquire lipids are also of great interest to the research community. Fatty acids can be taken up through the circulation or synthesized *de novo*. In fact, some cancer cell populations upregulate expression of CD36, a fatty acid scavenger that is also important for the survival of metastatic cells [180–182]. While some cell types preferentially consume lipids from their environment [130, 183], many tumors upregulate fatty acid biosynthetic machinery [184–186]. In human cancers, aggressiveness is correlated with upregulation of fatty acid synthesis machinery (FASN) but different cell types show varying sensitivity to FASN inhibition [187]. While sensitivity to FASN inhibition could not be explained by the relative rate of palmitate synthesis, application of ^{13}C glucose and lipidomics to quantify synthesis of intact lipids indicated that FASN inhibitor sensitivity correlated with

the synthesis of signaling lipids [187]. However, lipids are significantly more abundant in the body compared to cell culture media, so questions remained about the importance of *de novo* lipogenesis for tumor progression. To this end, fatty acid synthesis is readily quantified *in vivo* using $^2\text{H}_2\text{O}$, as deuterons are incorporated into fatty acids through numerous pathways [188]. Administration of $^2\text{H}_2\text{O}$ to tumor-bearing mice indicated that tumor lipids contained large fractions of newly synthesized fatty acids [189]. Similar results were obtained in both xenografts and GEMMs, which are better vascularized and likely to have adequate circulating lipids available [189]. Furthermore, treatment of these animal models with an AcCoA carboxylase inhibitor impeded growth and synergized with co-treatment carboplatin [189]. Taken together, while cell culture-based experiments will continue to be important for defining metabolic processes at the cellular and sub-cellular levels, these studies highlight the importance and utility of analyzing tumors in their physiologic microenvironment.

1.7 Conclusion

Metabolomics, stable isotope tracing, and metabolic flux analysis are powerful platform technologies that facilitate the study of human disease. Through careful design and execution of MFA experiments, researchers now have the ability to interrogate metabolic fluxes in a variety of biological contexts. Simplified systems provide molecular-level resolution but lack physiological relevance; *in vivo* models and patient studies have more clinical significance but provide less mechanistic insight (Figure 1.1). A wealth of new knowledge into the metabolic basis of tumorigenesis and cancer cell proliferation has now emerged over the past decade. Since each tissue and disease state involves distinct metabolic pathways, application of MFA to various biological systems offers a path that will be rich in new discoveries. For example, with a well-described role of metabolism [190], MFA is increasingly being applied to study unique features of hPSCs and their regenerative medicine applications [130, 191]. Established metabolic pathways

are now being observed to have distinct functions in certain tissues or cell types [192, 193], and new pathways are being discovered that modulate immune cell function [194, 195]. In all these situations, elucidation of metabolic fluxes will be essential to fully appreciate the mechanisms through which metabolism contributes to human disease.

1.8 Acknowledgements

We thank Mari Gartner and members of the Metallo Lab for their helpful feedback and apologize to those researchers whose work we were unable to cite. This work was supported by the California Institute of Regenerative Medicine (RB5-07356), an NSF CAREER Award (1454425), NIH grant (R01-CA188652), and a Camille and Henry Dreyfus Teacher-Scholar Award (all to C.M.M.). M.G.B. is supported by a NSF Graduate Research Fellowship (DGE-1144086).

Chapter 1, in full, is a reprint of the material as it appears in "Reverse engineering the cancer metabolic network using flux analysis to understand drivers of human disease," *Metabolic Engineering*, vol. 45, 2018. Mehmet G. Badur is the primary author of this publication. Christian M. Metallo is the corresponding author of this publication.

1.9 References

1. Cancer Genome Atlas Research, N., Weinstein, J. N., Collisson, E. A., Mills, G. B., Shaw, K. R., Ozenberger, B. A., Ellrott, K., Shmulevich, I., Sander, C. & Stuart, J. M. The Cancer Genome Atlas Pan-Cancer analysis project. *Nat Genet* **45**, 1113–20 (2013).
2. Cordes, T. & Metallo, C. M. Tracing insights into human metabolism using chemical engineering approaches. *Curr Opin Chem Eng* **14**, 72–81 (2016).
3. Lunt, S. Y. & Vander Heiden, M. G. Aerobic glycolysis: meeting the metabolic requirements of cell proliferation. *Annu Rev Cell Dev Biol* **27**, 441–64 (2011).
4. Park, J. O., Rubin, S. A., Xu, Y. F., Amador-Noguez, D., Fan, J., Shlomi, T. & Rabinowitz, J. D. Metabolite concentrations, fluxes and free energies imply efficient enzyme usage. *Nat Chem Biol* **12**, 482–9 (2016).

5. Bennett, B. D., Kimball, E. H., Gao, M., Osterhout, R., Van Dien, S. J. & Rabinowitz, J. D. Absolute metabolite concentrations and implied enzyme active site occupancy in *Escherichia coli*. *Nat Chem Biol* **5**, 593–9 (2009).
6. Nagrath, D., Avila-Elchiver, M., Berthiaume, F., Tilles, A. W., Messac, A. & Yarmush, M. L. Integrated energy and flux balance based multiobjective framework for large-scale metabolic networks. *Ann Biomed Eng* **35**, 863–85 (2007).
7. Beard, D. A., Liang, S. D. & Qian, H. Energy balance for analysis of complex metabolic networks. *Biophys J* **83**, 79–86 (2002).
8. Beard, D. A. & Qian, H. Thermodynamic-based computational profiling of cellular regulatory control in hepatocyte metabolism. *Am J Physiol Endocrinol Metab* **288**, E633–44 (2005).
9. Jacobus, W. E. Respiratory control and the integration of heart high-energy phosphate metabolism by mitochondrial creatine kinase. *Annu Rev Physiol* **47**, 707–25 (1985).
10. Hochachka, P. W. & McClelland, G. B. Cellular metabolic homeostasis during large-scale change in ATP turnover rates in muscles. *J Exp Biol* **200**, 381–6 (1997).
11. Lemons, J. M., Feng, X. J., Bennett, B. D., Legesse-Miller, A., Johnson, E. L., Raitman, I., Pollina, E. A., Rabitz, H. A., Rabinowitz, J. D. & Collier, H. A. Quiescent fibroblasts exhibit high metabolic activity. *PLoS Biol* **8**, e1000514 (2010).
12. Hackett, S. R., Zanutelli, V. R., Xu, W., Goya, J., Park, J. O., Perlman, D. H., Gibney, P. A., Botstein, D., Storey, J. D. & Rabinowitz, J. D. Systems-level analysis of mechanisms regulating yeast metabolic flux. *Science* **354** (2016).
13. Fiehn, O., Kopka, J., Dormann, P., Altmann, T., Trethewey, R. N. & Willmitzer, L. Metabolite profiling for plant functional genomics. *Nat Biotechnol* **18**, 1157–61 (2000).
14. Mitsuishi, Y., Taguchi, K., Kawatani, Y., Shibata, T., Nukiwa, T., Aburatani, H., Yamamoto, M. & Motohashi, H. Nrf2 redirects glucose and glutamine into anabolic pathways in metabolic reprogramming. *Cancer Cell* **22**, 66–79 (2012).
15. Lunt, S. Y., Muralidhar, V., Hosios, A. M., Israelsen, W. J., Gui, D. Y., Newhouse, L., Ogrodzinski, M., Hecht, V., Xu, K., Acevedo, P. N., Hollern, D. P., Bellinger, G., Dayton, T. L., Christen, S., Elia, I., Dinh, A. T., Stephanopoulos, G., Manalis, S. R., Yaffe, M. B., Andrechek, E. R., Fendt, S. M. & Vander Heiden, M. G. Pyruvate kinase isoform expression alters nucleotide synthesis to impact cell proliferation. *Mol Cell* **57**, 95–107 (2015).
16. Park, T. J., Reznick, J., Peterson, B. L., Blass, G., Omerbasic, D., Bennett, N. C., Kuich, P., Zasada, C., Browe, B. M., Hamann, W., Applegate, D. T., Radke, M. H., Kosten, T., Lutermann, H., Gavaghan, V., Eigenbrod, O., Begay, V., Amoroso, V. G., Govind, V.,

- Minshall, R. D., Smith, E. S. J., Larson, J., Gotthardt, M., Kempa, S. & Lewin, G. R. Fructose-driven glycolysis supports anoxia resistance in the naked mole-rat. *Science* **356**, 307–311 (2017).
17. Lewis, N. E., Schramm, G., Bordbar, A., Schellenberger, J., Andersen, M. P., Cheng, J. K., Patel, N., Yee, A., Lewis, R. A., Eils, R., Konig, R. & Palsson, B. O. Large-scale in silico modeling of metabolic interactions between cell types in the human brain. *Nat Biotechnol* **28**, 1279–85 (2010).
 18. Lackey, D. E., Lynch, C. J., Olson, K. C., Mostaedi, R., Ali, M., Smith, W. H., Karpe, F., Humphreys, S., Bedinger, D. H., Dunn, T. N., Thomas, A. P., Oort, P. J., Kieffer, D. A., Amin, R., Bettaieb, A., Haj, F. G., Permana, P., Anthony, T. G. & Adams, S. H. Regulation of adipose branched-chain amino acid catabolism enzyme expression and cross-adipose amino acid flux in human obesity. *Am J Physiol Endocrinol Metab* **304**, E1175–87 (2013).
 19. Johnson, C. H., Ivanisevic, J. & Siuzdak, G. Metabolomics: beyond biomarkers and towards mechanisms. *Nat Rev Mol Cell Biol* (2016).
 20. Hellerstein, M. K. New stable isotope-mass spectrometric techniques for measuring fluxes through intact metabolic pathways in mammalian systems: introduction of moving pictures into functional genomics and biochemical phenotyping. *Metab Eng* **6**, 85–100 (2004).
 21. Stephanopoulos, G. Metabolic fluxes and metabolic engineering. *Metab Eng* **1**, 1–11 (1999).
 22. Sauer, U. High-throughput phenomics: experimental methods for mapping fluxomes. *Curr Opin Biotechnol* **15**, 58–63 (2004).
 23. Buescher, J. M., Antoniewicz, M. R., Boros, L. G., Burgess, S. C., Brunengraber, H., Clish, C. B., DeBerardinis, R. J., Feron, O., Frezza, C., Ghesquiere, B., Gottlieb, E., Hiller, K., Jones, R. G., Kamphorst, J. J., Kibbey, R. G., Kimmelman, A. C., Locasale, J. W., Lunt, S. Y., Maddocks, O. D., Malloy, C., Metallo, C. M., Meuillet, E. J., Munger, J., Noh, K., Rabinowitz, J. D., Ralser, M., Sauer, U., Stephanopoulos, G., St-Pierre, J., Tennant, D. A., Wittmann, C., Vander Heiden, M. G., Vazquez, A., Vousden, K., Young, J. D., Zamboni, N. & Fendt, S. M. A roadmap for interpreting (13)C metabolite labeling patterns from cells. *Curr Opin Biotechnol* **34**, 189–201 (2015).
 24. Sauer, U. Metabolic networks in motion: 13C-based flux analysis. *Mol Syst Biol* **2**, 62 (2006).
 25. Metallo, C. M., Walther, J. L. & Stephanopoulos, G. Evaluation of 13C isotopic tracers for metabolic flux analysis in mammalian cells. *J Biotechnol* **144**, 167–74 (2009).

26. Crown, S. B., Ahn, W. S. & Antoniewicz, M. R. Rational design of (1)(3)C-labeling experiments for metabolic flux analysis in mammalian cells. *BMC Syst Biol* **6**, 43 (2012).
27. Wiechert, W. 13C metabolic flux analysis. *Metab Eng* **3**, 195–206 (2001).
28. Stephanopoulos, G., Aristidou, A. A. & Nielsen, J. H. *Metabolic engineering : principles and methodologies* xxi, 725 p. ISBN: 0126662606 (Academic Press, San Diego, 1998).
29. Zamboni, N. 13C metabolic flux analysis in complex systems. *Curr Opin Biotechnol* **22**, 103–8 (2011).
30. Antoniewicz, M. R., Kelleher, J. K. & Stephanopoulos, G. Elementary metabolite units (EMU): a novel framework for modeling isotopic distributions. *Metab Eng* **9**, 68–86 (2007).
31. Antoniewicz, M. R., Kelleher, J. K. & Stephanopoulos, G. Determination of confidence intervals of metabolic fluxes estimated from stable isotope measurements. *Metab Eng* **8**, 324–37 (2006).
32. Young, J. D. INCA: a computational platform for isotopically non-stationary metabolic flux analysis. *Bioinformatics* **30**, 1333–5 (2014).
33. Quek, L. E., Wittmann, C., Nielsen, L. K. & Kromer, J. O. OpenFLUX: efficient modelling software for 13C-based metabolic flux analysis. *Microb Cell Fact* **8**, 25 (2009).
34. Zamboni, N., Fischer, E. & Sauer, U. FiatFlux—a software for metabolic flux analysis from 13C-glucose experiments. *BMC Bioinformatics* **6**, 209 (2005).
35. Weitzel, M., Noh, K., Dalman, T., Niedenfuhr, S., Stute, B. & Wiechert, W. 13CFLUX2—high-performance software suite for (13)C-metabolic flux analysis. *Bioinformatics* **29**, 143–5 (2013).
36. Young, J. D., Walther, J. L., Antoniewicz, M. R., Yoo, H. & Stephanopoulos, G. An elementary metabolite unit (EMU) based method of isotopically nonstationary flux analysis. *Biotechnol Bioeng* **99**, 686–99 (2008).
37. Wiechert, W. The thermodynamic meaning of metabolic exchange fluxes. *Biophys J* **93**, 2255–64 (2007).
38. Vacanti, N. M., Divakaruni, A. S., Green, C. R., Parker, S. J., Henry, R. R., Ciaraldi, T. P., Murphy, A. N. & Metallo, C. M. Regulation of substrate utilization by the mitochondrial pyruvate carrier. *Mol Cell* **56**, 425–35 (2014).
39. Jiang, L., Shestov, A. A., Swain, P., Yang, C., Parker, S. J., Wang, Q. A., Terada, L. S., Adams, N. D., McCabe, M. T., Pietrak, B., Schmidt, S., Metallo, C. M., Dranka, B. P.,

- Schwartz, B. & DeBerardinis, R. J. Reductive carboxylation supports redox homeostasis during anchorage-independent growth. *Nature* **532**, 255–8 (2016).
40. Jiang, L., Boufersaoui, A., Yang, C., Ko, B., Rakheja, D., Guevara, G., Hu, Z. & DeBerardinis, R. J. Quantitative metabolic flux analysis reveals an unconventional pathway of fatty acid synthesis in cancer cells deficient for the mitochondrial citrate transport protein. *Metab Eng* (2016).
 41. McCloskey, D., Young, J. D., Xu, S., Palsson, B. O. & Feist, A. M. Modeling Method for Increased Precision and Scope of Directly Measurable Fluxes at a Genome-Scale. *Anal Chem* **88**, 3844–52 (2016).
 42. Gopalakrishnan, S. & Maranas, C. D. ¹³C metabolic flux analysis at a genome-scale. *Metab Eng* **32**, 12–22 (2015).
 43. Noh, K., Gronke, K., Luo, B., Takors, R., Oldiges, M. & Wiechert, W. Metabolic flux analysis at ultra short time scale: isotopically non-stationary ¹³C labeling experiments. *J Biotechnol* **129**, 249–67 (2007).
 44. Jazmin, L. J. & Young, J. D. Isotopically nonstationary ¹³C metabolic flux analysis. *Methods Mol Biol* **985**, 367–90 (2013).
 45. Young, J. D., Shastri, A. A., Stephanopoulos, G. & Morgan, J. A. Mapping photoautotrophic metabolism with isotopically nonstationary (¹³C) flux analysis. *Metab Eng* **13**, 656–65 (2011).
 46. Noh, K. & Wiechert, W. Experimental design principles for isotopically instationary ¹³C labeling experiments. *Biotechnol Bioeng* **94**, 234–51 (2006).
 47. Wiechert, W. & Noh, K. Isotopically non-stationary metabolic flux analysis: complex yet highly informative. *Curr Opin Biotechnol* **24**, 979–86 (2013).
 48. Nanchen, A., Fuhrer, T. & Sauer, U. Determination of metabolic flux ratios from ¹³C-experiments and gas chromatography-mass spectrometry data: protocol and principles. *Methods Mol Biol* **358**, 177–97 (2007).
 49. Yuan, J., Bennett, B. D. & Rabinowitz, J. D. Kinetic flux profiling for quantitation of cellular metabolic fluxes. *Nat Protoc* **3**, 1328–40 (2008).
 50. Munger, J., Bennett, B. D., Parikh, A., Feng, X. J., McArdle, J., Rabitz, H. A., Shenk, T. & Rabinowitz, J. D. Systems-level metabolic flux profiling identifies fatty acid synthesis as a target for antiviral therapy. *Nat Biotechnol* **26**, 1179–86 (2008).

51. Fan, J., Ye, J., Kamphorst, J. J., Shlomi, T., Thompson, C. B. & Rabinowitz, J. D. Quantitative flux analysis reveals folate-dependent NADPH production. *Nature* **510**, 298–302 (2014).
52. Maier, K., Hofmann, U., Bauer, A., Niebel, A., Vacun, G., Reuss, M. & Mauch, K. Quantification of statin effects on hepatic cholesterol synthesis by transient (13)C-flux analysis. *Metab Eng* **11**, 292–309 (2009).
53. Warburg, O., Wind, F. & Negelein, E. The Metabolism of Tumors in the Body. *J Gen Physiol* **8**, 519–30 (1927).
54. Warburg, O. On the origin of cancer cells. *Science* **123**, 309–14 (1956).
55. Weinhouse, S. On respiratory impairment in cancer cells. *Science* **124**, 267–9 (1956).
56. Burk, D. & Schade, A. L. On respiratory impairment in cancer cells. *Science* **124**, 270–2 (1956).
57. Hanahan, D. & Weinberg, R. A. Hallmarks of cancer: the next generation. *Cell* **144**, 646–74 (2011).
58. Pavlova, N. N. & Thompson, C. B. The Emerging Hallmarks of Cancer Metabolism. *Cell Metab* **23**, 27–47 (2016).
59. Boroughs, L. K. & DeBerardinis, R. J. Metabolic pathways promoting cancer cell survival and growth. *Nat Cell Biol* **17**, 351–9 (2015).
60. Vander Heiden, M. G. & DeBerardinis, R. J. Understanding the Intersections between Metabolism and Cancer Biology. *Cell* **168**, 657–669 (2017).
61. Farwell, M. D., Pryma, D. A. & Mankoff, D. A. PET/CT imaging in cancer: current applications and future directions. *Cancer* **120**, 3433–45 (2014).
62. Choi, C., Ganji, S. K., DeBerardinis, R. J., Hatanpaa, K. J., Rakheja, D., Kovacs, Z., Yang, X. L., Mashimo, T., Raisanen, J. M., Marin-Valencia, I., Pascual, J. M., Madden, C. J., Mickey, B. E., Malloy, C. R., Bachoo, R. M. & Maher, E. A. 2-hydroxyglutarate detection by magnetic resonance spectroscopy in IDH-mutated patients with gliomas. *Nat Med* **18**, 624–9 (2012).
63. Chaumeil, M. M., Larson, P. E., Woods, S. M., Cai, L., Eriksson, P., Robinson, A. E., Lupo, J. M., Vigneron, D. B., Nelson, S. J., Pieper, R. O., Phillips, J. J. & Ronen, S. M. Hyperpolarized [1-13C] glutamate: a metabolic imaging biomarker of IDH1 mutational status in glioma. *Cancer Res* **74**, 4247–57 (2014).

64. Venneti, S., Dunphy, M. P., Zhang, H., Pitter, K. L., Zanzonico, P., Campos, C., Carlin, S. D., La Rocca, G., Lyashchenko, S., Ploessl, K., Rohle, D., Omuro, A. M., Cross, J. R., Brennan, C. W., Weber, W. A., Holland, E. C., Mellinghoff, I. K., Kung, H. F., Lewis, J. S. & Thompson, C. B. Glutamine-based PET imaging facilitates enhanced metabolic evaluation of gliomas in vivo. *Sci Transl Med* **7**, 274ra17 (2015).
65. Rodrigues, T. B., Serrao, E. M., Kennedy, B. W., Hu, D. E., Kettunen, M. I. & Brindle, K. M. Magnetic resonance imaging of tumor glycolysis using hyperpolarized ¹³C-labeled glucose. *Nat Med* **20**, 93–7 (2014).
66. Weinberg, F. & Chandel, N. S. Mitochondrial metabolism and cancer. *Ann N Y Acad Sci* **1177**, 66–73 (2009).
67. DeBerardinis, R. J., Lum, J. J., Hatzivassiliou, G. & Thompson, C. B. The biology of cancer: metabolic reprogramming fuels cell growth and proliferation. *Cell Metab* **7**, 11–20 (2008).
68. Gasparre, G., Porcelli, A. M., Bonora, E., Pennisi, L. F., Toller, M., Iommarini, L., Ghelli, A., Moretti, M., Betts, C. M., Martinelli, G. N., Ceroni, A. R., Curcio, F., Carelli, V., Rugolo, M., Tallini, G. & Romeo, G. Disruptive mitochondrial DNA mutations in complex I subunits are markers of oncocyctic phenotype in thyroid tumors. *Proc Natl Acad Sci U S A* **104**, 9001–6 (2007).
69. King, A., Selak, M. A. & Gottlieb, E. Succinate dehydrogenase and fumarate hydratase: linking mitochondrial dysfunction and cancer. *Oncogene* **25**, 4675–82 (2006).
70. MacKenzie, E. D., Selak, M. A., Tennant, D. A., Payne, L. J., Crosby, S., Frederiksen, C. M., Watson, D. G. & Gottlieb, E. Cell-permeating alpha-ketoglutarate derivatives alleviate pseudohypoxia in succinate dehydrogenase-deficient cells. *Mol Cell Biol* **27**, 3282–9 (2007).
71. Xiao, M., Yang, H., Xu, W., Ma, S., Lin, H., Zhu, H., Liu, L., Liu, Y., Yang, C., Xu, Y., Zhao, S., Ye, D., Xiong, Y. & Guan, K. L. Inhibition of alpha-KG-dependent histone and DNA demethylases by fumarate and succinate that are accumulated in mutations of FH and SDH tumor suppressors. *Genes Dev* **26**, 1326–38 (2012).
72. Selak, M. A., Armour, S. M., MacKenzie, E. D., Boulahbel, H., Watson, D. G., Mansfield, K. D., Pan, Y., Simon, M. C., Thompson, C. B. & Gottlieb, E. Succinate links TCA cycle dysfunction to oncogenesis by inhibiting HIF-alpha prolyl hydroxylase. *Cancer Cell* **7**, 77–85 (2005).
73. Frezza, C., Zheng, L., Folger, O., Rajagopalan, K. N., MacKenzie, E. D., Jerby, L., Micaroni, M., Chaneton, B., Adam, J., Hedley, A., Kalna, G., Tomlinson, I. P., Pollard, P. J., Watson, D. G., Deberardinis, R. J., Shlomi, T., Ruppin, E. & Gottlieb, E. Haem

- oxygenase is synthetically lethal with the tumour suppressor fumarate hydratase. *Nature* **477**, 225–8 (2011).
74. Yan, H., Parsons, D. W., Jin, G., McLendon, R., Rasheed, B. A., Yuan, W., Kos, I., Batinic-Haberle, I., Jones, S., Riggins, G. J., Friedman, H., Friedman, A., Reardon, D., Herndon, J., Kinzler, K. W., Velculescu, V. E., Vogelstein, B. & Bigner, D. D. IDH1 and IDH2 mutations in gliomas. *N Engl J Med* **360**, 765–73 (2009).
 75. Balss, J., Meyer, J., Mueller, W., Korshunov, A., Hartmann, C. & von Deimling, A. Analysis of the IDH1 codon 132 mutation in brain tumors. *Acta Neuropathol* **116**, 597–602 (2008).
 76. Dang, L., Yen, K. & Attar, E. C. IDH mutations in cancer and progress toward development of targeted therapeutics. *Ann Oncol* **27**, 599–608 (2016).
 77. Parker, S. J. & Metallo, C. M. Metabolic consequences of oncogenic IDH mutations. *Pharmacol Ther* **152**, 54–62 (2015).
 78. Dang, L., White, D. W., Gross, S., Bennett, B. D., Bittinger, M. A., Driggers, E. M., Fantin, V. R., Jang, H. G., Jin, S., Keenan, M. C., Marks, K. M., Prins, R. M., Ward, P. S., Yen, K. E., Liau, L. M., Rabinowitz, J. D., Cantley, L. C., Thompson, C. B., Vander Heiden, M. G. & Su, S. M. Cancer-associated IDH1 mutations produce 2-hydroxyglutarate. *Nature* **462**, 739–44 (2009).
 79. Ma, S., Jiang, B., Deng, W., Gu, Z. K., Wu, F. Z., Li, T., Xia, Y., Yang, H., Ye, D., Xiong, Y. & Guan, K. L. D-2-hydroxyglutarate is essential for maintaining oncogenic property of mutant IDH-containing cancer cells but dispensable for cell growth. *Oncotarget* **6**, 8606–20 (2015).
 80. Figueroa, M. E., Abdel-Wahab, O., Lu, C., Ward, P. S., Patel, J., Shih, A., Li, Y., Bhagwat, N., Vasanthakumar, A., Fernandez, H. F., Tallman, M. S., Sun, Z., Wolniak, K., Peeters, J. K., Liu, W., Choe, S. E., Fantin, V. R., Paietta, E., Lowenberg, B., Licht, J. D., Godley, L. A., Delwel, R., Valk, P. J., Thompson, C. B., Levine, R. L. & Melnick, A. Leukemic IDH1 and IDH2 mutations result in a hypermethylation phenotype, disrupt TET2 function, and impair hematopoietic differentiation. *Cancer Cell* **18**, 553–67 (2010).
 81. Lu, C., Ward, P. S., Kapoor, G. S., Rohle, D., Turcan, S., Abdel-Wahab, O., Edwards, C. R., Khanin, R., Figueroa, M. E., Melnick, A., Wellen, K. E., O'Rourke, D. M., Berger, S. L., Chan, T. A., Levine, R. L., Mellinghoff, I. K. & Thompson, C. B. IDH mutation impairs histone demethylation and results in a block to cell differentiation. *Nature* **483**, 474–8 (2012).
 82. Turcan, S., Rohle, D., Goenka, A., Walsh, L. A., Fang, F., Yilmaz, E., Campos, C., Fabius, A. W., Lu, C., Ward, P. S., Thompson, C. B., Kaufman, A., Guryanova, O., Levine, R., Heguy, A., Viale, A., Morris, L. G., Huse, J. T., Mellinghoff, I. K. & Chan, T. A. IDH1

- mutation is sufficient to establish the glioma hypermethylator phenotype. *Nature* **483**, 479–83 (2012).
83. Xu, W., Yang, H., Liu, Y., Yang, Y., Wang, P., Kim, S. H., Ito, S., Yang, C., Wang, P., Xiao, M. T., Liu, L. X., Jiang, W. Q., Liu, J., Zhang, J. Y., Wang, B., Frye, S., Zhang, Y., Xu, Y. H., Lei, Q. Y., Guan, K. L., Zhao, S. M. & Xiong, Y. Oncometabolite 2-hydroxyglutarate is a competitive inhibitor of alpha-ketoglutarate-dependent dioxygenases. *Cancer Cell* **19**, 17–30 (2011).
 84. Izquierdo-Garcia, J. L., Viswanath, P., Eriksson, P., Cai, L., Radoul, M., Chaumeil, M. M., Blough, M., Luchman, H. A., Weiss, S., Cairncross, J. G., Phillips, J. J., Pieper, R. O. & Ronen, S. M. IDH1 Mutation Induces Reprogramming of Pyruvate Metabolism. *Cancer Res* **75**, 2999–3009 (2015).
 85. Grassian, A. R., Parker, S. J., Davidson, S. M., Divakaruni, A. S., Green, C. R., Zhang, X., Slocum, K. L., Pu, M., Lin, F., Vickers, C., Joud-Caldwell, C., Chung, F., Yin, H., Handly, E. D., Straub, C., Growney, J. D., Vander Heiden, M. G., Murphy, A. N., Pagliarini, R. & Metallo, C. M. IDH1 mutations alter citric acid cycle metabolism and increase dependence on oxidative mitochondrial metabolism. *Cancer Res* **74**, 3317–31 (2014).
 86. Chan, S. M., Thomas, D., Corces-Zimmerman, M. R., Xavy, S., Rastogi, S., Hong, W. J., Zhao, F., Medeiros, B. C., Tyvoll, D. A. & Majeti, R. Isocitrate dehydrogenase 1 and 2 mutations induce BCL-2 dependence in acute myeloid leukemia. *Nat Med* **21**, 178–84 (2015).
 87. Tateishi, K., Wakimoto, H., Iafrate, A. J., Tanaka, S., Loebel, F., Lelic, N., Wiederschain, D., Bedel, O., Deng, G., Zhang, B., He, T., Shi, X., Gerszten, R. E., Zhang, Y., Yeh, J. R., Curry, W. T., Zhao, D., Sundaram, S., Nigim, F., Koerner, M. V., Ho, Q., Fisher, D. E., Roeder, E. M., Kemeny, L. V., Samuels, Y., Flaherty, K. T., Batchelor, T. T., Chi, A. S. & Cahill, D. P. Extreme Vulnerability of IDH1 Mutant Cancers to NAD⁺ Depletion. *Cancer Cell* **28**, 773–84 (2015).
 88. Hosios, A. M., Hecht, V. C., Danai, L. V., Johnson, M. O., Rathmell, J. C., Steinhäuser, M. L., Manalis, S. R. & Vander Heiden, M. G. Amino Acids Rather than Glucose Account for the Majority of Cell Mass in Proliferating Mammalian Cells. *Dev Cell* **36**, 540–9 (2016).
 89. Wellen, K. E., Lu, C., Mancuso, A., Lemons, J. M., Ryczko, M., Dennis, J. W., Rabinowitz, J. D., Collier, H. A. & Thompson, C. B. The hexosamine biosynthetic pathway couples growth factor-induced glutamine uptake to glucose metabolism. *Genes Dev* **24**, 2784–99 (2010).
 90. Zhang, J., Fan, J., Venneti, S., Cross, J. R., Takagi, T., Bhinder, B., Djaballah, H., Kanai, M., Cheng, E. H., Judkins, A. R., Pawel, B., Baggs, J., Cherry, S., Rabinowitz, J. D.

- & Thompson, C. B. Asparagine plays a critical role in regulating cellular adaptation to glutamine depletion. *Mol Cell* **56**, 205–18 (2014).
91. DeBerardinis, R. J., Mancuso, A., Daikhin, E., Nissim, I., Yudkoff, M., Wehrli, S. & Thompson, C. B. Beyond aerobic glycolysis: transformed cells can engage in glutamine metabolism that exceeds the requirement for protein and nucleotide synthesis. *Proc Natl Acad Sci U S A* **104**, 19345–50 (2007).
 92. Badur, M. G., Zhang, H. & Metallo, C. M. Enzymatic passaging of human embryonic stem cells alters central carbon metabolism and glycan abundance. *Biotechnol J* **10**, 1600–11 (2015).
 93. Shin, C. S., Mishra, P., Watrous, J. D., Carelli, V., D'Aurelio, M., Jain, M. & Chan, D. C. The glutamate/cystine xCT antiporter antagonizes glutamine metabolism and reduces nutrient flexibility. *Nat Commun* **8**, 15074 (2017).
 94. Muir, A., Danai, L. V., Gui, D. Y., Waingarten, C. Y., Lewis, C. A. & Vander Heiden, M. G. Environmental cystine drives glutamine anaplerosis and sensitizes cancer cells to glutaminase inhibition. *Elife* **6** (2017).
 95. Commisso, C., Davidson, S. M., Soydaner-Azeloglu, R. G., Parker, S. J., Kamphorst, J. J., Hackett, S., Grabocka, E., Nofal, M., Drebin, J. A., Thompson, C. B., Rabinowitz, J. D., Metallo, C. M., Vander Heiden, M. G. & Bar-Sagi, D. Macropinocytosis of protein is an amino acid supply route in Ras-transformed cells. *Nature* **497**, 633–7 (2013).
 96. Kamphorst, J. J., Nofal, M., Commisso, C., Hackett, S. R., Lu, W., Grabocka, E., Vander Heiden, M. G., Miller, G., Drebin, J. A., Bar-Sagi, D., Thompson, C. B. & Rabinowitz, J. D. Human pancreatic cancer tumors are nutrient poor and tumor cells actively scavenge extracellular protein. *Cancer Res* **75**, 544–53 (2015).
 97. Davidson, S. M., Jonas, O., Keibler, M. A., Hou, H. W., Luengo, A., Mayers, J. R., Wyckoff, J., Del Rosario, A. M., Whitman, M., Chin, C. R., Condon, K. J., Lammers, A., Kellersberger, K. A., Stall, B. K., Stephanopoulos, G., Bar-Sagi, D., Han, J., Rabinowitz, J. D., Cima, M. J., Langer, R. & Vander Heiden, M. G. Direct evidence for cancer-cell-autonomous extracellular protein catabolism in pancreatic tumors. *Nat Med* **23**, 235–241 (2017).
 98. Sousa, C. M., Biancur, D. E., Wang, X., Halbrook, C. J., Sherman, M. H., Zhang, L., Kremer, D., Hwang, R. F., Witkiewicz, A. K., Ying, H., Asara, J. M., Evans, R. M., Cantley, L. C., Lyssiotis, C. A. & Kimmelman, A. C. Pancreatic stellate cells support tumour metabolism through autophagic alanine secretion. *Nature* **536**, 479–83 (2016).
 99. Yang, L., Achreja, A., Yeung, T. L., Mangala, L. S., Jiang, D., Han, C., Baddour, J., Marini, J. C., Ni, J., Nakahara, R., Wahlgig, S., Chiba, L., Kim, S. H., Morse, J., Pradeep,

- S., Nagaraja, A. S., Haemmerle, M., Kyunghye, N., Derichsweiler, M., Plackemeier, T., Mercado-Uribe, I., Lopez-Berestein, G., Moss, T., Ram, P. T., Liu, J., Lu, X., Mok, S. C., Sood, A. K. & Nagrath, D. Targeting Stromal Glutamine Synthetase in Tumors Disrupts Tumor Microenvironment-Regulated Cancer Cell Growth. *Cell Metab* **24**, 685–700 (2016).
100. Gebreselassie, N. A. & Antoniewicz, M. R. (13)C-metabolic flux analysis of co-cultures: A novel approach. *Metab Eng* **31**, 132–9 (2015).
101. Schell, J. C., Olson, K. A., Jiang, L., Hawkins, A. J., Van Vranken, J. G., Xie, J., Egnatchik, R. A., Earl, E. G., DeBerardinis, R. J. & Rutter, J. A role for the mitochondrial pyruvate carrier as a repressor of the Warburg effect and colon cancer cell growth. *Mol Cell* **56**, 400–13 (2014).
102. Divakaruni, A. S., Wiley, S. E., Rogers, G. W., Andreyev, A. Y., Petrosyan, S., Loviscach, M., Wall, E. A., Yadava, N., Heuck, A. P., Ferrick, D. A., Henry, R. R., McDonald, W. G., Colca, J. R., Simon, M. I., Ciaraldi, T. P. & Murphy, A. N. Thiazolidinediones are acute, specific inhibitors of the mitochondrial pyruvate carrier. *Proc Natl Acad Sci U S A* **110**, 5422–7 (2013).
103. Yang, C., Ko, B., Hensley, C. T., Jiang, L., Wasti, A. T., Kim, J., Sudderth, J., Calvaruso, M. A., Lumata, L., Mitsche, M., Rutter, J., Merritt, M. E. & DeBerardinis, R. J. Glutamine oxidation maintains the TCA cycle and cell survival during impaired mitochondrial pyruvate transport. *Mol Cell* **56**, 414–24 (2014).
104. McCommis, K. S., Chen, Z., Fu, X., McDonald, W. G., Colca, J. R., Kletzien, R. F., Burgess, S. C. & Finck, B. N. Loss of Mitochondrial Pyruvate Carrier 2 in the Liver Leads to Defects in Gluconeogenesis and Compensation via Pyruvate-Alanine Cycling. *Cell Metab* **22**, 682–94 (2015).
105. Gray, L. R., Sultana, M. R., Rauckhorst, A. J., Oonthonpan, L., Tompkins, S. C., Sharma, A., Fu, X., Miao, R., Pawa, A. D., Brown, K. S., Lane, E. E., Dohlman, A., Zepeda-Orozco, D., Xie, J., Rutter, J., Norris, A. W., Cox, J. E., Burgess, S. C., Potthoff, M. J. & Taylor, E. B. Hepatic Mitochondrial Pyruvate Carrier 1 Is Required for Efficient Regulation of Gluconeogenesis and Whole-Body Glucose Homeostasis. *Cell Metab* **22**, 669–81 (2015).
106. Ghosh, A., Tyson, T., George, S., Hildebrandt, E. N., Steiner, J. A., Madaj, Z., Schulz, E., Machiela, E., McDonald, W. G., Escobar Galvis, M. L., Kordower, J. H., Van Raamsdonk, J. M., Colca, J. R. & Brundin, P. Mitochondrial pyruvate carrier regulates autophagy, inflammation, and neurodegeneration in experimental models of Parkinson’s disease. *Sci Transl Med* **8**, 368ra174 (2016).
107. Divakaruni, A. S., Wallace, M., Buren, C., Martyniuk, K., Andreyev, A. Y., Li, E., Fields, J. A., Cordes, T., Reynolds, I. J., Bloodgood, B. L., Raymond, L. A., Metallo, C. M. &

- Murphy, A. N. Inhibition of the mitochondrial pyruvate carrier protects from excitotoxic neuronal death. *J Cell Biol* **216**, 1091–1105 (2017).
108. Eales, K. L., Hollinshead, K. E. & Tennant, D. A. Hypoxia and metabolic adaptation of cancer cells. *Oncogenesis* **5**, e190 (2016).
 109. Weinberg, F., Hamanaka, R., Wheaton, W. W., Weinberg, S., Joseph, J., Lopez, M., Kalyanaraman, B., Mutlu, G. M., Budinger, G. R. & Chandel, N. S. Mitochondrial metabolism and ROS generation are essential for Kras-mediated tumorigenicity. *Proc Natl Acad Sci U S A* **107**, 8788–93 (2010).
 110. Fan, J., Kamphorst, J. J., Mathew, R., Chung, M. K., White, E., Shlomi, T. & Rabinowitz, J. D. Glutamine-driven oxidative phosphorylation is a major ATP source in transformed mammalian cells in both normoxia and hypoxia. *Mol Syst Biol* **9**, 712 (2013).
 111. Le, A., Lane, A. N., Hamaker, M., Bose, S., Gouw, A., Barbi, J., Tsukamoto, T., Rojas, C. J., Slusher, B. S., Zhang, H., Zimmerman, L. J., Liebler, D. C., Slebos, R. J., Lorkiewicz, P. K., Higashi, R. M., Fan, T. W. & Dang, C. V. Glucose-independent glutamine metabolism via TCA cycling for proliferation and survival in B cells. *Cell Metab* **15**, 110–21 (2012).
 112. Des Rosiers, C., Di Donato, L., Comte, B., Laplante, A., Marcoux, C., David, F., Fernandez, C. A. & Brunengraber, H. Isotopomer analysis of citric acid cycle and gluconeogenesis in rat liver. Reversibility of isocitrate dehydrogenase and involvement of ATP-citrate lyase in gluconeogenesis. *J Biol Chem* **270**, 10027–36 (1995).
 113. Yoo, H., Antoniewicz, M. R., Stephanopoulos, G. & Kelleher, J. K. Quantifying reductive carboxylation flux of glutamine to lipid in a brown adipocyte cell line. *J Biol Chem* **283**, 20621–7 (2008).
 114. Metallo, C. M., Gameiro, P. A., Bell, E. L., Mattaini, K. R., Yang, J., Hiller, K., Jewell, C. M., Johnson, Z. R., Irvine, D. J., Guarente, L., Kelleher, J. K., Vander Heiden, M. G., Iliopoulos, O. & Stephanopoulos, G. Reductive glutamine metabolism by IDH1 mediates lipogenesis under hypoxia. *Nature* **481**, 380–4 (2012).
 115. Wise, D. R., Ward, P. S., Shay, J. E., Cross, J. R., Gruber, J. J., Sachdeva, U. M., Platt, J. M., DeMatteo, R. G., Simon, M. C. & Thompson, C. B. Hypoxia promotes isocitrate dehydrogenase-dependent carboxylation of alpha-ketoglutarate to citrate to support cell growth and viability. *Proc Natl Acad Sci U S A* **108**, 19611–6 (2011).
 116. Gameiro, P. A., Yang, J., Metelo, A. M., Perez-Carro, R., Baker, R., Wang, Z., Arreola, A., Rathmell, W. K., Olumi, A., Lopez-Larrubia, P., Stephanopoulos, G. & Iliopoulos, O. In vivo HIF-mediated reductive carboxylation is regulated by citrate levels and sensitizes VHL-deficient cells to glutamine deprivation. *Cell Metab* **17**, 372–85 (2013).

117. Hakimi, A. A., Reznik, E., Lee, C. H., Creighton, C. J., Brannon, A. R., Luna, A., Aksoy, B. A., Liu, E. M., Shen, R., Lee, W., Chen, Y., Stirdivant, S. M., Russo, P., Chen, Y. B., Tickoo, S. K., Reuter, V. E., Cheng, E. H., Sander, C. & Hsieh, J. J. An Integrated Metabolic Atlas of Clear Cell Renal Cell Carcinoma. *Cancer Cell* **29**, 104–16 (2016).
118. Okazaki, A., Gameiro, P. A., Christodoulou, D., Laviollette, L., Schneider, M., Chaves, F., Stemmer-Rachamimov, A., Yazinski, S. A., Lee, R., Stephanopoulos, G., Zou, L. & Iliopoulos, O. Glutaminase and poly(ADP-ribose) polymerase inhibitors suppress pyrimidine synthesis and VHL-deficient renal cancers. *J Clin Invest* **127**, 1631–1645 (2017).
119. Mullen, A. R., Wheaton, W. W., Jin, E. S., Chen, P. H., Sullivan, L. B., Cheng, T., Yang, Y., Linehan, W. M., Chandel, N. S. & DeBerardinis, R. J. Reductive carboxylation supports growth in tumour cells with defective mitochondria. *Nature* **481**, 385–8 (2012).
120. Gameiro, P. A., Laviolette, L. A., Kelleher, J. K., Iliopoulos, O. & Stephanopoulos, G. Co-factor balance by nicotinamide nucleotide transhydrogenase (NNT) coordinates reductive carboxylation and glucose catabolism in the tricarboxylic acid (TCA) cycle. *J Biol Chem* **288**, 12967–77 (2013).
121. Mullen, A. R., Hu, Z., Shi, X., Jiang, L., Boroughs, L. K., Kovacs, Z., Boriack, R., Rakheja, D., Sullivan, L. B., Linehan, W. M., Chandel, N. S. & DeBerardinis, R. J. Oxidation of alpha-ketoglutarate is required for reductive carboxylation in cancer cells with mitochondrial defects. *Cell Rep* **7**, 1679–90 (2014).
122. Fendt, S. M., Bell, E. L., Keibler, M. A., Olenchock, B. A., Mayers, J. R., Wasylenko, T. M., Vokes, N. I., Guarente, L., Vander Heiden, M. G. & Stephanopoulos, G. Reductive glutamine metabolism is a function of the alpha-ketoglutarate to citrate ratio in cells. *Nat Commun* **4**, 2236 (2013).
123. Stincone, A., Prigione, A., Cramer, T., Wamelink, M. M., Campbell, K., Cheung, E., Olin-Sandoval, V., Gruning, N., Kruger, A., Tauqeer Alam, M., Keller, M. A., Breitenbach, M., Brindle, K. M., Rabinowitz, J. D. & Ralser, M. The return of metabolism: biochemistry and physiology of the pentose phosphate pathway. *Biol Rev Camb Philos Soc* (2014).
124. Lee, W. N., Boros, L. G., Puigjaner, J., Bassilian, S., Lim, S. & Cascante, M. Mass isotope study of the nonoxidative pathways of the pentose cycle with [1,2-¹³C₂]glucose. *Am J Physiol* **274**, E843–51 (1998).
125. Katz, J., Rognstad, R. & Kemp, R. G. Isotope Discrimination Effects in the Metabolism of Tritiated Glucose. *J Biol Chem* **240**, PC1484–6 (1965).
126. Rendina, A. R., Hermes, J. D. & Cleland, W. W. Use of multiple isotope effects to study the mechanism of 6-phosphogluconate dehydrogenase. *Biochemistry* **23**, 6257–62 (1984).

127. Ben-Yoseph, O., Kingsley, P. B. & Ross, B. D. Metabolic loss of deuterium from isotopically labeled glucose. *Magn Reson Med* **32**, 405–9 (1994).
128. Ruhl, M., Le Coq, D., Aymerich, S. & Sauer, U. ¹³C-flux analysis reveals NADPH-balancing transhydrogenation cycles in stationary phase of nitrogen-starving *Bacillus subtilis*. *J Biol Chem* **287**, 27959–70 (2012).
129. Lewis, C. A., Parker, S. J., Fiske, B. P., McCloskey, D., Gui, D. Y., Green, C. R., Vokes, N. I., Feist, A. M., Vander Heiden, M. G. & Metallo, C. M. Tracing compartmentalized NADPH metabolism in the cytosol and mitochondria of mammalian cells. *Mol Cell* **55**, 253–63 (2014).
130. Zhang, H., Badur, M. G., Divakaruni, A. S., Parker, S. J., Jager, C., Hiller, K., Murphy, A. N. & Metallo, C. M. Distinct Metabolic States Can Support Self-Renewal and Lipogenesis in Human Pluripotent Stem Cells under Different Culture Conditions. *Cell Rep* **16**, 1536–47 (2016).
131. LaNoue, K. F. & Schoolwerth, A. C. Metabolite transport in mitochondria. *Annu Rev Biochem* **48**, 871–922 (1979).
132. Schafer, Z. T., Grassian, A. R., Song, L., Jiang, Z., Gerhart-Hines, Z., Irie, H. Y., Gao, S., Puigserver, P. & Brugge, J. S. Antioxidant and oncogene rescue of metabolic defects caused by loss of matrix attachment. *Nature* **461**, 109–13 (2009).
133. Grassian, A. R., Metallo, C. M., Coloff, J. L., Stephanopoulos, G. & Brugge, J. S. Erk regulation of pyruvate dehydrogenase flux through PDK4 modulates cell proliferation. *Genes Dev* **25**, 1716–33 (2011).
134. Piskounova, E., Agathocleous, M., Murphy, M. M., Hu, Z., Huddlestun, S. E., Zhao, Z., Leitch, A. M., Johnson, T. M., DeBerardinis, R. J. & Morrison, S. J. Oxidative stress inhibits distant metastasis by human melanoma cells. *Nature* **527**, 186–91 (2015).
135. Parker, S. J. & Metallo, C. M. Chasing One-Carbon Units to Understand the Role of Serine in Epigenetics. *Mol Cell* **61**, 185–6 (2016).
136. Locasale, J. W., Grassian, A. R., Melman, T., Lyssiotis, C. A., Mattaini, K. R., Bass, A. J., Heffron, G., Metallo, C. M., Muranen, T., Sharfi, H., Sasaki, A. T., Anastasiou, D., Mullarky, E., Vokes, N. I., Sasaki, M., Beroukhi, R., Stephanopoulos, G., Ligon, A. H., Meyerson, M., Richardson, A. L., Chin, L., Wagner, G., Asara, J. M., Brugge, J. S., Cantley, L. C. & Vander Heiden, M. G. Phosphoglycerate dehydrogenase diverts glycolytic flux and contributes to oncogenesis. *Nat Genet* **43**, 869–74 (2011).
137. Possemato, R., Marks, K. M., Shaul, Y. D., Pacold, M. E., Kim, D., Birsoy, K., Sethumadhavan, S., Woo, H. K., Jang, H. G., Jha, A. K., Chen, W. W., Barrett, F. G., Stransky, N.,

- Tsun, Z. Y., Cowley, G. S., Barretina, J., Kalaany, N. Y., Hsu, P. P., Ottina, K., Chan, A. M., Yuan, B., Garraway, L. A., Root, D. E., Mino-Kenudson, M., Brachtel, E. F., Driggers, E. M. & Sabatini, D. M. Functional genomics reveal that the serine synthesis pathway is essential in breast cancer. *Nature* **476**, 346–50 (2011).
138. Jain, M., Nilsson, R., Sharma, S., Madhusudhan, N., Kitami, T., Souza, A. L., Kafri, R., Kirschner, M. W., Clish, C. B. & Mootha, V. K. Metabolite profiling identifies a key role for glycine in rapid cancer cell proliferation. *Science* **336**, 1040–4 (2012).
139. Tibbetts, A. S. & Appling, D. R. Compartmentalization of Mammalian folate-mediated one-carbon metabolism. *Annu Rev Nutr* **30**, 57–81 (2010).
140. Fox, J. T. & Stover, P. J. Folate-mediated one-carbon metabolism. *Vitam Horm* **79**, 1–44 (2008).
141. Nilsson, R., Jain, M., Madhusudhan, N., Sheppard, N. G., Strittmatter, L., Kampf, C., Huang, J., Asplund, A. & Mootha, V. K. Metabolic enzyme expression highlights a key role for MTHFD2 and the mitochondrial folate pathway in cancer. *Nat Commun* **5**, 3128 (2014).
142. Locasale, J. W. Serine, glycine and one-carbon units: cancer metabolism in full circle. *Nat Rev Cancer* **13**, 572–83 (2013).
143. Maddocks, O. D., Berkers, C. R., Mason, S. M., Zheng, L., Blyth, K., Gottlieb, E. & Vousden, K. H. Serine starvation induces stress and p53-dependent metabolic remodelling in cancer cells. *Nature* **493**, 542–6 (2013).
144. Gravel, S. P., Hulea, L., Toban, N., Birman, E., Blouin, M. J., Zakikhani, M., Zhao, Y., Topisirovic, I., St-Pierre, J. & Pollak, M. Serine deprivation enhances antineoplastic activity of biguanides. *Cancer Res* **74**, 7521–33 (2014).
145. Ye, J., Fan, J., Venneti, S., Wan, Y. W., Pawel, B. R., Zhang, J., Finley, L. W., Lu, C., Lindsten, T., Cross, J. R., Qing, G., Liu, Z., Simon, M. C., Rabinowitz, J. D. & Thompson, C. B. Serine catabolism regulates mitochondrial redox control during hypoxia. *Cancer Discov* **4**, 1406–17 (2014).
146. Maddocks, O. D. K., Athineos, D., Cheung, E. C., Lee, P., Zhang, T., van den Broek, N. J. F., Mackay, G. M., Labuschagne, C. F., Gay, D., Kruiswijk, F., Blagih, J., Vincent, D. F., Campbell, K. J., Ceteci, F., Sansom, O. J., Blyth, K. & Vousden, K. H. Modulating the therapeutic response of tumours to dietary serine and glycine starvation. *Nature* **544**, 372–376 (2017).

147. Labuschagne, C. F., van den Broek, N. J., Mackay, G. M., Vousden, K. H. & Maddocks, O. D. Serine, but not glycine, supports one-carbon metabolism and proliferation of cancer cells. *Cell Rep* **7**, 1248–58 (2014).
148. DeNicola, G. M., Chen, P. H., Mullarky, E., Sudderth, J. A., Hu, Z., Wu, D., Tang, H., Xie, Y., Asara, J. M., Huffman, K. E., Wistuba, I., Minna, J. D., DeBerardinis, R. J. & Cantley, L. C. NRF2 regulates serine biosynthesis in non-small cell lung cancer. *Nat Genet* **47**, 1475–81 (2015).
149. Ben-Sahra, I., Hoxhaj, G., Ricoult, S. J., Asara, J. M. & Manning, B. D. mTORC1 induces purine synthesis through control of the mitochondrial tetrahydrofolate cycle. *Science* **351**, 728–33 (2016).
150. Zhang, W. C., Shyh-Chang, N., Yang, H., Rai, A., Umashankar, S., Ma, S., Soh, B. S., Sun, L. L., Tai, B. C., Nga, M. E., Bhakoo, K. K., Jayapal, S. R., Nichane, M., Yu, Q., Ahmed, D. A., Tan, C., Sing, W. P., Tam, J., Thirugananam, A., Noghabi, M. S., Pang, Y. H., Ang, H. S., Mitchell, W., Robson, P., Kaldis, P., Soo, R. A., Swarup, S., Lim, E. H. & Lim, B. Glycine decarboxylase activity drives non-small cell lung cancer tumor-initiating cells and tumorigenesis. *Cell* **148**, 259–72 (2012).
151. Vazquez, A., Markert, E. K. & Oltvai, Z. N. Serine biosynthesis with one carbon catabolism and the glycine cleavage system represents a novel pathway for ATP generation. *PLoS One* **6**, e25881 (2011).
152. Herbig, K., Chiang, E. P., Lee, L. R., Hills, J., Shane, B. & Stover, P. J. Cytoplasmic serine hydroxymethyltransferase mediates competition between folate-dependent deoxyribonucleotide and S-adenosylmethionine biosyntheses. *J Biol Chem* **277**, 38381–9 (2002).
153. Meiser, J., Tumanov, S., Maddocks, O., Labuschagne, C. F., Athineos, D., Van Den Broek, N., Mackay, G. M., Gottlieb, E., Blyth, K., Vousden, K., Kamphorst, J. J. & Vazquez, A. Serine one-carbon catabolism with formate overflow. *Sci Adv* **2**, e1601273 (2016).
154. Ducker, G. S., Chen, L., Morscher, R. J., Ghergurovich, J. M., Esposito, M., Teng, X., Kang, Y. & Rabinowitz, J. D. Reversal of Cytosolic One-Carbon Flux Compensates for Loss of the Mitochondrial Folate Pathway. *Cell Metab* **23**, 1140–53 (2016).
155. Samanta, D., Park, Y., Andrabi, S. A., Shelton, L. M., Gilkes, D. M. & Semenza, G. L. PHGDH Expression Is Required for Mitochondrial Redox Homeostasis, Breast Cancer Stem Cell Maintenance, and Lung Metastasis. *Cancer Res* **76**, 4430–42 (2016).
156. Metallo, C. M. & Vander Heiden, M. G. Metabolism strikes back: metabolic flux regulates cell signaling. *Genes Dev* **24**, 2717–22 (2010).

157. Kinnaird, A., Zhao, S., Wellen, K. E. & Michelakis, E. D. Metabolic control of epigenetics in cancer. *Nat Rev Cancer* **16**, 694–707 (2016).
158. Su, X., Wellen, K. E. & Rabinowitz, J. D. Metabolic control of methylation and acetylation. *Curr Opin Chem Biol* **30**, 52–60 (2016).
159. Zhao, S., Torres, A., Henry, R. A., Trefely, S., Wallace, M., Lee, J. V., Carrer, A., Sengupta, A., Campbell, S. L., Kuo, Y. M., Frey, A. J., Meurs, N., Viola, J. M., Blair, I. A., Weljie, A. M., Metallo, C. M., Snyder, N. W., Andrews, A. J. & Wellen, K. E. ATP-Citrate Lyase Controls a Glucose-to-Acetate Metabolic Switch. *Cell Rep* **17**, 1037–1052 (2016).
160. Wellen, K. E., Hatzivassiliou, G., Sachdeva, U. M., Bui, T. V., Cross, J. R. & Thompson, C. B. ATP-citrate lyase links cellular metabolism to histone acetylation. *Science* **324**, 1076–80 (2009).
161. Wang, Q., Zhang, Y., Yang, C., Xiong, H., Lin, Y., Yao, J., Li, H., Xie, L., Zhao, W., Yao, Y., Ning, Z. B., Zeng, R., Xiong, Y., Guan, K. L., Zhao, S. & Zhao, G. P. Acetylation of metabolic enzymes coordinates carbon source utilization and metabolic flux. *Science* **327**, 1004–7 (2010).
162. Starai, V. J., Celic, I., Cole, R. N., Boeke, J. D. & Escalante-Semerena, J. C. Sir2-dependent activation of acetyl-CoA synthetase by deacetylation of active lysine. *Science* **298**, 2390–2 (2002).
163. Mews, P., Donahue, G., Drake, A. M., Luczak, V., Abel, T. & Berger, S. L. Acetyl-CoA synthetase regulates histone acetylation and hippocampal memory. *Nature* **546**, 381–386 (2017).
164. Gut, P. & Verdin, E. The nexus of chromatin regulation and intermediary metabolism. *Nature* **502**, 489–98 (2013).
165. Cantoni, G. L. S-Adenosylmethionine - a New Intermediate Formed Enzymatically from L-Methionine and Adenosinetriphosphate. *Journal of Biological Chemistry* **204**, 403–416 (1953).
166. Lane, A. N. & Fan, T. W. Regulation of mammalian nucleotide metabolism and biosynthesis. *Nucleic Acids Res* **43**, 2466–85 (2015).
167. Davis, S. R., Stacpoole, P. W., Williamson, J., Kick, L. S., Quinlivan, E. P., Coats, B. S., Shane, B., Bailey, L. B. & Gregory J. F., 3. Tracer-derived total and folate-dependent homocysteine remethylation and synthesis rates in humans indicate that serine is the main one-carbon donor. *Am J Physiol Endocrinol Metab* **286**, E272–9 (2004).
168. Kottakis, F., Nicolay, B. N., Roumane, A., Karnik, R., Gu, H., Nagle, J. M., Boukhali, M., Hayward, M. C., Li, Y. Y., Chen, T., Liesa, M., Hammerman, P. S., Wong, K. K., Hayes,

- D. N., Shirihai, O. S., Dyson, N. J., Haas, W., Meissner, A. & Bardeesy, N. LKB1 loss links serine metabolism to DNA methylation and tumorigenesis. *Nature* **539**, 390–395 (2016).
169. Mentch, S. J., Mehrmohamadi, M., Huang, L., Liu, X., Gupta, D., Mattocks, D., Gomez Padilla, P., Ables, G., Bamman, M. M., Thalacker-Mercer, A. E., Nichenametla, S. N. & Locasale, J. W. Histone Methylation Dynamics and Gene Regulation Occur through the Sensing of One-Carbon Metabolism. *Cell Metab* **22**, 861–73 (2015).
 170. Maddocks, O. D., Labuschagne, C. F., Adams, P. D. & Vousden, K. H. Serine Metabolism Supports the Methionine Cycle and DNA/RNA Methylation through De Novo ATP Synthesis in Cancer Cells. *Mol Cell* **61**, 210–21 (2016).
 171. DeBerardinis, R. J. & Cheng, T. Q's next: the diverse functions of glutamine in metabolism, cell biology and cancer. *Oncogene* **29**, 313–24 (2010).
 172. Kung, H. N., Marks, J. R. & Chi, J. T. Glutamine synthetase is a genetic determinant of cell type-specific glutamine independence in breast epithelia. *PLoS Genet* **7**, e1002229 (2011).
 173. Tardito, S., Oudin, A., Ahmed, S. U., Fack, F., Keunen, O., Zheng, L., Miletic, H., Sakariassen, P. O., Weinstock, A., Wagner, A., Lindsay, S. L., Hock, A. K., Barnett, S. C., Ruppin, E., Morkve, S. H., Lund-Johansen, M., Chalmers, A. J., Bjerkvig, R., Niclou, S. P. & Gottlieb, E. Glutamine synthetase activity fuels nucleotide biosynthesis and supports growth of glutamine-restricted glioblastoma. *Nat Cell Biol* **17**, 1556–68 (2015).
 174. Sellers, K., Fox, M. P., Bousamra M., 2., Slone, S. P., Higashi, R. M., Miller, D. M., Wang, Y., Yan, J., Yuneva, M. O., Deshpande, R., Lane, A. N. & Fan, T. W. Pyruvate carboxylase is critical for non-small-cell lung cancer proliferation. *J Clin Invest* **125**, 687–98 (2015).
 175. Cheng, T., Sudderth, J., Yang, C., Mullen, A. R., Jin, E. S., Mates, J. M. & DeBerardinis, R. J. Pyruvate carboxylase is required for glutamine-independent growth of tumor cells. *Proc Natl Acad Sci U S A* **108**, 8674–9 (2011).
 176. Lussey-Lepoutre, C., Hollinshead, K. E., Ludwig, C., Menara, M., Morin, A., Castro-Vega, L. J., Parker, S. J., Janin, M., Martinelli, C., Ottolenghi, C., Metallo, C., Gimenez-Roqueplo, A. P., Favier, J. & Tennant, D. A. Loss of succinate dehydrogenase activity results in dependency on pyruvate carboxylation for cellular anabolism. *Nat Commun* **6**, 8784 (2015).
 177. Cardaci, S., Zheng, L., MacKay, G., van den Broek, N. J., MacKenzie, E. D., Nixon, C., Stevenson, D., Tumanov, S., Bulusu, V., Kamphorst, J. J., Vazquez, A., Fleming, S., Schiavi, F., Kalna, G., Blyth, K., Strathdee, D. & Gottlieb, E. Pyruvate carboxylation

- enables growth of SDH-deficient cells by supporting aspartate biosynthesis. *Nat Cell Biol* **17**, 1317–26 (2015).
178. Davidson, S. M., Papagiannakopoulos, T., Olenchock, B. A., Heyman, J. E., Keibler, M. A., Luengo, A., Bauer, M. R., Jha, A. K., O'Brien, J. P., Pierce, K. A., Gui, D. Y., Sullivan, L. B., Wasylenko, T. M., Subbaraj, L., Chin, C. R., Stephanopolous, G., Mott, B. T., Jacks, T., Clish, C. B. & Vander Heiden, M. G. Environment Impacts the Metabolic Dependencies of Ras-Driven Non-Small Cell Lung Cancer. *Cell Metab* **23**, 517–28 (2016).
 179. Hensley, C. T., Faubert, B., Yuan, Q., Lev-Cohain, N., Jin, E., Kim, J., Jiang, L., Ko, B., Skelton, R., Loudat, L., Wodzak, M., Klimko, C., McMillan, E., Butt, Y., Ni, M., Oliver, D., Torrealba, J., Malloy, C. R., Kernstine, K., Lenkinski, R. E. & DeBerardinis, R. J. Metabolic Heterogeneity in Human Lung Tumors. *Cell* **164**, 681–94 (2016).
 180. Pascual, G., Avgustinova, A., Mejetta, S., Martin, M., Castellanos, A., Attolini, C. S., Berenguer, A., Prats, N., Toll, A., Hueto, J. A., Bescos, C., Di Croce, L. & Benitah, S. A. Targeting metastasis-initiating cells through the fatty acid receptor CD36. *Nature* **541**, 41–45 (2017).
 181. Hale, J. S., Otvos, B., Sinyuk, M., Alvarado, A. G., Hitomi, M., Stoltz, K., Wu, Q., Flavahan, W., Levison, B., Johansen, M. L., Schmitt, D., Neltner, J. M., Huang, P., Ren, B., Sloan, A. E., Silverstein, R. L., Gladson, C. L., DiDonato, J. A., Brown, J. M., McIntyre, T., Hazen, S. L., Horbinski, C., Rich, J. N. & Lathia, J. D. Cancer stem cell-specific scavenger receptor CD36 drives glioblastoma progression. *Stem Cells* **32**, 1746–58 (2014).
 182. Nath, A., Li, I., Roberts, L. R. & Chan, C. Elevated free fatty acid uptake via CD36 promotes epithelial-mesenchymal transition in hepatocellular carcinoma. *Sci Rep* **5**, 14752 (2015).
 183. Yao, C. H., Fowle-Grider, R., Mahieu, N. G., Liu, G. Y., Chen, Y. J., Wang, R., Singh, M., Potter, G. S., Gross, R. W., Schaefer, J., Johnson, S. L. & Patti, G. J. Exogenous Fatty Acids Are the Preferred Source of Membrane Lipids in Proliferating Fibroblasts. *Cell Chem Biol* **23**, 483–93 (2016).
 184. Hatzivassiliou, G., Zhao, F., Bauer, D. E., Andreadis, C., Shaw, A. N., Dhanak, D., Hingorani, S. R., Tuveson, D. A. & Thompson, C. B. ATP citrate lyase inhibition can suppress tumor cell growth. *Cancer Cell* **8**, 311–21 (2005).
 185. Brusselmans, K., De Schrijver, E., Verhoeven, G. & Swinnen, J. V. RNA interference-mediated silencing of the acetyl-CoA-carboxylase- α gene induces growth inhibition and apoptosis of prostate cancer cells. *Cancer Res* **65**, 6719–25 (2005).

186. Milgraum, L. Z., Witters, L. A., Pasternack, G. R. & Kuhajda, F. P. Enzymes of the fatty acid synthesis pathway are highly expressed in in situ breast carcinoma. *Clin Cancer Res* **3**, 2115–20 (1997).
187. Benjamin, D. I., Li, D. S., Lowe, W., Heuer, T., Kemble, G. & Nomura, D. K. Diacylglycerol Metabolism and Signaling Is a Driving Force Underlying FASN Inhibitor Sensitivity in Cancer Cells. *ACS Chem Biol* **10**, 1616–23 (2015).
188. Previs, S. F., McLaren, D. G., Wang, S. P., Stout, S. J., Zhou, H., Herath, K., Shah, V., Miller, P. L., Wilsie, L., Castro-Perez, J., Johns, D. G., Cleary, M. A. & Roddy, T. P. New methodologies for studying lipid synthesis and turnover: looking backwards to enable moving forwards. *Biochim Biophys Acta* **1842**, 402–13 (2014).
189. Svensson, R. U., Parker, S. J., Eichner, L. J., Kolar, M. J., Wallace, M., Brun, S. N., Lombardo, P. S., Van Nostrand, J. L., Hutchins, A., Vera, L., Gerken, L., Greenwood, J., Bhat, S., Harriman, G., Westlin, W. F., Harwood H. J., J., Saghatelian, A., Kapeller, R., Metallo, C. M. & Shaw, R. J. Inhibition of acetyl-CoA carboxylase suppresses fatty acid synthesis and tumor growth of non-small-cell lung cancer in preclinical models. *Nat Med* **22**, 1108–1119 (2016).
190. Vacanti, N. M. & Metallo, C. M. Exploring metabolic pathways that contribute to the stem cell phenotype. *Biochim Biophys Acta* **1830**, 2361–9 (2013).
191. Gu, W., Gaeta, X., Sahakyan, A., Chan, A. B., Hong, C. S., Kim, R., Braas, D., Plath, K., Lowry, W. E. & Christofk, H. R. Glycolytic Metabolism Plays a Functional Role in Regulating Human Pluripotent Stem Cell State. *Cell Stem Cell* **19**, 476–490 (2016).
192. Green, C. R., Wallace, M., Divakaruni, A. S., Phillips, S. A., Murphy, A. N., Ciaraldi, T. P. & Metallo, C. M. Branched-chain amino acid catabolism fuels adipocyte differentiation and lipogenesis. *Nat Chem Biol* **12**, 15–21 (2016).
193. Mayers, J. R., Torrence, M. E., Danai, L. V., Papagiannakopoulos, T., Davidson, S. M., Bauer, M. R., Lau, A. N., Ji, B. W., Dixit, P. D., Hosios, A. M., Muir, A., Chin, C. R., Freinkman, E., Jacks, T., Wolpin, B. M., Vitkup, D. & Vander Heiden, M. G. Tissue of origin dictates branched-chain amino acid metabolism in mutant Kras-driven cancers. *Science* **353**, 1161–5 (2016).
194. Cordes, T., Wallace, M., Michelucci, A., Divakaruni, A. S., Sapcariu, S. C., Sousa, C., Koseki, H., Cabrales, P., Murphy, A. N., Hiller, K. & Metallo, C. M. Immunoresponsive Gene 1 and Itaconate Inhibit Succinate Dehydrogenase to Modulate Intracellular Succinate Levels. *J Biol Chem* **291**, 14274–84 (2016).
195. Lampropoulou, V., Sergushichev, A., Bambouskova, M., Nair, S., Vincent, E. E., Loginicheva, E., Cervantes-Barragan, L., Ma, X., Huang, S. C., Griss, T., Weinheimer, C. J., Khader, S.,

Randolph, G. J., Pearce, E. J., Jones, R. G., Diwan, A., Diamond, M. S. & Artyomov, M. N. Itaconate Links Inhibition of Succinate Dehydrogenase with Macrophage Metabolic Remodeling and Regulation of Inflammation. *Cell Metab* **24**, 158–66 (2016).

Chapter 2

Enzymatic passaging of human embryonic stem cells alters central carbon metabolism and glycan abundance

2.1 Abstract

To realize the potential of human embryonic stem cells (hESCs) in regenerative medicine and drug discovery applications, large numbers of cells that accurately recapitulate cell and tissue function must be robustly produced. Previous studies have suggested that genetic instability and epigenetic changes occur as a consequence of enzymatic passaging. However, the potential impacts of such passaging methods on the metabolism of hESCs have not been described. Using stable isotope tracing and mass spectrometry-based metabolomics we have explored how different passaging reagents impact hESC metabolism. Enzymatic passaging caused significant decreases in glucose utilization throughout central carbon metabolism along with attenuated *de novo* lipogenesis. In addition, we developed and validated a method for rapidly quantifying glycan abundance and isotopic labeling in hydrolyzed biomass. Enzymatic passaging reagents significantly altered

levels of glycans immediately after digestion but surprisingly glucose contribution to glycans was not affected. These results demonstrate that there is an immediate effect on hESC metabolism after enzymatic passaging in both central carbon metabolism and biosynthesis. HESCs subjected to enzymatic passaging are routinely placed in a state requiring re-synthesis of biomass components, subtly influencing their metabolic needs in a manner that may impact cell performance in regenerative medicine applications.

2.2 Introduction

Human embryonic stem cells (hESCs) are characterized by their ability to differentiate into the three terminal germ layers and self-renew indefinitely. This makes them ideal cell types for regenerative medicine and drug discovery applications. However, the impact of *in vitro* culture conditions on cell performance and stability must be monitored and validated to ensure these cells recapitulate actual tissue functions. Since the initial isolation and expansion of hESC lines on feeder layer conditions [1], more recently developed, chemically-defined culture conditions have become commonly used for the isolation and culture of hESCs and induced pluripotent stem cells (iPSCs) [2]. Along with the engineering of defined culture conditions, a concomitant development of enzymatic passaging methods to replace laborious mechanical passaging methods also occurred. Analysis of cells cultivated using these enzymatic passaging techniques has suggested these approaches increase karyotypic instability of hESCs [3–5]. Another recent study has indicated that enzymatic passaging may cause increased genetic instability and differential DNA methylation [6]. While these studies have addressed the effects of enzymatic passaging on cellular genetics and epigenetic alterations, the impacts of passaging method on cellular metabolism have not been examined.

HESC metabolism is characterized by a greater reliance on glycolysis compared to cells in the differentiated state [7–9]. Glycolytic flux is essential for maintenance of the stem

cell phenotype, as evidenced by the impact of inhibitors of glycolysis on pluripotency marker expression and cellular reprogramming [10, 11]. While glucose metabolism provides cellular energy by producing adenosine triphosphate (ATP) and reducing equivalents, glucose is also the primary carbon source for a myriad of biosynthetic precursors, including ribose for nucleotides, non-essential amino acids, and acetyl-coenzyme A (AcCoA) for lipids. Though commonly overlooked in studies of intermediary metabolism, glucose (in addition to glutamine) also provides the necessary building blocks for the synthesis of glycan moieties, which are essential for protein function and trafficking. Glycans are also the key components that comprise the glycocalyx, which surrounds the cell membrane of some cells [12]. Through the cleavage of extracellular proteins and their associated glycans, enzymatic digestion could affect the phenotype of hESCs by impacting their metabolic demands or ability to respond to extracellular signaling cues [13–17].

To understand the influence of enzymatic passaging on hESC metabolism we utilized stable isotope tracing and mass spectrometry-based metabolomics to characterize central carbon metabolism after passaging. We developed and applied a method for rapid quantitation of glycan, nucleotide, and amino acid pools to explore the impact of passaging reagents on hESC biomass. Finally, we determined how enzymatic passaging affects biosynthetic flux to lipids, nucleotides and carbohydrates. Our results demonstrate that enzymatic passaging alters hESC metabolism and the cell's ability to synthesize biosynthetic intermediates while highlighting the quantitative importance of metabolic flux to glycan pools.

2.3 Materials and Methods

2.3.1 Cell culture

WA09 hESCs (H9s) were maintained on Synthemax II-SC coated (Corning, Corning, NY) plates in mTESR1 (Stem Cell Technologies, Vancouver, BC). hESCs were passaged every 5 days by exposure to Versene (Gibco, Grand Island, NY) for 10 min at 37°C. Synthemax II-SC coating

was performed by dispensing 2 mL of working dilution (25 $\mu\text{g}/\text{mL}$) to each well of a 6-well of a tissue culture polystyrene plate and incubating for 2 hours. For isotopic labeling experiments, cells were maintained in mTESR1 media with uniformly-labeled glucose (tracer mTESR) by adding 5x mTESR1 supplement to custom DMEM/F-12. Custom DMEM/F-12 (Hyclone Laboratories, Logan, UT) without amino acids, D-glucose, sodium pyruvate, sodium bicarbonate, and phenol red was supplemented with all amino acids, sodium pyruvate, sodium bicarbonate (14 mM; Sigma-Aldrich, St. Louis, MO), HEPES (15mM; from 1M stock, Gibco, Grand Island, NY), and [U- $^{13}\text{C}_6$] Glucose (99%; Cambridge Isotopes, Cambridge, MA) at DMEM/F-12 levels.

2.3.2 Enzymatic passaging experiments

H9s (p29-35) were grown on Synthemax II-SC coated plates to 50-70% confluency. Cells were rinsed with 1 mL PBS and then exposed at 37°C to either 1 mL Versene for 10 minutes, Accutase (Innovative Cell Technology, San Diego, CA) for 5 minutes, or Trypsin-EDTA (0.25%; Gibco, Grand Island, NY) for 5 minutes. Versene-treated cells were then split to 3 wells by aspirating Versene and resuspending in 6 mL mTESR. Accutase-treated cells were split to 3 wells by adding 9 mL PBS to Accutase solution, centrifuging at 300g for 5 min, and resuspending in 6 mL mTESR after aspiration. Trypsin-treated cells were split to 3 wells by adding 9 mL PBS to Trypsin solution, centrifuging at 300g for 5 min, and resuspending pellet in 6 mL mTESR after aspiration. Cells traced immediately after passaging were resuspended in tracer mTESR. Cells traced 24 hours after passaging were resuspended in mTESR1 immediately after passaging, rinsed with PBS 24 hours later, and changed into tracer mTESR before extracting 4 hours later. For experiments with ROCK inhibitor, 5 μM of Y-27632 (Tocris, Avon, UK) was added to media.

For quantitation of biomass abundances after passaging, cells in triplicate were rinsed with 1 mL PBS and exposed at 37°C to 1mL Versene for 10 minutes, TrypLE Express (Gibco, Grand Island, NY) for 5 minutes, Accutase for 5 minutes, or Trypsin-EDTA for 5 minutes. 1 mL of PBS was immediately added after incubation to quench enzymatic digestion and then

transferred to 15 mL conical tube containing 7 mL PBS. Each well was then washed with 1 mL PBS and added to the respective conical tube. Cells were then centrifuged at 300g for 5 minutes and supernatant was aspirated. Cells were then washed twice by resuspension of the pellet in 1 mL 0.9% (w/v) saline, centrifugation at 300g for 5 minutes, and aspiration of supernatant. Pellets were then stored at -20°C for metabolite extraction.

2.3.3 Metabolite Extraction and GC-MS Analysis

Polar metabolites and fatty acids were extracted using methanol/water/chloroform as previously described [18]. Briefly, cells were rinsed with 0.9% (w/v) saline and 250 μ L of -80°C MeOH was added to quench metabolic reactions. 100 μ L of ice-cold water supplemented with 10 μ g/mL norvaline was then added to each well and cells were collected by scraping. The lysate was moved to a fresh 1.5 mL eppendorf tube and 250 μ L of -20°C chloroform supplemented with 10 μ g/mL heptadecanoate was added. After vortexing and centrifugation, the top aqueous layer and bottom organic layer were collected and dried under airflow. The remaining "interface" layer containing biomass was washed twice by addition of -80°C 500 μ L of MeOH, centrifugation at 21,000g, and decanting of supernatant. Interface layers were then dried by ambient air overnight and stored at -20°C. For cell pellets, a similar procedure was performed as previously described, except the cell pellet was resuspended in ice cold MeOH/water solution with norvaline by pipetting and then cells were lysed by vortexing for 1 min. Chloroform was then added and polar/non-polar fractions were collected. To prepare biomass components for relative quantitation and isotopomer analysis, acid hydrolysis of interface layer was performed by first drying the rinsed interface under airflow then incubating in 500 μ L of 6M HCl at 80°C for 2 hours. Hydrolyzed biomass solution was split to five aliquots and dried by airflow overnight for subsequent GC/MS analysis.

Fatty acids and polar metabolites were derivatized as previously described [18]. For fatty acids, dried nonpolar fraction was saponified and esterified to form fatty acid methyl esters

(FAMES) by addition of 500 μL of 2% (w/v) H_2SO_4 in MeOH and incubated at 50°C for 120 minutes. FAMES were then extracted by addition of saturated NaCl and hexane before collection and drying of the inorganic layer. For polar metabolites, methoxime-tBDMS derivatives were formed by addition of 15 μL 2% (w/v) methoxylamine hydrochloride (MP Biomedicals, Solon, OH) in pyridine and incubated at 45°C for 60 minutes. Samples were then silylated by addition of 15 μL of N-tert-butyldimethylsilyl-N-methyltrifluoroacetamide (MTBSTFA) with 1% tert-butyldimethylchlorosilane (tBDMS) (Regis Technologies, Morton Grove, IL) and incubated at 45°C for 30 minutes. For biomass analysis of sugars and glycan residues that were too large for tBDMS derivatization, methoxime-trimethylsilyl (TMS) derivatives were formed by addition of 15 μL 2% (w/v) methoxylamine hydrochloride (MP Biomedicals, Solon, OH) in pyridine and incubated at 37°C for 60 minutes. Samples were then silylated by addition of 15 μL of N-methyltrimethylsilyltrifluoroacetamide (MSTFA; Regis Technologies, Morton Grove, IL) and incubated at 45°C for 30 minutes.

Polar and interface samples were analyzed by GC-MS using a DB-35MS column (30m x 0.25mm i.d. x 0.25 μm , Agilent J&W Scientific, Santa Clara, CA) in an Agilent 7890B gas chromatograph (GC) interfaced with a 5977C mass spectrometer (MS). Electron impact ionization was performed with the MS scanning over the range of 100-650 m/z for polar metabolites and 70-850 m/z for biomass metabolites. For separation of polar metabolites the GC oven was held at 100°C for 1 min after injection, increased to 255°C at 3.5°C/min, and finally increased to 320°C at 15°C/min and held for 3 min. For separation of the biomass metabolites the GC oven was held at 80°C for 6 min after injection, increased to 300°C at 6°C/min and held for 10 min, and finally increased to 325°C at 10°C/min and held for 4 min.

Derivatized fatty acids were analyzed by GC-MS using a select FAME column (100m x 0.25mm i.d. x 0.25 μm ; Agilent J&W Scientific, Santa Clara, CA) as above, with the MS scanning over the range 120-400 m/z. For separation the GC oven was held at 80°C for 1 min after injection, increased to 160°C at 20°C/min, increased to 198°C at 1°C/min, and finally increased

to 250°C at 5°C/min and held for 15 min.

2.3.4 Mass isotopomer distributions, isotopomer spectral analysis (ISA), and flux analysis

Mass isotopomer distributions and total abundances were determined by integration of mass fragments (Table 1) and correcting for natural abundances using in-house algorithms [18]. Total abundances were normalized by counts of adenine and guanine. Isotopomer spectral analysis (ISA) was performed as previously described [18]. ISA compares experimental labeling of fatty acids to simulated labeling using a reaction network where C14:0 is condensation of 7 AcCoAs, C16:0 is condensation of 8 AcCoAs, C16:1c is condensation of 8 AcCoAs, C18:0 is condensation of 9 AcCoAs, and C18:1n9c is condensation of 9 AcCoAs. Parameters for contribution of glucose to lipogenic AcCoA (D value) and percentage of newly synthesized fatty acid (g(t) value) and their 95% confidence intervals are then calculated using best-fit model from INCA MFA software [19]. Per biomass molar quantitation of glucose, galactose, glucosamine, mannosamine, serine, ribose, and leucine was accomplished by determining the ratio of each and comparing to the molar amount of leucine in mammalian cells per gram dry weight [20]. Amino acid fragments were taken from previously described work and validated [21].

2.3.5 Statistical analyses

All results shown as averages of triplicates presented as mean \pm SD. P values were calculated using a Student's two-tailed t test; *, P value between 0.01 and 0.05; **, P value between 0.001 and 0.01; ***, P value <0.001 . All errors associated with ISA are 95% confidence intervals determined via confidence interval analysis [22].

Table 2.1: Metabolite fragments used for GC/MS analysis.

Metabolite	Derivatization	Fragments for integration	m/z	Positions of labeled carbons	Retention Time (min)
Alanine	TBDMS	C ₁₁ H ₂₆ O ₂ NSi ₂	260	123	13.1
Lactate	TBDMS	C ₁₁ H ₂₅ O ₃ Si ₂	261	123	11.9
Citrate	TBDMS	C ₂₆ H ₅₅ O ₇ Si ₄	591	123456	41.2
Adenine	TMS	C ₁₁ H ₂₁ N ₅ Si ₂	279		27.4
	TMS	C ₁₀ H ₁₈ N ₅ Si ₂	264		
Galactose	TMS	C ₁₃ H ₃₁ O ₃ Si ₃	319	3456	23.8
Glucose	TMS	C ₁₃ H ₃₁ O ₃ Si ₃	319	3456	23.9
Glucosamine	TMS	C ₁₃ H ₃₁ O ₃ Si ₃	319	3456	24.7
Guanine	TMS	C ₁₄ H ₂₉ ON ₅ Si ₃	367		31.5
	TMS	C ₁₃ H ₂₆ ON ₅ Si ₃	352		
Mannosamine	TMS	C ₁₃ H ₃₁ O ₃ Si ₃	319	3456	24.5
Ribose	TMS	C ₁₂ H ₃₁ O ₃ Si ₃	307	345	20.3
Serine	TMS	C ₁₁ H ₂₈ O ₃ NSi ₃	306	123	14.4
Leucine	TMS	C ₈ H ₂₀ NSi	158		12.1

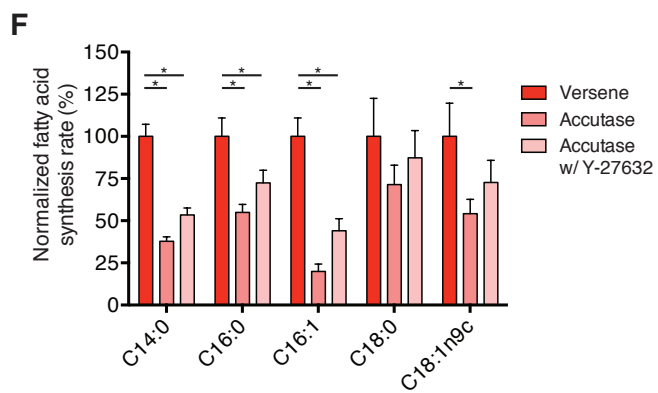
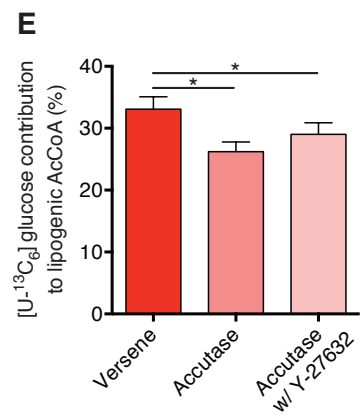
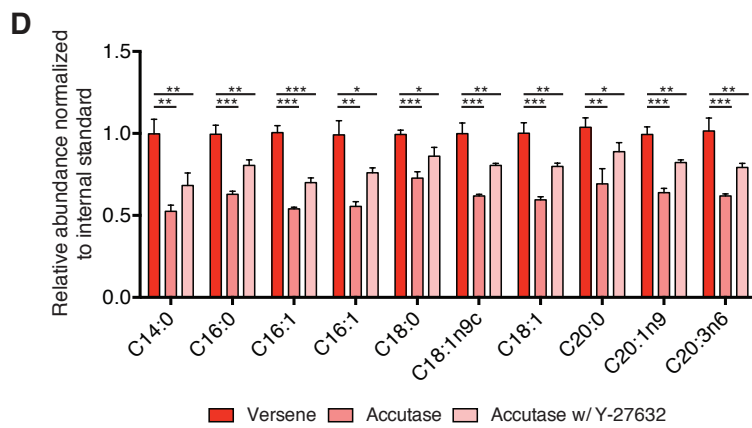
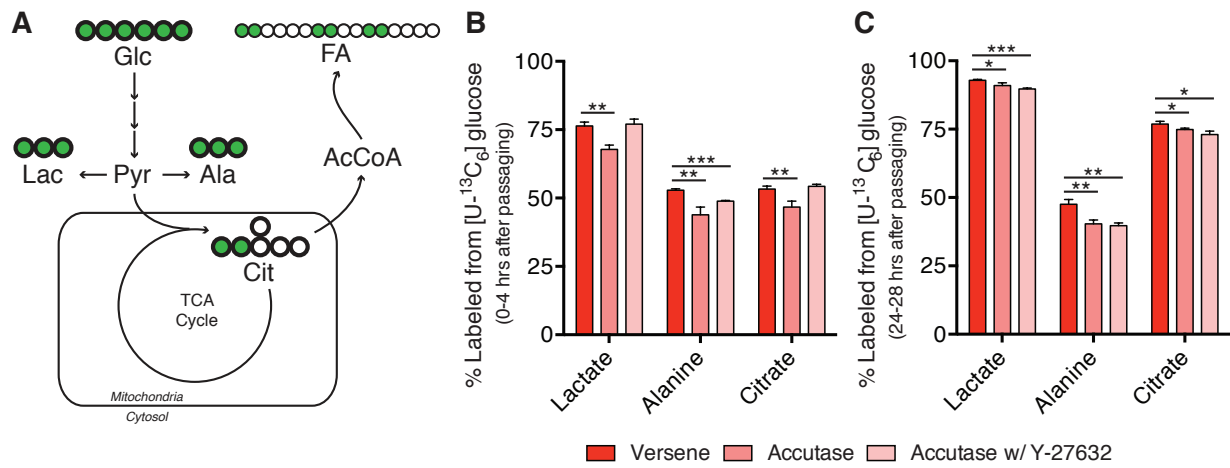
2.4 Results

2.4.1 Enzymatic passaging decreases glucose oxidation and fatty acid synthesis in hESCs

To investigate the effects of enzymatic passaging on hESC metabolism we used stable isotope tracing with [U-¹³C₆]glucose and GC/MS analysis to probe intermediary metabolism and lipid synthesis (Figure 2.1A). By quantifying the extent of metabolite labeling and pool sizes in hESCs after various treatments we were able to quantify relative changes in flux through each pathway. Accutase treatment induced a significant decrease in glucose contribution to both lactate and alanine as compared to clumped passaging (Versene treatment) (Figure 2.1B). Additionally, a significantly lower contribution of glucose to the TCA-intermediate citrate was seen in Accutase treated cells (Figure 2.1B and S2.1A). Importantly, the pool sizes of each metabolite 4 hours after enzyme treatment were similar to or lower than that observed with clumped passaging (Figure S2.1B). Therefore, the differential labeling we observed indicated that flux through glycolysis and into mitochondria were significantly decreased in Accutase treated cells. Similar changes in glucose-derived labeling were observed when cells were passaged with Trypsin, indicating

the impact on central carbon metabolism is not specific to Accutase (Figure S2.1D). Previous work has demonstrated that addition of a Rho-associated kinase (ROCK) inhibitor can prevent single cell dissociation-induced apoptosis [23]. To account for these effects we also investigated whether the addition of Y-27632 could rescue defects in glucose metabolism. While addition of ROCK inhibitor rescued labeling in lactate and citrate, flux to alanine only increased slightly (Figure 2.1B and S2.1A). Taken together, these results suggest that enzymatic passaging lowered flux through glycolysis and into the TCA cycle, and addition of ROCK inhibitor only partially rescued this metabolic phenotype.

Figure 2.1: Enzymatic passaging alters central carbon metabolism. (A) Atom-transition map depicting flow of [U-¹³C₆]glucose (UGlc) carbon through central carbon metabolism and lipid biosynthesis. Green circles depict ¹³C atoms and open circles depict ¹²C atoms. (B) Percentage of labeled metabolites from UGlc 4 hours after non-enzymatic or enzymatic passaging. Higher labeling indicates greater glucose usage for glycolysis, non-essential amino acid synthesis, and TCA metabolism. (C) Percentage of labeled metabolites from UGlc one day after non-enzymatic or enzymatic passaging (i.e., labeled from 24-28 hours after passaging). Defects in glucose catabolism mediated through enzymatic passaging are still present. (D) Relative abundance of fatty acid species after enzymatic or non-enzymatic passaging. (E) Contribution of UGlc to lipogenic AcCoA as determined by ISA model. Decrease in contribution is consistent with decreased labeling in the lipogenic metabolite citrate. (F) Normalized fatty acid flux for synthesized fatty acid species calculated using total pool size and fractional synthesis from ISA model. Error bars represent SD (B-D) or 95% CI (E-F) for three replicates. *, P value between 0.01 and 0.05; **, P value between 0.001 and 0.01; ***, P value <0.001 by Student's two-tailed t test; or, * indicates significance by nonoverlapping 95% confidence intervals



To determine whether enzymatic passaging elicited sustained effects on intermediary metabolism we quantified abundance and labeling of the same metabolite pools when applying tracer 24 hours after re-plating. Interestingly, even after 24 hours we still observed significant, though slight, decreases in lactate, alanine, and citrate abundances (Figure S2.1C) and labeling (Figure 2.1C). These data suggest that enzymatic passaging may impact cell metabolism last longer than the immediate period after passaging.

Having observed differences in flux to the lipogenic intermediate citrate, we then explored whether enzymatic passaging impacted lipid metabolism. Specifically, we quantified the relative abundance and isotopic labeling in various fatty acid species from saponified lipid fractions of hESCs. Measurement of total cellular fatty acid abundances showed a clear decrease in all measured species upon enzymatic passaging, and addition of ROCK inhibitor failed to rescue any defect (Figure 2.1D). Decreases in abundance were observed in saturated, unsaturated, and polyunsaturated fatty acids, implicating pan defects in lipid metabolism. Indeed, since decreases were observed in both non-essential (e.g. C16:0) and essential (e.g. C20:3n6) fatty acids, these data indicate that lipid synthesis and uptake were compromised in cells passaged using enzymatic reagents. To quantify biosynthetic fluxes in greater detail we then applied isotopomer spectral analysis (ISA) to determine the relative contribution of glucose to lipogenic AcCoA pools as well as the extent of *de novo* lipogenesis for each fatty acid measured [24]. Consistent with the above effects on glucose flux to citrate (Figure 2.1B), enzymatic passaging with and without ROCK inhibitor supplementation significantly decreased the extent of glucose conversion to lipogenic AcCoA as compared to clumped passaging (Figure 2.1E). Using both pool size (Figure 2.1D) and fractional synthesis/turnover data obtained from ISA, we observed that enzymatic passaging significantly decreased the synthesis rates of saturated myristic acid (C14:0), saturated palmitic acid (C16:0), and unsaturated palmitoleic acid (C16:1) (Figure 2.1F). In nearly all cases these effects were not rescued by addition of a ROCK inhibitor. These data therefore indicate that enzymatic passaging lowers the ability of hESCs to utilize glucose for biosynthesis in central

carbon metabolism and lipid synthesis.

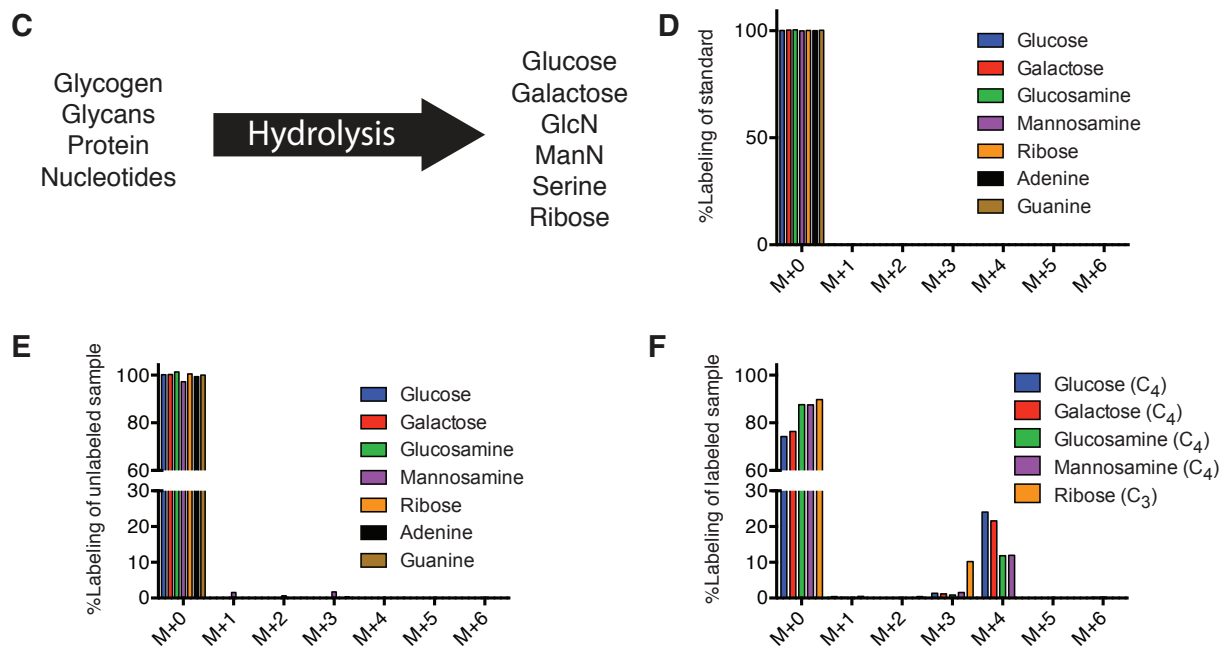
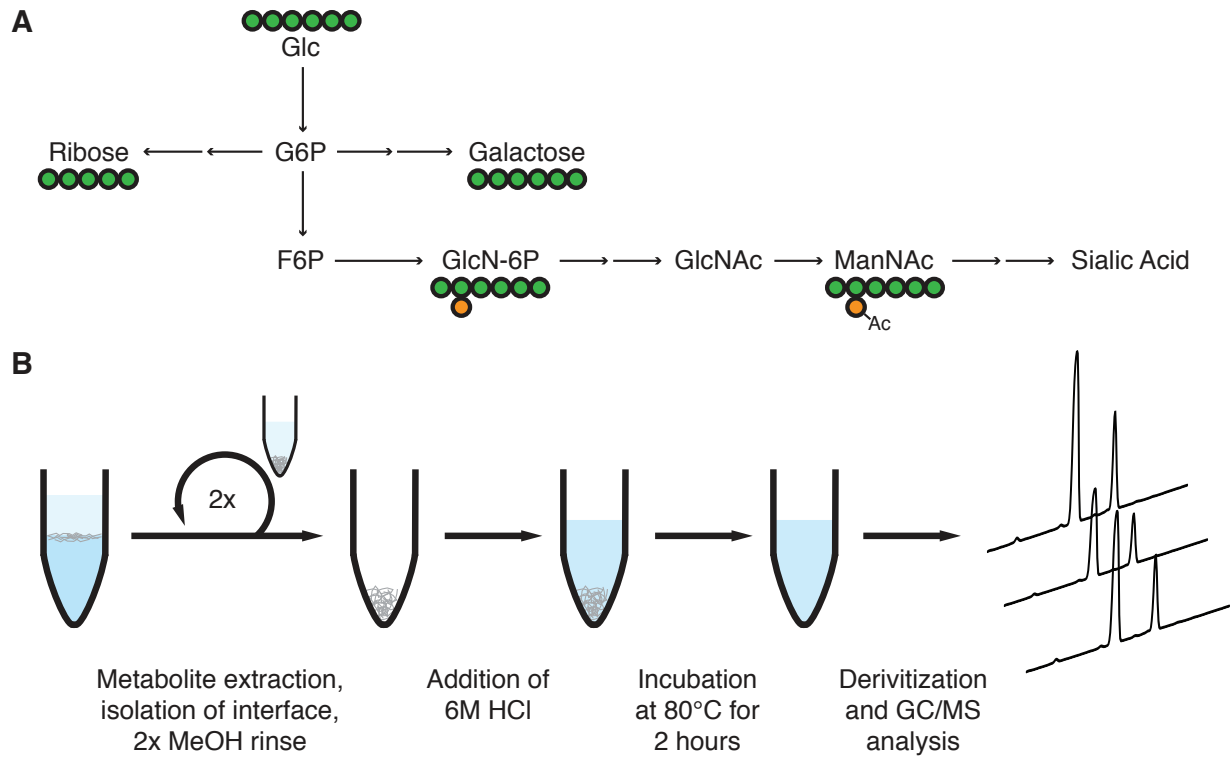
2.4.2 Rapid quantitation of total glycan pools and synthesis in hESCs

Rapidly dividing cells have considerable biosynthetic demands for structural components as well as bioenergetic demands for maintenance and division [25]. Glucose metabolism has been demonstrated as an essential source of carbon and ATP generation for hESC proliferation [26, 27]. At the nexus of glucose metabolism and biosynthesis, post-translational modifications (PTM) have also been demonstrated to be essential to maintain stem cell pluripotency and function [28–30]. Large classes of PTMs that also involve glucose metabolism are N-linked and O-linked glycosylation moieties [31, 32]. Indeed, N-linked glycosylation is the major structural component of the glycocalyx that surrounds cell membranes [31]. Given the significant abundance of these intermediates at the cell surface, we hypothesized that glycan pools and synthesis might be significantly affected by enzymatic passaging of hESCs.

To better quantify flux through the hexosamine biosynthesis pathway we developed a method for measuring relative glycan pool sizes and isotopic labeling from tracers in hESCs or other cultured cell types. While enzyme-mediated dissociation is commonly used for glycomics-platform analyses, such methods can be costly and time-consuming. Rather than conducting whole-glycan analyses we instead collected the biomass fraction of hESC extracts and performed acid hydrolysis to release individual glycan residues, nucleobases, sugars from nucleotides or glycogen, and proteinogenic amino acids. Acid hydrolysis is commonly used in metabolic flux analysis (MFA) applications, but the extent of labeling in glycans is not commonly measured [33]. This is particularly true in MFA applied to mammalian cells [34–36]. To validate our approach we analyzed standards for specific glycan residues and compared the mass isotopomer distributions (MIDs) of specific fragments to those measured in cells cultured in the presence of [U-¹³C₆]glucose. Glucose labeling was readily incorporated into glycan pools through the hexosamine biosynthesis pathway (Figure 2.2A). Acid hydrolysis of cellular biomass in turn

releases proteinogenic amino acids, ribose, sugars, and aminosugars for GC/MS analysis (Figure 2.2B). However, since several glycan species are labile in the conditions used for release, in some cases (e.g. acetylated glycan moieties) we relied on the measurement of proxy molecules (Figure 2.2C). The MIDs of specific glycan sugars from standards and hydrolyzed hESCs are depicted in Figure 2.2D-E and tabulated in Tables S2.1, S2.2; all of which were corrected for natural isotope abundance using in-house algorithms and calculated fragment formulae (Table 1). In each case the corrected MID matched that of the standards. Notably, some glycan sugars were not present at detectable levels to include here (e.g. fucose, xylose, mannose, galactosamine), and the relatively low abundance of mannosamine caused some deviation from unity in the measured and corrected MID. Furthermore, labeling from [U-¹³C₆]glucose indicated the number of carbons present from the parent molecule (Figure 2.2F). Although free metabolites were removed from the biomass interface prior to hydrolysis and derivatization, we conducted parallel treatments and quantitation on the free, polar metabolites present in our extract to the quantities in each subcellular pool. While serine, ribose, glucose, and glucosamine were 5-10-fold more abundant in biomass compared to free metabolites (including those present as nucleotide-sugars or phosphorylated intermediates), the abundance of galactose and mannosamine from biomass hydrolysates was only 2-fold higher than that quantified from free metabolites (Figure S2.2A). Therefore, this method allowed for the measurement of relative glycan residue abundance and labeling from cellular biomass pools (Figure 2.2B). Previous methods focusing on biomass pools have relied on targeted digestion of nucleotides, proteins, and glycans individually [37–39]. Our method instead allows profiling of all three classes of biosynthetic intermediates simultaneously.

Figure 2.2: Quantitation of glycan residue abundance and labeling in cellular biomass. (A) Atom-transition map depicting flow of [U-¹³C₆]glucose (UGlc) into ribose, galactose, and hexosamines. Green circles depict carbon atoms and orange circles depict nitrogen atoms. (B) Schematic of biomass hydrolysis method. Insoluble interface layer is isolated from initial methanol/water/chloroform quench/extraction, rinsed twice with methanol, and acid hydrolyzed. (C) Diagram of detectable metabolites after acid hydrolysis. Major macromolecules (nucleotides, protein, glycans) are broken down into primary components (ribose/nucleobases, amino acids, sugars/amino-sugars, respectively), which can be measured on GC/MS. (D) Corrected mass isotopomer distribution (MID) of each metabolite standard. Corrected M+0 peak equal to unity ensures accuracy of MIDs. (E) Corrected MID of metabolites from unlabeled cell hydrolysates. Corrected M+0 peak deviation from unity is informative of MID accuracy and potential contaminating fragments in hydrolysates. (F) Corrected MID of metabolites measured in hydrolysates from hESCs labeled using UGlc. Glucose, galactose, glucosamine, and mannosamine fragments have four carbons labeled from glucose. Ribose has three carbons labeled from glucose. Error bars represent SD (E-F) for three independent hydrolysates.



2.4.3 Glycan and carbohydrate pools are significantly depleted upon enzymatic passaging

To test the effect of enzymatic-treatment on glycan and macromolecule abundance immediately after dissociation, non-enzymatic (Versene) and enzymatic methods (TrypLE, Accutase, and Trypsin) of increasing dissociation strength were used to dissociate cells. All enzymatic reagents significantly altered carbohydrate abundances in biomass as compared to non-enzymatic control treatment (Figure 2.3A and 2.3B). However, while galactose abundance was significantly reduced with enzymatic treatment (Figure 2.3A), glucose abundance significantly increased (Figure 2.3B). Given the presence of glucose in cells as both glycosylation intermediate [32] and component of glycogen, the differential catabolism of glycogen presumably caused such changes. Indeed, this result would be expected given the decreased flux through glycolysis observed in Figure 2.1. Galactose, on the other hand, is primarily present in cells as the glycan residue proximate to terminal sialylation [40].

Similar to our results quantifying galactose, the abundance of glucosamine and mannosamine also decreased with increasing strength of passaging reagents used (Figure 2.3C-D). Importantly, even milder reagents like TrypLE and Accutase showed a significant reduction in abundance of both amino sugars as compared to non-enzymatic control (Figure 2.3C-D). As expected, intracellular serine and ribose levels were unaffected by extracellular enzymatic digestion (Figure 2.3E-F). These results suggest that enzymatic passaging significantly affects biomass composition directly after dissociation.

2.4.4 Biosynthetic fluxes to nucleotides and glycans are similar in cultured hESCs

Since the total pools of specific glycans as well as the flux to various fatty acids in biomass were significantly altered after enzymatic passaging, we then hypothesized that fluxes to these

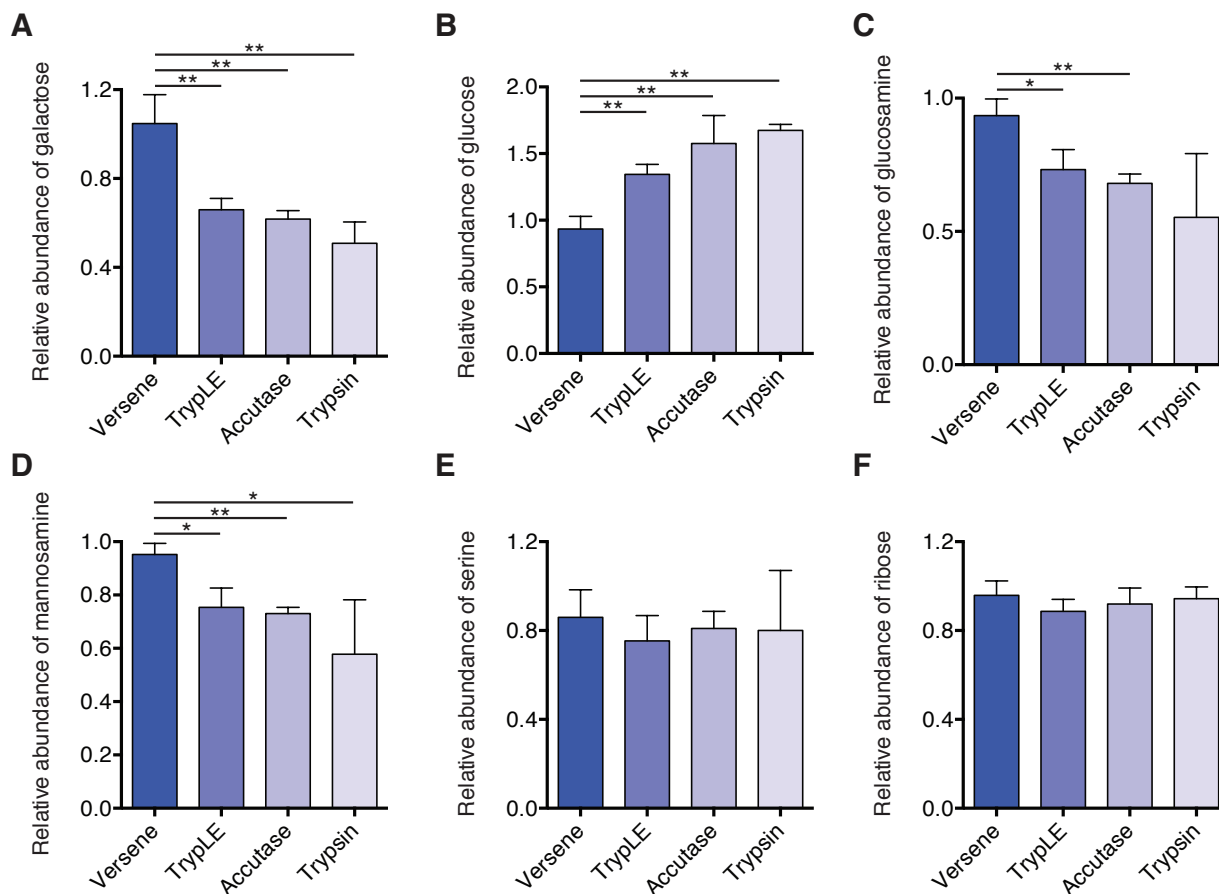


Figure 2.3: Enzymatic passaging alters glycan abundance of hESCs. (A-F) Relative abundance of biomass-derived galactose (A), glucose (B), glucosamine (C), mannosamine (D), serine (E), and ribose (F) immediately after passaging. All data is reported relative to Versene. Decreases in hexose (galactose) and hexosamine (mannosamine and glucosamine) abundances suggest glycans are impacted by enzymatic passaging. This change in abundance is not observed in protein-derived amino acids (serine) or nucleotide/cofactor-derived ribose. Error bars represent SD (A-F) for three replicates. *, P value between 0.01 and 0.05; **, P value between 0.001 and 0.01; ***, P value <0.001 by Student's two-tailed t test.

and other (e.g. nucleotides, protein) biomass pools of hESCs cells would be affected in a similar manner. We again employed stable isotope tracing with [U-¹³C₆]glucose and GC/MS analysis to quantify labeling of hydrolyzed hESC biomass, focusing on components that are representative of protein (serine), nucleotide (ribose), and hexosamine synthesis (Figure 2.2A-C). Cells treated with Accutase and ROCK inhibitor exhibited a slight decrease in labeling of proteinogenic serine (Figure 2.4A), although this measurement is impacted by changes in serine synthesis and uptake from the culture medium. Ribose labeling indicated that enzymatic passaging also decreased the extent of ribose labeling with or without ROCK inhibitor (Figure 2.4A).

Surprisingly, upon examining labeling from glucose in glycan moieties we observed minimal effects when comparing non-enzymatic to enzymatic passaging (Figure 2.4B). While a slight decrease in labeling of biomass-derived glucose was noted upon Accutase treatment, this result was likely due to the increased pool size maintained in enzyme treated cells after passaging (Figure 2.3B). Since routine passaging using enzymatic reagents is an extremely common and frequent insult experienced by hESCs cultivated *in vitro*, we calculated the flux to each biomass compartments using pool size and labeling information. Glucose and serine were not included in these calculations to avoid convoluting effects of glycogen turnover and serine uptake. While molar fluxes associated with galactose, glucosamine, and mannosamine synthesis were significantly lower than that observed for ribose in hESCs (Figure 2.4C), flux to glycans in aggregate were similar to that observed for nucleotides (Figure 2.4D). These results highlight the significance of glucose flux to galactose and through the hexosamine biosynthesis pathway (Figure 2.4D). Notably, the flux of glucose to glycans was unaffected by enzymatic digestion (Figure 2.4C) due to the rapid recovery of pool sizes after the initial 4 hours of growth (Figure S2.2B). This finding is perhaps not surprising due to long term selection experienced by hESCs in standard culture. On the other hand, these calculations demonstrate how high the flux to glycan moieties is in standard culture conditions. Although nucleotides are routinely considered a large biosynthetic pool, our measurements indicate that flux to glycans is approximately the same as

that of ribose, which is a component of RNA and various cofactors (e.g. ATP, NAD+) (Figure 2.4D).

Taking these results together, although abundance of glycan moieties is significantly altered after enzymatic digestion, the flux through these pathways is high enough to recover from these cleavage events. However, the contribution of glucose to fatty acids, proteinogenic amino acids, and nucleotides remains diminished, suggesting that such passaging methods impact metabolism for at least several hours after hESC subculture.

2.5 Discussion

We have demonstrated that the use of enzymatic reagents of hESCs has an immediate and significant impact on metabolic activity after passaging. Through the use of ^{13}C MFA we have demonstrated that glucose flux through glycolysis and the TCA cycle as well as lipid biosynthesis are decreased after splitting cells using enzyme-based passaging methods. Using a method that can rapidly probe the abundance and labeling of glycans in hydrolyzed biomass, we observed that enzymatic passaging significantly impacts the abundance of glycan moieties in hESCs.

2.5.1 Potential pitfalls in advanced hESC culture methods

For the past decade efforts in stem cell bioprocess engineering have focused on the development of well-defined but less laborious methods of cell expansion. While there is a clear need to streamline processes and assimilate current good manufacturing practices (cGMPs) [41], these advances come at the expense of compromising the stem cell niche. Widely used stem cells lines (H1, H9, etc.) were isolated in fully undefined conditions derived from mESC engineering from the early 1980s [1, 42, 43]. Here we demonstrate that the transition to more "modern" passaging methods has direct consequences on cell function and behavior.

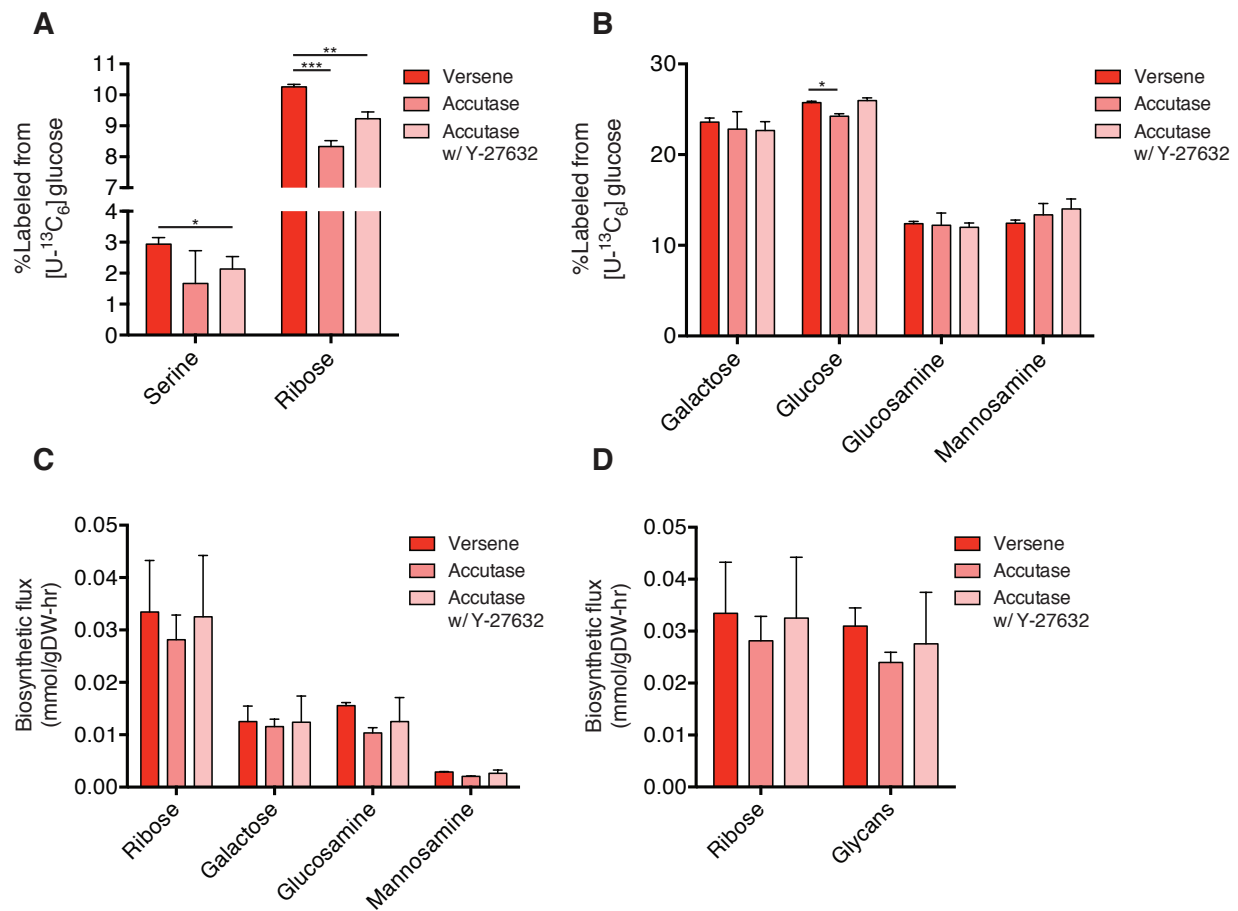


Figure 2.4: Biosynthetic fluxes to glycans and nucleotides are similar in cultured hESCs.

(A) Percentage of labeled serine and ribose in cells cultured for 4 hours after passaging in the presence of $[U-^{13}C_6]$ glucose (UGlc). (B) Percentage of labeled glycan moieties from biomass in cells treated as in (A). (C) Quantitation of biosynthetic flux to different metabolites calculated using MIDs and molar pool sizes. (D) Comparison of fluxes to ribose versus glycans demonstrates similar biosynthetic needs in hESCs. Error bars represent SD (A-D) for three replicates. *, P value between 0.01 and 0.05; **, P value between 0.001 and 0.01; ***, P value <0.001 by Student's two-tailed t test.

2.5.2 Potential selective pressure of enzymatic passaging through altered metabolism

Presumably, treatment with enzymatic reagents leads to proteolytic cleavage of various receptors and other proteoglycans at the cell surface. In turn, the decreased receptor abundance mitigates the responsiveness of cells to endogenous signaling factors and exogenous growth factors in hESC media. A wide range of cell surface proteins may drive this phenotype, including solute carriers, glucose transporters, and receptor tyrosine kinases. Indeed, the increased abundance of glucose within enzyme-passaged cells indicates that cells may even be compromised with respect to their ability to access glycogen pools. Energetic stress has previously been associated with cells cultured for 24 hours under non-adherent conditions (i.e., detachment from the matrix) [44, 45], but the immediate impacts on metabolism after dissociation were not previously appreciated. Although cells presumably recover rapidly to replenish glycan and biosynthetic intermediate pools, even a temporary selective pressure like that observed here will have lasting and significant effects on cell populations. Such effects may impact cells from the time of isolation (i.e., blastocyst or primary cell isolation) throughout passaging *in vitro*. Indeed, any functional application that makes use of hESCs or their derivatives requires that they accurately represent the metabolic activity of the somatic tissues that one attempts to model. For example, the metabolic behavior of hPSC-derived cardiomyocytes is known to significantly differ compared to adult heart cells with respect to their capacity for fatty acid oxidation [46, 47]. The extent of developmental maturation and selective pressures due to *in vitro* culture on such phenomena must both be considered.

2.5.3 Glycocalyx is a significant biomass pool in cultured hESCs

We also developed an analytical method for quantifying the overall abundance and isotopic labeling of glycan residues, proteinogenic amino acids, and ribose moieties from nucleotides and cofactors in cell cultures. This approach highlighted the profound impact of enzyme passaging

on carbohydrate and glycan abundances in cells. While this method contrasts traditional methods of enzyme-mediated digestion of glycans from their protein cores and direct analysis of their structures (i.e., glycomics), the rapid nature of our methods makes it attractive for studying general effects on hexosamine metabolism. Furthermore, analysis of glycan biomass affords reliable quantitation of overall synthesis rates compared to measurements of sugar nucleotides. The glycocalyx and glycosylation profile is particularly important for cell signaling and protein function [48, 49]. Recent studies also suggest that modulation of flux through the hexosamine biosynthesis pathway directly impacts the glycoprofile of cells [50]. Consistent with this concept, we demonstrate that glucose flux to glycans is similar to that observed for flux to ribose, which contributes to nucleotide synthesis and maintenance of cellular redox [51, 52]. As such, hexosamine biosynthesis is an underappreciated biomass sink in metabolic studies. Indeed, studies on the metabolism of cancer cells and stem cells commonly ignore the importance of glycan production while focusing primarily on the importance of nucleotide, lipid, and amino acid metabolism [53–57]. Far fewer studies address or attempt to quantify or modulate flux to glycans [17, 58].

2.5.4 Concluding thoughts

These results and other recent studies [6, 59] are beginning to illustrate how the *in vitro* culture environment influences hESC phenotype. Cells are routinely subjected to periods of starvation during incubation with passaging reagents as well as cleavage of their glycocalyx and cell surface proteins. As cultures age, changes to gene expression and epigenetic markers will be selected for to deal with these stresses. In this context, upregulation of flux through the hexosamine biosynthesis pathway is to be expected. Future engineering strategies must identify and address sources of cellular stresses at the genomic, transcriptional, signaling, and metabolic levels in order to mitigate the deleterious effects of *in vitro* culture in regenerative medicine applications.

2.6 Acknowledgements

This research was supported by the California Institute of Regenerative Medicine (RB5-07356), NIH grant (5 R01 CA188652-02), and a Searle Scholar Award to C.M.M. M.G.B. is supported by a NSF Graduate Research Fellowship (DGE-1144086).

Chapter 2, in full, is a reprint of the material as it appears in "Enzymatic passaging of human embryonic stem cells alters central carbon metabolism and glycan abundance," *Biotechnology Journal*, vol. 10, 2015. Mehmet G. Badur is the primary author of this publication. Hui Zhang is a co-author of this publication. Christian M. Metallo is the corresponding author of this publication.

2.7 References

1. Thomson, J. A., Itskovitz-Eldor, J., Shapiro, S. S., Waknitz, M. A., Swiergiel, J. J., Marshall, V. S. & Jones, J. M. Embryonic stem cell lines derived from human blastocysts. *Science* **282**, 1145–7 (1998).
2. Ludwig, T. E., Levenstein, M. E., Jones, J. M., Berggren, W. T., Mitchen, E. R., Frane, J. L., Crandall, L. J., Daigh, C. A., Conard, K. R., Piekarczyk, M. S., Llanas, R. A. & Thomson, J. A. Derivation of human embryonic stem cells in defined conditions. *Nat Biotechnol* **24**, 185–7 (2006).
3. Buzzard, J. J., Gough, N. M., Crook, J. M. & Colman, A. Karyotype of human ES cells during extended culture. *Nat Biotechnol* **22**, 381–2, author reply 382 (2004).
4. Draper, J. S., Smith, K., Gokhale, P., Moore, H. D., Maltby, E., Johnson, J., Meisner, L., Zwaka, T. P., Thomson, J. A. & Andrews, P. W. Recurrent gain of chromosomes 17q and 12 in cultured human embryonic stem cells. *Nat Biotechnol* **22**, 53–4 (2004).
5. Mitalipova, M. M., Rao, R. R., Hoyer, D. M., Johnson, J. A., Meisner, L. F., Jones, K. L., Dalton, S. & Stice, S. L. Preserving the genetic integrity of human embryonic stem cells. *Nat Biotechnol* **23**, 19–20 (2005).
6. Garitaonandia, I., Amir, H., Boscolo, F. S., Wambua, G. K., Schultheisz, H. L., Sabatini, K., Morey, R., Waltz, S., Wang, Y. C., Tran, H., Leonardo, T. R., Nazor, K., Slavin, I., Lynch, C., Li, Y., Coleman, R., Gallego Romero, I., Altun, G., Reynolds, D., Dalton, S., Parast, M., Loring, J. F. & Laurent, L. C. Increased risk of genetic and epigenetic instability

- in human embryonic stem cells associated with specific culture conditions. *PLoS One* **10**, e0118307 (2015).
7. Panopoulos, A. D., Yanes, O., Ruiz, S., Kida, Y. S., Diep, D., Tautenhahn, R., Herrerias, A., Batchelder, E. M., Plongthongkum, N., Lutz, M., Berggren, W. T., Zhang, K., Evans, R. M., Siuzdak, G. & Izpisua Belmonte, J. C. The metabolome of induced pluripotent stem cells reveals metabolic changes occurring in somatic cell reprogramming. *Cell Res* **22**, 168–77 (2012).
 8. Shyh-Chang, N., Daley, G. Q. & Cantley, L. C. Stem cell metabolism in tissue development and aging. *Development* **140**, 2535–47 (2013).
 9. Zhang, J., Khvorostov, I., Hong, J. S., Oktay, Y., Vergnes, L., Nuebel, E., Wahjudi, P. N., Setoguchi, K., Wang, G., Do, A., Jung, H. J., McCaffery, J. M., Kurland, I. J., Reue, K., Lee, W. N., Koehler, C. M. & Teitell, M. A. UCP2 regulates energy metabolism and differentiation potential of human pluripotent stem cells. *EMBO J* **30**, 4860–73 (2011).
 10. Folmes, C. D., Nelson, T. J., Martinez-Fernandez, A., Arrell, D. K., Lindor, J. Z., Dzeja, P. P., Ikeda, Y., Perez-Terzic, C. & Terzic, A. Somatic oxidative bioenergetics transitions into pluripotency-dependent glycolysis to facilitate nuclear reprogramming. *Cell Metab* **14**, 264–71 (2011).
 11. Zhang, J., Nuebel, E., Daley, G. Q., Koehler, C. M. & Teitell, M. A. Metabolic regulation in pluripotent stem cells during reprogramming and self-renewal. *Cell Stem Cell* **11**, 589–95 (2012).
 12. Reitsma, S., Slaaf, D. W., Vink, H., van Zandvoort, M. A. & oude Egbrink, M. G. The endothelial glycocalyx: composition, functions, and visualization. *Pflugers Arch* **454**, 345–59 (2007).
 13. Fang, M., Shen, Z., Huang, S., Zhao, L., Chen, S., Mak, T. W. & Wang, X. The ER UDPase ENTPD5 promotes protein N-glycosylation, the Warburg effect, and proliferation in the PTEN pathway. *Cell* **143**, 711–24 (2010).
 14. Lau, K. S., Partridge, E. A., Grigorian, A., Silvescu, C. I., Reinhold, V. N., Demetriou, M. & Dennis, J. W. Complex N-glycan number and degree of branching cooperate to regulate cell proliferation and differentiation. *Cell* **129**, 123–34 (2007).
 15. Lauzier, B., Vaillant, F., Merlen, C., Gelinias, R., Bouchard, B., Rivard, M. E., Labarthe, F., Dolinsky, V. W., Dyck, J. R., Allen, B. G., Chatham, J. C. & Des Rosiers, C. Metabolic effects of glutamine on the heart: anaplerosis versus the hexosamine biosynthetic pathway. *J Mol Cell Cardiol* **55**, 92–100 (2013).

16. Metallo, C. M. & Vander Heiden, M. G. Metabolism strikes back: metabolic flux regulates cell signaling. *Genes Dev* **24**, 2717–22 (2010).
17. Wellen, K. E., Lu, C., Mancuso, A., Lemons, J. M., Ryczko, M., Dennis, J. W., Rabinowitz, J. D., Collier, H. A. & Thompson, C. B. The hexosamine biosynthetic pathway couples growth factor-induced glutamine uptake to glucose metabolism. *Genes Dev* **24**, 2784–99 (2010).
18. Grassian, A. R., Parker, S. J., Davidson, S. M., Divakaruni, A. S., Green, C. R., Zhang, X., Slocum, K. L., Pu, M., Lin, F., Vickers, C., Joud-Caldwell, C., Chung, F., Yin, H., Handly, E. D., Straub, C., Growney, J. D., Vander Heiden, M. G., Murphy, A. N., Pagliarini, R. & Metallo, C. M. IDH1 mutations alter citric acid cycle metabolism and increase dependence on oxidative mitochondrial metabolism. *Cancer Res* **74**, 3317–31 (2014).
19. Young, J. D. INCA: a computational platform for isotopically non-stationary metabolic flux analysis. *Bioinformatics* **30**, 1333–5 (2014).
20. Sheikh, K., Forster, J. & Nielsen, L. K. Modeling hybridoma cell metabolism using a generic genome-scale metabolic model of *Mus musculus*. *Biotechnology Progress* **21**, 112–121 (2005).
21. Wegner, A., Weindl, D., Jager, C., Sapcariu, S. C., Dong, X., Stephanopoulos, G. & Hiller, K. Fragment formula calculator (FFC): determination of chemical formulas for fragment ions in mass spectrometric data. *Anal Chem* **86**, 2221–8 (2014).
22. Antoniewicz, M. R., Kelleher, J. K. & Stephanopoulos, G. Determination of confidence intervals of metabolic fluxes estimated from stable isotope measurements. *Metab Eng* **8**, 324–37 (2006).
23. Watanabe, K., Ueno, M., Kamiya, D., Nishiyama, A., Matsumura, M., Wataya, T., Takahashi, J. B., Nishikawa, S., Nishikawa, S., Muguruma, K. & Sasai, Y. A ROCK inhibitor permits survival of dissociated human embryonic stem cells. *Nat Biotechnol* **25**, 681–6 (2007).
24. Kharroubi, A. T., Masterson, T. M., Aldaghlis, T. A., Kennedy, K. A. & Kelleher, J. K. Isotopomer spectral analysis of triglyceride fatty acid synthesis in 3T3-L1 cells. *Am J Physiol* **263**, E667–75 (1992).
25. Metallo, C. M. & Vander Heiden, M. G. Understanding metabolic regulation and its influence on cell physiology. *Mol Cell* **49**, 388–98 (2013).
26. Vacanti, N. M. & Metallo, C. M. Exploring metabolic pathways that contribute to the stem cell phenotype. *Biochim Biophys Acta* **1830**, 2361–9 (2013).

27. Xu, X., Duan, S., Yi, F., Ocampo, A., Liu, G. H. & Izpisua Belmonte, J. C. Mitochondrial regulation in pluripotent stem cells. *Cell Metab* **18**, 325–32 (2013).
28. Folmes, C. D., Dzeja, P. P., Nelson, T. J. & Terzic, A. Metabolic plasticity in stem cell homeostasis and differentiation. *Cell Stem Cell* **11**, 596–606 (2012).
29. Wang, Y. C., Lin, V., Loring, J. F. & Peterson, S. E. The 'sweet' spot of cellular pluripotency: protein glycosylation in human pluripotent stem cells and its applications in regenerative medicine. *Expert Opin Biol Ther*, 1–9 (2015).
30. Wang, Y. C., Peterson, S. E. & Loring, J. F. Protein post-translational modifications and regulation of pluripotency in human stem cells. *Cell Res* **24**, 143–60 (2014).
31. Dennis, J. W., Nabi, I. R. & Demetriou, M. Metabolism, cell surface organization, and disease. *Cell* **139**, 1229–41 (2009).
32. Moremen, K. W., Tiemeyer, M. & Nairn, A. V. Vertebrate protein glycosylation: diversity, synthesis and function. *Nat Rev Mol Cell Biol* **13**, 448–62 (2012).
33. Long, C. P. & Antoniewicz, M. R. Quantifying Biomass Composition by Gas Chromatography/Mass Spectrometry. *Analytical Chemistry* **86**, 9423–9427 (2014).
34. Hofmann, U., Maier, K., Nicbel, A., Vacun, G., Reuss, M. & Mauch, K. Identification of metabolic fluxes in hepatic cells from transient C-13-labeling experiments: Part I. Experimental observations. *Biotechnology and Bioengineering* **100**, 344–354 (2008).
35. Munger, J., Bennett, B. D., Parikh, A., Feng, X. J., McArdle, J., Rabitz, H. A., Shenk, T. & Rabinowitz, J. D. Systems-level metabolic flux profiling identifies fatty acid synthesis as a target for antiviral therapy. *Nature Biotechnology* **26**, 1179–1186 (2008).
36. Murphy, T. A., Dang, C. V. & Young, J. D. Isotopically nonstationary ¹³C flux analysis of Myc-induced metabolic reprogramming in B-cells. *Metab Eng* **15**, 206–17 (2013).
37. Fountoulakis, M. & Lahm, H. W. Hydrolysis and amino acid composition of proteins. *J Chromatogr A* **826**, 109–34 (1998).
38. Jang-Lee, J., North, S. J., Sutton-Smith, M., Goldberg, D., Panico, M., Morris, H., Haslam, S. & Dell, A. Glycomic profiling of cells and tissues by mass spectrometry: fingerprinting and sequencing methodologies. *Methods Enzymol* **415**, 59–86 (2006).
39. Miranda-Santos, I., Gramacho, S., Pineiro, M., Martinez-Gomez, K., Fritz, M., Hollemeyer, K., Salvador, A. & Heinzle, E. Mass isotopomer analysis of nucleosides isolated from RNA and DNA using GC/MS. *Anal Chem* **87**, 617–23 (2015).

40. Tomiya, N., Narang, S., Lee, Y. C. & Betenbaugh, M. J. Comparing N-glycan processing in mammalian cell lines to native and engineered lepidopteran insect cell lines. *Glycoconjugate Journal* **21**, 343–360 (2004).
41. Unger, C., Skottman, H., Blomberg, P., Dilber, M. S. & Hovatta, O. Good manufacturing practice and clinical-grade human embryonic stem cell lines. *Hum Mol Genet* **17**, R48–53 (2008).
42. Evans, M. J. & Kaufman, M. H. Establishment in culture of pluripotential cells from mouse embryos. *Nature* **292**, 154–6 (1981).
43. Martin, G. R. Isolation of a pluripotent cell line from early mouse embryos cultured in medium conditioned by teratocarcinoma stem cells. *Proc Natl Acad Sci U S A* **78**, 7634–8 (1981).
44. Grassian, A. R., Metallo, C. M., Coloff, J. L., Stephanopoulos, G. & Brugge, J. S. Erk regulation of pyruvate dehydrogenase flux through PDK4 modulates cell proliferation. *Genes Dev* **25**, 1716–33 (2011).
45. Schafer, Z. T., Grassian, A. R., Song, L., Jiang, Z., Gerhart-Hines, Z., Irie, H. Y., Gao, S., Puigserver, P. & Brugge, J. S. Antioxidant and oncogene rescue of metabolic defects caused by loss of matrix attachment. *Nature* **461**, 109–13 (2009).
46. Kim, C., Wong, J., Wen, J., Wang, S., Wang, C., Spiering, S., Kan, N. G., Forcales, S., Puri, P. L., Leone, T. C., Marine, J. E., Calkins, H., Kelly, D. P., Judge, D. P. & Chen, H. S. Studying arrhythmogenic right ventricular dysplasia with patient-specific iPSCs. *Nature* **494**, 105–10 (2013).
47. Lopaschuk, G. D. & Jaswal, J. S. Energy metabolic phenotype of the cardiomyocyte during development, differentiation, and postnatal maturation. *J Cardiovasc Pharmacol* **56**, 130–40 (2010).
48. Hoosdally, S. J., Andress, E. J., Wooding, C., Martin, C. A. & Linton, K. J. The Human Scavenger Receptor CD36: glycosylation status and its role in trafficking and function. *J Biol Chem* **284**, 16277–88 (2009).
49. Schmid-Schonbein, G. W. An emerging role of degrading proteinases in hypertension and the metabolic syndrome: autodigestion and receptor cleavage. *Curr Hypertens Rep* **14**, 88–96 (2012).
50. Almaraz, R. T., Aich, U., Khanna, H. S., Tan, E., Bhattacharya, R., Shah, S. & Yarema, K. J. Metabolic oligosaccharide engineering with N-Acyl functionalized ManNAc analogs: cytotoxicity, metabolic flux, and glycan-display considerations. *Biotechnol Bioeng* **109**, 992–1006 (2012).

51. Fan, J., Ye, J., Kamphorst, J. J., Shlomi, T., Thompson, C. B. & Rabinowitz, J. D. Quantitative flux analysis reveals folate-dependent NADPH production. *Nature* **510**, 298–302 (2014).
52. Lewis, C. A., Parker, S. J., Fiske, B. P., McCloskey, D., Gui, D. Y., Green, C. R., Vokes, N. I., Feist, A. M., Vander Heiden, M. G. & Metallo, C. M. Tracing compartmentalized NADPH metabolism in the cytosol and mitochondria of mammalian cells. *Mol Cell* **55**, 253–63 (2014).
53. Benjamin, D. I., Li, D. S., Lowe, W., Heuer, T., Kemble, G. & Nomura, D. K. Diacylglycerol Metabolism and Signaling Is a Driving Force Underlying FASN Inhibitor Sensitivity in Cancer Cells. *ACS Chem Biol* (2015).
54. Jain, M., Nilsson, R., Sharma, S., Madhusudhan, N., Kitami, T., Souza, A. L., Kafri, R., Kirschner, M. W., Clish, C. B. & Mootha, V. K. Metabolite profiling identifies a key role for glycine in rapid cancer cell proliferation. *Science* **336**, 1040–4 (2012).
55. Metallo, C. M., Gameiro, P. A., Bell, E. L., Mattaini, K. R., Yang, J., Hiller, K., Jewell, C. M., Johnson, Z. R., Irvine, D. J., Guarente, L., Kelleher, J. K., Vander Heiden, M. G., Iliopoulos, O. & Stephanopoulos, G. Reductive glutamine metabolism by IDH1 mediates lipogenesis under hypoxia. *Nature* **481**, 380–4 (2012).
56. Moussaieff, A., Rouleau, M., Kitsberg, D., Cohen, M., Levy, G., Barasch, D., Nemirovski, A., Shen-Orr, S., Laevsky, I., Amit, M., Bomze, D., Elena-Herrmann, B., Scherf, T., Nissim-Rafinia, M., Kempa, S., Itskovitz-Eldor, J., Meshorer, E., Aberdam, D. & Nahmias, Y. Glycolysis-mediated changes in acetyl-CoA and histone acetylation control the early differentiation of embryonic stem cells. *Cell Metab* **21**, 392–402 (2015).
57. Shiraki, N., Shiraki, Y., Tsuyama, T., Obata, F., Miura, M., Nagae, G., Aburatani, H., Kume, K., Endo, F. & Kume, S. Methionine metabolism regulates maintenance and differentiation of human pluripotent stem cells. *Cell Metab* **19**, 780–94 (2014).
58. Almaraz, R. T., Tian, Y., Bhattarcharya, R., Tan, E., Chen, S. H., Dallas, M. R., Chen, L., Zhang, Z., Zhang, H., Konstantopoulos, K. & Yarema, K. J. Metabolic flux increases glycoprotein sialylation: implications for cell adhesion and cancer metastasis. *Mol Cell Proteomics* **11**, M112 017558 (2012).
59. Laurent, L. C., Ulitsky, I., Slavin, I., Tran, H., Schork, A., Morey, R., Lynch, C., Harness, J. V., Lee, S., Barrero, M. J., Ku, S., Martynova, M., Semechkin, R., Galat, V., Gottesfeld, J., Izpisua Belmonte, J. C., Murry, C., Keirstead, H. S., Park, H. S., Schmidt, U., Laslett, A. L., Muller, F. J., Nievergelt, C. M., Shamir, R. & Loring, J. F. Dynamic changes in the copy number of pluripotency and cell proliferation genes in human ESCs and iPSCs during reprogramming and time in culture. *Cell Stem Cell* **8**, 106–18 (2011).

Chapter 3

Distinct metabolic states can support self-renewal and lipogenesis in human pluripotent stem cells under different culture conditions

3.1 Abstract

Recent studies have suggested that human pluripotent stem cells (hPSCs) depend primarily on glycolysis and only increase oxidative metabolism during differentiation. Here we demonstrate that both glycolytic and oxidative metabolism can support hPSC growth, and the metabolic phenotype of hPSCs is largely driven by nutrient availability. We comprehensively characterized hPSC metabolism using $^{13}\text{C}/^2\text{H}$ stable isotope tracing and flux analysis to define the metabolic pathways supporting hPSC bioenergetics and biosynthesis. Whereas glycolytic flux consistently supported hPSC growth, chemically-defined media strongly influenced that state of mitochondrial respiration and fatty acid metabolism. Lipid deficiency dramatically reprogramed pathways

associated with fatty acid biosynthesis and NADPH regeneration, altering the mitochondrial function of cells and driving flux through the oxidative pentose phosphate pathway. Lipid supplementation mitigates this metabolic reprogramming and increases oxidative metabolism. These results demonstrate that self-renewing hPSCs can present distinct metabolic states and highlight the importance of medium nutrients on mitochondrial function and development.

3.2 Introduction

Given their virtually unlimited expansion potential and differentiation capacity, human pluripotent stem cells (hPSCs) offer unique opportunities in the study of human development, biochemical screening in specific lineages, and regenerative medicine. Successful establishment of culture conditions able to maintain human embryonic stem cells (hESCs) and induced pluripotent stem cells (iPSCs) in the undifferentiated state represented critical steps in advancing these technologies to practice [1, 2]. However, the large quantity of cells needed for screening and tissue engineering applications poses a challenge that must still be addressed [3]. Initial protocols for hPSC self-renewal mimicked the *in vivo* microenvironment by using feeder cell co-culture or medium conditioned by feeder cells to support hPSC expansion [3, 4]. However, current good manufacturing practices (cGMP) and FDA guidelines that encourage the use of xenobiotic-free systems in clinical applications of hPSCs have driven efforts to develop chemically defined and/or xenobiotic-free media and substrates for hPSC maintenance [5–7]. In recent years such chemically defined formulations have supplanted undefined conditions as the gold standard for expansion of hPSCs [8, 9]. However, the metrics for evaluation of such media have often been limited to proliferation, pluripotency, and gene expression analyses, an established challenge which must still be overcome [10]. Indeed, recent studies now suggest that culture and/or passaging conditions can influence the genetic stability, metabolism, and differentiation potential of hPSCs [11–13]. The specific metabolic features of hPSCs adapted to chemically defined media must be

elucidated in greater detail to develop improved hPSC models and related biomedical products.

Several recent studies have identified critical metabolic pathways necessary for cellular reprogramming and/or maintaining pluripotency, evoking a broader interest in applying hPSCs to study nutrition, development, and metabolic disease [14]. Glycolytic flux is commonly high in hPSC cultures, and inhibition of glucose metabolism potentially limits reprogramming efficiency [15–17]. Metabolites that serve as substrates for epigenetic markers such as acetylation and methylation have also emerged as critical regulators of pluripotency [18–21]. Broader characterization of the hPSC metabolome has also identified key differences in mitochondrial function and lipid metabolism between hPSCs, mESCs, and their derivatives [16, 22]. In addition, compounds that promote mitochondrial metabolism can negatively influence cellular reprogramming [15–17], leading to the generalized concept that oxidative mitochondrial metabolism is "antagonistic" to the pluripotent state [23]. However, some evidence suggests that mitochondria are active in hESCs [24]. Similar to recent developments in tumor biology [25], critical roles for mitochondria in hPSC growth are likely to emerge.

Here we have conducted a comprehensive analysis of metabolic fluxes in hPSCs. Using an array of ^{13}C and ^2H tracers we have investigated the metabolic pathways that support hPSC biosynthesis and growth. Surprisingly, we have observed that distinct metabolic states marked by high mitochondrial flux and governed by nutrient availability can maintain hESC self-renewal, challenging the notion that mitochondrial function is dispensable for stem cell function. Chemically defined medium drives hPSCs to regulate mitochondrial pathways to support lipid biosynthesis at the expense of oxidative metabolism. Media containing lipid supplements maintain pluripotency while augmenting respiration and mitochondrial metabolism. Taken together, these results demonstrate that nutrient availability and the microenvironment (in particular, medium choice) profoundly impacts hPSC metabolism.

3.3 Materials and Methods

3.3.1 Human pluripotent stem cell culture

Human embryonic stem cell lines, HUES9 and WA09 (H9), and human induced pluripotent stem cell line, iPS(IMR90)-c4, were maintained on plates coated with Matrigel (Corning Life Sciences) at $8.8 \mu\text{g}/\text{cm}^2$ and adapted to murine embryonic fibroblast-conditioned medium (MEF-CM), Essential 8 medium (Life Technologies), and mTeSR1 medium (Stem Cell Technologies) for at least three passages before experiments. All hPSCs were passaged every 5 days by exposure to Accutase (Innovative Cell Technology) for 5 to 10 min at 37°C . For metabolic flux experiments, 1X MEM non-essential amino acid solution was added into E8 media to control for amino acid levels. Tracer MEF-CM consisted of low glucose or glutamine free MEF-CM supplemented with either [^{13}C]glucose or [^{13}C]glutamine tracers, respectively. Tracer chemically defined media consisted of glucose or glutamine-free E8 medium supplemented with [^{13}C]glutamine, [^{13}C]glucose or [^2H]glucose, or E8 medium supplemented with [^{13}C]palmitate. All tracers were purchased from Cambridge Isotopes. Additional details described in Supplemental Procedure.

3.3.2 Immunocytochemistry

HESCs were harvested and resuspended in 1% (v/v) paraformaldehyde and then fixed in 90% cold methanol. Cell pellets were incubated with a 1:100 dilution of human OCT-3/4 primary mouse antibody (Santa Cruz; C-10) and a 1:1000 dilution of the secondary antibody conjugated with Alexa Fluor 488 (Molecular Probes). The OCT4+ cells were detected by BD flow cytometry and results were analyzed by FlowJo. For microscopy image, the adherent cells were fixed in 4% (v/v) paraformaldehyde. Cells were incubated with the 1:100 dilution of human OCT-3/4 primary mouse antibody and the 1:1000 dilution of the secondary antibody conjugated with Alexa Fluor 488. Cells were subsequently washed and incubated with Hoechst 33342 nucleus staining solution.

3.3.3 Metabolite extraction and derivatization

Polar metabolites and fatty acids were extracted using methanol/water/chloroform. Briefly, spent media was removed, and cells were rinsed with 0.9% (w/v) saline and 250 μL of -80°C methanol was added to quench metabolism. 100 μL of ice-cold water containing 1 μg norvaline internal standard was added to each well. Both solution and cells were collected via scraping. Cell lysates were transferred to fresh sample tubes and 250 μL of -20°C chloroform containing 1 μg heptadecanoate (internal standard for fatty acids) and 1 μg coprostan-3-ol (internal standard for cholesterol) was added. After vortexing and centrifugation, the top aqueous layer (polar metabolites) and bottom organic layer (lipids) were collected and dried under airflow. All reagents were purchased from Sigma-Aldrich.

Derivatization of polar metabolites was performed using the Gerstel MultiPurpose Sampler (MPS 2XL). Dried polar metabolites were dissolved in 20 μL of 2% (w/v) methoxyamine hydrochloride (MP Biomedicals) in pyridine and held at 37°C for 60 minutes. Subsequent conversion to their tert-butyldimethylsilyl (tBDMS) derivatives was accomplished by adding 30 μL N-methyl-N-(tert-butyldimethylsilyl) trifluoroacetamide + 1% tert-butyldimethylchlorosilane (Regis Technologies) and incubating at 37°C for 30 minutes. Fatty acid methyl esters (FAMES) were generated by dissolving dried fatty acids in 0.5 mL 2% (v/v) methanolic sulfuric acid (Sigma-Aldrich) and incubating at 50°C for 2 hours. FAMES were subsequently extracted in 1 mL hexane with 0.1 mL saturated sodium chloride. FAME samples subsequently were aliquoted to two tubes for direct analysis or cholesterol derivatization. One dried FAME extract was converted to cholesterol trimethylsilyl (TMS) derivatives by adding 30 μL N-Methyl-N-(trimethylsilyl) trifluoroacetamide (Regis Technologies) and incubating at 37°C for 30 minutes.

3.3.4 Gas chromatography/mass spectrometry analysis

Gas chromatography/mass spectrometry (GC/MS) analysis was performed using an Agilent 7890A with a 30 m DB-35MS capillary column (Agilent Technologies) connected to an Agilent 5975C MS. GC/MS was operated under electron impact (EI) ionization at 70 eV. In splitless mode, 1 μ L sample was injected at 270°C, using helium as the carrier gas at a flow rate of 1 mL/min. For analysis of organic and amino acid derivatives, the GC oven temperature was held at 100°C for 2 minutes, increased to 255°C at 3.5°C/min, then ramped to 320°C at 15°C/min for a total run time of approximately 50 minutes. For measurement of FAMES, the GC oven temperature was held at 100°C for 3 minutes, then to 205°C at 25°C/min, further increased to 230°C at 5°C/min and ramped up to 300°C at 25°C/min for a total run time of approximately 15 minutes. For measurement of cholesterol, the GC oven temperature was held at 150°C for 1 minute, then to 260°C at 20°C/min, then held for 3 minutes, and further increased to 280°C at 10°C/min and held for 15 minutes, finally ramped up to 325°C for a total run time of approximately 30 minutes. The MS source and quadrupole were held at 230°C and 150°C, respectively, and the detector was operated in scanning mode, recording ion abundance in the range of 100-650 m/z.

3.3.5 Metabolite quantification and isotopomer spectral analysis

For quantification of metabolites and mass isotopomer distributions, selected ion fragments were integrated and corrected for natural isotope abundance using an in-house, MATLAB-based algorithm and metabolite fragments listed in Supplemental Table. Total abundances were normalized by counts of internal standard control. Isotopomer spectral analysis (ISA) for quantitation of [1,2-¹³C]glucose and [U-¹³C₆]glucose contribution to lipogenic AcCoA and [3-²H]glucose contribution to lipogenic NADPH were calculated as previously described [26, 27]. Specifically, the relative enrichment of the lipogenic AcCoA and NADPH pools from a given

tracer and the percentage of newly synthesized fatty acids were estimated from a best-fit model using the INCA MFA software package [28]. The 95% confidence intervals for both parameters were determined by evaluating the sensitivity of the sum of squared residuals between measured and simulated palmitate mass isotopomer distributions to small flux variations [29].

3.3.6 Mole percent enrichment measurement

Mole percent enrichment (MPE) of isotopes was calculated as the percent of all atoms within the metabolite pool that are labeled:

$$\frac{\sum_{i=1}^n M_i \cdot i}{n}$$

where n is the number of carbon atoms in the metabolite and M_i is the relative abundance of the i^{th} mass isotopomer.

3.3.7 Extracellular flux and oxidative pentose phosphate pathway flux measurements

Per protein extracellular fluxes, including glucose/glutamine uptake and lactate/glutamate secretion, were calculated by subtracting final spent medium from initial medium substrate concentrations measured using a Young Springs Instrument 2950 and normalized by the integral dry weights of hPSCs over 24 hours [26]. Quantification of oxidative pentose phosphate pathway (PPP) flux was determined by extracellular glucose uptake flux times the ratio of $\frac{M+1}{(M+1)+(M+2)}$ pyruvate or lactate derived from [1,2- ^{13}C]glucose.

3.3.8 Cell dry weight measurements

HPSCs were harvested and counted at 90% confluence. Cell pellets were dried by ambient air at 50°C for three days. Total weights of cell pellets were then measured and weight per million cells was calculated.

3.3.9 ATP-linked oxygen consumption rate measurements

Respiration was measured in viable hPSCs using a Seahorse XF96 Analyzer. HPSCs were assayed in fresh culture media. ATP-linked oxygen consumption rate (OCR) was calculated as the oxygen consumption rate sensitive to 2 mg/mL oligomycin in each culture condition and normalized by cell abundance. Each culture condition sample had at least four biological replicates analyzed. Cell abundance was indicated by the total fluorescence after stained with Hoechst 33342 [30].

3.3.10 Gene expression analysis

Total mRNA was isolated from 75% confluent hPSCs using RNA isolation kit (RNeasy Mini Kit; Qiagen). Isolated RNA was reverse transcribed using cDNA synthesis kit (iScript Reverse Transcription Supermix; Bio-Rad). Real-time PCR (RT-PCR) was performed using SYBR green reagent (iTaQ Universal SYBR Green Supermix; Bio-Rad). Relative expression was determined using Livak ($\Delta\Delta CT$) method with *GAPDH* as housekeeping gene. Primers used were taken from Primerbank [31] and tabulated in Supplemental Table. All commercial kits were used per the manufacturer's protocol.

3.3.11 Statistical analyses

All results shown as averages of triplicates (at least) presented as mean \pm SEM. P values were calculated using a Student's two-tailed t test; *, P value between 0.01 and 0.05; **, P

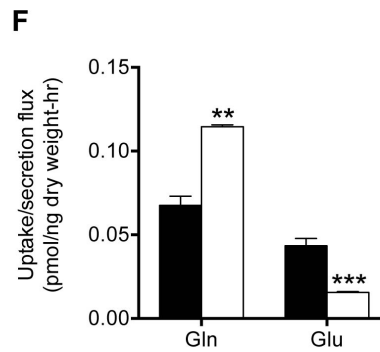
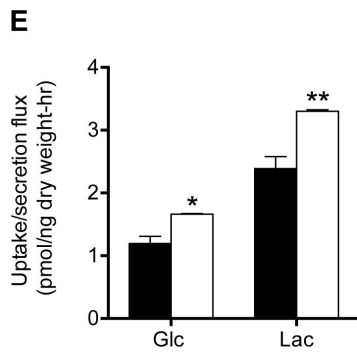
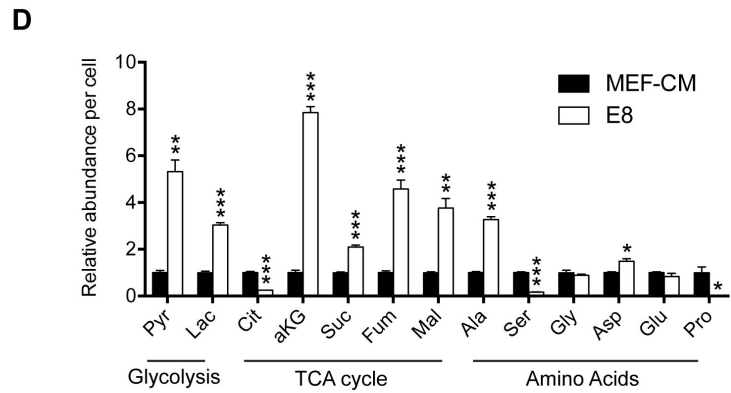
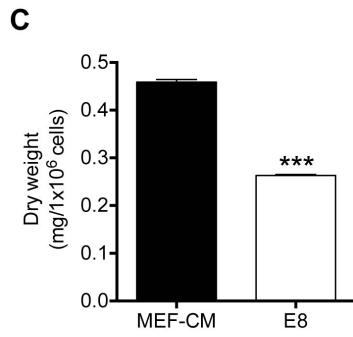
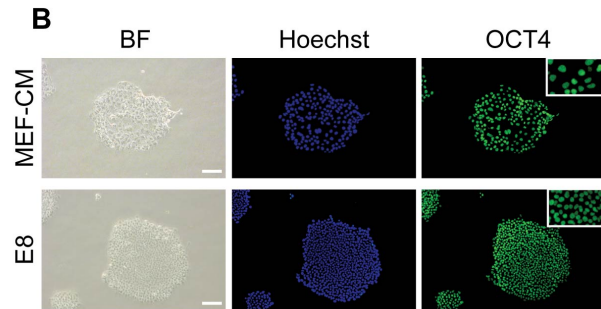
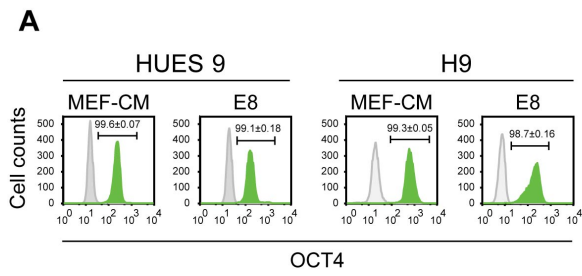
value between 0.001 and 0.01; ***, P value <0.001. All errors associated with ISA were 95% confidence intervals determined via confidence interval analysis.

3.4 Results

3.4.1 Medium choice influences hESC metabolic states

To define the critical metabolic features of self-renewing hPSC we quantified intracellular metabolite abundances, nutrient uptake, and byproduct secretion in undifferentiated HUES 9 and H9 cells. As researchers employ a variety of validated media formulations to maintain hPSCs [1, 9], we compared the metabolic state of hESCs in murine embryonic fibroblast conditioned medium (MEF-CM) or more chemically defined, commercially available media such as Essential 8 (E8). We employed this strategy to deconvolute media-specific metabolic pathway functions from cellular pluripotency. HESCs were maintained in each media formulation for at least three passages. Consistent with previous observations establishing during the establishment of these media [1, 9], hESCs in all conditions exhibited robust expression of Oct4 (Figure 3.1A-B). Notably, we observed a more compact, flattened colony morphology of hESCs cultured in chemically defined media and a larger non-nuclear area of hESCs cultured in MEF-CM, suggesting a difference in the quantity of cytosolic biomass between both pluripotent cells (Figure 3.1B). We also noted striking differences in the dry cell weight of hESCs adapted to chemically defined media, which was nearly 50% lower than that observed in MEF-CM cells (Figure 3.1C and S3.2A).

Figure 3.1: Distinct metabolic states exist in hESCs adapted to MEF-CM versus chemically defined media. HUES 9 and H9 hESCs were cultured in either MEF-CM or chemically defined media for at least three passages. (A) Percentage of OCT4+ hESCs. OCT4 in green, IgG control in gray. (B) Representative HUES 9 hESC colonies. Scale bar represents 100 μm . Inset shows increased distance between nuclei in MEF-CM cells. (C) Dry cell weight per million HUES 9 hESCs. (D) Relative intracellular metabolite abundance of HUES 9 hESCs normalized by cell number and MEF-CM sample. Metabolite abbreviations described in Supplemental Text. (E) Glucose uptake and lactate secretion fluxes of HUES 9 hESC. (F) Glutamine uptake and glutamate secretion fluxes of HUES 9 hESCs. (A, C-F) All results shown as mean \pm SEM. (C-F) P values were calculated using a Student's two-tailed t test relative to MEF-CM condition; *, P value between 0.01 and 0.05; **, P value between 0.001 and 0.01; ***, P value <0.001 .



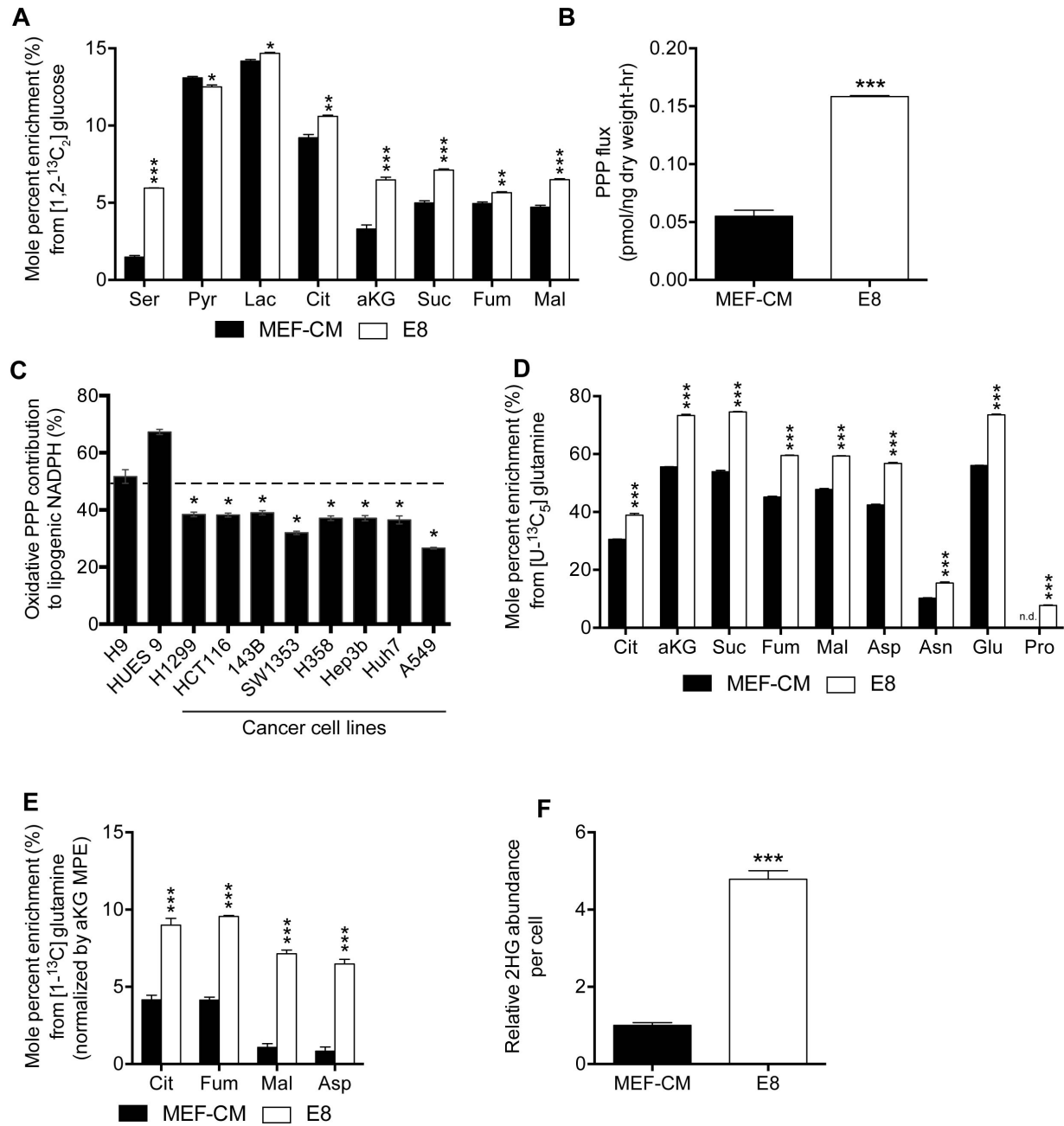
To gain more insights into pathway-specific differences across these conditions we next quantified the abundance of intracellular organic and amino acids in each hESC population. In chemically defined media we observed consistent increases in the per cell abundance of pyruvate, lactate, and most tricarboxylic acid (TCA) intermediates (Figure 3.1D and S3.2B), despite the smaller cell size (Figure 3.1C and S3.2A). A major exception to these trends was citrate, which was present at significantly lower levels in E8 media. Consistent with these differences, glycolytic flux in E8 was significantly higher on a per protein basis (Figure 3.1E). Additionally, glutamine consumption was markedly elevated in chemically defined media, and net glutamine anaplerosis (i.e., glutamine uptake minus glutamate secretion or entry of glutamine carbon into the TCA cycle) was increased 4 fold (Figure 3.1F). These results suggest that different hPSC media drive metabolic reprogramming of hESCs independent of pluripotency.

3.4.2 Media-dependent reprogramming of amino acid and NADPH metabolism

The inherent redundancy of metabolic networks allows for multiple pathways and substrates to support cellular bioenergetics and biosynthesis. Indeed, the differences observed in the above metabolic characterizations suggests that intermediary metabolic fluxes are altered in hESCs cultured in MEF-CM versus chemically defined media. To investigate these changes in greater detail we cultured HUES 9 and H9 cells in the presence of [^{13}C]glucose, [^2H]glucose, or [^{13}C]glutamine tracers and quantified isotopic labeling to probe central carbon metabolism (see Figure S4.1 for atom transition maps). With the exception of serine, the contribution of glucose carbon to glycolytic and TCA intermediates was not dramatically impacted by media choice (Figure 3.2A and S3.3). On the other hand, flux of glucose through the oxidative pentose phosphate pathway (PPP) was increased 3-fold in E8 media as compared to MEF-CM (Figure 3.2B). To better quantify how oxidative PPP flux contributes to NADPH regeneration we quantified label transfer from [$3\text{-}^2\text{H}$]glucose to palmitate and performed isotopomer spectral analysis

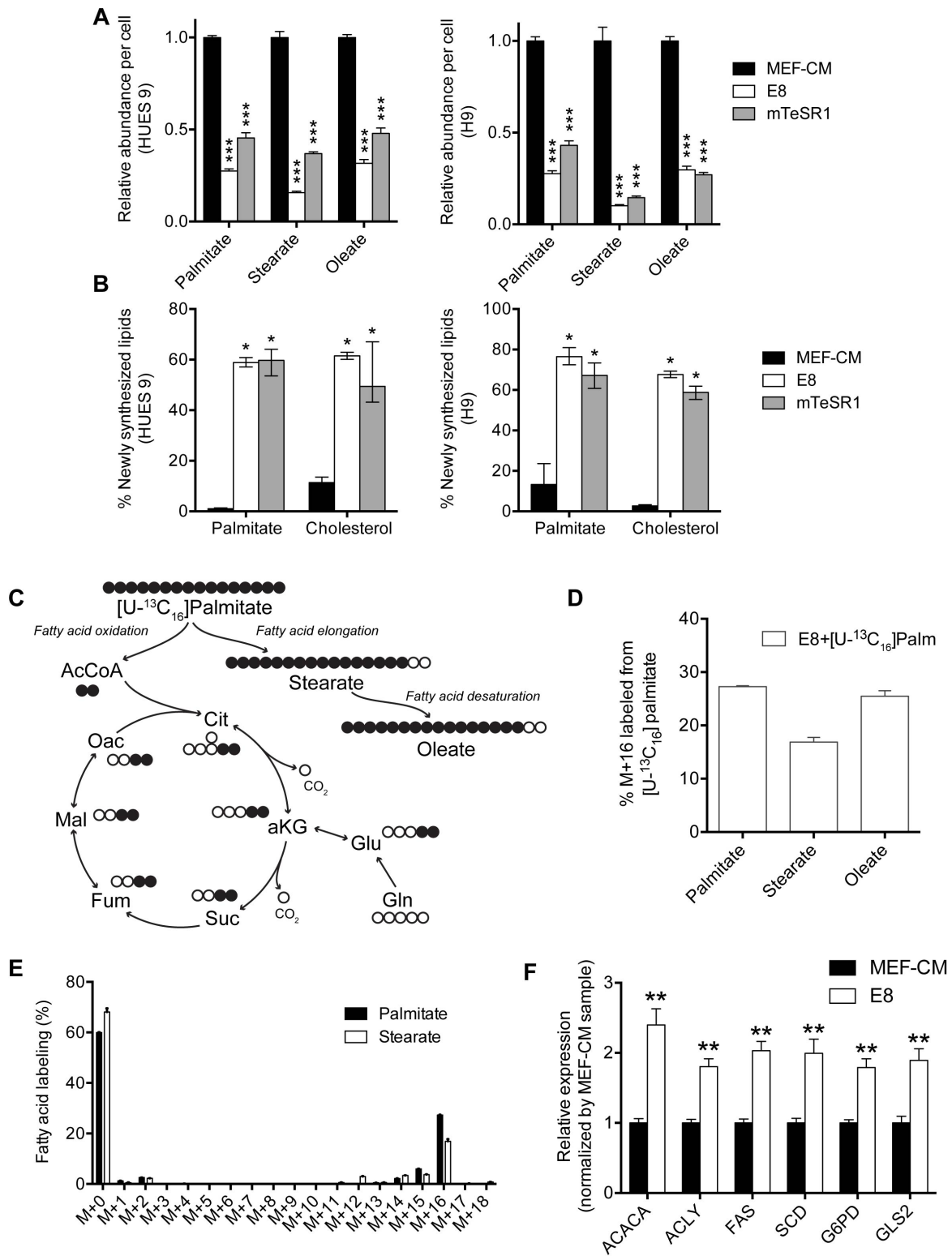
(ISA) [27]. In E8 medium the oxidative PPP accounted for $52\pm 2\%$ and $67\pm 1\%$ of cytosolic NADPH pool H9 and HUES 9 hESCs, respectively (Figure 3.2C). As the oxidative PPP is often upregulated in highly proliferative cells, such as tumors, to support nucleotide and fatty acid synthesis [32], we also performed the same tests in multiple established stable cancer cell lines. We found the contribution of PPP flux to NADPH production to be significantly higher in hPSCs than that observed in all cancer cell lines tested (Figure 3.2C, Supplemental Procedure), even when growing cancer cells in E8 media rather than DMEM + FBS (Figure S3.2C).

Figure 3.2: Media choice influences glucose, glutamine, and NADPH metabolism. (A) Mole percent enrichment (MPE) from [1,2-¹³C]glucose in HUES 9 hESCs throughout intermediary metabolism. (B) Absolute flux through the oxidative PPP in HUES 9 hESCs. (C) Contribution of oxidative PPP to lipogenic NADPH as determined by ISA in hESCs and cancer cells. (D) MPE from [U-¹³C₅]glutamine in HUES 9 hESCs throughout intermediary metabolism. (E) MPE of TCA intermediates from [1-¹³C]glutamine (normalized by MPE of αKG) in HUES 9 hESCs. (F) Relative abundance of 2HG in HUES 9 hESCs normalized by cell number and MEF-CM sample. (A-B, D-F) All results shown as mean ± SEM. P values were calculated using a Student's two-tailed t test relative to MEF-CM condition; *, P value between 0.01 and 0.05; **, P value between 0.001 and 0.01; ***, P value <0.001. (C) Results shown as mean and 95% CI. *, Significance indicated by non-overlapping 95% confidence intervals.



Glutamine is another important substrate that fuels mitochondrial metabolism in proliferating cells [33, 34]. When culturing HUES 9 or H9 hESCs in the presence of [U-¹³C₅]glutamine we observed significant changes in the overall contribution and labeling patterns of various TCA intermediates and amino acids in MEF-CM versus E8 media (Figure 3.2D, S3.2D, and S3.4). These data indicated that glutaminolysis was highly active in hESCs cultured on all media to support TCA cycle anaplerosis but significantly higher in defined media (Figure 3.2D, S3.2D, and S3.4). Notably, cells became cytostatic upon glutamine withdrawal (data not shown), in contrast to murine ESCs which can proliferate in the absence of available glutamine [35]. Increased M+3 labeling of citrate, malate, fumarate, and aspartate suggested that reductive carboxylation and ATP-citrate lyase activity (in the case of citrate) were both elevated in cells cultured in E8 (Figure S3.4). We confirmed that glutamine-mediated reductive carboxylation flux was increased in chemically defined culture media by tracing the contribution of [1-¹³C]glutamine to various intermediates (Figure 3.2E). This NADPH-dependent pathway can fuel lipid biosynthesis via citrate and is particularly active under conditions of oxidative stress or hypoxia inducible factor (HIF) stabilization [36–39]. In addition, we observed elevated levels of 2HG in cells grown in chemically defined medium (Figure 3.2F). We confirmed this metabolite as the (R)-2HG enantiomer via chiral chromatography (Figure S3.2E, supplemental methods), suggesting this 2HG was produced by *IDH1*. However, levels present in all conditions were significantly lower than that required for modulation of αKG-dependent dioxygenase activity [40, 41]. These results suggest that the TCA cycle, the central hub of mitochondrial oxidative energy generation, resides in distinct states within hESCs depending on the nutritional environment of cells.

Figure 3.3: HESCs adapted to chemically defined media upregulate lipid biosynthesis. (A) Relative fatty acid abundance in cells adapted to MEF-CM, E8, and mTeSR1 normalized by MEF-CM sample. Left and right panel are HUES 9 and H9 hESCs respectively. (B) Percentage of newly synthesized palmitate and cholesterol after 24 hours. Left and right panel are HUES 9 and H9 hESCs respectively. (C) Schematic diagram of [U-¹³C₁₆]palmitate metabolism. Open circles depict ¹²C and filled circles depict ¹³C atoms. Metabolite abbreviations described in Supplemental Text. (D) Percentage of M+16 fatty acids in HUES 9 hESCs cultured in E8+ BSA-bound [U-¹³C₁₆]palmitate and 1 mM carnitine (E) Mass isotopomer distribution of palmitate and stearate in HUES 9 hESCs cultured in E8 with BSA-bound [U-¹³C₁₆]palmitate and 1 mM carnitine. (F) Expression of genes encoding various metabolic enzymes in HUES 9 hESCs adapted to E8 relative to cells in MEF-CM. (A, D-F) All results shown as mean ± SEM. (A, F) P values were calculated using a Student's two-tailed t test relative to MEF-CM condition; *, P value between 0.01 and 0.05; **, P value between 0.001 and 0.01; ***, P value <0.001. (B) Results shown as mean and 95% CI. *, Significance indicated by non-overlapping 95% confidence intervals.



3.4.3 Chemically defined medium dramatically increases lipogenesis

The increased reductive carboxylation and 2HG production noted above provides some mechanistic insight into why oxidative PPP flux is elevated in defined media. However, in addition to the changes in intermediary metabolism, we observed significant decreases in per cell fatty acid abundances in HUES 9 and H9 hESCs maintained in more defined media such as E8 and mTeSR1 versus MEF-CM (Figure 3.3A), consistent with our observation of decreased dry cell weight of hESCs in the latter (Figure 3.1C and S3.2A). We next employed [U-¹³C₆]glucose and ISA to quantify *de novo* lipogenesis in hESCs cultured in the same media panel. This analysis highlighted drastic changes in the extent that hESCs synthesized fatty acids and cholesterol in different media. Whereas hESCs exhibited minimal lipogenesis in MEF-CM over 24 hours, HUES 9 and H9 cells synthesized 50-80% of their palmitate and cholesterol in E8 or mTeSR1 over the same time period (Figure 3.3B). Notably, the contribution of glucose to lipogenic AcCoA pools did not change appreciably in different media, consistent with glucose labeling of citrate under each condition (Figure S3.5A-B). These results demonstrate that hESCs exhibit marked differences in lipid biosynthesis when cultured in different media.

Both MEF-CM and mTeSR1 formulations contain exogenous lipid supplements (Albumin and Chemically Defined Lipid Concentrate, respectively) that may support hPSC growth, though our results indicate the levels present in mTeSR1 are insufficient. To further dissect how exogenous lipids are used and metabolized in chemically defined media we supplemented E8 with albumin-bound [U-¹³C₁₆]palmitate (U-Palm E8) as the sole source of fatty acids (Figure 3.3C). After 24 hours we quantified fatty acid and TCA intermediate labeling in hESCs. No appreciable isotope enrichment was detected in citrate or other TCA metabolites (data not shown), indicating β -oxidation is not employed by self-renewing hESCs to generate AcCoA. However, M+16 labeling of C16:0 palmitate and C18:0 stearate was observed, suggesting exogenous fatty acids are readily utilized and elongated in hESCs cultured in chemically defined medium (Figure 3.3D-E).

The metabolic changes outlined above center around pathways associated with *de novo* lipogenesis, NADPH regeneration, and glutaminolysis. To better understand how cells coordinate the observed changes in metabolic flux we quantified the expression of various enzymes catalyzing these reactions. Consistent with this metabolic shift toward lipid biosynthesis and NADPH production, we observed significant increases in the expression of *ACACA*, *ACLY*, *FAS*, *SCD*, *G6PD*, and *GLS2* (Figure 3.3F). Importantly, all of these genes (with the exception of *GLS2*) are targets of the sterol response element binding proteins (SREBPs), providing evidence that cells sense lipid deficiency and respond transcriptionally through the established SREBP pathway [42]. Recent studies have implicated *GLS2* specifically in both antioxidant function and necessary for differentiation [43–45]. These results indicate that nutritional availability influences both metabolic fluxes and gene expression in hESCs.

3.4.4 Lipid supplementation mitigates hESC metabolic reprogramming

Our results demonstrate that hESCs in different medium compositions can self-renew in distinct metabolic states, exemplified by drastic changes in NADPH, lipid, and amino acid metabolism. More specifically, these differences suggest that insufficient lipid availability in media, including mTeSR1 and E8, drive media-induced metabolic reprogramming that influences metabolic rates (as indicated above) and potentially cellular epigenetics [18]. To determine whether lipids produced by irradiated murine embryonic fibroblasts (MEFs) drove these changes we conditioned media in the presence of [U-¹³C₆]glucose. While glucose was readily metabolized by MEFs to citrate (Figure S3.5C), no appreciable accumulation of labeled lipids was observed after conditioning (Figure S3.5D). This finding suggests that lipids present in basal medium may support hESC growth.

The predominant lipid source in basal hESC medium is AlbuMAX within the Knockout Serum Replacer (KSR) supplement. This reagent contains albumin, fatty acids, cholesterol, and other lipids, and in some background media it can improve hESC growth [46]. To deter-

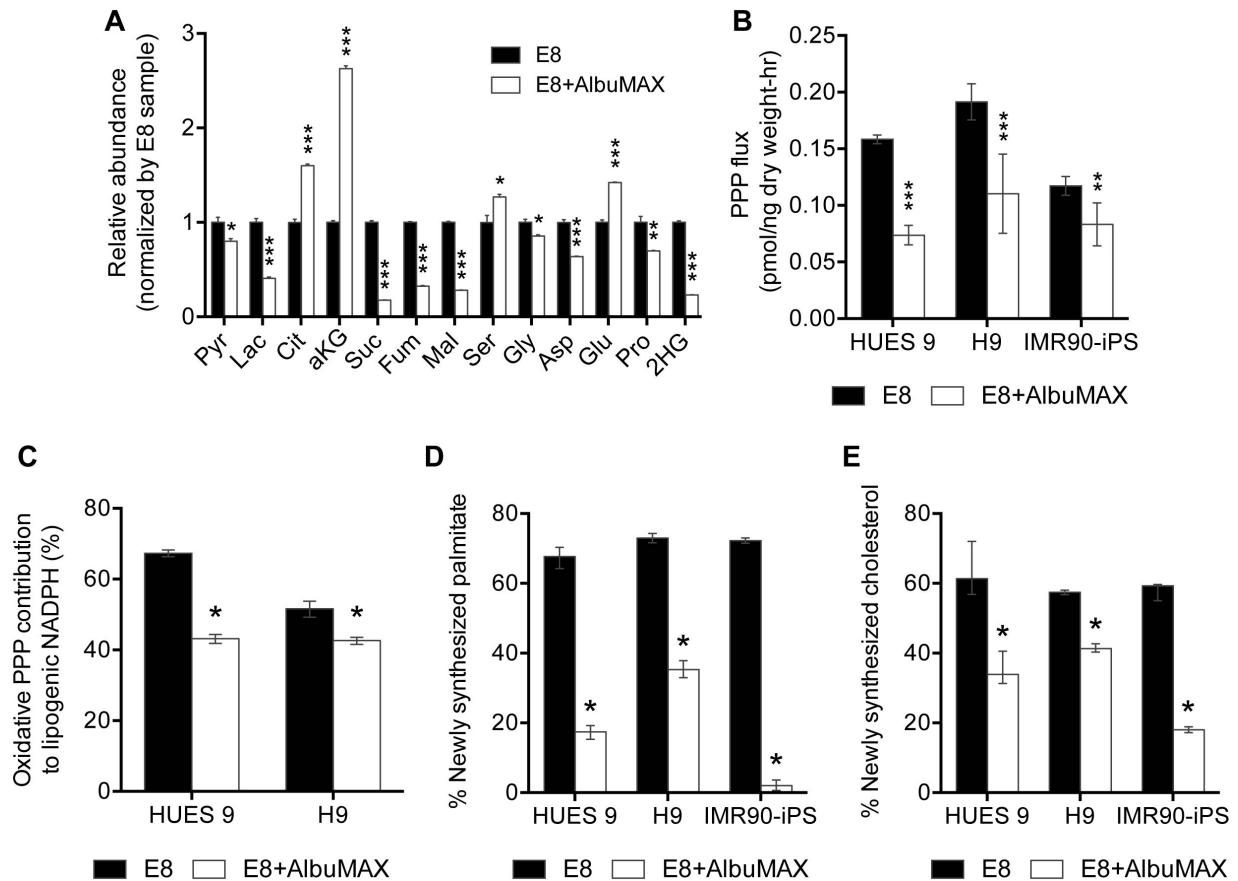


Figure 3.4: Lipid supplementation mitigates media-induced metabolic flux alterations.

HPSCs were cultured in either E8 or E8 with 1.6% (w/v) AlbuMAX for at least three passages. (A) Relative metabolite abundance of HUES 9 hESCs normalized by cell number and E8 sample. (B) Absolute oxidative PPP fluxes in hPSCs. (C) Contribution of oxidative PPP to lipogenic NADPH as determined by ISA in HUES 9 and H9 cells. (D) Percentage of newly synthesized palmitate after 24 hours. (E) Percentage of newly synthesized cholesterol after 24 hours. (A-B) All results shown as mean \pm SEM. P values were calculated using a Student's two-tailed t test relative to E8; *, P value between 0.01 and 0.05; **, P value between 0.001 and 0.01; ***, P value <0.001. (C-E) Results shown as mean and 95% CI. *, Significance indicated by non-overlapping 95% confidence intervals.

mine whether lipid supplementation in chemically defined media can mitigate the metabolic reprogramming described above we added AlbuMAX to E8 at a final concentration of 1.6% (E8+AlbuMAX), equivalent to that present in MEF-CM. Short-term addition of AlbuMAX did not affect *OCT4* expression, though more extensive studies are required to demonstrate its ability to support long-term hPSC expansion in specific media backgrounds (Figure S3.5E). Notably, AlbuMAX supplementation to E8 rescued some of the changes in intracellular metabolite levels that we observed in defined medium. Specifically, glycolytic (Pyr, Lac) and various TCA intermediates (Suc, Fum, Mal) decreased significantly, while levels of the lipogenic metabolite citrate and aKG were increased (Figure 3.4A). Only a marginal impact on glucose uptake and lactate secretion was observed (Figure S3.5F), presumably due to the importance of glycolysis for pluripotency [15–17] and the need for continued NEAA biosynthesis (e.g. serine, glycine), which were not supplemented further. However, net glutamine anaplerosis decreased in HUES 9 cells after addition of AlbuMAX as noted by the increased glutamate secretion observed (Figure S3.5G).

Additionally, we quantified relevant flux changes in cells cultured in lipid-supplemented E8 versus basal E8 media. Oxidative PPP flux was significantly decreased in HUES 9 and H9 cells under these conditions (Figure 3.4B). Furthermore, the contribution of PPP flux to lipogenic NADPH was also decreased in these cells (Figure 3.4C). Less robust changes may have occurred in PPP flux in IMR90-iPSC cultures since they were maintained for an extended number of passages in lipid-deficient media prior to supplementation (Figure 3.4B). On the other hand, fatty acid (palmitate) and cholesterol synthesis were significantly decreased in all hPSCs upon AlbuMAX addition (Figure 3.4D-E).

Lipid supplementation also influenced the general phenotype of hPSCs. Lipid supplementation significantly decreased the transcription of most enzymes involved in *de novo* lipogenesis that were previously observed to be upregulated in chemically defined media, with consistent results obtained in HUES 9 and H9 hESCs as well as an IMR90-derived iPSC line (Figure

3.5A-C). Additionally, per cell dry weight increased significantly in E8+AlbuMAX HUES 9, H9, and IMR90-iPSC cultures (Figure 3.5D). In our hands HUES 9 cell growth was not affected by growth in E8+AlbuMAX when additional BSA was included in the formulation; however, some growth suppression was observed in H9 and IMR90-iPS hPSCs (data not shown), indicating additional optimization of lipid supplement-background media combinations may be needed. To more functionally characterize mitochondria under these conditions we conducted respirometry analysis. Basal, ATP-linked oxygen consumption was significantly lower in HUES 9 cells cultured in E8 compared to those maintained in MEF-CM (Figure 3.5E and S3.6A). Consistent with the rescue experiments above, supplementation of AlbuMAX to E8 significantly increased respiration of HUES 9, H9, and IMR90-iPSCs (Figure 3.5F and S3.6A-C). Taken together, these data indicate that lipid deficiency of chemically defined media induced a profound reliance on biosynthetic fluxes, owing to the need for structural lipids in proliferating hESCs. In turn, this metabolic reprogramming influences the respiratory state, gene expression profile, and mitochondrial function of hPSCs. These data strongly contrast the concept of mitochondrial inactivity as a key requirement for pluripotency-associated metabolic reprogramming and illustrate the confounding effects of nutrient-availability in hPSC metabolic studies.

3.5 Discussion

The prevailing view of hPSC metabolism is highly reminiscent of tumor cell metabolism in that aerobic glycolysis is thought to be favored over oxidative mitochondrial metabolism [23, 47–49]. These findings are supported by metabolic studies predominantly conducted in chemically defined media and/or the impact of metabolic inhibitors on reprogramming efficiency in fast-growing cultures [15–17]. In other studies using MEF-CM as the primary maintenance condition metabolic analysis was limited to respirometry with little focus on pathways involved in biosynthesis [50, 51]. Our results demonstrate that distinct metabolic states can support

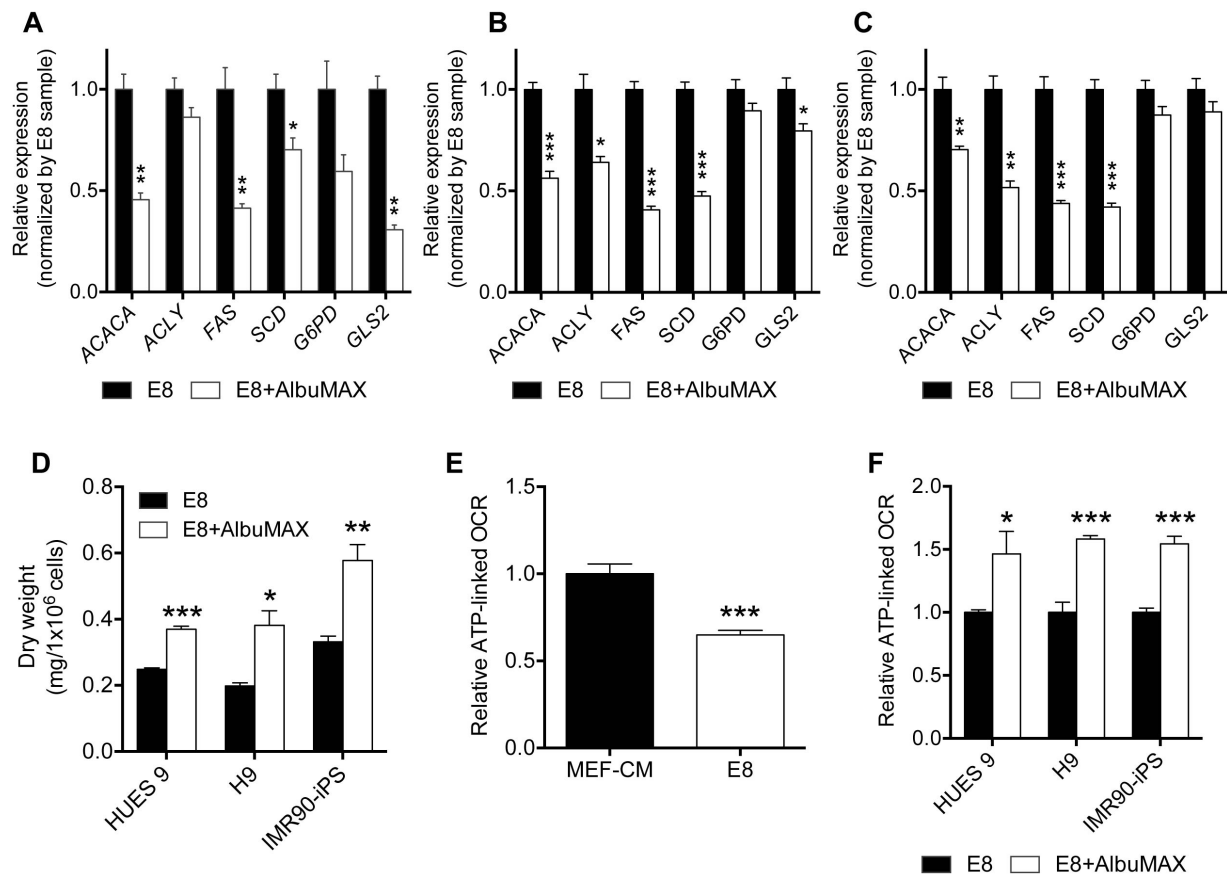


Figure 3.5: Lipid supplementation mitigates media-induced metabolic enzyme expression and mitochondrial state alterations. (A-C) Expression of genes encoding various metabolic enzymes in hPSCs adapted to E8+AlbuMAX relative to cells in E8. (A) HUES 9; (B) H9; (C) IMR90-iPS. (D) Dry cell weight per million hPSCs (E) Relative ATP-linked OCR of HUES 9 hESC in MEF-CM and E8, normalized by MEF-CM sample. (F) Relative ATP-linked OCR of hPSCs cells in E8 and E8+AlbuMAX, normalized by E8 sample. All results shown as mean \pm SEM. P values were calculated using a Student's two-tailed t test relative to E8 condition; *, P value between 0.01 and 0.05; **, P value between 0.001 and 0.01; ***, P value $<$ 0.001.

self-renewing hESCs when cultured in different nutrient conditions (Figure 3.6). In cancer biology recent studies have shed light on the importance of mitochondria for tumor cell growth and survival as well as the potential efficacy of mitochondrial inhibitors as therapies [25, 52]. Although glycolysis similarly supports hESC growth in all conditions, our data suggests that oxidative mitochondrial metabolism is highly active in hESCs when lipids are present and sustained by glutamine anaplerosis. Amino acid availability also presumably affected serine, glycine, asparagine, and proline metabolism in our system, as each of these metabolites was differentially labeled in MEF-CM chemically defined media.

While numerous studies have demonstrated that pluripotency and proliferation are robustly maintained in both MEF-CM and chemically defined media alternatives [8, 9], our MFA experiments indicate that hPSCs are capable of adapting metabolism to different nutrient conditions while maintaining their self-renewal capacity. In particular, medium lipid deficiency influences the metabolic state of hESCs such that they strongly upregulate pathways involved in lipid biosynthesis and NADPH regeneration (i.e., the oxidative PPP). This metabolic state may render cells more susceptible to oxidative stresses. For example, high NADPH consumption fueling lipid synthesis in cancer cells can increase their susceptibility to metabolic or environmental stresses [53]. Additionally, G6PD deficiency is a relatively common inborn error of metabolism (IEM) in the human population [54]. As such, mutations in *G6PD* may affect the efficiency of iPSC reprogramming in some populations or potentially impact the genetic stability and redox sensitivity of hPSCs cultured in chemically defined or more specifically lipid-free media.

HPSC applications in disease-modeling, drug screening, and regenerative medicine all require the robust production of differentiated lineages that correctly recapitulate the metabolic functions of somatic tissue. Organogenesis is a complex, multistep process that requires significant energy, biomass, and signaling cues; metabolism plays an essential role in all aspects of these processes. Subjecting hPSCs to selective pressures *in vitro* such as medium lipid deficiency may limit their ability to accurately represent normal tissue function in subsequent applications

without giving rise to "harmful" genetic alterations [55]. Furthermore, culture and passaging conditions as well as time can influence the genetic and epigenetic stability of hPSCs [11, 56] or metabolic rates after subculture [12]. Our MFA results provide potential mechanisms that may be exploited to alleviate some of the stresses associated with long-term *in vitro* expansion. Specifically, addition of particular lipids may enhance or better control hPSC expansion and differentiation. As such, pluripotency analysis (e.g. teratoma formation) and proliferation alone may not be suitable metrics for the evaluation of hPSC culture media and intracellular metabolic fluxes should also be considered. MFA is an ideal and underutilized tool for such applications.

Numerous studies have recently implicated metabolites or culture conditions in regulating cellular epigenetics and differentiation propensity of pluripotent stem cells. Metabolites that impact methylation [19, 20, 35] and acetylation [18] can influence differentiation but likely play more critical roles in cellular bioenergetics and biosynthesis. Indeed, it is unclear how global changes in the abundance of SAM or AcCoA can impact the specific epigenetic state of pluripotency genes. Other studies have recently identified key differences in the predisposition of cells to differentiate to neural or hematopoietic lineages when culturing or priming cells in MEF-CM versus more nutrient-limited media such as E8 or mTeSR1 [13, 57]. Finally, the mitochondrial state and lipid profile of cells changes significantly during the course of mESC and hESC differentiation [22]. Our results therefore demonstrate the importance of considering the broader nutritional environment and intracellular metabolic state of hPSCs when characterizing metabolic regulation in stem cells and designing hPSC media.

3.6 Acknowledgements

HUES 9 hESC was provided by Prof. Shyni Varghese (University of California, San Diego). H9 hESC and IMR90 iPSC were provided by Prof. Sean Palecek (University of Wisconsin-Madison).

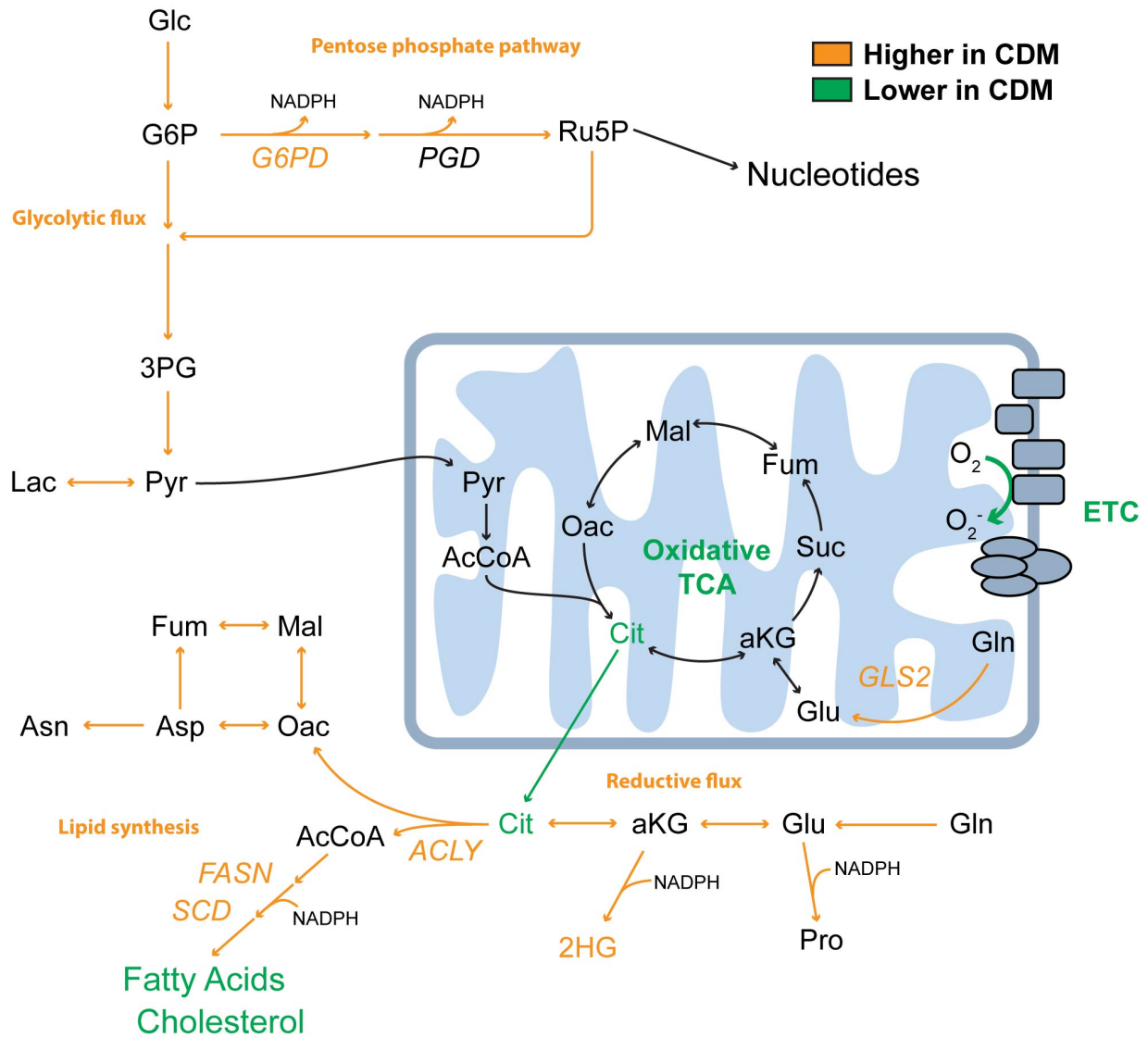


Figure 3.6: Nutrient availability reprograms intermediary metabolism in hPSCs. Culture of hPSCs in chemically defined media (CDM) reprograms glucose, glutamine, lipid, and NADPH metabolism. Lipid deficiency induces the upregulation of oxidative PPP flux for NADPH synthesis, *de novo* lipogenesis, and reductive carboxylation while diverting carbon from the TCA cycle and decreasing mitochondrial respiration (ATP-linked activity of mitochondrial electron transport chain, ETC). Amino acid deficiencies influence glutaminolysis, synthesis of proline, asparagine, and serine, which are upregulated in hPSCs cultured in defined media. Metabolic genes described in italics. Metabolite abbreviations described in Supplemental Text.

The authors acknowledge Yongsung Hwang, Shyni Varghese, and members of the Metallo lab for technical assistance and helpful discussions. This research was supported by the California Institute of Regenerative Medicine grant (RB5-07356), National Institutes of Health grant (R01CA188652), a Searle Scholar Award to C.M.M, a NSF CAREER Award (1454425) to C.M.M., and a NSF Graduate Research fellowship (DGE-1144086) to M.G.B. The authors declare no financial or commercial conflict of interest.

Chapter 3, in full, is a reprint of the material as it appears in "Distinct metabolic states can support self-renewal and lipogenesis in human pluripotent stem cells under different culture conditions," *Cell Reports*, vol. 16, 2016. Mehmet G. Badur and Hui Zhang are the co-primary authors of this publication. Ajit S. Divakaruni, Seth J. Parker, Christian Jager, Karsten Hiller, and Anne N. Murphy are co-authors of this publication. Christian M. Metallo is the corresponding author of this publication.

3.7 References

1. Thomson, J. A., Itskovitz-Eldor, J., Shapiro, S. S., Waknitz, M. A., Swiergiel, J. J., Marshall, V. S. & Jones, J. M. Embryonic stem cell lines derived from human blastocysts. *Science* **282**, 1145–7 (1998).
2. Takahashi, K. & Yamanaka, S. Induction of pluripotent stem cells from mouse embryonic and adult fibroblast cultures by defined factors. *Cell* **126**, 663–76 (2006).
3. Desai, N., Rambhia, P. & Gishto, A. Human embryonic stem cell cultivation: historical perspective and evolution of xeno-free culture systems. *Reprod Biol Endocrinol* **13**, 9 (2015).
4. Villa-Diaz, L. G., Ross, A. M., Lahann, J. & Krebsbach, P. H. Concise review: The evolution of human pluripotent stem cell culture: from feeder cells to synthetic coatings. *Stem Cells* **31**, 1–7 (2013).
5. Kirouac, D. C. & Zandstra, P. W. The systematic production of cells for cell therapies. *Cell Stem Cell* **3**, 369–81 (2008).
6. Hyun, I., Lindvall, O., Ahrlund-Richter, L., Cattaneo, E., Cavazzana-Calvo, M., Cossu, G., De Luca, M., Fox, I. J., Gerstle, C., Goldstein, R. A., Hermeren, G., High, K. A., Kim,

- H. O., Lee, H. P., Levy-Lahad, E., Li, L., Lo, B., Marshak, D. R., McNab, A., Munsie, M., Nakauchi, H., Rao, M., Rooke, H. M., Valles, C. S., Srivastava, A., Sugarman, J., Taylor, P. L., Veiga, A., Wong, A. L., Zoloth, L. & Daley, G. Q. New ISSCR guidelines underscore major principles for responsible translational stem cell research. *Cell Stem Cell* **3**, 607–9 (2008).
7. Carpenter, M. K. & Couture, L. A. Regulatory considerations for the development of autologous induced pluripotent stem cell therapies. *Regen Med* **5**, 569–79 (2010).
 8. Ludwig, T. E., Bergendahl, V., Levenstein, M. E., Yu, J., Probasco, M. D. & Thomson, J. A. Feeder-independent culture of human embryonic stem cells. *Nat Methods* **3**, 637–46 (2006).
 9. Chen, G., Gulbranson, D. R., Hou, Z., Bolin, J. M., Ruotti, V., Probasco, M. D., Smuga-Otto, K., Howden, S. E., Diol, N. R., Propson, N. E., Wagner, R., Lee, G. O., Antosiewicz-Bourget, J., Teng, J. M. & Thomson, J. A. Chemically defined conditions for human iPSC derivation and culture. *Nat Methods* **8**, 424–9 (2011).
 10. Ungrin, M., O'Connor, M., Eaves, C. & Zandstra, P. W. Phenotypic analysis of human embryonic stem cells. *Curr Protoc Stem Cell Biol* **Chapter 1**, Unit 1B 3 (2007).
 11. Laurent, L. C., Ulitsky, I., Slavin, I., Tran, H., Schork, A., Morey, R., Lynch, C., Harness, J. V., Lee, S., Barrero, M. J., Ku, S., Martynova, M., Semechkin, R., Galat, V., Gottesfeld, J., Izpisua Belmonte, J. C., Murry, C., Keirstead, H. S., Park, H. S., Schmidt, U., Laslett, A. L., Muller, F. J., Nievergelt, C. M., Shamir, R. & Loring, J. F. Dynamic changes in the copy number of pluripotency and cell proliferation genes in human ESCs and iPSCs during reprogramming and time in culture. *Cell Stem Cell* **8**, 106–18 (2011).
 12. Badur, M. G., Zhang, H. & Metallo, C. M. Enzymatic passaging of human embryonic stem cells alters central carbon metabolism and glycan abundance. *Biotechnol J* (2015).
 13. Lee, J. B., Graham, M., Collins, T. J., Lee, J. H., Hong, S. H., McNicol, A. J., Shapovalova, Z. & Bhatia, M. Reversible lineage-specific priming of human embryonic stem cells can be exploited to optimize the yield of differentiated cells. *Stem Cells* **33**, 1142–52 (2015).
 14. Ben-Zvi, D. & Melton, D. A. Modeling human nutrition using human embryonic stem cells. *Cell* **161**, 12–7 (2015).
 15. Folmes, C. D., Nelson, T. J., Martinez-Fernandez, A., Arrell, D. K., Lindor, J. Z., Dzeja, P. P., Ikeda, Y., Perez-Terzic, C. & Terzic, A. Somatic oxidative bioenergetics transitions into pluripotency-dependent glycolysis to facilitate nuclear reprogramming. *Cell Metab* **14**, 264–71 (2011).

16. Panopoulos, A. D., Yanes, O., Ruiz, S., Kida, Y. S., Diep, D., Tautenhahn, R., Herrerias, A., Batchelder, E. M., Plongthongkum, N., Lutz, M., Berggren, W. T., Zhang, K., Evans, R. M., Siuzdak, G. & Izpisua Belmonte, J. C. The metabolome of induced pluripotent stem cells reveals metabolic changes occurring in somatic cell reprogramming. *Cell Res* **22**, 168–77 (2012).
17. Zhu, S., Li, W., Zhou, H., Wei, W., Ambasudhan, R., Lin, T., Kim, J., Zhang, K. & Ding, S. Reprogramming of human primary somatic cells by OCT4 and chemical compounds. *Cell Stem Cell* **7**, 651–5 (2010).
18. Moussaieff, A., Rouleau, M., Kitsberg, D., Cohen, M., Levy, G., Barasch, D., Nemirovski, A., Shen-Orr, S., Laevsky, I., Amit, M., Bomze, D., Elena-Herrmann, B., Scherf, T., Nissim-Rafinia, M., Kempa, S., Itskovitz-Eldor, J., Meshorer, E., Aberdam, D. & Nahmias, Y. Glycolysis-mediated changes in acetyl-CoA and histone acetylation control the early differentiation of embryonic stem cells. *Cell Metab* **21**, 392–402 (2015).
19. Shiraki, N., Shiraki, Y., Tsuyama, T., Obata, F., Miura, M., Nagae, G., Aburatani, H., Kume, K., Endo, F. & Kume, S. Methionine metabolism regulates maintenance and differentiation of human pluripotent stem cells. *Cell Metab* **19**, 780–94 (2014).
20. Wang, J., Alexander, P., Wu, L., Hammer, R., Cleaver, O. & McKnight, S. L. Dependence of mouse embryonic stem cells on threonine catabolism. *Science* **325**, 435–9 (2009).
21. Shyh-Chang, N., Locasale, J. W., Lyssiotis, C. A., Zheng, Y., Teo, R. Y., Ratanasirintraoort, S., Zhang, J., Onder, T., Unternaehrer, J. J., Zhu, H., Asara, J. M., Daley, G. Q. & Cantley, L. C. Influence of threonine metabolism on S-adenosylmethionine and histone methylation. *Science* **339**, 222–6 (2013).
22. Yanes, O., Clark, J., Wong, D. M., Patti, G. J., Sanchez-Ruiz, A., Benton, H. P., Trauger, S. A., Despons, C., Ding, S. & Siuzdak, G. Metabolic oxidation regulates embryonic stem cell differentiation. *Nat Chem Biol* **6**, 411–7 (2010).
23. Zhang, J., Nuebel, E., Daley, G. Q., Koehler, C. M. & Teitell, M. A. Metabolic regulation in pluripotent stem cells during reprogramming and self-renewal. *Cell Stem Cell* **11**, 589–95 (2012).
24. Zhang, J., Khvorostov, I., Hong, J. S., Oktay, Y., Vergnes, L., Nuebel, E., Wahjudi, P. N., Setoguchi, K., Wang, G., Do, A., Jung, H. J., McCaffery, J. M., Kurland, I. J., Reue, K., Lee, W. N., Koehler, C. M. & Teitell, M. A. UCP2 regulates energy metabolism and differentiation potential of human pluripotent stem cells. *EMBO J* **30**, 4860–73 (2011).
25. Viale, A., Pettazzoni, P., Lyssiotis, C. A., Ying, H., Sanchez, N., Marchesini, M., Carugo, A., Green, T., Seth, S., Giuliani, V., Kost-Alimova, M., Muller, F., Colla, S., Nezi, L., Genovese, G., Deem, A. K., Kapoor, A., Yao, W., Brunetto, E., Kang, Y., Yuan, M., Asara,

- J. M., Wang, Y. A., Heffernan, T. P., Kimmelman, A. C., Wang, H., Fleming, J. B., Cantley, L. C., DePinho, R. A. & Draetta, G. F. Oncogene ablation-resistant pancreatic cancer cells depend on mitochondrial function. *Nature* **514**, 628–32 (2014).
26. Vacanti, N. M., Divakaruni, A. S., Green, C. R., Parker, S. J., Henry, R. R., Ciaraldi, T. P., Murphy, A. N. & Metallo, C. M. Regulation of substrate utilization by the mitochondrial pyruvate carrier. *Mol Cell* **56**, 425–35 (2014).
 27. Lewis, C. A., Parker, S. J., Fiske, B. P., McCloskey, D., Gui, D. Y., Green, C. R., Vokes, N. I., Feist, A. M., Vander Heiden, M. G. & Metallo, C. M. Tracing compartmentalized NADPH metabolism in the cytosol and mitochondria of mammalian cells. *Mol Cell* **55**, 253–63 (2014).
 28. Young, J. D. INCA: a computational platform for isotopically non-stationary metabolic flux analysis. *Bioinformatics* **30**, 1333–5 (2014).
 29. Antoniewicz, M. R., Kelleher, J. K. & Stephanopoulos, G. Determination of confidence intervals of metabolic fluxes estimated from stable isotope measurements. *Metab Eng* **8**, 324–37 (2006).
 30. Divakaruni, A. S., Paradise, A., Ferrick, D. A., Murphy, A. N. & Jastroch, M. Analysis and interpretation of microplate-based oxygen consumption and pH data. *Methods Enzymol* **547**, 309–54 (2014).
 31. Wang, X., Spandidos, A., Wang, H. & Seed, B. PrimerBank: a PCR primer database for quantitative gene expression analysis, 2012 update. *Nucleic Acids Res* **40**, D1144–9 (2012).
 32. Patra, K. C. & Hay, N. The pentose phosphate pathway and cancer. *Trends Biochem Sci* **39**, 347–54 (2014).
 33. DeBerardinis, R. J., Mancuso, A., Daikhin, E., Nissim, I., Yudkoff, M., Wehrli, S. & Thompson, C. B. Beyond aerobic glycolysis: transformed cells can engage in glutamine metabolism that exceeds the requirement for protein and nucleotide synthesis. *Proc Natl Acad Sci U S A* **104**, 19345–50 (2007).
 34. Ahn, C. S. & Metallo, C. M. Mitochondria as biosynthetic factories for cancer proliferation. *Cancer Metab* **3**, 1 (2015).
 35. Carey, B. W., Finley, L. W., Cross, J. R., Allis, C. D. & Thompson, C. B. Intracellular alpha-ketoglutarate maintains the pluripotency of embryonic stem cells. *Nature* **518**, 413–6 (2015).
 36. Metallo, C. M., Gameiro, P. A., Bell, E. L., Mattaini, K. R., Yang, J., Hiller, K., Jewell, C. M., Johnson, Z. R., Irvine, D. J., Guarente, L., Kelleher, J. K., Vander Heiden, M. G.,

- Iliopoulos, O. & Stephanopoulos, G. Reductive glutamine metabolism by IDH1 mediates lipogenesis under hypoxia. *Nature* **481**, 380–4 (2012).
37. Mullen, A. R., Wheaton, W. W., Jin, E. S., Chen, P. H., Sullivan, L. B., Cheng, T., Yang, Y., Linehan, W. M., Chandel, N. S. & DeBerardinis, R. J. Reductive carboxylation supports growth in tumour cells with defective mitochondria. *Nature* **481**, 385–8 (2012).
 38. Wise, D. R., Ward, P. S., Shay, J. E., Cross, J. R., Gruber, J. J., Sachdeva, U. M., Platt, J. M., DeMatteo, R. G., Simon, M. C. & Thompson, C. B. Hypoxia promotes isocitrate dehydrogenase-dependent carboxylation of alpha-ketoglutarate to citrate to support cell growth and viability. *Proc Natl Acad Sci U S A* **108**, 19611–6 (2011).
 39. Fendt, S. M., Bell, E. L., Keibler, M. A., Olenchock, B. A., Mayers, J. R., Wasylenko, T. M., Vokes, N. I., Guarente, L., Vander Heiden, M. G. & Stephanopoulos, G. Reductive glutamine metabolism is a function of the alpha-ketoglutarate to citrate ratio in cells. *Nat Commun* **4**, 2236 (2013).
 40. Xu, W., Yang, H., Liu, Y., Yang, Y., Wang, P., Kim, S. H., Ito, S., Yang, C., Wang, P., Xiao, M. T., Liu, L. X., Jiang, W. Q., Liu, J., Zhang, J. Y., Wang, B., Frye, S., Zhang, Y., Xu, Y. H., Lei, Q. Y., Guan, K. L., Zhao, S. M. & Xiong, Y. Oncometabolite 2-hydroxyglutarate is a competitive inhibitor of alpha-ketoglutarate-dependent dioxygenases. *Cancer Cell* **19**, 17–30 (2011).
 41. Grassian, A. R., Parker, S. J., Davidson, S. M., Divakaruni, A. S., Green, C. R., Zhang, X., Slocum, K. L., Pu, M., Lin, F., Vickers, C., Joud-Caldwell, C., Chung, F., Yin, H., Handly, E. D., Straub, C., Growney, J. D., Vander Heiden, M. G., Murphy, A. N., Pagliarini, R. & Metallo, C. M. IDH1 mutations alter citric acid cycle metabolism and increase dependence on oxidative mitochondrial metabolism. *Cancer Res* **74**, 3317–31 (2014).
 42. Porstmann, T., Santos, C. R., Griffiths, B., Cully, M., Wu, M., Leever, S., Griffiths, J. R., Chung, Y. L. & Schulze, A. SREBP activity is regulated by mTORC1 and contributes to Akt-dependent cell growth. *Cell Metab* **8**, 224–36 (2008).
 43. Hu, W., Zhang, C., Wu, R., Sun, Y., Levine, A. & Feng, Z. Glutaminase 2, a novel p53 target gene regulating energy metabolism and antioxidant function. *Proc Natl Acad Sci U S A* **107**, 7455–60 (2010).
 44. Suzuki, S., Tanaka, T., Poyurovsky, M. V., Nagano, H., Mayama, T., Ohkubo, S., Lokshin, M., Hosokawa, H., Nakayama, T., Suzuki, Y., Sugano, S., Sato, E., Nagao, T., Yokote, K., Tatsuno, I. & Prives, C. Phosphate-activated glutaminase (GLS2), a p53-inducible regulator of glutamine metabolism and reactive oxygen species. *Proc Natl Acad Sci U S A* **107**, 7461–6 (2010).

45. Velletri, T., Romeo, F., Tucci, P., Peschiaroli, A., Annicchiarico-Petruzzelli, M., Niklison-Chirou, M. V., Amelio, I., Knight, R. A., Mak, T. W., Melino, G. & Agostini, M. GLS2 is transcriptionally regulated by p73 and contributes to neuronal differentiation. *Cell Cycle* **12**, 3564–73 (2013).
46. Garcia-Gonzalo, F. R. & Izpisua Belmonte, J. C. Albumin-associated lipids regulate human embryonic stem cell self-renewal. *PLoS One* **3**, e1384 (2008).
47. Vander Heiden, M. G., Locasale, J. W., Swanson, K. D., Sharfi, H., Heffron, G. J., Amador-Noguez, D., Christofk, H. R., Wagner, G., Rabinowitz, J. D., Asara, J. M. & Cantley, L. C. Evidence for an alternative glycolytic pathway in rapidly proliferating cells. *Science* **329**, 1492–9 (2010).
48. Vacanti, N. M. & Metallo, C. M. Exploring metabolic pathways that contribute to the stem cell phenotype. *Biochim Biophys Acta* **1830**, 2361–9 (2013).
49. Prigione, A., Fauler, B., Lurz, R., Lehrach, H. & Adjaye, J. The senescence-related mitochondrial/oxidative stress pathway is repressed in human induced pluripotent stem cells. *Stem Cells* **28**, 721–33 (2010).
50. Zhou, W., Choi, M., Margineantu, D., Margaretha, L., Hesson, J., Cavanaugh, C., Blau, C. A., Horwitz, M. S., Hockenbery, D., Ware, C. & Ruohola-Baker, H. HIF1alpha induced switch from bivalent to exclusively glycolytic metabolism during ESC-to-EpiSC/hESC transition. *EMBO J* **31**, 2103–16 (2012).
51. Folmes, C. D., Dzeja, P. P., Nelson, T. J. & Terzic, A. Metabolic plasticity in stem cell homeostasis and differentiation. *Cell Stem Cell* **11**, 596–606 (2012).
52. Wheaton, W. W., Weinberg, S. E., Hamanaka, R. B., Soberanes, S., Sullivan, L. B., Anso, E., Glasauer, A., Dufour, E., Mutlu, G. M., Budigner, G. S. & Chandel, N. S. Metformin inhibits mitochondrial complex I of cancer cells to reduce tumorigenesis. *Elife* **3**, e02242 (2014).
53. Jeon, S. M., Chandel, N. S. & Hay, N. AMPK regulates NADPH homeostasis to promote tumour cell survival during energy stress. *Nature* **485**, 661–5 (2012).
54. Stanton, R. C. Glucose-6-phosphate dehydrogenase, NADPH, and cell survival. *IUBMB Life* **64**, 362–9 (2012).
55. Peterson, S. E. & Loring, J. F. Genomic instability in pluripotent stem cells: implications for clinical applications. *J Biol Chem* **289**, 4578–84 (2014).
56. Garitaonandia, I., Amir, H., Boscolo, F. S., Wambua, G. K., Schultheisz, H. L., Sabatini, K., Morey, R., Waltz, S., Wang, Y. C., Tran, H., Leonardo, T. R., Nazor, K., Slavin, I., Lynch, C., Li, Y., Coleman, R., Gallego Romero, I., Altun, G., Reynolds, D., Dalton, S.,

- Parast, M., Loring, J. F. & Laurent, L. C. Increased risk of genetic and epigenetic instability in human embryonic stem cells associated with specific culture conditions. *PLoS One* **10**, e0118307 (2015).
57. Lippmann, E. S., Estevez-Silva, M. C. & Ashton, R. S. Defined human pluripotent stem cell culture enables highly efficient neuroepithelium derivation without small molecule inhibitors. *Stem Cells* **32**, 1032–42 (2014).

Chapter 4

Lipid availability influences the metabolic maturation of hPSC-derived cardiomyocytes

4.1 Introduction

The promise of stem-cell derived cardiomyocytes (CMs) has been driven by a critical need for durable cell sources for tissue engineering or toxicity screening applications [1–4]. With the limited regenerative capacity of the adult heart, research efforts have focused on the development of protocols that allow for relatively homogeneous cardiac differentiation. Recent protocols now allow purities approaching >90% without the use of growth factors in partially- or fully-defined conditions [5, 6]. However these protocols generate functionally immature cardiomyocytes which lack the proper electrical connectivity, force generation, and metabolic phenotype to properly mimic their *in vivo* counterparts [7, 8]. Preclinical models of CM transplantation have shown potential increased arrhythmia risk and demonstrated the need for functional maturation [9, 10]. Recapitulation of native mitochondrial function and bioenergetics will be essential to drive

maturation.

While simple aging of cells has generated some success [11], this is impractical for bioprocess scale up and quantities needed eventually *in vivo* after myocardial infarction (i.e. delivery of up to 10^9 cells) [2, 12]. Efforts to speed up functional maturation of CMs *in vitro* have focused on physical cues [13], electrical stimulation [14, 15], and physical microenvironment [16–18] but metabolic manipulation through media provides a promising potential avenue [19].

The bioenergetic demands of the developing and adult heart require a dramatic upregulation of ATP production, which is marked by a transition from a highly glycolytic pluripotent stem cell to a somatic cell relying primarily on oxidative phosphorylation [20]. Recent work has demonstrated that this mitochondrial shift is necessary for proper CM development [21]. Moreover, the increase in mitochondrial activity is marked by the catabolism a diverse set of carbon sources in the adult heart that drives proper CM function in the fasted and fed states (e.g. fatty acids, ketone bodies, branched-chain amino acids) [22, 23]. As with other measures of CM function, the metabolism of hPSC-derived CMs is fetal-like with heavy reliance on glycolysis and glucose oxidation and presents a roadblock for their utility [24, 25]. However recent work has definitively demonstrated that activating mitochondrial function through galactose supplementation induces a more mature CM metabolism (i.e. fatty acid oxidation) and better function in hPSC-derived CMs [26]. However, the role of mitochondrial substrate switching during CM differentiation and the role of fatty acid biosynthesis/oxidation during maturation remains unknown.

We hypothesized that by examining CM metabolism during differentiation we could identify key pathways that modulate CM function. Indeed, we found that immature hPSC-derived CMs suppress glutaminolysis as compared to hPSCs themselves. However, these cells fail to activate fatty acid oxidation (FAO) during differentiation. Day-by-day tracing revealed an activation of enzyme expression and mitochondrial catabolism of key substrates during differentiation, suggesting a correct differentiation program and some other obstacle to proper

CM function. Examination of lipid metabolism gene expression revealed aberrant fatty acid oxidation and synthesis pathway expression, leading us to hypothesize that lack of fatty acid supplementation in gold-standard differentiation medias forces CMs to synthesize structural lipids instead of oxidizing them for fuel. Supplementation of complex fatty acid mixtures improves mitochondrial function and substrate oxidation. Together this suggests that nutritional microenvironments must be considered when designing maintenance conditions as improper reprogramming of the metabolic network can prevent other physiologic functions.

4.2 Materials and Methods

4.2.1 Human pluripotent stem cell (hPSC) culture

Human embryonic stem cell line WA09 (H9) and induced pluripotent stem cell line iPS(IMR90iPS)-c4 were supplied by WiCell Research Institute. HPSCs were routinely maintained in mTeSR1 media (Stem Cell Technologies) on growth factor-reduced Matrigel (Corning Life Sciences) at $8.8 \mu\text{g}/\text{cm}^2$ and passaged every 4 days using ReLeSR (Stem Cell Technologies). All hPSCs experiments were conducted with cells ranging from 40 and 70 passages. For metabolic tracing experiment, hPSCs were adapted to chemically defined media TeSR-E8 media (Stem Cell Technologies) for at least one passage, and all hPSCs were detached and plated by exposure to Accutase (Innovative Cell Technology).

4.2.2 Cardiomyocyte differentiation

All hPSCs were cultured for at least five passages post thaw before beginning differentiation. HPSCs were differentiated by the adapted chemically defined cardiomyocyte generation protocol [6]. Briefly, hPSCs were dissociated using a 0.5 mM EDTA (Life Technologies) in PBS without CaCl_2 or MgCl_2 (Corning Life Sciences) for 7 minutes at room temperature. HPSCs

were plated at 3.0×10^5 cells per well in mTeSR1 or TeSR-E8 media (Stem Cell Technologies) supplemented with $2 \mu\text{M}$ Thiazovivin (Selleck Chemicals) for the first 24 hours after passage. HPSCs were fed for 3-5 days until they reached $>90\%$ confluence. To initiate differentiate, cells were washed with PBS 1X and the culture medium was changed to CDM3, consisting of RPMI 1640 medium (Life Technologies), $500 \mu\text{g/mL}$ *O. sativa*-derived recombinant human albumin (A0237, Sigma-Aldrich), and $213 \mu\text{g/mL}$ L-ascorbic acid 2-phosphate (49752, Sigma-Aldrich), with $6 \mu\text{M}$ CHIR 99021 (Selleck Chemicals) for 48 hours. Media was then changed to CDM3 with $2 \mu\text{M}$ Wnt Inhibitor C59 (Selleck Chemicals) for 48 hours. Cells were then dissociated with TrypLE Express (Life Technologies) and plated onto Matrigel coated plates in CDM3 supplemented with 200 nM Thiazovivin at a density of 1×10^6 cells per well. After cardiomyocyte beating was observed (on day 7 to 8), Glucose free CDM3 medium with 10 mM sodium DL-lactate (Sigma-Aldrich), were used for further *in vitro* cardiomyocyte purification (2 to 4 days). Cardiomyocytes were then maintained in CDM3 with media changes every 48 hours. For hPSCs-derived CMs cultured with nutrient lipid supplement, CDM3 containing AlbuMAX ($1.6\% \text{ w/v}$; Life Technologies) were added in after day 8. Media was completely replaced every 48 hours thereafter.

4.2.3 ^{13}C metabolic tracing

For tracer experiments, culture medium was removed, cells were rinsed with PBS, and tracer media was added to wells. Tracer media consisted of glutamine, glucose, amino acid free RPMI1640 (US Biologics) supplemented with proper levels of ^{12}C amino acids, organic acids, and carbohydrates not being traced. If a more replete condition was being tested (i.e. additional nutrients added to basal media), ^{12}C metabolites were added to other tracer arms to ensure equivalent nutrient state (i.e. add ^{12}C lactate to a ^{13}C glucose trace). The following tracers were used: $[\text{U-}^{13}\text{C}_5]$ glutamine (Cambridge Isotope Laboratory), $[\text{U-}^{13}\text{C}_6]$ glucose (Cambridge Isotope Laboratory), $[\text{3-}^{13}\text{C}]$ pyruvate (2mM ; Cambridge Isotope Laboratory), $[\text{3-}^{13}\text{C}]$ lactate

(2mM; Cambridge Isotope Laboratory), [U-¹³C₆]leucine (Cambridge Isotope Laboratory), [U-¹³C₄]β-hydroxybutyrate (2mM; Sigma), [U-¹³C₈]octanoate, or [U-¹³C₁₆]palmitate (Cambridge Isotope Laboratory). [U-¹³C]palmitate was first non-covalently conjugated to ultra fatty acid free BSA (Roche) as previously described [27]. BSA conjugated [U-¹³C₁₆]palmitate was added to each culture medium along with additional L-carnitine at 50 μM (5% v/v) and 0.5 mM, respectively.

4.2.4 Metabolite extraction and derivatization

Cellular metabolites and fatty acids were extracted using methanol/water/chloroform. Briefly, spent media was removed, and cells were rinsed with 0.9% (w/v) saline and 500 μL of -80°C MeOH was added to quench metabolism. 200 μL of ice-cold water containing 5 μg/mL norvaline (internal standard for organic acids and amino acids) was added to each well. Both solution and cells were collected via scraping. Cell lysates were transferred to fresh Eppendorf tube and 500 μL of -20°C CHCl₃ containing 2 μg/mL D31-palmitic acid (internal standard for fatty acids) was added. After vortexing and centrifugation, the top aqueous layer and bottom organic layer were collected and dried.

Derivatization of aqueous metabolites was performed using the Gerstel MultiPurpose Sampler (MPS 2XL). Dried aqueous metabolites were dissolved in 20 μL of 2% (w/v) methoxyamine hydrochloride (MP Biomedicals) in pyridine and held at 37°C for 60 minutes. Subsequent conversion to their tert-butyldimethylsilyl derivatives was accomplished by adding 30 μL N-methyl-N-(tert-butyldimethylsilyl) trifluoroacetamide + 1% tert-butyldimethylchlorosilane (Regis Technologies) and incubating at 37°C for 30 minutes. Fatty acid methyl esters (FAMES) were generated by dissolving dried fatty acids in 0.5 mL 2% (v/v) methanolic sulfuric acid (Sigma-Aldrich) and incubating at 50°C for 2 hours. FAMES were subsequently extracted in 1 mL hexane with 0.1 mL saturated NaCl. Cholesterol was derivatized from dried FAME fraction by first dissolving in 20 μL pyridine and then adding 30 μL N-methyl-N-trimethylsilyl-trifluoroacetamide

(Macherey-Nagel) at 37°C for 30 minutes.

4.2.5 GC/MS analysis

Gas chromatography/mass spectrometry (GC/MS) analysis was performed using an Agilent 7890A with a 30 m DB-35MS capillary column (Agilent Technologies) connected to an Agilent 5975C MS. GC/MS was operated under electron impact (EI) ionization at 70 eV. One microliter sample was injected in splitless mode at 270°C, using helium as the carrier gas at a flow rate of 1 ml/min. For analysis of organic and amino acid derivatives, the GC oven temperature was held at 100°C for 2 minutes, increased to 255°C at 3.5°C/min, then ramped to 320°C at 15°C/min for a total run time of approximately 50 minutes. For measurement of FAMES, the GC oven temperature was held at 100°C for 3 minutes, then to 205°C at 25°C/min, further increased to 230°C at 5°C/min and ramped up to 300°C at 25°C/min for a total run time of approximately 15 minutes. For measurement of cholesterol, the GC oven temperature was held at 150°C for 1 minute, then to 260°C at 20°C/min, then held for 3 minutes, and further increased to 280°C at 10°C/min and held for 15 minutes, finally ramped up to 325°C for a total run time of approximately 30 minutes. The MS source and quadrupole were held at 230°C and 150°C, respectively, and the detector was operated in scanning mode, recording ion abundance in the range of 100 - 650 m/z.

4.2.6 Mole percent enrichment calculation

Mole percent enrichment (MPE) of isotopes was calculated as the percent of all atoms within the metabolite pool that are labeled:

$$\frac{\sum_{i=1}^n M_i \cdot i}{n}$$

where n is the number of carbon atoms in the metabolite and M_i is the relative abundance of the i^{th} mass isotopomer. Citrate MPE derived from different nutrient tracers represent the flux of labeled nutrients into cellular central carbon metabolism.

4.2.7 Isotopomer spectral analysis (ISA)

For quantification of metabolites and mass isotopomer distributions, selected ion fragments were integrated and corrected for natural isotope abundance using MATLAB-based algorithm and metabolite fragments listed in Table 4.1. Total abundances were normalized by counts of internal standard control. Isotopomer spectral analysis (ISA) for quantitation of ^{13}C contribution to lipogenic AcCoA was calculated as previously described [27]. Specifically, the relative enrichment of the lipogenic AcCoA pools from a given tracer and the percentage of newly synthesized fatty acids were estimated from a best-fit model using the INCA MFA software package [28]. The 95% confidence intervals for both parameters were determined by evaluating the sensitivity of the sum of squared residuals between measured and simulated palmitate mass isotopomer distributions to small flux variations [29].

4.2.8 Oxygen Consumption Measurement

Respiration was measured in viable hPSC-derived cardiomyocytes using a Seahorse XF96 Analyzer. HPSC-derived cardiomyocytes were assayed in fresh culture media. ATP-linked respiration was calculated as the oxygen consumption rate sensitive to 2 mg/mL oligomycin in each culture condition and normalized by cell abundance. Each culture condition sample had at least four biological replicates analyzed. Cell abundance was indicated by the total fluorescence after stained with Hoechst 33342 [30].

Table 4.1: Metabolite fragments used for GC/MS analysis.

Metabolite	m/z	Fragments for integration
α -Ketoglutarate	346	$C_{14}H_{28}O_5NSi_2$
Alanine	260	$C_{11}H_{26}O_2NSi_2$
Aspartate	418	$C_{18}H_{40}O_4NSi_3$
Lactate	261	$C_{11}H_{25}O_3Si_2$
	233	$C_{10}H_{25}O_2Si_2$
Citrate	459	$C_{20}H_{39}O_6Si_3$
Fumarate	287	$C_{12}H_{23}O_4Si_2$
Glutamate	432	$C_{19}H_{42}O_4NSi_3$
Glutamine	431	$C_{19}H_{43}O_3N_2Si_3$
Glycine	246	$C_{10}H_{24}O_2NSi_2$
Malate	419	$C_{18}H_{39}O_5Si_3$
Norvaline	288	$C_{13}H_{30}O_2NSi_2$
Proline	330	$C_{16}H_{36}O_2NSi_2$
Pyruvate	174	$C_6H_{12}O_3NSi$
Serine	390	$C_{17}H_{40}O_3NSi_3$
Succinate	289	$C_{12}H_{25}O_4Si_2$
Myristate	242	$C_{15}H_{30}O_2$
Palmitate	270	$C_{17}H_{34}O_2$
Stearate	298	$C_{19}H_{38}O_2$
Oleate	296	$C_{19}H_{36}O_2$
Cholesterol	458	$C_{33}H_{54}OSi$

4.2.9 Gene expression analysis

Total mRNA was isolated from cells using MirVana kit for RNA extraction per the manufacturer's protocol. Isolated RNA was reverse transcribed using Qiagen kit for cDNA synthesis per the manufacturer's protocol. Real-time PCR (RT-PCR) was performed using SYBR green reagent (iTaQ Universal SYBR Green Supermix) per the manufacturer's protocol. Relative expression was determined using Livak ($\Delta\Delta CT$) method with *GAPDH* as housekeeping gene. Primers used are tabulated in Table 4.2 and were taken from Harvard Primer bank [31].

Table 4.2: RT-PCR primers.

Gene	Forward Primer	Reverse Primer
<i>ACACA</i>	TCACACCTGAAGACCTTAAAGCC	AGCCACACTGCTTGTACTG
<i>ACADM</i>	GGAAGCAGATACCCAGGAAT	AGCTCCGTCACCAATTAACAT
<i>ACADV</i>	TCAGAGCATCGGTTTCAAAGG	AGGGCTCGGTTAGACAGAAAG
<i>ACLY</i>	ATCGGTTCAAGTATGCTCGGG	GACCAAGTTTTCCACGACGTT
<i>ACSL1</i>	CTTATGGGCTTCGGAGCTTTT	CAAGTAGTGCGGATCTTCGTG
<i>BCAT1</i>	AGCCCTGCTCTTTGTACTCTT	CCAGGCTCTTACATACTTGGGA
<i>BCAT2</i>	GCTCAACATGGACCGGATG	CCGCACATAGAGGCTGGTG
<i>BCKDHA</i>	CCAATGCCAACAGGGTCGT	CCGCGATACTGCTCAGAGG
<i>BCKDHB</i>	GATTTGGAATCGGAATTGCGG	CAGAGCGATAGCGATACTTGG
<i>CD36</i>	CTTTGGCTTAATGAGACTGGGAC	GCAACAAACATCACCACACCA
<i>CPT1B</i>	CCTGCTACATGGCAACTGCTA	AGAGGTGCCCAATGATGGGA
<i>FAS</i>	ACAGCGGGGAATGGGTACT	GACTGGTACAACGAGCGGAT
<i>G6PD</i>	CGAGGCCGTCACCAAGAAC	GTAGTGGTCGATGCGGTAGA
<i>GLS</i>	AGGGTCTGTTACCTAGCTTGG	ACGTTGCAATCCTGTAGATTT
<i>GLS2</i>	GGCCATGTGGATCGCATCTT	ACAGGTCTGGGTTTACTTGG
<i>LDHA</i>	TTGACCTACGTGGCTTGGAAAG	GGTAACGGAATCGGGCTGAAT
<i>LDHB</i>	CCTCAGATCGTCAAGTACAGTCC	ATCACGCGGTGTTTGGGTAAT
<i>LPL</i>	TCATTCCCGGAGTAGCAGAGT	GGCCACAAGTTTTGGCACC
<i>PDK4</i>	GGAGCATTCTCGCGCTACA	ACAGGCAATTCTTGTGCGAAA
<i>PPM1K</i>	ATAACCGCATTGATGAGCCAA	CGCACCCACATTTTCCAAG
<i>SCD</i>	GCCCCTCTACTTGAAGACGA	AAGTGATCCCATACAGGGCTC

4.2.10 Immunocytochemistry

HPSCs were harvested and resuspended in 1% (v/v) paraformaldehyde and then fixed in 90% cold methanol. Cell pellets were incubated with a 1:200 dilution of human cTnT primary mouse antibody (ThermoFisher) overnight at 4°C. The solution was removed, cell pellets washed with PBS, and incubated with a 1:1000 dilution of the secondary antibody conjugated with Alexa Fluor 488 at room temperature for 30 minutes. The cTnT+ cells were detected by BD flow cytometer. For microscopy adherent cells were fixed in 4% (v/v) paraformaldehyde. Cells were incubated with a 1:200 dilution of human cTnT primary mouse antibody for 1 hour at room temperature. The solution was removed, cells were incubated with a 1:1000 dilution of the secondary antibody conjugated with Alexa Fluor 488 at room temperature for 20 minutes. Cells were subsequently washed and incubated with DAPI nucleus staining solution at room temperature for 15 minutes. Images at 20X were captured with a Zeiss fluorescent microscope.

4.2.11 Statistical analyses

All results shown as averages of triplicates presented as mean \pm SEM unless otherwise noted. P values were calculated using a Student's two-tailed t test; *, P value between 0.01 and 0.05; **, P value between 0.001 and 0.01; ***, P value <0.001. All errors associated with ISA were 95% confidence intervals determined via confidence interval analysis. *, statistically significance indicated as non-overlapping confidence.

4.3 Results

4.3.1 Cardiac differentiation increases glucose oxidation of hPSCs

We used an established protocol to differentiate hPSCs of human embryonic stem cell H9 and human induced pluripotent stem cell IMR90iPSC into cardiac troponin T (cTnT+)

cardiomyocytes. hPSC cardiomyocytes were differentiated and maintained in chemically defined CDM3 medium (RPMI1640 containing 500 $\mu\text{g}/\text{mL}$ *O. sativa*-derived recombinant human albumin (rHA) and 213 $\mu\text{g}/\text{mL}$ L-ascorbic acid 2-phosphate) and either CHIR99021 or WntC59 to modulate Wnt/ β -catenin signaling to promote cardiac lineage specific differentiation. To obtain high purity cardiomyocyte cultures glucose was replaced with lactate for one week to select for cardiac cells. We achieved high efficiency cardiomyocyte differentiation, with over 80% cTNT+ cells after 21 days of differentiation (Figure 4.1A), which increased further upon lactate selection (Figure 4.1B). As proper metabolic function is critical for *in vitro* development of hPSC-derived cardiomyocytes, we subsequently investigated the metabolic features of cardiomyocytes continually cultured in serum free CDM3 media.

We recently applied $^{13}\text{C}/^2\text{H}$ metabolic tracing to demonstrate that hPSCs primarily fuel TCA metabolism using glutamine rather than glucose, as the latter is shunted toward lipid biosynthetic pathways under most hPSC culture conditions [32]. Here we similarly quantified how ^{13}C glucose contributed to TCA intermediates in hPSCs versus hPSC-derived cardiomyocytes. Upon terminal differentiation to the cardiac lineage we observed a significant increase in glucose oxidation within mitochondria (Figure 4.1C). Therefore, while glutamine-mediated anaplerosis is important for maintaining hPSCs in the undifferentiated state, differentiated cardiomyocytes exhibit increased mitochondrial glucose metabolism. However, the dependence on glucose oxidation to generate citrate (above 50%) also suggested that hPSC-cardiomyocytes differentiated using this approach are metabolically immature, since human adult cardiomyocytes only exhibit limited glucose contribution to TCA substrates [24, 33].

4.3.2 Nutrient consumption of hPSC-derived cardiomyocytes

Cardiac tissue is metabolically active and requires efficient nutrient consumption to meet the significant bioenergetic demands of beating cardiomyocytes (with full ATP turnover occurring over 6 times per minute) [34]. Mature cardiac cells are able to produce energy from multiple

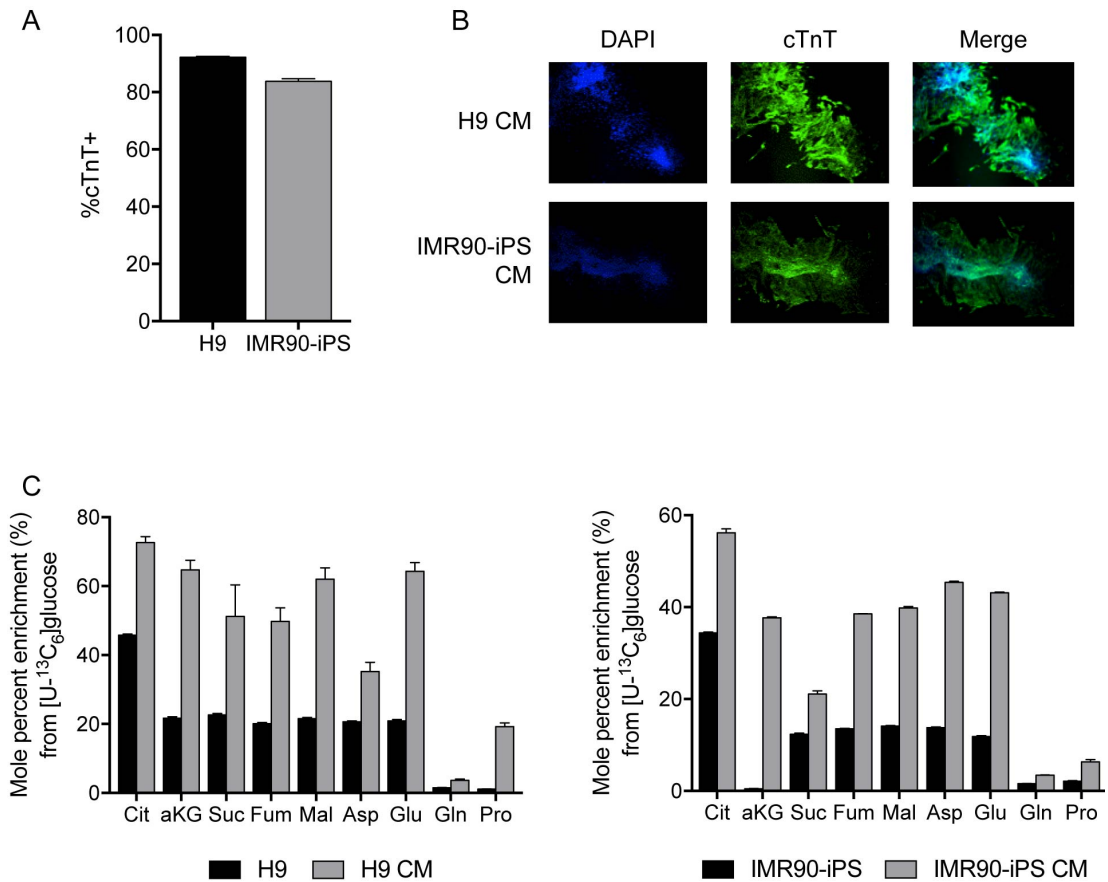


Figure 4.1: hPSC-derived cardiomyocytes primarily oxidize glucose. (A) cTnT+ flow cytometry of D21 differentiating CMs. (B) Immunofluorescent images of lactate-selected CMs. (C) Central carbon metabolite enrichment from [U-¹³C₆]glucose in undifferentiated and differentiated H9 (left) and IMR90-iPS (right) cells.

substrates, including fatty acids, glucose, lactate, pyruvate, ketone bodies and branched chain amino acids [35, 36]. As such, hPSC-derived cardiomyocyte should exhibit activation of these specific pathways upon differentiation. Importantly, the nutritional microenvironment *in vivo* is vastly different than that of *in vitro* culture conditions used for hPSC-derived cardiomyocyte differentiation, which could limit the metabolic maturation of these cells [37]. Notably, consistent with reports from *ex vivo* rat hearts, hPSC-cardiomyocytes in CDM3 media utilized glucose rather than glutamine to generate TCA intermediates (Figure 4.2A) [38].

We next evaluated whether these derivatives would efficiently consume other substrates that commonly fuel cardiac metabolism by tracing individual cultures with ^{13}C -labeled glucose, pyruvate, lactate, glutamine, leucine, β -hydroxybutyrate and palmitate tracers. We formulated CDM3 media with these nutrients to measure [^{13}C]nutrient fluxes into citrate and observed significant incorporation from most nutrients (Figure 4.2B). Notably, β -hydroxybutyrate was significant and supplanted a significant quantify of glucose flux into the TCA cycle. However, the efficiency of fatty acid oxidation was relatively low, as [^{13}C]palmitate contributed minimally to citrate in these cultures (Figure 4.2B). Since lipid oxidation is a feature of mature cardiomyocytes [39], our results suggested that hPSC-derived cardiomyocytes may genetically activate metabolic enzymes, but the further energetic activation of the metabolic pathways may be restricted.

4.3.3 Metabolic activation during hPSC cardiac differentiation

To further investigate how metabolic pathway flux and transcription changed during hPSC-derived cardiomyocyte differentiation we quantified substrate contributions to citrate and pathway-specific gene expression during the first 12 days of hPSC cardiac differentiation. Specifically, cells were maintained in CDM3 media and cells were traced with designated substrates for 24 hours prior to collection of samples for transcriptional and metabolomics analyses at designed time points (Figure 4.3). As expected in our more replete culture condition, we observed a significant decrease of glucose and glutamine consumption over time (Figure 4.3A-B). On the other

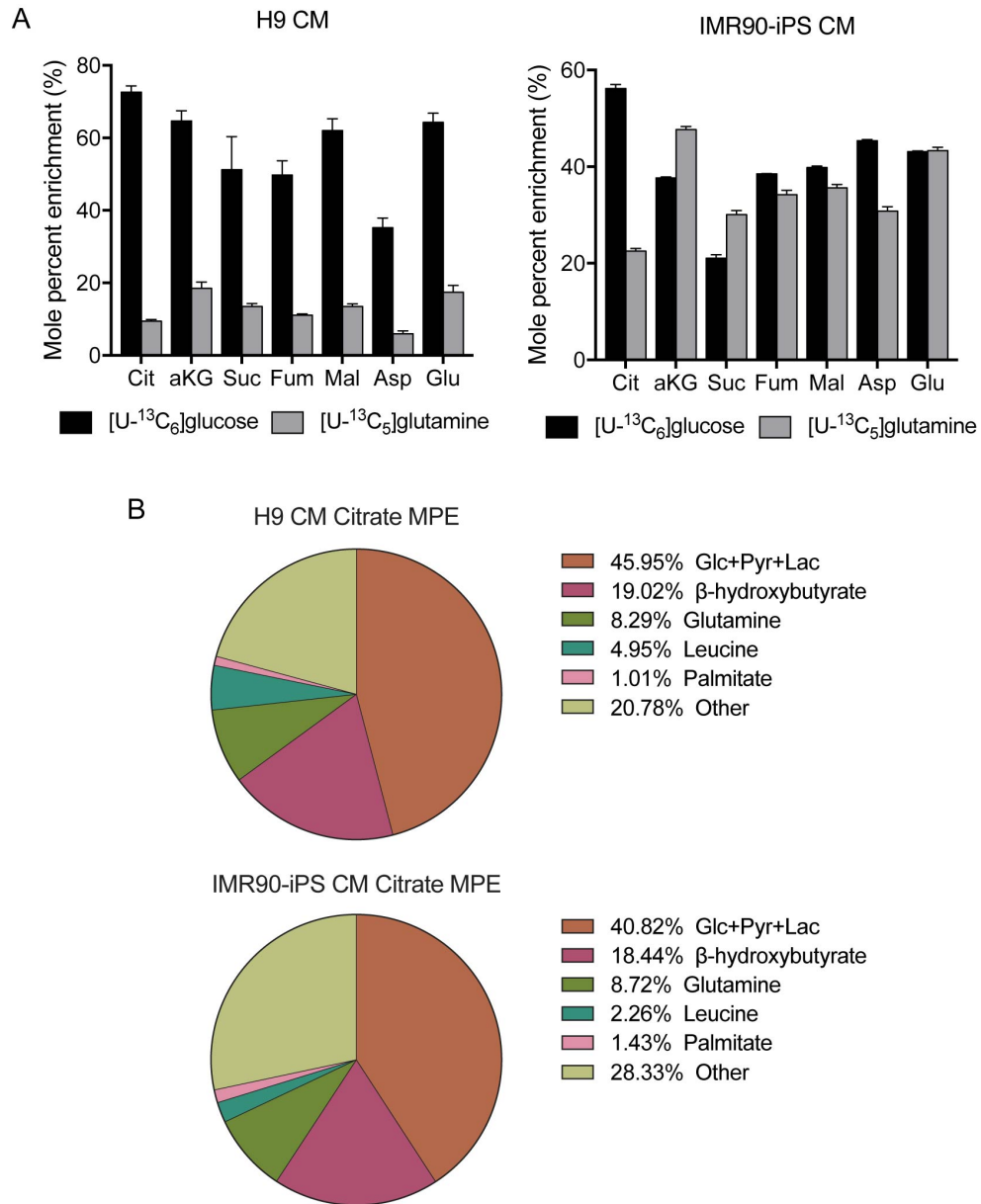
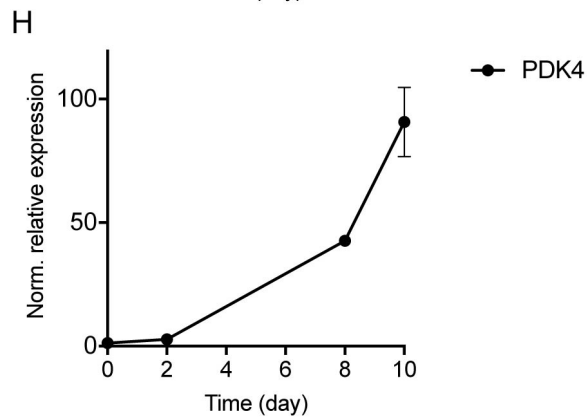
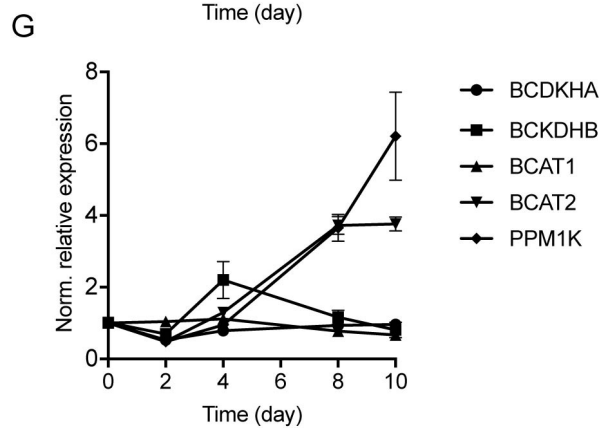
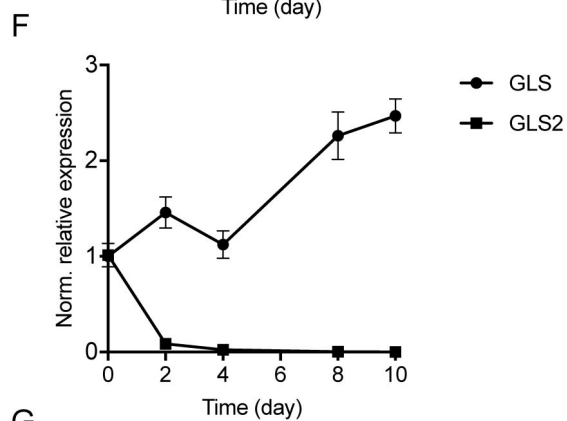
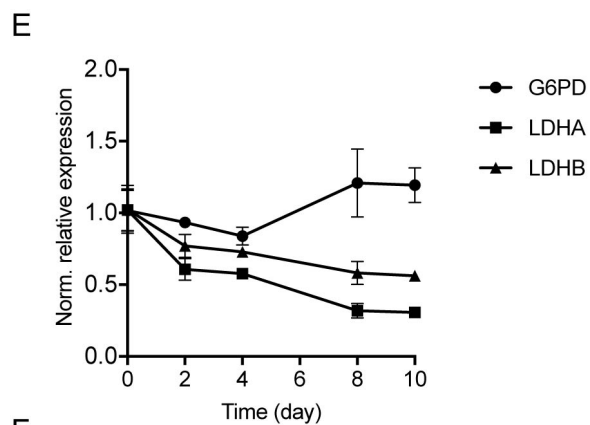
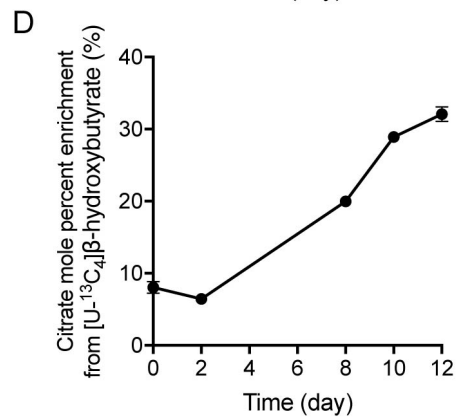
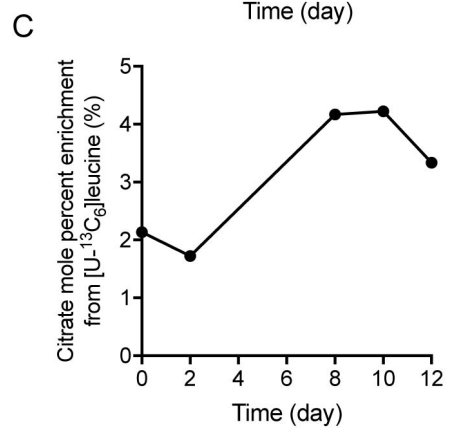
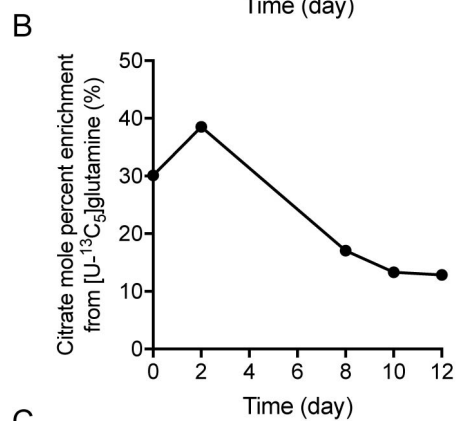
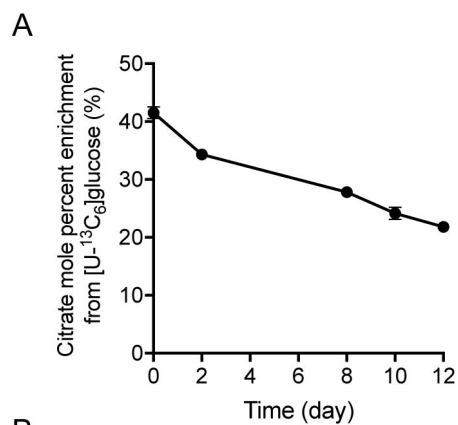


Figure 4.2: hPSC-derived cardiomyocytes are metabolically immature. (A) Central carbon metabolite enrichment from [U-¹³C₆]glucose and [U-¹³C₅]glutamine in H9-derived (left) and IMR90-iPS-derived (right) CMs. (B) Citrate mole percent enrichment from various ¹³C tracers in complex media; H9-derived (top) and IMR90-iPS-derived (bottom) CMs.

hand, differentiating hPSCs significantly increased oxidation of leucine and β -hydroxybutyrate throughout the cardiac differentiation program (Figure 4.3C-D). Consistent with the observed changes in substrate oxidation to citrate, the gene expression results showed similar trends for specific enzyme isoforms. We found expression of glycolytic enzyme LDHs significantly decreased but not the pentose phosphate pathway enzyme *G6PD* (Figure 4.3E). Although the expression level of both LDH isozymes was slightly decreased, the heart isoform *LDHB* exhibited higher levels than *LDHA* (Figure 4.3E). The glutamine consumption gene GLSs showed an isoform specific change, *GLS* gene expression increased but *GLS2* significantly dropped to extremely low level (Figure 4.3F). Importantly, our recent study comparing hPSC adapted to different nutrient conditions found *GLS2* specifically upregulated in hPSCs maintained in chemically defined media [32]. In contrast to glutamine metabolism, branched chain amino acid (BCAA) consumption showed an increased trend as leucine contribution to citrate was increased over time. Expression of enzymes involved in BCAA catabolism were upregulated with increases in mitochondrial isoform *BCAT2* but not cytosolic isoform *BCAT1* observed (Figure 4.3G). In addition, the mitochondrial phosphatase *PPMIK*, which promotes branched chain keto acid dehydrogenase complex (BCKDHC) activity through dephosphorylation, was also significantly upregulated (Figure 4.3G). Furthermore, the significant increase in β -hydroxybutyrate consumption indicated that ketone body metabolism was highly upregulated during cardiogenesis (Figure 4.3D). Comparing to the decrease of glucose oxidation (Figure 4.3A), these results suggested the lower efficiency of cells to produce acetyl-coenzyme A (AcCoA) via pyruvate dehydrogenase (PDH). Importantly, *PDK4*, which negatively regulates PDHC through phosphorylation, was highly upregulated (Figure 4.3H). All these results indicated that hPSCs during cardiac lineage specific differentiation exhibited upregulation of multiple metabolic pathway enzyme gene expressions, but the in fact metabolic contribution relied on the present of specific nutrients such as ketone bodies.

Figure 4.3: Day-by-day tracing reveals metabolic pathway activation and suppression during cardiac differentiation. Citrate mole percent enrichment from (A) [U-¹³C₆]glucose, (B) [U-¹³C₅]glutamine, (C) [U-¹³C₆]leucine, and (D) [U-¹³C₄]β-hydroxybutyrate during cardiac differentiation. Tracer added at specified day and metabolites extracted after 24 hours. (E-H) Metabolic gene expression during cardiac differentiation.



4.3.4 Changes in lipid metabolism during hPSC cardiac differentiation

We previously described high rates of *de novo* lipogenesis in hPSCs cultured in defined media, and hPSC cardiac differentiation is commonly performed in similarly defined culture media [32]. We therefore hypothesized that lipid metabolism might change significantly during cardiogenesis. We first quantified the extent of fatty acid synthesis during differentiation. We observed a dramatic decrease in *de novo* fatty acid synthesis as cells committed to the cardiac lineage (Figure 4.4A). Consistent with this observation, we also found significant less contribution of the glucose-derived AcCoA into lipid synthesis when the ketone body, β -hydroxybutyrate, is added (Figure 4.4B). This indicates differentiating hPSCs may more efficiently oxidize ketone bodies for *de novo* fatty acid synthesis, consistent with trends observed in citrate MPE (Figure 4.3A-D).

Since nutrient lipids were very limited in serum free media, hPSC highly relied on *de novo* lipid synthesis for growth and survival (Figure 4.4C), the suppression of *de novo* lipid synthesis, especially for unsaturated fatty acid oleate, would negatively affect the growth and development of cardiac differentiating hPSCs [40]. Although limited lipids were present in CDM3 media, the gene expression of enzymes involved in lipid consumption were significantly upregulated in cardiac differentiating hPSCs (Figure 4.4D). We found cardiac specific isoform *CPT1B* (the rate-limit enzyme of long-chain fatty acid β -oxidation pathway), *ACADVL* (the first step enzyme in β -oxidation), and *ACADM* (enzyme in medium fatty acid oxidation) were all significantly upregulated. At the same time, expression of the fatty acid transporter *CD36* was and *ACSL1*, which plays important role in lipid biosynthesis and degradation, also increased. In contrast, genes encoding lipogenic enzymes did not change appreciably, including *FASN*, *ACLY*, *ACACA* and *SCD*.

These results suggested that hPSC-cardiomyocytes differentiate in lipid-deficient conditions and are unable to adequately synthesize or oxidize lipids necessary for maturation or energy generation consistent with developmental studies [41]. As such, cells genetically activated

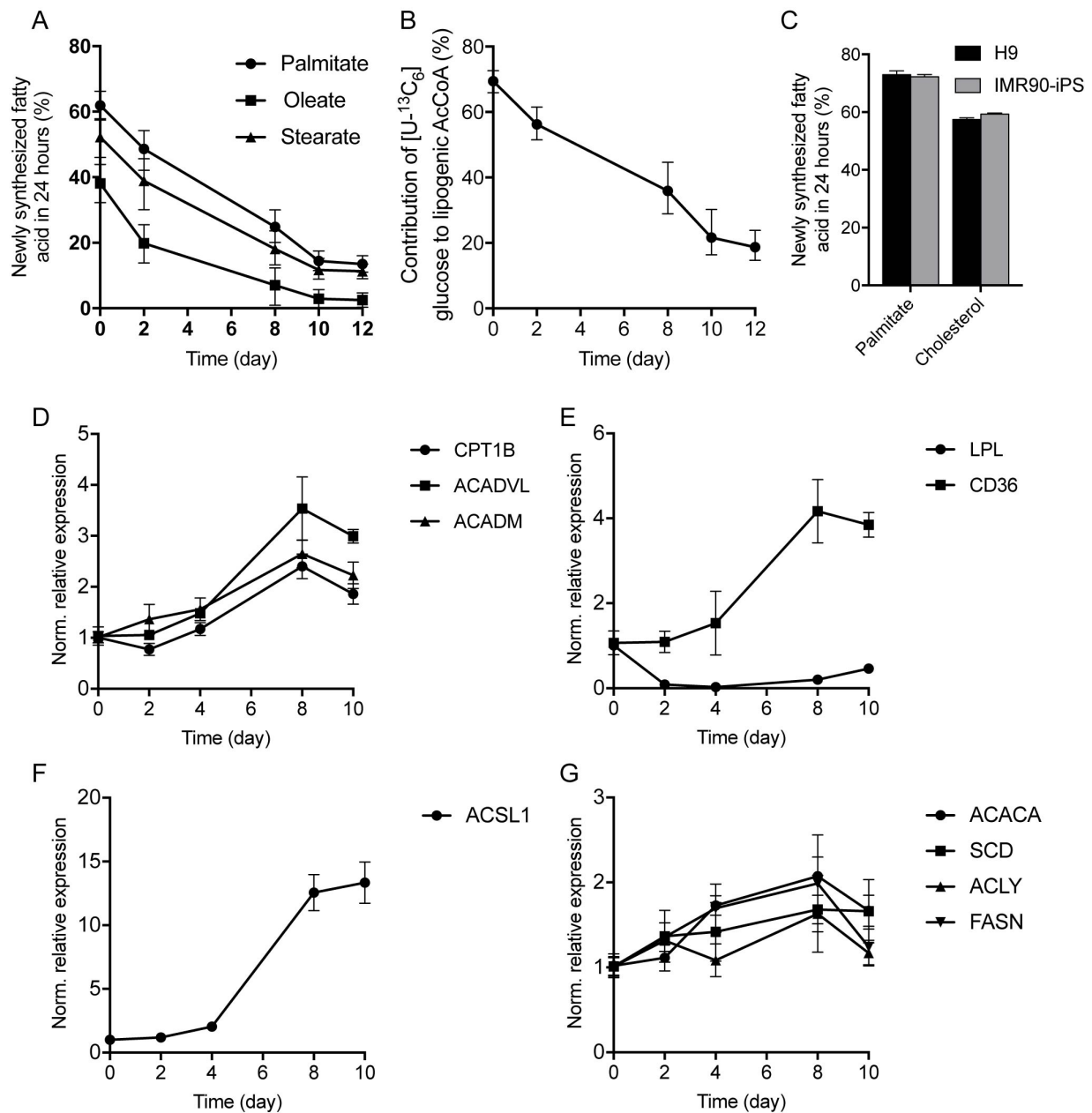


Figure 4.4: *De novo* lipogenesis is suppressed during cardiac differentiation. (A) Percent newly synthesized fatty acid in 24 hours during cardiac differentiation. (B) Contribution of [U-¹³C₆]glucose to lipogenic AcCoA during cardiac differentiation. (C) Percent newly synthesized palmitate and cholesterol in 24 hours in hPSCs. (D-G) Fatty acid synthesis and β -oxidation gene expression during cardiac differentiation.

lipid oxidation without sufficient nutrient lipid supplement from either *de novo* synthesis or extracellular uptake. Consequently, the development of hPSC-derived cardiomyocyte, especially maturation process might be artificially suppressed in serum-free CDM3 media.

4.3.5 Immature metabolic features of hPSC-derived cardiomyocytes cultured in lipid insufficient environment

To test the above hypothesis, we supplied nutrient lipid mixture AlbuMAX into hPSCs cardiac differentiating culture on day 10 of differentiation and subsequently compared the metabolic phenotypes of hPSC-derived cardiomyocytes with or without lipid addition on day 28 of differentiation. AlbuMAX is a lipid-rich bovine serum albumin comprising of a complex mixture of mostly free fatty acids [42]. We quantified the fatty acid concentrations in AlbuMAX and commonly used cell culture albumins, BSA and rHA, to determine what fatty acids were being supplied to CMs (Table 4.3). AlbuMAX supplementation provides an exogenous source of saturated, monounsaturated, and polyunsaturated fatty acids relative to albumin alone.

Table 4.3: Fatty acid concentrations in commonly used albumin media supplements. Data presented as mean \pm SD of technical triplicates (pmol/mg albumin).

	Albumax	BSA	rHA
Myristate (C14:0)	570 \pm 40	1 \pm 2	0 \pm 0
Pentadecanoate (C15:0)	200 \pm 30	0.65 \pm 0.03	0.7 \pm 0.9
Palmitate (C16:0)	6200 \pm 600	240 \pm 30	120 \pm 30
Palmitoleate (C16:1n7)	64 \pm 8	0 \pm 0	0 \pm 0
Heptadecanoate (C17:0)	360 \pm 40	9.9 \pm 0.8	0.6 \pm 0.7
Stearate (C18:0)	6500 \pm 700	240 \pm 30	38 \pm 19
Oleate (C18:1n9)	650 \pm 80	6.1 \pm 0.4	5.3 \pm 1.2

Importantly, lipid supplementation did not impact cardiomyocyte purity after differentiation (Figure 4.5A). We also observed a moderate increase of energetic oxidative phosphorylation (Figure 4.5B). As lipid accumulation and mitochondrial maturation are typical signs of cardiomyocyte development, our results demonstrated that nutrient lipids are a crucial factor to regulate

cardiomyocyte growth and promote further metabolic maturation. These results also indicated that serum free chemically defined media similar to CDM3 would be not suitable culture condition to long-term maintain and promote functional maturation of hPSC-derived cardiomyocytes *in vitro*.

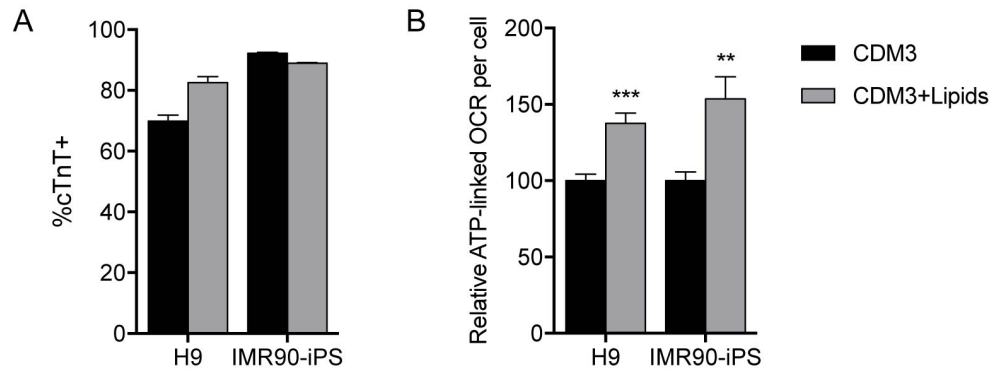


Figure 4.5: Lipid supplementation activates mitochondrial activity. (A) cTnT+ flow cytometry of CMs cultured with and without lipids. (B) Relative ATP-linked oxygen consumption for CMs cultured with and without lipids.

4.3.6 Nutrient lipids improve metabolic maturation of hPSC-derived cardiomyocytes

To further explore the metabolic impacts of lipid supplementation in cardiomyocyte cultures, we performed metabolic functional test of lipid oxidation in day 28 hPSC-derived cardiomyocytes with or without nutrient lipid supplement. We first measured the fatty acid abundance of hPSC-derived cardiomyocytes. Nutrient lipid supplement significantly enhanced cellular fatty acid levels, including both saturated and unsaturated fatty acids (Figure 4.6A). These observation were consisted with the observation of nutrient lipid contributing into hPSC-derived cardiomyocyte biomass and subcellular structure formation (Figure 4.5D). In addition, the increased saturated fatty acids also suggested the enhanced nutrient lipid uptake to fuel fatty acid oxidation, which met with the lipid metabolic enzyme gene expression found in the time-dependent metabolic pathway activation analysis (Figure 4.4D). Therefore, we applied ^{13}C -labeled glucose, glutamine, leucine, and palmitate tracers to these cultures and measured

[¹³C]nutrient fluxes into citrate. We found the nutrient lipid supplement specifically decreased the glucose oxidation and enhanced fatty acid oxidation dramatically (Figure 4.6B). Furthermore, we also used [1-¹³C]octanoate and showed short chain fatty acid oxidation also increased in the hPSC-derived cardiomyocytes cultured with nutrient lipids (Figure 4.6C). All these results suggested that nutrient lipids improve general activation of cellular fatty acid metabolism, including both biomass synthesis and energetic oxidation.

4.4 Discussion

Taken together, our study for first time comprehensively investigated the metabolic features of hPSC-derived cardiomyocytes during differentiation and maturation *in vitro*. We demonstrated that hPSC-derived cardiomyocytes are metabolically immature but possess the ability to oxidize some expected substrates (i.e. ketone bodies but not fatty acids). Examination of the metabolic state during differentiation revealed the correct phenotype of functional substrate oxidation and required enzyme expression. However, while we observed expected downregulation of *de novo* lipogenesis and upregulation of FAO enzyme expression, maintenance of DNL enzyme expression suggested a critical need for lipid synthesis. Exogenous supplementation of fatty acids and lipids improved cardiac mitochondrial activity and importantly FAO.

The pursuit of chemically-defined media for hPSC maintenance and differentiation inadvertently motivated the development of minimal medias. And while these conditions can support the generation of proper marker expression and some desired phenotypes, the lack of exogenous supplementation requires biosynthetic flux activation uncharacteristic of a somatic cell. Hallmarks of a maturing CM include rapid hypertrophy after birth, acquisition of sarcoplasmic reticulum for proper calcium handling, and maturation of mitochondrial networks, which all require increased membrane abundance and structural lipid biogenesis [43]. However, as CMs differentiate and mature, increased *CPT1B* expression requires decreased DNL to prevent malonyl-CoA-mediated

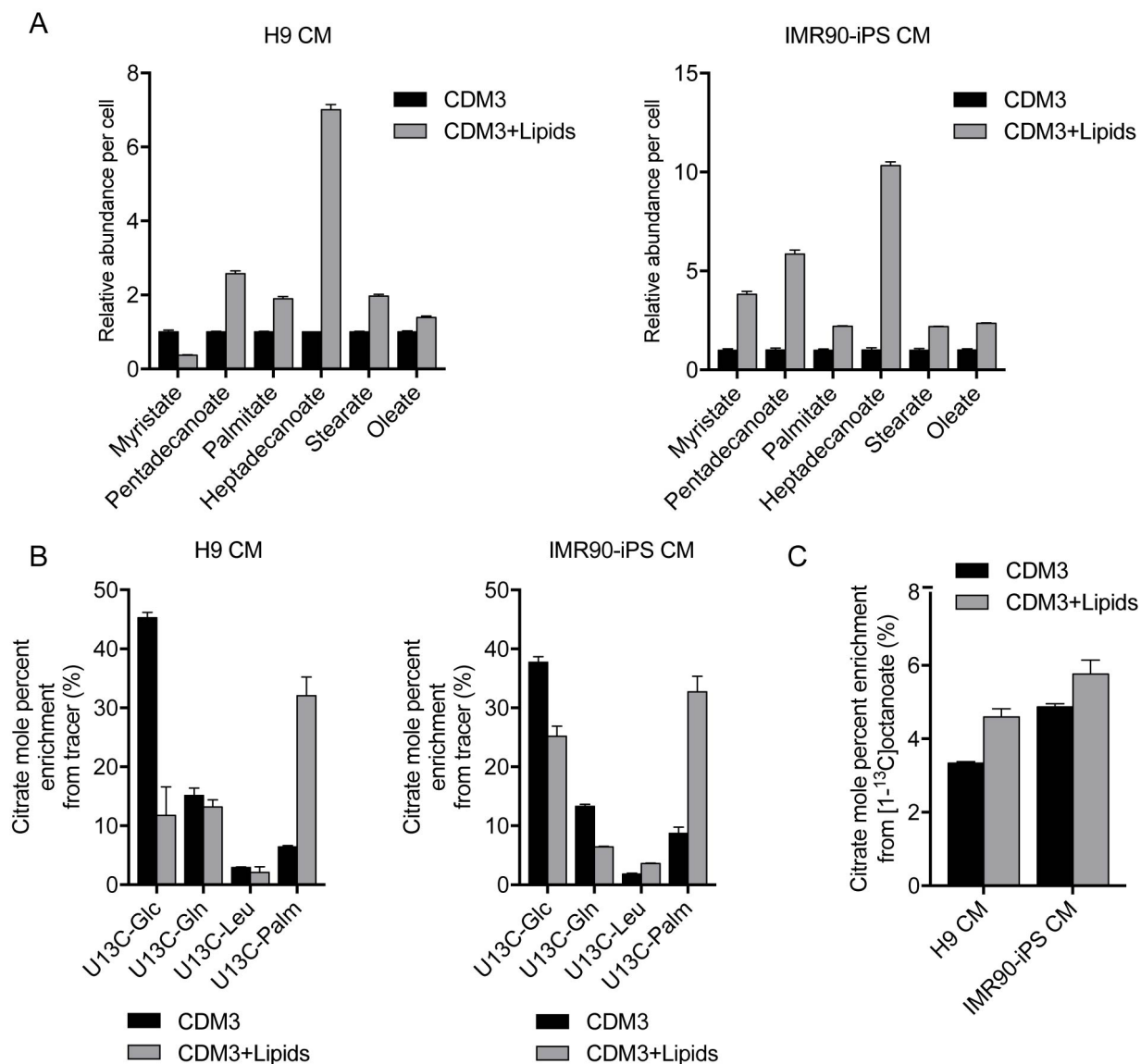


Figure 4.6: Lipid supplementation increases intracellular fatty acid availability and β -oxidation. (A) Relative intracellular fatty acid abundance per cell in H9 (left) and IMR90-iPS (right) CMs cultured with and without lipids. (B) Citrate mole percent enrichment from specific ^{13}C tracer in H9 (left) and IMR90-iPS (right) CMs. β -oxidation of fatty acids is increased when CMs are cultured with lipids. (C) Citrate mole percent enrichment from $[1-^{13}\text{C}]$ octanoate in CMs cultured with and without lipids.

suppression of FAO [44, 45]. This is exemplified in the heart by the dramatic decrease in ACC and increase in MCD activity during post-natal development [43, 46]. Therefore FAO and DNL are antagonistic processes in the maturing heart and CMs are reliant on exogenous fat sources *in vivo*. Additionally CDM3 utilized in this study lacks essential ω -3 and ω -6 fatty acids needed for proper lipid composition and cardiac function [47, 48]. These essential fatty acids are needed for cardiolipin production, important for proper mitochondrial biogenesis/fusion, and could prevent increased oxidative metabolism [49]. Again demonstrating that CMs cannot properly mature *in vitro* given nutrients supplied by gold standard media conditions.

Our approach of providing exogenous nutrients through complex, animal-derived supplements provides one potential avenue to address these issues. Other works have successfully used more replete conditions in CM differentiation through defined cocktail addition [5, 50]. Cellular physiology must guide the development of new nutrient conditions that promote desired cell performance. Metabolic flux analysis has long been used to identify industrially-relevant cellular bottlenecks [51] and now is being applied to understand alterations in hPSCs [32, 52] and cancer [37]. Metabolic requirements of non-traditional substrates to support cellular growth is an emerging concept [53, 54] and has already been used to improve cellular differentiation [55]. For example immature hPSC-derived CMs showed a preference for oxidation of β HB when supplied in our culture conditions, consistent with the pathophysiology of the heart, and should be explored as potential maturation agent [56, 57]. Indeed galactose and fatty acid supplementation has already been utilized to functional mature CMs and demonstrates the utility of these approaches [26]. These results demonstrate that environmental nutrient conditions can drive *in vitro* maturation of hPSC-derived cardiomyocytes and proper metabolic phenotypes are necessary for development.

4.5 Acknowledgements

The authors acknowledge members of the Metallo lab for technical assistance and helpful discussions. This research was supported by the California Institute of Regenerative Medicine grant (RB5-07356), National Institutes of Health grant R01CA188652, and a Searle Scholar Award to C.M.M and a NSF Graduate Research fellowship (DGE-1144086) to M.G.B. The authors declare no financial or commercial conflict of interest.

Chapter 4 is currently being prepared for submission for publication. Mehmet G. Badur, Hui Zhang, Sean Spierling, Ajit Divakaruni, Noah E. Meurs, Anne N. Murphy, and Mark Mercola are co-authors of this material. Christian M. Metallo is the corresponding author of this publication.

4.6 References

1. Ye, L., Chang, Y. H., Xiong, Q., Zhang, P., Zhang, L., Somasundaram, P., Lepley, M., Swingen, C., Su, L., Wendel, J. S., Guo, J., Jang, A., Rosenbush, D., Greder, L., Dutton, J. R., Zhang, J., Kamp, T. J., Kaufman, D. S., Ge, Y. & Zhang, J. Cardiac repair in a porcine model of acute myocardial infarction with human induced pluripotent stem cell-derived cardiovascular cells. *Cell Stem Cell* **15**, 750–61 (2014).
2. Chong, J. J., Yang, X., Don, C. W., Minami, E., Liu, Y. W., Weyers, J. J., Mahoney, W. M., Van Biber, B., Cook, S. M., Palpant, N. J., Gantz, J. A., Fugate, J. A., Muskheli, V., Gough, G. M., Vogel, K. W., Astley, C. A., Hotchkiss, C. E., Baldessari, A., Pabon, L., Reinecke, H., Gill, E. A., Nelson, V., Kiem, H. P., Laflamme, M. A. & Murry, C. E. Human embryonic-stem-cell-derived cardiomyocytes regenerate non-human primate hearts. *Nature* **510**, 273–7 (2014).
3. Takeda, M., Miyagawa, S., Fukushima, S., Saito, A., Ito, E., Harada, A., Matsuura, R., Iseoka, H., Sougawa, N., Mochizuki-Oda, N., Matsusaki, M., Akashi, M. & Sawa, Y. Development of In Vitro Drug-Induced Cardiotoxicity Assay by Using Three-Dimensional Cardiac Tissues Derived from Human Induced Pluripotent Stem Cells. *Tissue Eng Part C Methods* **24**, 56–67 (2018).
4. Matsa, E., Burridge, P. W. & Wu, J. C. Human stem cells for modeling heart disease and for drug discovery. *Sci Transl Med* **6**, 239ps6 (2014).

5. Lian, X., Hsiao, C., Wilson, G., Zhu, K., Hazeltine, L. B., Azarin, S. M., Raval, K. K., Zhang, J., Kamp, T. J. & Palecek, S. P. Robust cardiomyocyte differentiation from human pluripotent stem cells via temporal modulation of canonical Wnt signaling. *Proc Natl Acad Sci U S A* **109**, E1848–57 (2012).
6. Burridge, P. W., Matsa, E., Shukla, P., Lin, Z. C., Churko, J. M., Ebert, A. D., Lan, F., Diecke, S., Huber, B., Mordwinkin, N. M., Plews, J. R., Abilez, O. J., Cui, B., Gold, J. D. & Wu, J. C. Chemically defined generation of human cardiomyocytes. *Nat Methods* **11**, 855–60 (2014).
7. Yang, X., Pabon, L. & Murry, C. E. Engineering adolescence: maturation of human pluripotent stem cell-derived cardiomyocytes. *Circ Res* **114**, 511–23 (2014).
8. Kolanowski, T. J., Antos, C. L. & Guan, K. Making human cardiomyocytes up to date: Derivation, maturation state and perspectives. *Int J Cardiol* **241**, 379–386 (2017).
9. Liao, S. Y., Liu, Y., Siu, C. W., Zhang, Y., Lai, W. H., Au, K. W., Lee, Y. K., Chan, Y. C., Yip, P. M., Wu, E. X., Wu, Y., Lau, C. P., Li, R. A. & Tse, H. F. Proarrhythmic risk of embryonic stem cell-derived cardiomyocyte transplantation in infarcted myocardium. *Heart Rhythm* **7**, 1852–9 (2010).
10. Zhang, Y. M., Hartzell, C., Narlow, M. & Dudley S. C., J. Stem cell-derived cardiomyocytes demonstrate arrhythmic potential. *Circulation* **106**, 1294–9 (2002).
11. Lundy, S. D., Zhu, W. Z., Regnier, M. & Laflamme, M. A. Structural and functional maturation of cardiomyocytes derived from human pluripotent stem cells. *Stem Cells Dev* **22**, 1991–2002 (2013).
12. Behfar, A., Crespo-Diaz, R., Terzic, A. & Gersh, B. J. Cell therapy for cardiac repair—lessons from clinical trials. *Nat Rev Cardiol* **11**, 232–46 (2014).
13. Ronaldson-Bouchard, K., Ma, S. P., Yeager, K., Chen, T., Song, L., Sirabella, D., Morikawa, K., Teles, D., Yazawa, M. & Vunjak-Novakovic, G. Advanced maturation of human cardiac tissue grown from pluripotent stem cells. *Nature* **556**, 239–243 (2018).
14. Radisic, M., Park, H., Shing, H., Consi, T., Schoen, F. J., Langer, R., Freed, L. E. & Vunjak-Novakovic, G. Functional assembly of engineered myocardium by electrical stimulation of cardiac myocytes cultured on scaffolds. *Proc Natl Acad Sci U S A* **101**, 18129–34 (2004).
15. Nunes, S. S., Miklas, J. W., Liu, J., Aschar-Sobbi, R., Xiao, Y., Zhang, B., Jiang, J., Masse, S., Gagliardi, M., Hsieh, A., Thavandiran, N., Laflamme, M. A., Nanthakumar, K., Gross, G. J., Backx, P. H., Keller, G. & Radisic, M. Biowire: a platform for maturation of human pluripotent stem cell-derived cardiomyocytes. *Nat Methods* **10**, 781–7 (2013).

16. Ribeiro, A. J., Ang, Y. S., Fu, J. D., Rivas, R. N., Mohamed, T. M., Higgs, G. C., Srivastava, D. & Pruitt, B. L. Contractility of single cardiomyocytes differentiated from pluripotent stem cells depends on physiological shape and substrate stiffness. *Proc Natl Acad Sci U S A* **112**, 12705–10 (2015).
17. Shadrin, I. Y., Allen, B. W., Qian, Y., Jackman, C. P., Carlson, A. L., Juhas, M. E. & Bursac, N. Cardiopatch platform enables maturation and scale-up of human pluripotent stem cell-derived engineered heart tissues. *Nat Commun* **8**, 1825 (2017).
18. Ulmer, B. M., Stoehr, A., Schulze, M. L., Patel, S., Gucek, M., Mannhardt, I., Funcke, S., Murphy, E., Eschenhagen, T. & Hansen, A. Contractile Work Contributes to Maturation of Energy Metabolism in hiPSC-Derived Cardiomyocytes. *Stem Cell Reports* **10**, 834–847 (2018).
19. Tohyama, S., Hattori, F., Sano, M., Hishiki, T., Nagahata, Y., Matsuura, T., Hashimoto, H., Suzuki, T., Yamashita, H., Satoh, Y., Egashira, T., Seki, T., Muraoka, N., Yamakawa, H., Ohgino, Y., Tanaka, T., Yoichi, M., Yuasa, S., Murata, M., Suematsu, M. & Fukuda, K. Distinct metabolic flow enables large-scale purification of mouse and human pluripotent stem cell-derived cardiomyocytes. *Cell Stem Cell* **12**, 127–37 (2013).
20. Gaspar, J. A., Doss, M. X., Hengstler, J. G., Cadenas, C., Hescheler, J. & Sachinidis, A. Unique metabolic features of stem cells, cardiomyocytes, and their progenitors. *Circ Res* **114**, 1346–60 (2014).
21. Hom, J. R., Quintanilla, R. A., Hoffman, D. L., de Mesy Bentley, K. L., Molkentin, J. D., Sheu, S. S. & Porter G. A., J. The permeability transition pore controls cardiac mitochondrial maturation and myocyte differentiation. *Dev Cell* **21**, 469–78 (2011).
22. Lloyd, S. G., Wang, P., Zeng, H. & Chatham, J. C. Impact of low-flow ischemia on substrate oxidation and glycolysis in the isolated perfused rat heart. *Am J Physiol Heart Circ Physiol* **287**, H351–62 (2004).
23. Kolwicz S. C., J., Purohit, S. & Tian, R. Cardiac metabolism and its interactions with contraction, growth, and survival of cardiomyocytes. *Circ Res* **113**, 603–16 (2013).
24. Lopaschuk, G. D. & Spafford, M. A. Energy substrate utilization by isolated working hearts from newborn rabbits. *Am J Physiol* **258**, H1274–80 (1990).
25. Razeghi, P., Young, M. E., Alcorn, J. L., Moravec, C. S., Frazier, O. H. & Taegtmeier, H. Metabolic gene expression in fetal and failing human heart. *Circulation* **104**, 2923–31 (2001).

26. Correia, C., Koshkin, A., Duarte, P., Hu, D., Teixeira, A., Domian, I., Serra, M. & Alves, P. M. Distinct carbon sources affect structural and functional maturation of cardiomyocytes derived from human pluripotent stem cells. *Sci Rep* **7**, 8590 (2017).
27. Vacanti, N. M., Divakaruni, A. S., Green, C. R., Parker, S. J., Henry, R. R., Ciaraldi, T. P., Murphy, A. N. & Metallo, C. M. Regulation of substrate utilization by the mitochondrial pyruvate carrier. *Mol Cell* **56**, 425–35 (2014).
28. Young, J. D. INCA: a computational platform for isotopically non-stationary metabolic flux analysis. *Bioinformatics* **30**, 1333–5 (2014).
29. Antoniewicz, M. R., Kelleher, J. K. & Stephanopoulos, G. Determination of confidence intervals of metabolic fluxes estimated from stable isotope measurements. *Metab Eng* **8**, 324–37 (2006).
30. Divakaruni, A. S., Paradyse, A., Ferrick, D. A., Murphy, A. N. & Jastroch, M. Analysis and interpretation of microplate-based oxygen consumption and pH data. *Methods Enzymol* **547**, 309–54 (2014).
31. Wang, X., Spandidos, A., Wang, H. & Seed, B. PrimerBank: a PCR primer database for quantitative gene expression analysis, 2012 update. *Nucleic Acids Res* **40**, D1144–9 (2012).
32. Zhang, H., Badur, M. G., Divakaruni, A. S., Parker, S. J., Jager, C., Hiller, K., Murphy, A. N. & Metallo, C. M. Distinct Metabolic States Can Support Self-Renewal and Lipogenesis in Human Pluripotent Stem Cells under Different Culture Conditions. *Cell Rep* **16**, 1536–1547 (2016).
33. Lopaschuk, G. D., Spafford, M. A. & Marsh, D. R. Glycolysis is predominant source of myocardial ATP production immediately after birth. *Am J Physiol* **261**, H1698–705 (1991).
34. Jacobus, W. E. Respiratory control and the integration of heart high-energy phosphate metabolism by mitochondrial creatine kinase. *Annu Rev Physiol* **47**, 707–25 (1985).
35. Li, T., Zhang, Z., Kolwicz S. C., J., Abell, L., Roe, N. D., Kim, M., Zhou, B., Cao, Y., Ritterhoff, J., Gu, H., Raftery, D., Sun, H. & Tian, R. Defective Branched-Chain Amino Acid Catabolism Disrupts Glucose Metabolism and Sensitizes the Heart to Ischemia-Reperfusion Injury. *Cell Metab* **25**, 374–385 (2017).
36. Bartelds, B., Gratama, J. W., Knoester, H., Takens, J., Smid, G. B., Aarnoudse, J. G., Heymans, H. S. & Kuipers, J. R. Perinatal changes in myocardial supply and flux of fatty acids, carbohydrates, and ketone bodies in lambs. *Am J Physiol* **274**, H1962–9 (1998).
37. Cantor, J. R., Abu-Remaileh, M., Kanarek, N., Freinkman, E., Gao, X., Louissaint A., J., Lewis, C. A. & Sabatini, D. M. Physiologic Medium Rewires Cellular Metabolism and

- Reveals Uric Acid as an Endogenous Inhibitor of UMP Synthase. *Cell* **169**, 258–272 e17 (2017).
38. Lauzier, B., Vaillant, F., Merlen, C., Gelinas, R., Bouchard, B., Rivard, M. E., Labarthe, F., Dolinsky, V. W., Dyck, J. R., Allen, B. G., Chatham, J. C. & Des Rosiers, C. Metabolic effects of glutamine on the heart: anaplerosis versus the hexosamine biosynthetic pathway. *J Mol Cell Cardiol* **55**, 92–100 (2013).
 39. Khairallah, M., Labarthe, F., Bouchard, B., Danialou, G., Petrof, B. J. & Des Rosiers, C. Profiling substrate fluxes in the isolated working mouse heart using ¹³C-labeled substrates: focusing on the origin and fate of pyruvate and citrate carbons. *Am J Physiol Heart Circ Physiol* **286**, H1461–70 (2004).
 40. Ben-David, U., Gan, Q. F., Golan-Lev, T., Arora, P., Yanuka, O., Oren, Y. S., Leikin-Frenkel, A., Graf, M., Garippa, R., Boehringer, M., Gromo, G. & Benvenisty, N. Selective elimination of human pluripotent stem cells by an oleate synthesis inhibitor discovered in a high-throughput screen. *Cell Stem Cell* **12**, 167–79 (2013).
 41. Joshi, V. C. & Sidbury J. B., J. Fatty acid synthesis in chick embryonic heart and liver during development. *Dev Biol* **42**, 282–71 (1975).
 42. Garcia-Gonzalo, F. R. & Izpisua Belmonte, J. C. Albumin-associated lipids regulate human embryonic stem cell self-renewal. *PLoS One* **3**, e1384 (2008).
 43. Lopaschuk, G. D. & Jaswal, J. S. Energy metabolic phenotype of the cardiomyocyte during development, differentiation, and postnatal maturation. *J Cardiovasc Pharmacol* **56**, 130–40 (2010).
 44. Saggerson, D. Malonyl-CoA, a key signaling molecule in mammalian cells. *Annu Rev Nutr* **28**, 253–72 (2008).
 45. Van Weeghel, M., Abdurrachim, D., Nederlof, R., Argmann, C. A., Houtkooper, R. H., Hagen, J., Nabben, M., Denis, S., Ciapaite, J., Kolwicz S. C., J., Lopaschuk, G. D., Auwerx, J., Nicolay, K., Des Rosiers, C., Wanders, R. J., Zuurbier, C. J., Prompers, J. J. & Houten, S. M. Increased cardiac fatty acid oxidation in a mouse model with decreased malonyl-CoA sensitivity of CPT1B. *Cardiovasc Res* (2018).
 46. Reszko, A. E., Kasumov, T., David, F., Thomas, K. R., Jobbins, K. A., Cheng, J. F., Lopaschuk, G. D., Dyck, J. R., Diaz, M., Des Rosiers, C., Stanley, W. C. & Brunengraber, H. Regulation of malonyl-CoA concentration and turnover in the normal heart. *J Biol Chem* **279**, 34298–301 (2004).

47. Duda, M. K., O'Shea, K. M. & Stanley, W. C. omega-3 polyunsaturated fatty acid supplementation for the treatment of heart failure: mechanisms and clinical potential. *Cardiovasc Res* **84**, 33–41 (2009).
48. Spector, A. A. & Yorek, M. A. Membrane lipid composition and cellular function. *J Lipid Res* **26**, 1015–35 (1985).
49. Paradies, G., Paradies, V., De Benedictis, V., Ruggiero, F. M. & Petrosillo, G. Functional role of cardiolipin in mitochondrial bioenergetics. *Biochim Biophys Acta* **1837**, 408–17 (2014).
50. Pei, F., Jiang, J., Bai, S., Cao, H., Tian, L., Zhao, Y., Yang, C., Dong, H. & Ma, Y. Chemical-defined and albumin-free generation of human atrial and ventricular myocytes from human pluripotent stem cells. *Stem Cell Res* **19**, 94–103 (2017).
51. Long, C. P., Gonzalez, J. E., Feist, A. M., Palsson, B. O. & Antoniewicz, M. R. Dissecting the genetic and metabolic mechanisms of adaptation to the knockout of a major metabolic enzyme in *Escherichia coli*. *Proc Natl Acad Sci U S A* **115**, 222–227 (2018).
52. Badur, M. G., Zhang, H. & Metallo, C. M. Enzymatic passaging of human embryonic stem cells alters central carbon metabolism and glycan abundance. *Biotechnol J* **10**, 1600–11 (2015).
53. Pavlova, N. N., Hui, S., Ghergurovich, J. M., Fan, J., Intlekofer, A. M., White, R. M., Rabinowitz, J. D., Thompson, C. B. & Zhang, J. As Extracellular Glutamine Levels Decline, Asparagine Becomes an Essential Amino Acid. *Cell Metab* **27**, 428–438 e5 (2018).
54. Sousa, C. M., Biancur, D. E., Wang, X., Halbrook, C. J., Sherman, M. H., Zhang, L., Kremer, D., Hwang, R. F., Witkiewicz, A. K., Ying, H., Asara, J. M., Evans, R. M., Cantley, L. C., Lyssiotis, C. A. & Kimmelman, A. C. Pancreatic stellate cells support tumour metabolism through autophagic alanine secretion. *Nature* **536**, 479–83 (2016).
55. Beyer, B. A., Fang, M., Sadrian, B., Montenegro-Burke, J. R., Plaisted, W. C., Kok, B. P. C., Saez, E., Kondo, T., Siuzdak, G. & Lairson, L. L. Metabolomics-based discovery of a metabolite that enhances oligodendrocyte maturation. *Nat Chem Biol* **14**, 22–28 (2018).
56. Nagao, M., Toh, R., Irino, Y., Mori, T., Nakajima, H., Hara, T., Honjo, T., Satomi-Kobayashi, S., Shinke, T., Tanaka, H., Ishida, T. & Hirata, K. beta-Hydroxybutyrate elevation as a compensatory response against oxidative stress in cardiomyocytes. *Biochem Biophys Res Commun* **475**, 322–8 (2016).
57. Gormsen, L. C., Svart, M., Thomsen, H. H., Sondergaard, E., Vendelbo, M. H., Christensen, N., Tolbod, L. P., Harms, H. J., Nielsen, R., Wiggers, H., Jessen, N., Hansen, J., Botker,

H. E. & Moller, N. Ketone Body Infusion With 3-Hydroxybutyrate Reduces Myocardial Glucose Uptake and Increases Blood Flow in Humans: A Positron Emission Tomography Study. *J Am Heart Assoc* **6** (2017).

Chapter 5

Combinatorial CRISPR-Cas9 metabolic screens reveal critical redox control points dependent on the KEAP1-NRF2 regulatory axis

5.1 Abstract

The metabolic pathways fueling tumor growth have been well characterized, but the specific impact of transforming events on network topology and enzyme essentiality remains poorly understood. To this end, we performed combinatorial CRISPR-Cas9 screens on a set of 51 carbohydrate metabolism genes that represent glycolysis and the pentose phosphate pathway. This high-throughput methodology enabled systems-level interrogation of metabolic gene dispensability, interactions, and compensation across multiple cell types. The metabolic impact of specific combinatorial knockouts were validated using ^{13}C and ^2H isotope tracing, and, these assays together revealed key nodes controlling redox homeostasis along the *KEAP1-NRF2* signaling axis.

Specifically, targeting *KEAP1* in combination with oxidative PPP enzymes mitigated the deleterious effects of these knockouts on growth rates. These results demonstrate how our integrated framework, combining genetic, transcriptomic, and flux measurements, can improve elucidation of metabolic network alterations, and guide precision targeting of metabolic vulnerabilities based on tumor genetics.

5.2 Introduction

Cancer cells are characterized by unchecked cellular proliferation and the ability to move into distant cellular niches, requiring a rewiring of metabolism to increase biosynthesis and maintain redox homeostasis. This reprogramming of cellular metabolism is now considered an essential hallmark of tumorigenesis [1]. Since the metabolic network is highly redundant at the isozyme and pathway-levels, reprogramming is an emergent behavior of the network and manifests itself in non-obvious ways. For instance, a unique metabolic feature of tumor cells is a reliance on aerobic glycolysis to satisfy biosynthetic and ATP demands [2]. This metabolic rewiring is coordinated, in part, by the selective expression of distinct isozymes, which may benefit the cell by offering different kinetics or modes of regulation [3–5]. However, isozyme switching is not solely a consequence of genomic instability and instead can be a coordinated step in tumorigenesis that facilitates cancer cell growth and survival [6, 7]. Therefore, understanding which isozymes and pathway branch points are important and how they interact with and compensate for one another is necessary to effectively target metabolism in cancer cells.

In this regard, the advent of CRISPR screening technology now provides a rapid, high-throughput means to functionally characterize large gene sets [8, 9]. This analysis has led to greater annotation of essential genes in human cancers and context-dependent dispensability [10, 11]. Correspondingly, single-gene knockout (SKO) CRISPR screens have been able to identify important genes in redox homeostasis and oxidative phosphorylation in conjunction

with metabolic perturbations [12, 13]. However, in the context of mammalian metabolism the SKO CRISPR approach comes with limitations, as redundancies and plasticity of the metabolic network may allow the system to remodel around a SKO, thereby confounding analyses of impact on cellular fitness. To overcome this challenge, our group and others recently developed combinatorial gene knockout screening approaches which may provide a more suitable platform to study gene dispensability and also systematically map their interactions [14–18].

Utilizing this combinatorial CRISPR genetic screening format, coupled with interrogation of metabolic fluxes, we systematically studied the dispensability and interactions within a set of genes encoding enzymes involved in carbohydrate metabolism, including glycolysis and the pentose phosphate pathway. We illustrated functional relationships between dominant and minor isozymes in various families and discovered multiple genetic interactions within and across glucose catabolic pathways. Aldolase and enzymes in the oxidative pentose phosphate pathway (oxPPP) emerged as critical drivers of fitness in two cancer cell lines, HeLa and A549. Distinctions in this dependence are influenced by the *KEAP1-NRF2* signaling axis, which coordinates the cellular antioxidant pathway in response to redox stress. We found loss or mutation of *KEAP1* E3-ubiquitin ligase upregulates *NRF2*-mediated transcription of genes involved in glutathione synthesis and NADPH regeneration, making the oxPPP less important for NADPH production and less critical for cell growth in these contexts. Thus, mutation status of the *KEAP1-NRF2* regulatory axis should be considered when designing therapeutic strategies that target redox pathways in cancer cells.

5.3 Materials and Methods

5.3.1 Cell lines and culture conditions

HEK293T, A549, HeLa-AAVS-Cas9-Hygro, A549-AAVS-Cas9-Hygro cells were grown in DMEM supplemented with 10% FBS, 2 mM L-glutamine, 100 units/mL of penicillin, 100

$\mu\text{g/mL}$ of streptomycin, and $0.25 \mu\text{g/mL}$ of Amphotericin B. HeLa-AAVS-Cas9-Hygro and A549-AAVS-Cas9-Hygro cells were purchased from GeneCopoeia.

5.3.2 Dual-gRNA library design and cloning

A set of 51 genes, encompassing glycolysis, gluconeogenesis, pentose phosphate pathway, and glucose entry into the TCA cycle were selected for this study. Three unique 20-bp sgRNAs were designed for each target gene and three scrambled, non-targeting sequence absent from the genome were used as control. The dual sgRNA construct library comprised all pairwise gRNA combinations between either two genes or a gene and a scramble, resulting in 11,475 double-gene-knockout constructs and 459 single-gene-knockout constructs. The dual-gRNA library was generated as previously described (Figure S5.1A) [17]. Briefly, the oligonucleotides with dual-gRNA spacers were synthesized by CustomArray Inc., amplified and assembled into the LentiGuide-Puro vector (Addgene 52963). Independent bacterial clones obtained in step I library were counted to ensure 50x library coverage. Subsequently, the step I library was digested by BsmBI and an insert contained a gRNA scaffold and a mouse U6 promoter were cloned in the middle of two spacers. Again, 50x library coverage was ensured.

5.3.3 Lentivirus production

One 15cm dish of HEK293T cells at 60% confluent were transfected with $3 \mu\text{g}$ PMD2.G, $12 \mu\text{g}$ of lenti-gag/pol/PCMV8.2, and $9 \mu\text{g}$ of lentiviral vector (library or single constructs) using $36 \mu\text{l}$ of Lipofectamine 2000. Medium containing viral particles were harvested 48 hrs and 72 hrs after transfection, then concentrated with Centricon Plus-20 100,000 NMWL centrifugal ultrafilters, divided into aliquots and frozen at -80°C .

5.3.4 CRISPR/Cas9 dual-gRNA screening

CRISPR Cas9 nuclease stable expressing HeLa and A549 cells were obtained from GeneCopoeia and grown in DMEM medium with 10% FBS and Antibiotic-Antimycotic. Hygromycin B was added at the concentrations of 200 $\mu\text{g/ml}$ or 100 $\mu\text{g/ml}$ for HeLa and A549 cells, respectively. For each screen, cells were seeded in three 15cm dishes at a density of 1×10^7 per ml and transduced with the lentiviral dual gRNA library at a low MOI of 0.1-0.3. Puromycin was added at 48 h after transduction at a concentration of 5 $\mu\text{g/ml}$. Then the cells were cultured and passaged for every 3-4 days while 1×10^7 cells were sampled at days 3, 14, 21 and 28 and stored at -80°C until extraction of genomic DNA. Two biological replicates of the screens were performed for each cell line.

5.3.5 Quantification of dual gRNAs abundance

Genomic DNA of the cells were purified using Qiagen DNeasy Blood and Tissue Kits. To amplify the dual gRNAs from each sample, we used 20 μg of genomic DNA as template across ten 50 μL PCR reactions with Kapa Hifi polymerase. By testing the amplification efficiency, we used 22 - 24 cycles at an annealing temperature of 55°C with the following primers:

Forward: ACACTCTTTCCCTACACGACGCTCTTCCGATCTTATATATCTTGTGGAA-AGGACGAAACACCG;

Reverse: GACTGGAGTTCAGACGTGTGCTCTTCCGATCTCCTTATTTTAACTTGC-TATTTCTAGCTCTA.

The amplicons were pooled and purified with Agencourt AMPure XP bead at a double selection of 0.55x and then 0.8x. The samples were quantified with Qubit dsDNA High Sensitivity Kit. To attach Illumina sequencing adaptors and indexes, we used 50 ng of purified step I PCR product as template across four 50- μL PCR reactions with Kapa Hifi polymerase using primers of Next Multiplex Oligos for Illumina (New England Biosciences). 7 or 8 PCR cycles were carried

out at an annealing temperature of 72 °C. The PCR product were purified twice with Agencourt AMPure XP bead at 0.8x ratio, quantified, pooled and sequenced on an Illumina HiSeq rapid-run mode for 75 cycles paired-end runs.

5.3.6 Computation of single and double gene knockout fitness and genetic interaction scores

Analysis was performed with a previously reported software pipeline constructed from Python, R and Jupyter Notebooks (<https://github.com/ucsd-ccbb/mali-dual-crispr-pipeline>). The following details are adapted from our published paper [17]. Briefly, the two gRNA sequences were extracted and trimmed to 19bp from 3' end, and then aligned to the known library sequences with one mismatch allowed. We determined a minimum threshold for read counts based on the histograms and masked out pairwise gRNA constructs that have read counts below the threshold. The read counts were used for analysis of fitness and genetic interaction scores as follows:

1. *Estimation of fitness of each pairwise gRNA construct.* The logarithmic transformation of the frequency of each pairwise gRNA construct in the population is:

$$x_c = \log_2 \frac{N_c}{\sum_c N_c}$$

where N_c is the number of cells in the population expressing construct c . We assume that each cell subpopulation grows exponentially:

$$N_c(t) = N_c(0)x2^{(f_c+f_0)t}$$

where t is a given time point; f_c is the fitness of construct c ; f_0 is the absolute fitness of

reference cells which don't express any constructs. Combining these two equations, we get:

$$x_c(t) = a_c + f_c t - \log_2 \sum_c 2^{a_c + f_c t}$$

where $a_c \equiv x_c(0)$ as the initial condition and $\sum_c 2^{x_c} = 1$ in the whole population. Fitting to this equation from experimental data of frequencies $X_c(t)$, we minimize the sum of squares:

$$E(a_c, f_c) = \sum_c \sum_t [X_c(t) - x_c(t)]^2$$

Here E is invariant under the substitution $f_c \rightarrow f_c + \delta$, where δ is an arbitrary constant, which can be fixed by setting the mean non-targeting gRNA fitness to zero. To resolve this, one should find the minimum of the function:

$$E_\lambda \equiv E - \lambda (\sum_c 2^{a_c} - 1)$$

where λ is the Lagrange multiplier. This solution equals:

$$\frac{\partial E_\lambda}{\partial a_c} = \frac{\partial E_\lambda}{\partial f_c} = \frac{\partial E_\lambda}{\partial \lambda} = 0$$

When the number of constructs is large, $\sum_c 1 \gg 1$, the approximation solution is:

$$f_c = \frac{\text{Cov}(X_c, t)}{\text{Var}(t)} + \delta$$

and

$$a_c = \bar{X}_c - f_c \bar{t} - \log_2 \sum_c 2^{\bar{X}_c - f_c \bar{t}}$$

where the bars indicate means over time points. The a_c values do not depend on the choice of δ .

2. *Estimation of single gRNA fitness and gRNA-gRNA interactions.* For each construct containing gRNAs g and g' , we define:

$$f_c = f_g + f_{g'} + \pi_{gg'}$$

where $\pi_{gg'}$ is the gRNA-gRNA interaction scores. f_c is calculated from step (1). f_g values are found by robust fitting of this equation. The gRNA-level $\pi_{gg'}$ scores are the residuals of the robust fit.

3. *Computation of gene level fitness based on weighted average of gRNA fitness.* We ranked the three gRNAs targeting to the same gene as $r(g) \in 0, 1, 2$ in ascending order of $|f_g|$. The gene-level fitness values are calculated as the weighted means of gRNA fitness values with weights given by the squares of gRNA ranks, $r^2(g)$. The gene-level interaction scores are calculated as the weighted means of gRNA-gRNA interaction scores with weights given by the products of gRNA ranks, $r(g)r(g')$.
4. *Correction by replicates.* As we performed biological replicates for each experiment, we combine replicates for more power rather than looking for two f_c separately. We fit a single optimal f_c from all data points excludes those below the threshold, with the assumption that f_c does not change across experiments while the initial conditions a_c may be different. The raw P value associate to each f_c is:

$$t_c = \frac{f_c}{SE(f_c)}$$

where $SE(f_c)$ is the standard error of f_c :

$$SE(f_c) = \frac{\sqrt{\sum_t [X_c(t) - x_c(t)]^2}}{\sqrt{(n_c - 2) \sum_t (t^2 - \bar{t}^2)}}$$

The raw P values then are transformed into posterior probabilities, PP_c , according to the

theory of Storey. To scale the genetic interaction scores for comparison across different experiments, we calculated a genetic interaction z score by dividing the $\pi_{gg'}$ of each two genes by $s.d. = \sqrt{n-2}SE(f_c)$ of genetic interaction pairs in a given experiment. We consider an interaction to be a meaningful candidate if it has an absolute z score above 3.

5. *Calculation of false discovery rates by numerical Bayesian ensemble of experiments.* We assign a fitness value to each construct c on the basis of change in fitness relative to the standard deviation of repeated measurements. The assigned value is either 0 with probability $(1 - PP_c)$, or a random number within $\bar{f}_c \pm s.d.$ We perform 1000 permutations and reported gene level f_g and $\pi_{gg'}$ for each permutation. The false discovery rate (FDR) of genetic interactions (π) is calculated as the odds ratio between the observed and permuted results in the null model, which is obtained by mean-centering of the marginal distribution of every $\pi_{gg'}$.

5.3.7 Single-gRNA construct cloning

The LentiGuide-Puro vector were linearized using restriction enzyme BsmBI at 55°C for 3 hours. For each individual gRNA, two oligonucleotides containing the spacer sequences were synthesized as listed in Supplemental Table S1 in [19]. The two oligos were annealed and extended to make a double stranded DNA fragment using Kapa Hifi polymerase. The fragment was purified and subjected to Gibson assembly (New England Biolabs) with the linearized LentiGuide-Puro vector.

5.3.8 Competitive cell growth assay

We developed a competitive cell growth assay to assess the effect of gene perturbations by mixing control tdTomato+ cells with tdTomato- cells expressing a gRNA of interest (Figure 5.3A) and sampling relative growth rates through time by flow cytometry. Cas9-expressing cells

were transduced with EF1A- tdTomato-T2A-puromycin lentivirus and cultured under puromycin selection for stable expression of tdTomato. To measure the negative impact of a gRNA introduced gene perturbation on the cellular proliferation rate, the Cas9-expressing cells were cultured in 12-well-plate and transduced with gRNA lentivirus at a high MOI (>5) . The day after transduction, the Cas9-expressing cells were resuspended, counted, mixed with tdTomato+ Cas9-expressing cells, and re-seed into 12-well-plate. The cells were sampled every 3 or 4 days to score the tdTomato+/tdTomato- ratio by longitudinal flow cytometric analysis. By assuming the exponential growth of the cells, from time t_1 to t_2 , the growth of cells (tdTomato+ or gRNA expressing) in the mixture population fits to the equation:

$$N_C(t_2) = N_C(t_1) \times 2^{(f_0 + \Delta f_c)(t_2 - t_1)}$$

where N_c is the cell number of the certain cell subtype, f_0 is the absolute fitness of reference cells which in this case is the tdTomato+ cells, and Δf_c is fitness measurements of the certain cell subtype. For a certain gRNA (or a pair of gRNA), the Δf_{gRNA} is able to be calculated easily according to the equation without measuring the absolutely fitness of reference cells f_0 :

$$\frac{N_{gRNA}(t_2)}{N_0(t_2)} = \frac{N_c(t_1) \times 2^{(f_0 + \Delta f_{gRNA})(t_2 - t_1)}}{N_0(t_1) \times 2^{(f_0)(t_2 - t_1)}}$$

Although the percentage of tdTomato+ cells in the mixtures with the cells expressing non-targeting control gRNAs was stable over time, we normalize the fitness of gRNA of interest to non-targeting control gRNAs for side by side comparisons. The cell viability of a gRNA of interest (non-log transformed fitness) relative to non-targeting controls showed in Figure 5.3 is as follows:

$$F_{gRNA} = \frac{2^{(\Delta f_{gRNA})(t_2 - t_1)}}{2^{(\Delta f_{gNTC})(t_2 - t_1)}} \times 100\%$$

The expected cell viability of a pair of gRNAs calculated according to:

$$F_{gRNA1,gRNA2} = F_{gRNA1} \times F_{gRNA2}$$

In addition, f_0 is able to be measured by counting of the absolute cell number over time base on the equation (1). Then the effects of a gene perturbation (eg. *PGD*) relative to non-targeting controls (NTC) in a certain cell subtype (eg. *KEAP1* mutations) are calculable as follows:

$$R_{PGD,KEAP1} = \frac{(f_0 + \Delta f_{PGD,KEAP1}) - (f_0 + \Delta f_{NTC,KEAP1})}{f_0 + \Delta f_{PGD,KEAP1}}$$

5.3.9 RNA sequencing data analysis

RNA sequencing data were obtained from the ENCODE project (GSE30567, sample GSM765402 and GSM758564 for HeLa and A549 cell lines respectively). The results were expressed as the average value of reads per kilobase of transcript per million mapped reads (RPKM) across two biological replicates. The average RPKM values were log2 transformed for Pearson correlation analysis.

5.3.10 Stable isotope tracing

For isotopic labeling experiments, cells were cultured in glucose- and glutamine-free media (Gibco) supplemented with 10% dialyzed FBS, 100 U/mL penicillin/streptomycin, 4mM glutamine (Sigma), and 20 mM of either [3-²H]glucose (98%, Cambridge Isotope Laboratories), [U-¹³C₆]glucose (99%, Cambridge Isotope Laboratories), or [1,2-¹³C]glucose (99%, Cambridge Isotope Laboratories).

Cells were rinsed with PBS before addition of tracing media. For glycolytic measurements, basal media was changed 1hr before addition of tracer media and extracted at indicated time intervals. For measurement of shunting through oxPPP, cells were traced for 4hrs. For estimation

of PGD contribution to cytosolic NADPH, cells were traced for 48hrs.

5.3.11 Metabolite Extraction and GC-MS Analysis

Cells were rinsed with 0.9% (w/v) saline and 250 μ L of -80°C MeOH was added to quench metabolic reactions. 100 μ L of ice-cold water supplemented with 10 $\mu\text{g/mL}$ norvaline was then added to each well and cells were collected by scraping. The lysate was moved to a fresh 1.5 mL eppendorf tube and 250 μ L of -20°C chloroform supplemented with 4 $\mu\text{g/mL}$ D31 palmitate was added. After vortexing and centrifugation, the top aqueous layer and bottom organic layer were collected and dried under airflow.

Derivatization of aqueous metabolites was performed using the Gerstel MultiPurpose Sampler (MPS 2XL). Methoxime-tBDMS derivatives were formed by addition of 15 μ L 2% (w/v) methoxylamine hydrochloride (MP Biomedicals) in pyridine and incubated at 45°C for 60 minutes. Samples were then silylated by addition of 15 μ L of N-tert-butyldimethylsilyl-N-methyltrifluoroacetamide (MTBSTFA) with 1% tert-butyldimethylchlorosilane (tBDMS) (Regis Technologies) and incubated at 45°C for 30 minutes. Aqueous metabolites were analyzed by GC-MS using a DB-35MS column (30 m x 0.25 mm i.d. x 0.25 μm , Agilent J&W Scientific, Santa Clara, CA) in an Agilent 7890B gas chromatograph (GC) interfaced with a 5977C mass spectrometer (MS). Electron impact ionization was performed with the MS scanning over the range of 100-650 m/z for polar metabolites. For separation of aqueous metabolites the GC oven was held at 100°C for 1 min after injection, increased to 255°C at $3.5^{\circ}\text{C}/\text{min}$, and finally increased to 320°C at $15^{\circ}\text{C}/\text{min}$ and held for 3 min.

Dried organic fraction was saponified and esterified to form fatty acid methyl esters (FAMES) by addition of 500 μ L of 2% (w/v) H_2SO_4 in MeOH and incubated at 50°C for 120 minutes. FAMES were then extracted by addition of saturated NaCl and hexane before collection and drying of the inorganic layer. Derivatized fatty acids were analyzed by GC-MS using a select FAME column (100 m x 0.25 mm i.d. x 0.25 μm ; Agilent J&W Scientific) as above, with the

MS scanning over the range 120-400 m/z. For separation the GC oven was held at 80°C for 1 min after injection, increased to 160°C at 20°C/min, increased to 198°C at 1°C/min, and finally increased to 250°C at 5°C/min and held for 15 min.

5.3.12 Metabolite integration and isotopomer spectral analysis (ISA)

Mass isotopomer distributions and total abundances were determined by integration of mass fragments (Supplemental Table S1 in [19]) and correcting for natural abundances using MATLAB-based algorithm. Glycolytic flux was estimated by normalizing pyruvate, lactate, or alanine abundance by the sum of intracellular branched-chain amino acids abundance and M+3 label. Oxidative PPP shunting was estimated by $\frac{M+1}{(M+1)+(M+2)}$ labeling on pyruvate from [1,2-¹³C]glucose [20]. Isotopomer spectral analysis (ISA) was performed to estimate contribution of oxPPP to cytosolic NADPH as previously described [21]. ISA compares experimental labeling of fatty acids to simulated labeling using a reaction network where C16:0 is condensation of 14 NADPHs. Parameters for contribution of PGD to lipogenic NADPH (D value) and percentage of newly synthesized fatty acid (g(t) value) and their 95% confidence intervals are then calculated using best-fit model from INCA MFA software [22].

5.3.13 Immunoblotting

Cultured cells were washed with cold PBS and harvested on ice with mPER (Pierce Biotechnology) with freshly added 1x HALT inhibitor (Thermo Fisher Scientific). Protein concentration was determined by BCA assay and equal amounts of protein were resolved on SDS-PAGE gel and transferred to nitrocellulose membrane. Membrane was blocked with 5% milk in TBST (Tris-buffered saline with 0.1% Tween 20) for 2-3hrs and incubated overnight at 4°C with primary antibody: anti-Vinculin (Abcam), anti-G6PD (Cell Signaling Technologies), anti-PGD (Santa Cruz Biotechnology), anti-KEAP1 (Proteintech), anti-HA (Abcam), or anti-Nrf2

(Cell Signaling Technology). Blots were then incubated with secondary antibody for 1hr at room temp, Anti-Rabbit HRP-conjugate (Cell Signaling Technology) or Anti-Mouse HRP-conjugate (Cell Signaling Technology). Finally blots were incubated with ECL substrate (BioRad) and imaged.

5.3.14 RT-PCR

Total mRNA was isolated from cells using RNA isolation kit (RNeasy Mini Kit; Qiagen). Isolated RNA was reverse transcribed using cDNA synthesis kit (High-capacity cDNA Reverse Transcription Kit; Thermo Fisher Scientific). Real-time PCR was performed using SYBR green reagent (iQaq Universeal SYBR Green Supermix; Bio-Rad). Relative expression was determined using Livak ($\Delta\Delta CT$) method with *RPL27* and *RPLP0* as housekeeping genes. Primers used were taken from Primerbank [23] and tabulated in Supplemental Table S1 in [19]. All commercial kits were used per the manufacturer's protocol.

5.3.15 Glutathione measurement

Intracellular glutathione was measure using Glutathione Assay Kit (Sigma) per manufacturer's protocol. Ten centimeter dishes of cells were assayed in quintuplicate and cells were counted in parallel for normalization.

5.3.16 Statistical analyses

Unless indicated, all results shown as mean \pm SEM of biological triplicates. P values were calculated using a Student's two-tailed t test; *, P value between 0.01 and 0.05; **, P value between 0.001 and 0.01; ***, P value <0.001

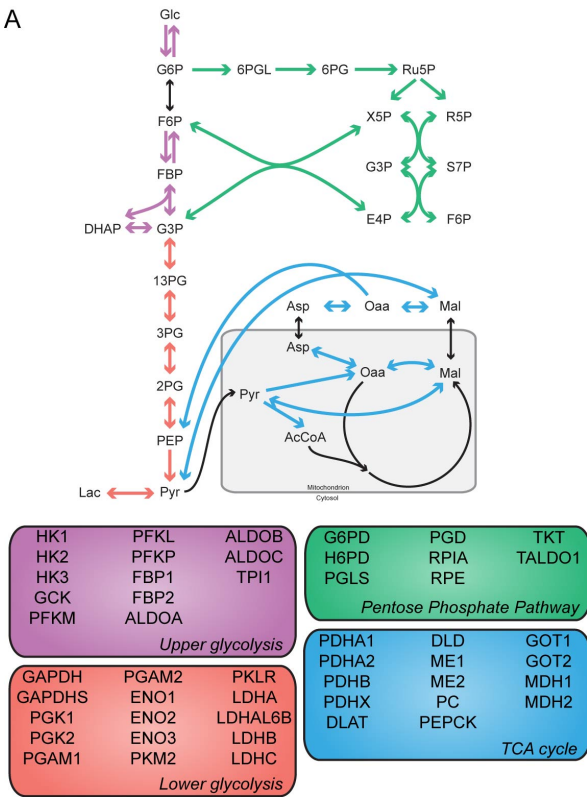
5.4 Results

5.4.1 Combinatorial CRISPR-Cas9 screening to probe metabolic networks

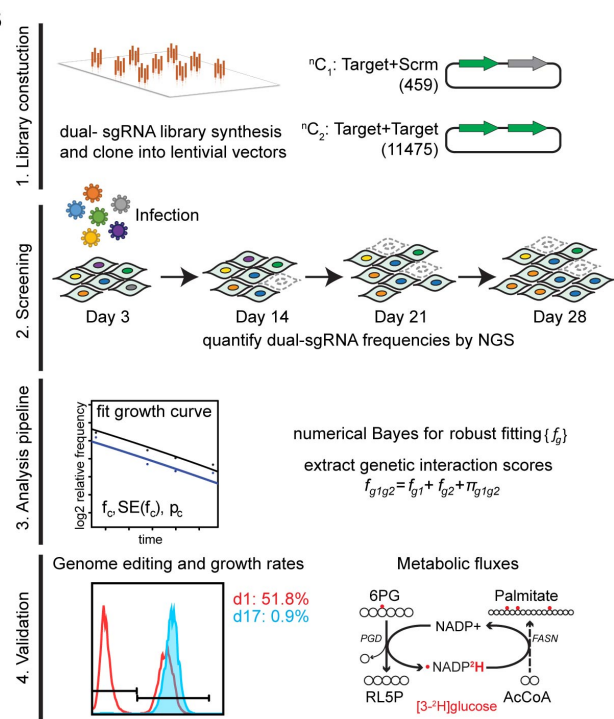
To systematically study the dispensability and interactions of genes underlying carbohydrate metabolism, we applied a combinatorial CRISPR screening approach [17] to interrogate singly and in combination a set of 51 genes, encompassing glycolysis, gluconeogenesis, pentose phosphate pathway, and glucose entry into the TCA cycle (Figure 5.1A). We generated 3 sgRNAs per gene such that 9 unique constructs were present for every gene-pair, resulting in a dual-sgRNA library consisting of 459 elements targeting genes individually, as well as 11,475 unique elements targeting two different genes simultaneously (Table S1 in [19]). The dual-sgRNA constructs were synthesized from oligonucleotide arrays, cloned into a lentiviral vector, and then transduced into HeLa or A549 cells stably expressing Cas9 (Figure 5.1B, S5.1A-B). Through sampling of sgRNA frequencies at days 3, 14, 21, and 28 (Figure S5.1C-D), both robust gene-level fitness values (f_g) and also interaction scores (π_{gg}) were computed. Finally, impact of SKOs and dual-gene knockouts (DKOs) on cellular growth and metabolic fluxes were validated in a targeted fashion.

Figure 5.1: Experimental design. (A) Schematic pathway diagram of carbohydrate metabolism, and list of 51 targeted enzymes. (B) Schematic overview of the combinatorial CRISPR-Cas9 screening approach. A dual-gRNA library in which each element targets either gene-gene pairs or gene-scramble pairs, to assay dual and single gene perturbations, was constructed from array-based oligonucleotide pools. Competitive growth based screens were performed, and the relative abundance of dual-gRNAs were sampled over multiple time points. The fitness and genetic interactions were computed via a numerical Bayes model and key hits were validated using both competitive cell growth assays and measurement of metabolic fluxes.

A



B

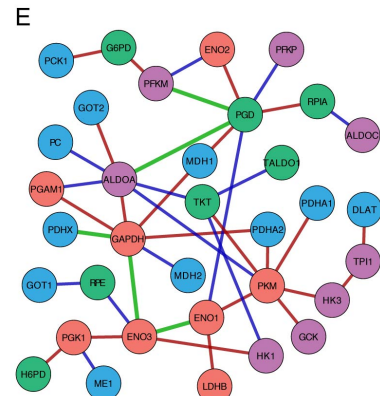
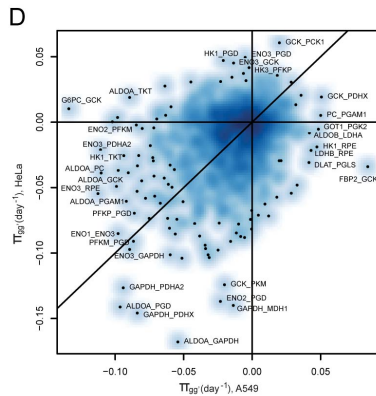
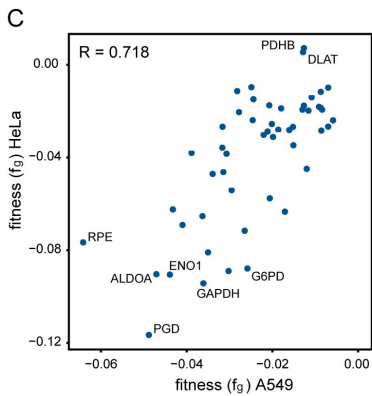
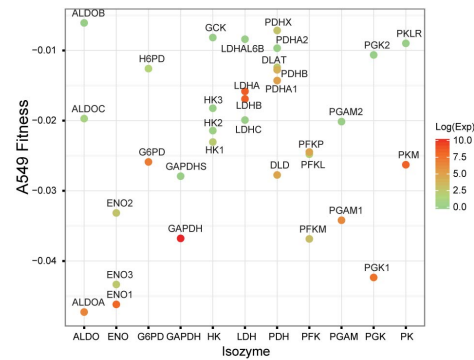
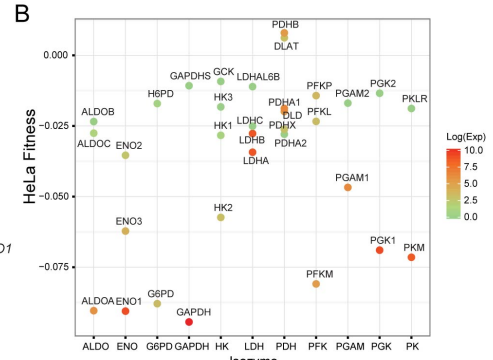
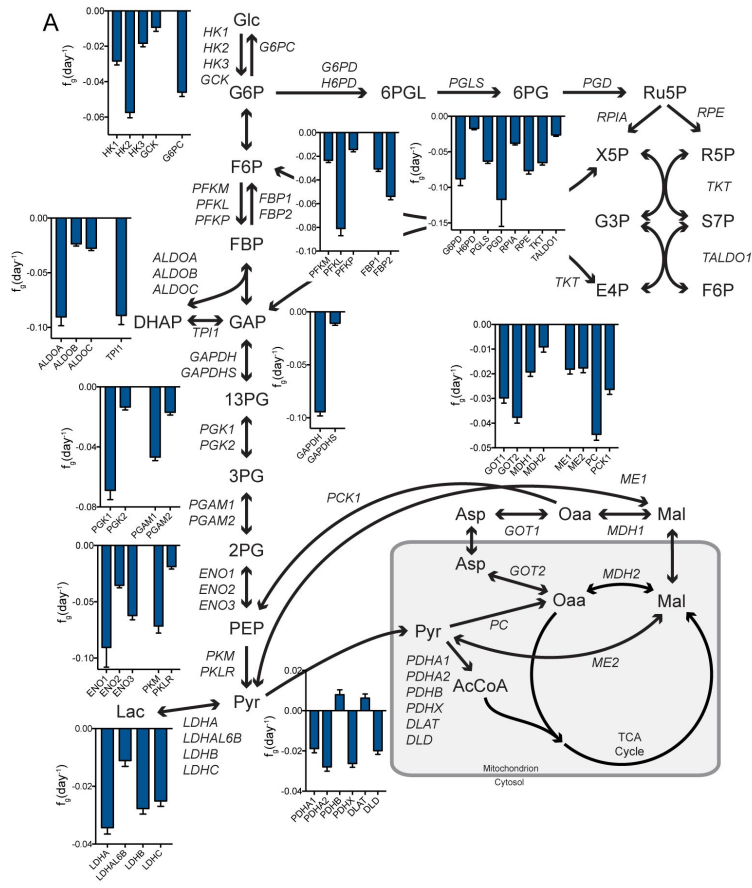


5.4.2 Mapping metabolic gene dependencies in glucose catabolism

Upon analyzing fitness scores for individual gene knockouts across the metabolic network (Table S2 in [19]), we noted that for most (but not all) isozyme families, a dominant gene showed the greatest indispensability (Figure 5.2A and S5.2A). Consistent with the notion of a "cancer-specific" isozyme [24], *HK2*, *ALDOA*, *PGK1*, and *PFKL* all showed a fitness defect greater than two-fold higher as compared to other isozymes. However not all families exemplified this dynamic, with *ENO1/ENO3* and the lactate dehydrogenase (LDH) family showing similar dispensability across gene members (Figure 5.2A and S5.2A). The general dispensability of SKOs within the LDH family is notable given the critical role of glycolysis in the maintenance of cancer cell homeostasis and concomitant need to regenerate cytosolic NAD⁺ when relying on glycolytic flux [25]. Importantly nodes central to the regeneration of reducing equivalents (NADH and NADPH) - *GAPDH*, *G6PD*, and *PGD* - were found to be critical for cellular growth (Figure 5.2A and S5.2A).

We hypothesized that gene expression could explain why certain genes were less dispensable and why certain families did not display a dominant member. Indeed, lower fitness score may be associated with higher gene expression ($R = -0.461$, $p\text{-value} = 6.7e-04$ and $R = -0.429$, $p\text{-value} = 1.7e-03$, for HeLa and A549 cells respectively). These expression-driven differences also partially explained dynamics within isozyme families. For instance, *ALDOA* had a much lower fitness score and higher gene expression as compared to *ALDOB* and *ALDOC* (Figure 5.2B). *ENO1* and *ENO3* both displayed negative fitness scores and both were more highly expressed than *ENO2* (Figure 5.2B-C). However, the dispensable isozyme families LDH and PDH (key for maintenance of glycolytic flux and oxidation of pyruvate respectively) were also found to be highly expressed in both cell types (Figure 5.2B-C). With each family having more than two member enzymes, this result demonstrates that vital functions of cell metabolism can be carried out by multiple genes and show surprising resiliency through isozyme compensation or network behavior.

Figure 5.2: Combinatorial CRISPR screens reveal metabolic network dependencies. (A) SKO fitness scores for HeLa cells, plotted as f_g (day^{-1}), with a more negative score representing a loss in fitness with SKO. Plotted as mean \pm SD. (B) Multi-isoform family member fitness scores and gene expression for HeLa (top) and A549 (bottom) cells. (C) Relative comparison of SKO fitness scores (f_g) across both cells. (D) Relative comparison of genetic interaction scores (π_{gg}) across both cell lines. (E) Combined genetic interaction map of both cell lines. Green solid line represents interactions observed in both cell lines. Red and blue lines represent significant genetic interactions in A549 and HeLa cells respectively.



To this end, SKO knockouts correlated well ($R = 0.718$, $p\text{-value} = 3.1e-09$) across both cell lines (Figure 5.2C). This correlation extended to expression of all enzymes ($R = 0.938$, $p\text{-value} < 2.2e-16$). Furthermore, HeLa fitness scores correlated well with previously published HeLa screening data ($R = 0.664$, $p\text{-value} = 1.435e-07$) [10]. However, these results exemplify the challenge in understanding metabolic topology through screening individual genes: few metabolic genes are essential, and essential elements are typically conserved across all cell types.

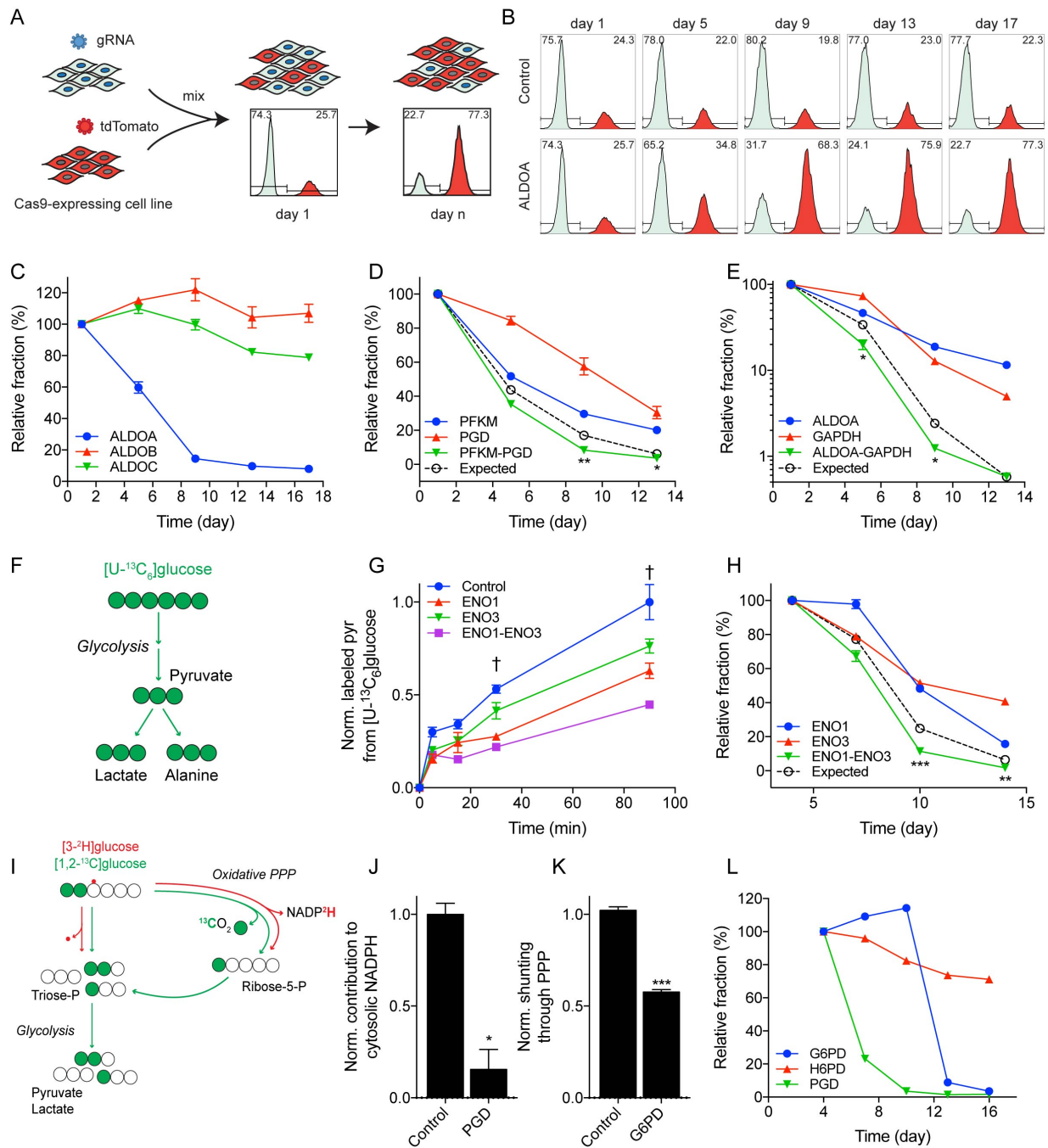
We subsequently hypothesized that gene interactions could provide information on metabolic network topology and cell-specific adaptations in these pathways. Indeed, a notable number of gene pairs were found to significantly interact (Figure 5.2D-E, Table S3 in [19]). Specifically, after filtering for genes with $RPKM < 0.15$, we observed 35 interactions ($z\text{-score} < -3$) in the combined HeLa and A549 interaction network (Figure S5.2B and Table S4 in [19]), of which 10 (30%) have been previously reported as protein-protein interactions [26]. Five gene pair interactions were shared across both cell types.

Notably, the conserved interaction of *ENO1/ENO3* demonstrates the possible compensation observed in SKO results (Figure 5.2A). Previous results have demonstrated that passenger deletion of *ENO1* in glioblastoma (GBM) cell lines increases their dependence on *ENO2* and generates a GBM synthetic lethality [27]. As *ENO2* is only expressed in neural tissues, our results suggest that *ENO1* and *ENO3* may compensate for one another in these cell lines. Additionally, redox-associated genes, *GAPDH* and *PGD*, had many interacting partners, consistent with their negative SKO fitness scores and metabolic functions (Figure 5.2E). As NAD(P)H is required for both bioenergetics and biosynthetic reactions, alteration of cofactor balance or regeneration fluxes could have large impacts on distal reactions within the network.

5.4.3 Validation of significant SKO and DKO results on cellular fitness and metabolic fluxes

Next, to functionally validate the screening results, competition assays and metabolic flux measurements were conducted in the presence of SKO and DKO pairs. Competition assays were performed by mixing control tdTomato+ cells expressing an empty vector, with tdTomato- cells expressing a gRNA of interest (Figure 5.3A), and relative growth rates were assayed by quantifying the ratio of +/- cells in the mixture via flow cytometry (Figure 5.3B). Dominant family member isozyme fitness was observed in the ALDO family (Figure 5.3C), and significant gene interactions over additive SKO effects were observed in multiple gene pairs (Figure 5.3D-E). Correspondingly, perturbations in glycolytic flux were observed through dynamic labeling of metabolites (i.e. pyruvate, lactate, alanine) from ^{13}C -labeled glucose ([U- $^{13}\text{C}_6$]glucose) (Figure 5.3F). Notably, DKO of *ENO1* and *ENO3* significantly decreased flux through glycolysis compared to control and SKOs (Figure 5.3G, S5.3A-B) and also displayed significantly lower fitness (Figure 5.3H). Finally, we applied specific ^{13}C and ^2H tracers to quantify how the oxPPP contributed to NADPH regeneration (Figure 5.3I) [20, 21]. SKO knockout of oxPPP enzymes was indeed observed to lower flux (Figure 5.3J-K) and fitness (Figure 5.3L and S5.3C) through this pathway.

Figure 5.3: Screening results validated through targeted fitness and metabolic flux measurements. (A) Schematic of cell competition assay used to validate growth. A Cas9-expressing cell is transduced with a sgRNA lentivirus of interest (tdTomato-) and mixed with a control Cas9-expressing cell transduced with a tdTomato lentivirus (tdTomato+). The cells are grown together and the percentage of control (tdTomato+) cells is used to assess relative fitness of SKO. (B) Non-targeting control (top) is stable for duration of experiment and shows no fitness changes. SKO of *ALDOA* (bottom) shows decreased fitness over time as control cells take over population. (C) SKO competition assay of ALDO isozyme family. *ALDOA* shows greatest loss of fitness. (D) Growth validation of *PFKM/PGD* genetic interaction. DKO (green) shows significantly greater decrease in fitness over additive SKO effect (black). (E) Growth validation of *ALDOA/GAPDH* interaction. (F) Atom transition map depicting glycolysis. Fully labeled ([U-¹³C₆]glucose) leads to fully labeled pyruvate, lactate, and alanine. (G) Metabolic validation of DKO interaction in *ENO1/ENO3*. DKO significantly lowered flux through glycolysis over control or SKOs. † indicates statistical significance (p<0.05) for all conditions as compared to DKO (H) Growth validation of *ENO1/ENO3* interaction. (I) Atom transition map depicting oxPPP tracing. [3-²H]glucose labels cytosolic NADPH through oxPPP. Labeling on glycolytic intermediates from [1,2-¹³C]glucose is changed by shunting of glucose through oxPPP. (J) Metabolic validation of *PGD* SKO at day 4. oxPPP contributes less NADPH with *PGD* knockout. Plotted as mean ± 95% CI. * indicates statistical significance by non-overlapping confidence intervals. (K) Metabolic validation of *G6PD* SKO at day 7. Less glucose is shunted through oxPPP with *G6PD* knockout. (L) SKO competition assay of oxPPP enzymes. All experiments were performed in HeLa cells. (C-E, G-H, K-L) Data plotted as mean ± SEM.



5.4.4 Comparison of metabolic liabilities across cell lines reveals key role of *KEAP1-NRF2*

We next focused on differences in the screens of these two cell lines to explore how oncogenic status contributes to metabolic reprogramming. By conducting screens in A549 and HeLa cells and comparing fitness results, we could also gain insights into the impact of SKO results in combination with endogenous mutations. Notably, screening results suggested and we validated that SKO of oxPPP genes (i.e., *G6PD* and *PGD*) impacted the growth and survival of HeLa cells more dramatically than A549 cells (Figure 5.4A, S5.4A, and S5.3C) with observed editing rates in each cell line 95% (Figure S5.3D). Intriguingly, the expression of *G6PD* and *PGD* in these cell lines showed the opposite trend, with A549 cells expressing these genes at significantly higher levels but having a lower dependence on them to maintain growth and viability (Figure 5.4A and S5.4A). As the oxPPP is critical for maintaining redox homeostasis (i.e. NADPH regeneration) [28], mutations within control points of redox metabolism could drive this differential sensitivity and further extend the interactions of metabolic genes to known oncogenes or tumor suppressors.

In this regard, A549 NSCLC cells harbor a loss of function mutation in *KEAP1* while this regulatory axis is functional in HeLa cells. Loss of function mutation of *KEAP1* is observed in 20-50% of non-small-cell lung cancers (NSCLCs) [29]. *KEAP1* is a redox-sensitive E3 ubiquitin ligase that targets oxidized *NRF2*, the master transcriptional regulator of the cellular antioxidant response [30–32] and previous work has demonstrated an ability of *NRF2* to alter metabolic fluxes [33–35]. Consequently, we hypothesized that the mutational status of this pathway potentially influenced oxPPP sensitivity.

Knockout of *KEAP1* in HeLa cells significantly increased *NRF2* levels and expression of oxPPP enzymes *G6PD* and *PGD* (Figure S5.3E and S5.4B) consistent with the increased expression levels observed in A549 cells (*KEAP1*-deficient) relative to HeLa cells (*KEAP1*

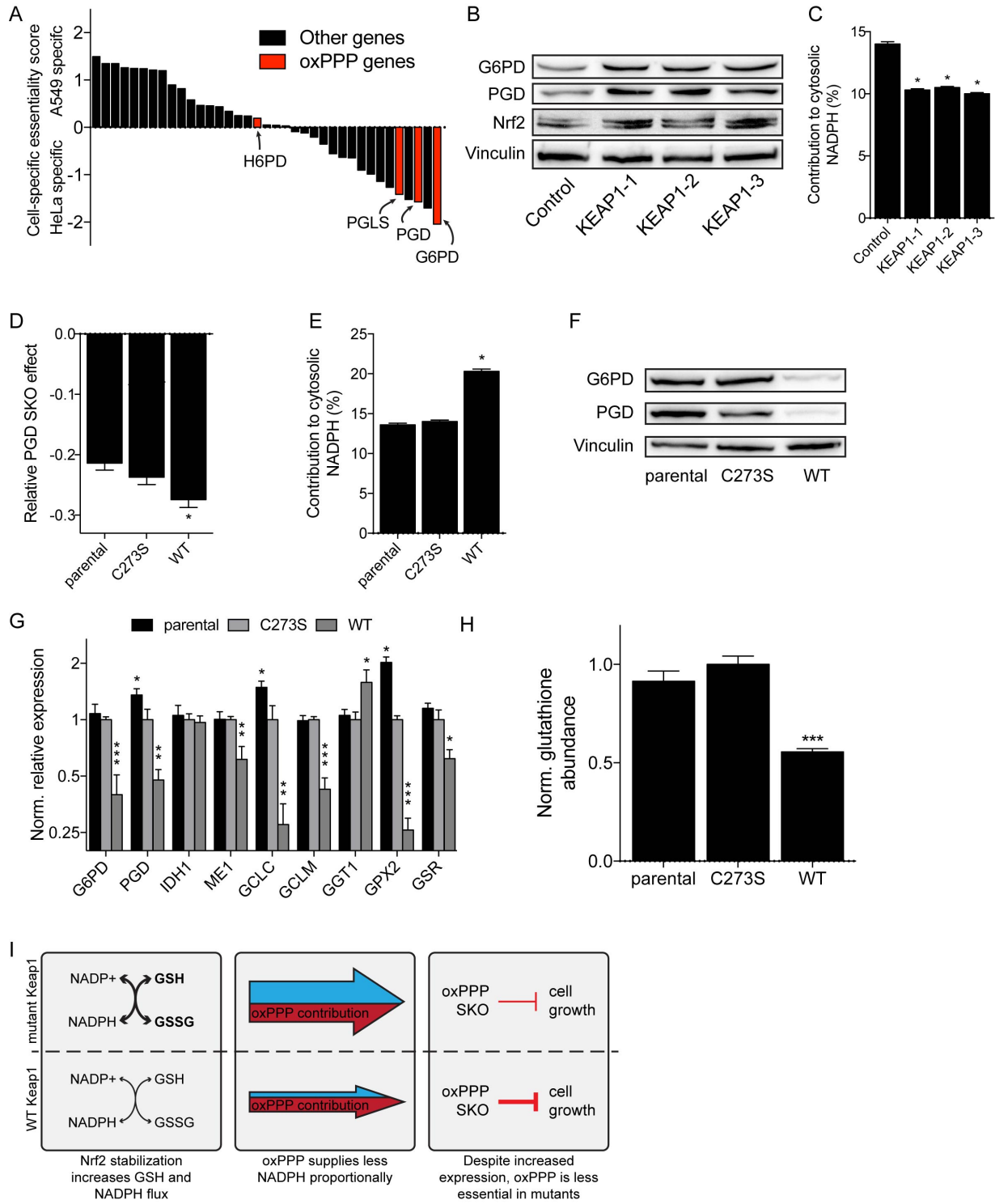
WT) (Figure S5.5A, bottom left). We next determined how oxPPP flux contributed to cytosolic NADPH pools using [3-²H]glucose in *KEAP1* KO cells [21]. For all sgRNAs we observed a significant decrease in labeling (Figure 5.4C), which indicates higher pathway flux and loss of label via glutathione-mediated H-D exchange [36]. This enhanced glutathione buffering capacity is consistent with the greater dispensability of oxPPP enzymes observed in A549 cells as compared to HeLa cells (Figure 5.4A).

We next hypothesized that *KEAP1* mutational status could directly alter sensitivity to SKO of oxPPP enzymes and quantified the impact of such SKOs on the fitness and metabolism of an isogenic panel of A549 cells. Ectopic expression of wild type (WT) *KEAP1* decreased *NRF2* stabilization as compared to constitutively active C273S mutant *KEAP1* [37] (Figure S5.4B). Interestingly, overexpression of either mutant or WT *KEAP1* increased *NRF2* levels as compared to parental cells (Figure S5.4B). Re-expression of WT *KEAP1* in A549 cells increased cell sensitivity to *PGD* knockout as compared to C273S *KEAP1* mutant cells (Figure 5.4D and S5.4C), highlighting the role of *KEAP1* in regulating oxPPP enzyme expression and flux. Consistent with these fitness results and the above metabolic measurements, WT *KEAP1* expression increased the contribution of *PGD* to cytosolic NADPH regeneration (Figure 5.4E) and decreased expression of oxPPP enzymes (Figure 5.4F).

Finally, we hypothesized that *KEAP1* remodels redox metabolism due to its canonical role in the cellular antioxidant response. Indeed, expression of WT *KEAP1* was found to both decrease expression of NADPH-regenerating enzymes and those involved in glutathione (GSH) synthesis (Figure 5.4G). Consistent with decreased expression of GSH synthesis enzymes, intracellular glutathione levels were decreased by 45% upon expression of WT *KEAP1* (Figure 5.4H). Presumably, the decreased buffering capacity by GSH and lower expression of other NADPH regenerating contributes to the increased dependence on oxPPP flux observed in cells expressing WT *KEAP1*. A model therefore emerges from our screening results, whereby *KEAP1* mutational status alters the relative importance of the oxPPP by modulating expression of the

redox network to drive GSH synthesis and regeneration (Figure 5.4I).

Figure 5.4: KEAP1 mutational status alters redox metabolism and impact of oxPPP gene knockouts on cellular fitness. (A) Plot of cell-specific fitness scores for expressed genes. Positive scores are SKOs that are essential in A549s and negative scores are SKOs more essential in HeLa cells. The cell-specific essentiality scores respond to the z-score transformed residuals of linear regression of HeLa and A549 SKO fitness, shown in Figure S5.4A. (B) Immunoblot of *KEAP1* SKO in HeLa cells. (C) Contribution of oxPPP to cytosolic NADPH with *KEAP1* SKO in HeLa cells. Plotted as mean \pm 95% CI. * indicates statistical significance by non-overlapping confidence intervals. (D) Relative *PGD* SKO effect in A549s with *KEAP1* mutant panel. (E) Contribution of oxPPP to cytosolic NADPH in A549s with *KEAP1* mutant panel. Plotted as mean \pm 95% CI. * indicates statistical significance by non-overlapping confidence intervals. (F) Immunoblot of A549s with *KEAP1* mutant panel. (G) Normalized relative gene expression of A549s with *KEAP1* mutant panel. (H) Glutathione measurement in A549 with *KEAP1* mutant panel (n=5). (I) Schematic of how KEAP1 mutational status alters relative metabolism and oxPPP dispensability. (D, G, H) Data plotted as mean \pm SEM.



5.5 Discussion

While it is clear that cancer cells rely on aerobic glycolysis to maintain biosynthetic fluxes and ATP demands [38], how the underlying metabolic network topology changes in response to specific oncogenic events is not fully clear. In this study, we comprehensively interrogated metabolic gene dispensability, interaction, and compensation through a combinatorial CRISPR-Cas9 screening approach. Key nodes within glycolysis were found to significantly interact with one another (e.g. *ALDOA* and *PGD*) in an emergent network behavior. Many of these interactions were conserved across cells of different origin, implying such enzyme interaction pairs harbor some function that warrant future interrogation.

Other interactions were demonstrative of metabolic compensation within isozyme families (e.g. *ENO1* and *ENO3*) and consistent with previously described mechanisms of metabolic synthetic lethality [27, 39]. These observed network features present a new opportunity through combinatorial (pairwise) screening to understand if/how cells can adapt around loss of a metabolic enzyme. Knowing if a solid tumor of interest is pharmacologically vulnerable to a metabolic inhibitor *a priori* will allow for future precision medicine applications.

In fact, by comparing relative SKO scores across cell types, we were able to elucidate a paradoxical resistance to targeting the oxPPP along the *KEAP1-NRF2* axis. Even though cells potently upregulated expression of oxPPP enzymes upon loss of *KEAP1*, cells were less vulnerable to KO of enzymes in this metabolic pathway. In this case, alternate NADPH regeneration pathways and increased antioxidant buffering by GSH pools provides compensation and survival benefits to cells. Our NADPH tracing data demonstrated that cells lacking functional *KEAP1* exhibit higher oxPPP flux, as evidenced by reduced labeling due to increased H-D exchange through glutathione-related pathways [36]. Indeed, elevated oxPPP enzyme levels and increased glutathione pools would specifically increase exchange flux, resulting in the observed decrease in labeling downstream of [3-²H]glucose. The integration of such functional measurements with

genetic screening and transcriptional results provides better context to interpret the observed metabolic reprogramming downstream of KEAP1-NRF2.

Our results suggest that *KEAP1* mutational status must be considered when targeting the oxPPP therapeutically. In fact, recent work has implicated *KEAP1* mutational status as a driver of metabolic reprogramming and potential targeting of glutaminase in pre-clinical models of lung adenocarcinoma [40]. Consistent with our findings, *KEAP1* mutation increases intracellular glutathione levels and need for cysteine, causing an increased need for glutamine anaplerosis to support glutamate/cysteine antiporter flux (*SLC7A11*) [40, 41]. Other recent work has also implicated *KEAP1* mutational status as a driver of chemotherapeutic resistance in preclinical models of lung cancer and further demonstrates the need for new paradigms connecting oncogenic mutations to cancer cell survival [42].

Moving forward, it will be important to perform such screens across a larger number of cell types to elucidate a more comprehensive picture of metabolic network reprogramming. The high throughput methodology presented here increases the feasibility of such studies. We note also that comparing the absolute fitness values in screens across cell lines can be confounded by various factors. These include differences in relative cell growth and expression of CRISPR effectors among others, and thus devising new strategies for normalization will be valuable to improve the utility of future screening data sets. We also note the critical importance of sgRNA efficacy, and anticipate that continued improvements in sgRNA design [43–45] will be critical to improving consistency and signal-to-noise in the assays. Finally, layering in data from complementary perturbation strategies such as CRISPR activation/inhibition and small molecule inhibition should enable charting of more comprehensive networks underlying cellular function and transformation.

Discovery of the unique metabolic features in transformed cells has spurred much interest in exploiting metabolic vulnerabilities for drug discovery [46]. In fact, metabolic inhibitors have been developed as single agent therapeutics and combination therapeutics for many different

cancer types [47]. However, these agents have found varying success in the clinic due an inability to determine proper cancer types in preclinical development. While cancer cells share common hallmarks of metabolic reprogramming, cell-of-origin and tumorigenic drivers uniquely influence the direction and extent of metabolic reprogramming. The new paradigm of incorporating combinatorial CRISPR screening, transcriptomic information, and metabolic flux measurements presented here will provide a new platform to address this limitation. By interrogating metabolism at the network-level, new therapeutic targets may be identified, and clinicians may become better equipped at identifying the most responsive patient populations.

5.6 Acknowledgements

We would like to acknowledge members of the Mali and Metallo labs for their helpful discussions, Alex Thomas and Nathan Lewis for help with sgRNA designs, and Eric Bennett for KEAP1 vectors. This work was supported by the California Institute of Regenerative Medicine (RB5-07356 to C.M.M.), NIH grant (R01CA188652 to C.M.M.), Camille and Henry Dreyfus Teacher-Scholar (to C.M.M.), NSF CAREER (to C.M.M.), Searle Scholar Award (to C.M.M.), UCSD Institutional Funds (to P.M.), NIH grant (R01HG009285 to P.M.), NIH grant (R01CA222826 to P.M.), the Burroughs Wellcome Fund (1013926 to P.M.), the March of Dimes Foundation (5-FY15-450 to P.M.), and the Kimmel Foundation (SKF-16-150 to P.M.). M.G.B. is supported by a NSF Graduate Research Fellowship (DGE-1144086).

Chapter 5, in full, is a reprint of the material as it appears in "Combinatorial CRISPR-Cas9 Metabolic Screens Reveal Critical Redox Control Points Dependent on the KEAP1-NRF2 Regulatory Axis," *Molecular Cell*, vol. 69, 2018. Mehmet G. Badur and Dongxin Zhao are the co-primary authors of this publication. Jens Luebeck, Jose H. Magana, Amanda Birmingham, Roman Sasik, Christopher S. Ahn, and Trey Ideker are co-authors of this publication. Christian M. Metallo and Prashant Mali are the co-corresponding authors of this publication.

5.7 References

1. Pavlova, N. N. & Thompson, C. B. The Emerging Hallmarks of Cancer Metabolism. *Cell Metab* **23**, 27–47 (2016).
2. Hensley, C. T., Faubert, B., Yuan, Q., Lev-Cohain, N., Jin, E., Kim, J., Jiang, L., Ko, B., Skelton, R., Loudat, L., Wozniak, M., Klimko, C., McMillan, E., Butt, Y., Ni, M., Oliver, D., Torrealba, J., Malloy, C. R., Kernstine, K., Lenkinski, R. E. & DeBerardinis, R. J. Metabolic Heterogeneity in Human Lung Tumors. *Cell* **164**, 681–94 (2016).
3. Chaneton, B., Hillmann, P., Zheng, L., Martin, A. C., Maddocks, O. D., Chokkathukalam, A., Coyle, J. E., Jankevics, A., Holding, F. P., Vousden, K. H., Frezza, C., O'Reilly, M. & Gottlieb, E. Serine is a natural ligand and allosteric activator of pyruvate kinase M2. *Nature* **491**, 458–62 (2012).
4. Christofk, H. R., Vander Heiden, M. G., Harris, M. H., Ramanathan, A., Gerszten, R. E., Wei, R., Fleming, M. D., Schreiber, S. L. & Cantley, L. C. The M2 splice isoform of pyruvate kinase is important for cancer metabolism and tumour growth. *Nature* **452**, 230–3 (2008).
5. Patra, K. C., Wang, Q., Bhaskar, P. T., Miller, L., Wang, Z., Wheaton, W., Chandel, N., Laakso, M., Muller, W. J., Allen, E. L., Jha, A. K., Smolen, G. A., Clasquin, M. F., Robey, B. & Hay, N. Hexokinase 2 is required for tumor initiation and maintenance and its systemic deletion is therapeutic in mouse models of cancer. *Cancer Cell* **24**, 213–228 (2013).
6. Castaldo, G., Calcagno, G., Sibillo, R., Cuomo, R., Nardone, G., Castellano, L., Del Vecchio Blanco, C., Budillon, G. & Salvatore, F. Quantitative analysis of aldolase A mRNA in liver discriminates between hepatocellular carcinoma and cirrhosis. *Clin Chem* **46**, 901–6 (2000).
7. Guzman, G., Chennuri, R., Chan, A., Rea, B., Quintana, A., Patel, R., Xu, P. Z., Xie, H. & Hay, N. Evidence for heightened hexokinase II immunoreexpression in hepatocyte dysplasia and hepatocellular carcinoma. *Dig Dis Sci* **60**, 420–6 (2015).
8. Shalem, O., Sanjana, N. E., Hartenian, E., Shi, X., Scott, D. A., Mikkelsen, T. S., Heckl, D., Ebert, B. L., Root, D. E., Doench, J. G. & Zhang, F. Genome-scale CRISPR-Cas9 knockout screening in human cells. *Science* **343**, 84–7 (2014).
9. Wang, T., Wei, J. J., Sabatini, D. M. & Lander, E. S. Genetic screens in human cells using the CRISPR-Cas9 system. *Science* **343**, 80–4 (2014).
10. Hart, T., Chandrashekhar, M., Aregger, M., Steinhart, Z., Brown, K. R., MacLeod, G., Mis, M., Zimmermann, M., Fradet-Turcotte, A., Sun, S., Mero, P., Dirks, P., Sidhu, S., Roth,

- F. P., Rissland, O. S., Durocher, D., Angers, S. & Moffat, J. High-Resolution CRISPR Screens Reveal Fitness Genes and Genotype-Specific Cancer Liabilities. *Cell* **163**, 1515–26 (2015).
11. Wang, T., Birsoy, K., Hughes, N. W., Krupczak, K. M., Post, Y., Wei, J. J., Lander, E. S. & Sabatini, D. M. Identification and characterization of essential genes in the human genome. *Science* **350**, 1096–101 (2015).
 12. Arroyo, J. D., Jourdain, A. A., Calvo, S. E., Ballarano, C. A., Doench, J. G., Root, D. E. & Mootha, V. K. A Genome-wide CRISPR Death Screen Identifies Genes Essential for Oxidative Phosphorylation. *Cell Metab* **24**, 875–885 (2016).
 13. Birsoy, K., Wang, T., Chen, W. W., Freinkman, E., Abu-Remaileh, M. & Sabatini, D. M. An Essential Role of the Mitochondrial Electron Transport Chain in Cell Proliferation Is to Enable Aspartate Synthesis. *Cell* **162**, 540–51 (2015).
 14. Boettcher, M., Tian, R., Blau, J., Markegard, E., Wu, D., Biton, A., Zaitlen, N., McCormick, F., Kampmann, M. & McManus, M. T. Decoding directional genetic dependencies through orthogonal CRISPR/Cas screens. *bioRxiv* (2017).
 15. Chow, R. D., Wang, G., Codina, A., Ye, L. & Chen, S. Mapping in vivo genetic interactions through Cpf1 crRNA array screening. *bioRxiv* (2017).
 16. Han, K., Jeng, E. E., Hess, G. T., Morgens, D. W., Li, A. & Bassik, M. C. Synergistic drug combinations for cancer identified in a CRISPR screen for pairwise genetic interactions. *Nat Biotechnol* (2017).
 17. Shen, J. P., Zhao, D., Sasik, R., Luebeck, J., Birmingham, A., Bojorquez-Gomez, A., Licon, K., Klepper, K., Pekin, D., Beckett, A. N., Sanchez, K. S., Thomas, A., Kuo, C. C., Du, D., Roguev, A., Lewis, N. E., Chang, A. N., Kreisberg, J. F., Krogan, N., Qi, L., Ideker, T. & Mali, P. Combinatorial CRISPR-Cas9 screens for de novo mapping of genetic interactions. *Nat Methods* (2017).
 18. Wong, A. S., Choi, G. C., Cui, C. H., Pregernig, G., Milani, P., Adam, M., Perli, S. D., Kazer, S. W., Gaillard, A., Hermann, M., Shalek, A. K., Fraenkel, E. & Lu, T. K. Multiplexed barcoded CRISPR-Cas9 screening enabled by CombiGEM. *Proc Natl Acad Sci U S A* **113**, 2544–9 (2016).
 19. Zhao, D., Badur, M. G., Leubeck, J., Magana, J., Birmingham, A., Sasik, R., Ahn, C. S., Ideker, T., Metallo, C. M. & Mali, P. Combinatorial CRISPR-Cas9 Metabolic Screens Reveal Critical Redox Control Points Dependent on the KEAP1-NRF2 Regulatory Axis. *Mol Cell* **69**, 699–708 (2018).

20. Lee, W. N., Boros, L. G., Puigjaner, J., Bassilian, S., Lim, S. & Cascante, M. Mass isotopomer study of the nonoxidative pathways of the pentose cycle with [1,2-¹³C₂]glucose. *Am J Physiol* **274**, E843–51 (1998).
21. Lewis, C. A., Parker, S. J., Fiske, B. P., McCloskey, D., Gui, D. Y., Green, C. R., Vokes, N. I., Feist, A. M., Vander Heiden, M. G. & Metallo, C. M. Tracing compartmentalized NADPH metabolism in the cytosol and mitochondria of mammalian cells. *Mol Cell* **55**, 253–63 (2014).
22. Young, J. D. INCA: a computational platform for isotopically non-stationary metabolic flux analysis. *Bioinformatics* **30**, 1333–5 (2014).
23. Wang, X., Spandidos, A., Wang, H. & Seed, B. PrimerBank: a PCR primer database for quantitative gene expression analysis, 2012 update. *Nucleic Acids Res* **40**, D1144–9 (2012).
24. Hay, N. Reprogramming glucose metabolism in cancer: can it be exploited for cancer therapy? *Nat Rev Cancer* **16**, 635–49 (2016).
25. Vander Heiden, M. G., Cantley, L. C. & Thompson, C. B. Understanding the Warburg effect: the metabolic requirements of cell proliferation. *Science* **324**, 1029–33 (2009).
26. Stark, C., Breitkreutz, B. J., Reguly, T., Boucher, L., Breitkreutz, A. & Tyers, M. BioGRID: a general repository for interaction datasets. *Nucleic Acids Res* **34**, D535–9 (2006).
27. Muller, F. L., Colla, S., Aquilanti, E., Manzo, V. E., Genovese, G., Lee, J., Eisenson, D., Narurkar, R., Deng, P., Nezi, L., Lee, M. A., Hu, B., Hu, J., Sahin, E., Ong, D., Fletcher-Sananikone, E., Ho, D., Kwong, L., Brennan, C., Wang, Y. A., Chin, L. & DePinho, R. A. Passenger deletions generate therapeutic vulnerabilities in cancer. *Nature* **488**, 337–42 (2012).
28. Kuehne, A., Emmert, H., Soehle, J., Winnefeld, M., Fischer, F., Wenck, H., Gallinat, S., Terstegen, L., Lucius, R., Hildebrand, J. & Zamboni, N. Acute Activation of Oxidative Pentose Phosphate Pathway as First-Line Response to Oxidative Stress in Human Skin Cells. *Mol Cell* **59**, 359–71 (2015).
29. Singh, A., Misra, V., Thimmulappa, R. K., Lee, H., Ames, S., Hoque, M. O., Herman, J. G., Baylin, S. B., Sidransky, D., Gabrielson, E., Brock, M. V. & Biswal, S. Dysfunctional KEAP1-NRF2 interaction in non-small-cell lung cancer. *PLoS Med* **3**, e420 (2006).
30. DeNicola, G. M., Karreth, F. A., Humpton, T. J., Gopinathan, A., Wei, C., Frese, K., Mangal, D., Yu, K. H., Yeo, C. J., Calhoun, E. S., Scrimieri, F., Winter, J. M., Hruban, R. H., Iacobuzio-Donahue, C., Kern, S. E., Blair, I. A. & Tuveson, D. A. Oncogene-induced Nrf2 transcription promotes ROS detoxification and tumorigenesis. *Nature* **475**, 106–9 (2011).

31. Ishii, T., Itoh, K., Takahashi, S., Sato, H., Yanagawa, T., Katoh, Y., Bannai, S. & Yamamoto, M. Transcription factor Nrf2 coordinately regulates a group of oxidative stress-inducible genes in macrophages. *J Biol Chem* **275**, 16023–9 (2000).
32. Thimmulappa, R. K., Mai, K. H., Srisuma, S., Kensler, T. W., Yamamoto, M. & Biswal, S. Identification of Nrf2-regulated genes induced by the chemopreventive agent sulforaphane by oligonucleotide microarray. *Cancer Res* **62**, 5196–203 (2002).
33. DeNicola, G. M., Chen, P. H., Mullarky, E., Sudderth, J. A., Hu, Z., Wu, D., Tang, H., Xie, Y., Asara, J. M., Huffman, K. E., Wistuba, I., Minna, J. D., DeBerardinis, R. J. & Cantley, L. C. NRF2 regulates serine biosynthesis in non-small cell lung cancer. *Nat Genet* **47**, 1475–81 (2015).
34. Mitsuishi, Y., Taguchi, K., Kawatani, Y., Shibata, T., Nukiwa, T., Aburatani, H., Yamamoto, M. & Motohashi, H. Nrf2 redirects glucose and glutamine into anabolic pathways in metabolic reprogramming. *Cancer Cell* **22**, 66–79 (2012).
35. Thimmulappa, R. K., Lee, H., Rangasamy, T., Reddy, S. P., Yamamoto, M., Kensler, T. W. & Biswal, S. Nrf2 is a critical regulator of the innate immune response and survival during experimental sepsis. *J Clin Invest* **116**, 984–95 (2006).
36. Zhang, Z., Chen, L., Liu, L., Su, X. & Rabinowitz, J. D. Chemical Basis for Deuterium Labeling of Fat and NADPH. *J Am Chem Soc* **139**, 14368–14371 (2017).
37. Zhang, D. D. & Hannink, M. Distinct cysteine residues in Keap1 are required for Keap1-dependent ubiquitination of Nrf2 and for stabilization of Nrf2 by chemopreventive agents and oxidative stress. *Mol Cell Biol* **23**, 8137–51 (2003).
38. Hsu, P. P. & Sabatini, D. M. Cancer cell metabolism: Warburg and beyond. *Cell* **134**, 703–7 (2008).
39. Dey, P., Baddour, J., Muller, F., Wu, C. C., Wang, H., Liao, W. T., Lan, Z., Chen, A., Gutschner, T., Kang, Y., Fleming, J., Satani, N., Zhao, D., Achreja, A., Yang, L., Lee, J., Chang, E., Genovese, G., Viale, A., Ying, H., Draetta, G., Maitra, A., Wang, Y. A., Nagrath, D. & DePinho, R. A. Genomic deletion of malic enzyme 2 confers collateral lethality in pancreatic cancer. *Nature* **542**, 119–123 (2017).
40. Romero, R., Sayin, V. I., Davidson, S. M., Bauer, M. R., Singh, S. X., LeBoeuf, S. E., Karakousi, T. R., Ellis, D. C., Bhutkar, A., Sanchez-Rivera, F. J., Subbaraj, L., Martinez, B., Bronson, R. T., Prigge, J. R., Schmidt, E. E., Thomas, C. J., Goparaju, C., Davies, A., Dolgalev, I., Heguy, A., Allaj, V., Poirier, J. T., Moreira, A. L., Rudin, C. M., Pass, H. I., Vander Heiden, M. G., Jacks, T. & Papagiannakopoulos, T. Keap1 loss promotes Kras-driven lung cancer and results in dependence on glutaminolysis. *Nat Med* (2017).

41. Muir, A., Danai, L. V., Gui, D. Y., Waingarten, C. Y., Lewis, C. A. & Vander Heiden, M. G. Environmental cystine drives glutamine anaplerosis and sensitizes cancer cells to glutaminase inhibition. *Elife* **6** (2017).
42. Krall, E. B., Wang, B., Munoz, D. M., Ilic, N., Raghavan, S., Niederst, M. J., Yu, K., Ruddy, D. A., Aguirre, A. J., Kim, J. W., Redig, A. J., Gainor, J. F., Williams, J. A., Asara, J. M., Doench, J. G., Janne, P. A., Shaw, A. T., McDonald Iii, R. E., Engelman, J. A., Stegmeier, F., Schlabach, M. R. & Hahn, W. C. KEAP1 loss modulates sensitivity to kinase targeted therapy in lung cancer. *Elife* **6** (2017).
43. Chari, R., Mali, P., Moosburner, M. & Church, G. M. Unraveling CRISPR-Cas9 genome engineering parameters via a library-on-library approach. *Nat Methods* **12**, 823–6 (2015).
44. Doench, J. G., Fusi, N., Sullender, M., Hegde, M., Vaimberg, E. W., Donovan, K. F., Smith, I., Tothova, Z., Wilen, C., Orchard, R., Virgin, H. W., Listgarten, J. & Root, D. E. Optimized sgRNA design to maximize activity and minimize off-target effects of CRISPR-Cas9. *Nat Biotechnol* **34**, 184–91 (2016).
45. Erard, N., Knott, S. R. V. & Hannon, G. J. A CRISPR Resource for Individual, Combinatorial, or Multiplexed Gene Knockout. *Mol Cell* **67**, 348–354 e3 (2017).
46. Vander Heiden, M. G. Targeting cancer metabolism: a therapeutic window opens. *Nat Rev Drug Discov* **10**, 671–84 (2011).
47. Tennant, D. A., Duran, R. V. & Gottlieb, E. Targeting metabolic transformation for cancer therapy. *Nat Rev Cancer* **10**, 267–277 (2010).

Chapter 6

Oncogenic R132 IDH1 mutations limit NADPH for *de novo* lipogenesis through (D)2-hydroxyglutarate production in fibrosarcoma cells

6.1 Abstract

Neomorphic mutations in NADP-dependent isocitrate dehydrogenases (*IDH1* and *IDH2*) contribute to tumorigenesis in several cancers. While significant research has focused on the epigenetic phenotypes associated with (D)2-hydroxyglutarate (D2HG) accumulation, the metabolic consequences of these mutations may also provide therapeutic opportunities. Here we apply flux-based approaches to genetically-engineered sarcoma cell lines with an endogenous *IDH1* mutation to examine the metabolic impacts of increased D2HG production and altered IDH flux as a function of *IDH1* mutation or expression. We demonstrate that R132 *IDH1* mutations alter glutamine metabolism to support D2HG production and secretion, which consumes NADPH

at rates similar to that required for *de novo* lipogenesis. In turn, IDH1 R132C^{+/-} cells exhibit increased dependence on exogenous lipid sources for growth, as removal of medium lipids slows cellular growth more dramatically in IDH1 mutant cells compared to those expressing wild-type or enzymatically inactive alleles. NADPH regeneration may be limiting for lipogenesis and potentially redox homeostasis in *IDH1* mutant tumors, highlighting critical links between cellular biosynthesis and redox metabolism.

6.2 Introduction

Mutations in isocitrate dehydrogenase 1 (*IDH1*) and 2 (*IDH2*) drive tumorigenesis in acute myeloid leukemias, gliomas, sarcomas, and other tumors [1–4]. These gain-of-function mutations modify the activity of IDH1 and IDH2 such that the major reaction catalyzed is the NADPH-mediated reduction of α -ketoglutarate (α KG) to (D)2-hydroxyglutarate (D2HG) [5, 6]. In addition, mutant IDH1 and IDH2 exhibit decreased activity for the wild-type (WT) reaction, which reversibly interconverts isocitrate and NADP⁺ with α KG, CO₂, and NADPH [6]. Therefore, cells harboring such IDH mutations exhibit metabolic reprogramming to compensate for these changes in enzyme activity.

Under hypoxic conditions, IDH1 mutant cells exhibit increased oxidative TCA flux, respiration, and decreased growth [7]. While IDH1 mutant cells do not increase reductive carboxylation in hypoxia to the same extent as cells expressing only WT IDH1, mitochondrial metabolism and redox pathways are re-wired to support the growth of mutant IDH1 cells in culture and *in vivo* [8, 9]. More generally, IDH1 mutant cells exhibit various defects in mitochondrial metabolism which may be therapeutically exploited by targeting NAMPT, BCL2, or other targets [10–13]. These results demonstrate that IDH1 mutant cells exhibit similar metabolism to cells expressing WT IDH1 under basal conditions but altered metabolic states under conditions of bioenergetic or redox stress.

IDH1 is not thought to be a major source of NADPH in mammals [14]. IDH1^{-/-} mice exhibit phenotypes only in select tissues or in response to specific stresses (i.e. nutrient deprivation) [15]. In culture, overall IDH-mediated exchange flux is high, and the reverse reaction can support lipogenesis or compartment-specific redox maintenance in cancer cells under conditions of metabolic stress [16–18]. The oxidative pentose phosphate pathway (oxPPP) is classically thought to be the primary pathway through which NADPH is regenerated in the cytosol [19]. Recent studies using ²H tracing support this concept, where the oxidative PPP exhibits the highest contribution to cytosolic NADPH regeneration supporting biosynthesis [20, 21]. Cell lines engineered to express mutant IDH1 enzymes exhibit increased oxPPP flux and differential lipid synthesis [22], highlighting the importance of this pathway. On the other hand, knockout of oxPPP enzymes is particularly deleterious for cancer cell growth [23].

To better understand how mutations in IDH1 impact NADPH metabolism we applied ¹³C and ²H metabolic flux analysis to an isogenic panel of fibrosarcoma cell lines that endogenously express IDH1^{+R132C} or were engineered to express a WT, R132C mutant, or enzymatically dead IDH1 enzyme after knocking out the original mutant allele [24]. These cell lines recapitulate changes in anchorage-independent growth driven by mutant IDH1 [24] as well as the metabolic defects documented to occur under hypoxia. 2HG production and secretion were a major sink of NADPH in IDH1^{+R132C} cells, though cells could sufficiently compensate by upregulating oxidative PPP flux. However, in lipid-deficient conditions D2HG production and secretion presented a metabolic liability that negatively impacted *de novo* lipogenic flux and *in vitro* cell growth. These results demonstrate that IDH1 R132 mutations may be considered a significant redox liability in tumors, rendering them susceptible to metabolic stress.

6.3 Materials and Methods

6.3.1 Cell culture and stable isotope tracing

HT1080 and HCT116 cells were grown in DMEM supplemented with 10% FBS and 100 U/mL penicillin/streptomycin. HT1080 parental cells were obtained from ATCC. HCT116 parental and IDH1 knock-in clones (+/R132C; 2H1 and 2A9) were obtained from Horizon Discovery. Cells were maintained in humidified incubator at 5% CO₂. For hypoxia experiments, cells were maintained in humidified glove box (Coy) at 5% CO₂ and 1% O₂.

For delipidated cell growth experiments, cells were plated in basal DMEM media. Cells were then allowed to adhere for 4 hours and then media was exchanged to delipidated media. Final cell counts were obtained after 48 hours.

For isotopic labeling experiments, cells were plated in basal growth experiments and then rinsed with PBS before addition of tracing media. Cells were cultured in glucose- and glutamine-free media (Gibco) supplemented with 10% dialyzed FBS, 100 U/mL penicillin/streptomycin, 4mM glutamine, and 25mM glucose. For glutamine tracing, cells were supplied ¹²C glucose (Sigma) and [U-¹³C₅]glutamine (99%, Cambridge Isotope Laboratories). For glucose tracing, cells were supplied ¹²C glutamine (Sigma) and either [3-²H]glucose (99%, Cambridge Isotope Laboratories), [4-²H]glucose (99%, Omicron Biochemicals), [U-¹³C₆]glucose (99%, Cambridge Isotope Laboratories), or [1,2-¹³C]glucose (99%, Cambridge Isotope Laboratories). For delipidated tracing experiments, media was prepared in same way except using 10% dialyzed and delipidated FBS.

6.3.2 Delipidation of FBS

Normal or dialyzed FBS (Gibco) was delipidated by first stirring 20 mg/mL fumed silica (Sigma) for 3 hrs in ambient conditions. FBS slurry was then clarified by repeated centrifugation at 2000 g for 20 min. Supernatant was then sterile filtered (0.2 m), aliquoted, and stored for at

-20°C for future use.

6.3.3 Metabolite Extraction and GC-MS Analysis

Cells were rinsed with 0.9% (w/v) saline and 250 μ L of -80°C MeOH was added to quench metabolic reactions. 100 μ L of ice-cold water supplemented with 10 μ g/mL norvaline was then added to each well and cells were collected by scraping. The lysate was moved to a fresh 1.5 mL sample tube and 250 μ L of -20°C chloroform supplemented with 4 μ g/mL D31 palmitate was added. After vortexing and centrifugation, the top aqueous layer and bottom organic layer were collected and dried under airflow.

Derivatization of aqueous metabolites was performed using the Gerstel MultiPurpose Sampler (MPS 2XL). Methoxime- derivatives were formed by addition of 15 μ L 2% (w/v) methoxylamine hydrochloride (MP Biomedicals) in pyridine and incubated at 45°C for 60 minutes. Samples were then silylated by addition of 15 μ L of N-tert-butyldimethylsilyl-N-methyltrifluoroacetamide (MTBSTFA) with 1% tert-butyldimethylchlorosilane (tBDMS) (Regis Technologies) and incubated at 45°C for 30 minutes. Aqueous metabolites were analyzed by GC-MS using a DB-35MS column (30 m x 0.25 mm i.d. x 0.25 μ m, Agilent J&W Scientific, Santa Clara, CA) installed in an Agilent 7890B gas chromatograph (GC) interfaced with a 5977C mass spectrometer (MS). For separation of aqueous metabolites, the GC oven was held at 100°C for 1 min after injection, increased to 255°C at 3.5°C/min, and finally increased to 320°C at 15°C/min and held for 3 min. Electron impact ionization was performed with the MS scanning over the range of 100-650 m/z.

Dried organic fraction was saponified and esterified to form fatty acid methyl esters (FAMES) by addition of 500 μ L of 2% (w/v) H₂SO₄ in MeOH and incubated at 50°C for 120 minutes. FAMES were then extracted by addition of saturated NaCl and hexane before collection and drying of the inorganic layer. Derivatized fatty acids were analyzed by GC-MS using a select FAME column (100 m x 0.25 mm i.d. x 0.25 μ m; Agilent J&W Scientific) installed in an Agilent

7890A gas chromatograph (GC) interfaced with a 5975C mass spectrometer (MS). For separation the GC oven was held at 80°C for 1 min after injection, increased to 160°C at 20°C/min, increased to 198°C at 1°C/min, and finally increased to 250°C at 5°C/min and held for 15 min. Electron impact ionization was performed with the MS scanning over the range of 120-400 m/z.

6.3.4 Metabolite integration and isotopomer spectral analysis (ISA)

Isotopologue distributions and total abundances were determined by integration of mass fragments (Table S6.1) and correcting for natural abundances using in-house MATLAB-based algorithm.

Isotopomer spectral analysis (ISA) was performed to estimate contribution of oxPPP to cytosolic NADPH as previously described [25]. ISA compares experimental labeling of palmitate after 72 hr trace with [3-²H]glucose to simulated labeling using a reaction network where C16:0 is condensation of 14 NADPHs. Parameters for contribution of PGD to lipogenic NADPH (D value) and percentage of newly synthesized fatty acid (g(t) value) and their 95% confidence intervals are then calculated using best-fit model from INCA MFA software [26]. Contribution of oxPPP was then estimated by doubling D value to account for stoichiometry of the oxPPP pathway.

Estimation of contribution of glucose and glutamine to lipogenic AcCoA was conducted as similar method to oxPPP contribution. Experimental fatty acid labeling from [U-¹³C₆]glucose or [U-¹³C₅]glutamine after 72 hr trace was compared to simulated labeling using a reaction network where C16:0 is condensation of 8 AcCoA. ISA data plotted as mean ± 95% CI. * indicates statistical significance by non-overlapping confidence intervals.

6.3.5 Measurement of extracellular and intracellular fluxes

Initial and final concentrations of extracellular glucose, lactate, glutamine, and glutamate were determined by Yellow Springs Analyzer 2950 instrument. In parallel, cells were plated for

initial and final cell counts. Plated cells were pre-adapted to delipidated DMEM media for 24 hrs before experiment.

The extracellular fluxes were described by the following differential equations:

$$\frac{dX}{dt} = \mu X$$

$$\frac{dN_i}{dt} = q_i X$$

$$\frac{dN_{gln}}{dt} = q_i X - k N_{gln}$$

where, X is concentration of cells, μ is cellular growth (hr^{-1}), N is extracellular moles of metabolite i present, q_i is cell-specific consumption rate of metabolite i (mol/cell-hr), and k is first-order degradation rate of glutamine in cell culture (hr^{-1}). k was set to 0.0045 hr^{-1} as determined in literature [27].

Solution of ODEs yielded the following equations which we used to find extracellular fluxes:

$$X = X_0 e^{\mu t}$$

$$q_i = \frac{\mu(N_i - N_{i,0})}{\left(\frac{1}{\mu+k}\right)(X - X_0 e^{-kt})}$$

$$q_{gln} = \frac{N_{gln} - N_{gln,0} e^{-kt}}{\left(\frac{1}{\mu+k}\right)(X - X_0 e^{-kt})}$$

where subscript 0 signifies initial concentration.

For oxPPP measurement, glucose uptake measurement was coupled to ratio of $\frac{M1}{(M1+M2)}$ lactate label from $[1,2-^{13}\text{C}]$ glucose tracer.

6.3.6 NADPH consumption

For fatty acid synthesis, consumption was defined as NADPH flux required to support biosynthesis of myristate (C14:0), palmitate (C16:0), stearate (C18:0), and oleate (C18:1) as these are predominantly synthesized species [14]. Cells were traced with [U-¹³C₆]glucose for 24 hrs and extracted for intracellular metabolites. In parallel, initial and final cell counts were taken. Per cell molar abundance of fatty acid species was determined by GC/MS. Percentage newly synthesized fatty acid determined by ISA with reaction network where C14:0 is condensation of 7 AcCoA, C16:0 is condensation of 8 AcCoA, C18:0 is condensation of 9 AcCoA, and C18:1 is condensation of 9 AcCoA. Molar fatty acid synthesis flux was then calculated by dividing molar newly synthesized fatty acids by integral viable cell density over experimental time period. NADPH flux was then calculated by stoichiometric requirement of 12 NADPH per myristate, 14 NADPH per palmitate, 16 NADPH per stearate, and 17 NADPH per oleate.

For 2HG production fluxes, consumption was defined as NADPH flux required to support 2HG efflux and maintenance of intracellular abundance. Initial and final concentrations of extracellular 2HG were determined by GCMS analysis and use of external standard curves. Per cell molar abundance of 2HG was determined by GCMS at final time point. Efflux was then calculated similarly as above and dilutive flux was calculated by dividing intracellular concentration by specific growth rate. NADPH flux was then calculated by stoichiometric requirement of one NADPH per 2HG.

6.3.7 RT-PCR

Total mRNA was isolated from cells using RNA isolation kit (RNeasy Mini Kit; QIAGEN). Isolated RNA was reverse transcribed using cDNA synthesis kit (High-capacity cDNA Reverse Transcription Kit; Thermo Fisher Scientific). Real-time PCR was performed using SYBR green reagent (iTaq Universal SYBR Green Supermix; Bio-Rad). Relative expression was determined

using Livak ($\Delta\Delta\text{CT}$) method with *GAPDH* as housekeeping gene. Primers used were taken from Primerbank [28] and tabulated in Table S6.2. All commercial kits were used per the manufacturer's protocol.

6.3.8 Quantification and Statistical Analysis

Unless indicated, all results shown as mean \pm SEM of biological triplicates. P values were calculated using a Student's two-tailed t test; *, P value between 0.01 and 0.05; **, P value between 0.001 and 0.01; ***, P value <0.001 . Unless indicated, all normalization and statistical tests compared to WT cells.

6.4 Results

6.4.1 Use of genetically-engineered HT1080 fibrosarcoma cell lines to dissect enzymatic functions of *IDH1* and mutant *IDH1*

D2HG production in cells harboring R132 mutations in *IDH1* is dramatically increased and has an established role in tumorigenesis. Here we interrogated redox metabolism of fibrosarcoma cells using a genetically-engineered panel of cell lines that recapitulate the metabolic reprogramming associated with oncogenic *IDH1* mutations. In this system, the mutant *IDH1* allele was knocked out of HT1080 fibrosarcoma cells (+/R132C) generating HT1080 heterozygous cell line for *IDH1* (+/-). Next, an isogenic *IDH1* mutant panel was then re-expressed in the HT1080 *IDH1* (+/-) cell line generating vector control (PB; +/-), engineered wild-type *IDH1* (WT; +/+), re-expressed *IDH1* mutant (R132C; +/-R132C), and catalytically-dead double mutant, (T77A; +/- R132C-T77A) cell lines [24]. As depicted in Figure 6.1A, these cell lines exhibit distinct reprogramming of IDH1 enzymatic activity such that PB and WT cells maintain endogenous activity and do not readily produce D2HG, R132C mutants have reduced endogenous IDH1

activity and produce D2HG, while T77A mutants have reduced endogenous IDH1 activity and do not accumulate D2HG [24]. Therefore, we could interrogate the distinct metabolic consequences of modulating WT IDH1 activity as well as neomorphic D2HG production by IDH1 R132C.

We first quantified per cell organic and amino acid abundances in each cell type, observing R132C-specific changes in abundance of glutamine and aKG (Figure 6.1B). In addition, we detected increased levels of non-essential amino acids (i.e. Glu, Ser, Pro, and Asp), consistent with previously described increases in glutaminolysis in *IDH1* mutant cells [7, 12]. We also observed elevated levels of Gly3P in R132C cells, suggesting that mitochondrial and/or cytosolic redox metabolism is perturbed in D2HG producing cells (Figure 6.1B). On the other hand, intracellular abundance of most glycolytic metabolites, TCA metabolites, and other amino acids were not perturbed by altered IDH1 enzymatic function (Figure 6.1B). These results are consistent with general dispensability of IDH1 function in basal culture conditions [7].

Next, we characterized alterations in IDH flux in this isogenic fibrosarcoma cell line panel. Under conditions of hypoxia, IDH1 and IDH2 can support *de novo* lipogenesis by catalyzing the reductive carboxylation of aKG to isocitrate, which is subsequently metabolized to citrate and acetyl-coenzyme A (AcCoA) [17]. We previously demonstrated that HCT116 cells harboring *IDH1* mutations are defective in their ability to convert glutamine carbon to citrate and AcCoA [7]. To this end, we cultured each HT1080 cell line in the presence of uniformly-labeled ¹³C glutamine ([U-¹³C₅]glutamine) and quantified the isotopologue distribution of metabolites in central carbon metabolism (Figure 6.1C). We observed a significant decrease in M+5 citrate in R132C cells cultured in hypoxia compared to those expressing only functional wild-type IDH1, indicating that R132C-expressing cells were limited in their ability to generate citrate via reductive carboxylation (Figure 6.1D and S6.1A). We also observed a concomitant increase in M+4 citrate in R132C cells, consistent with previously described reliance of IDH1 mutant cells on oxidative glutaminolysis in hypoxia (Figure S6.1A-B) [7]. We also observed altered labeling of aspartate from [U-¹³C₅]glutamine that is consistent with decreased reductive carboxylation flux

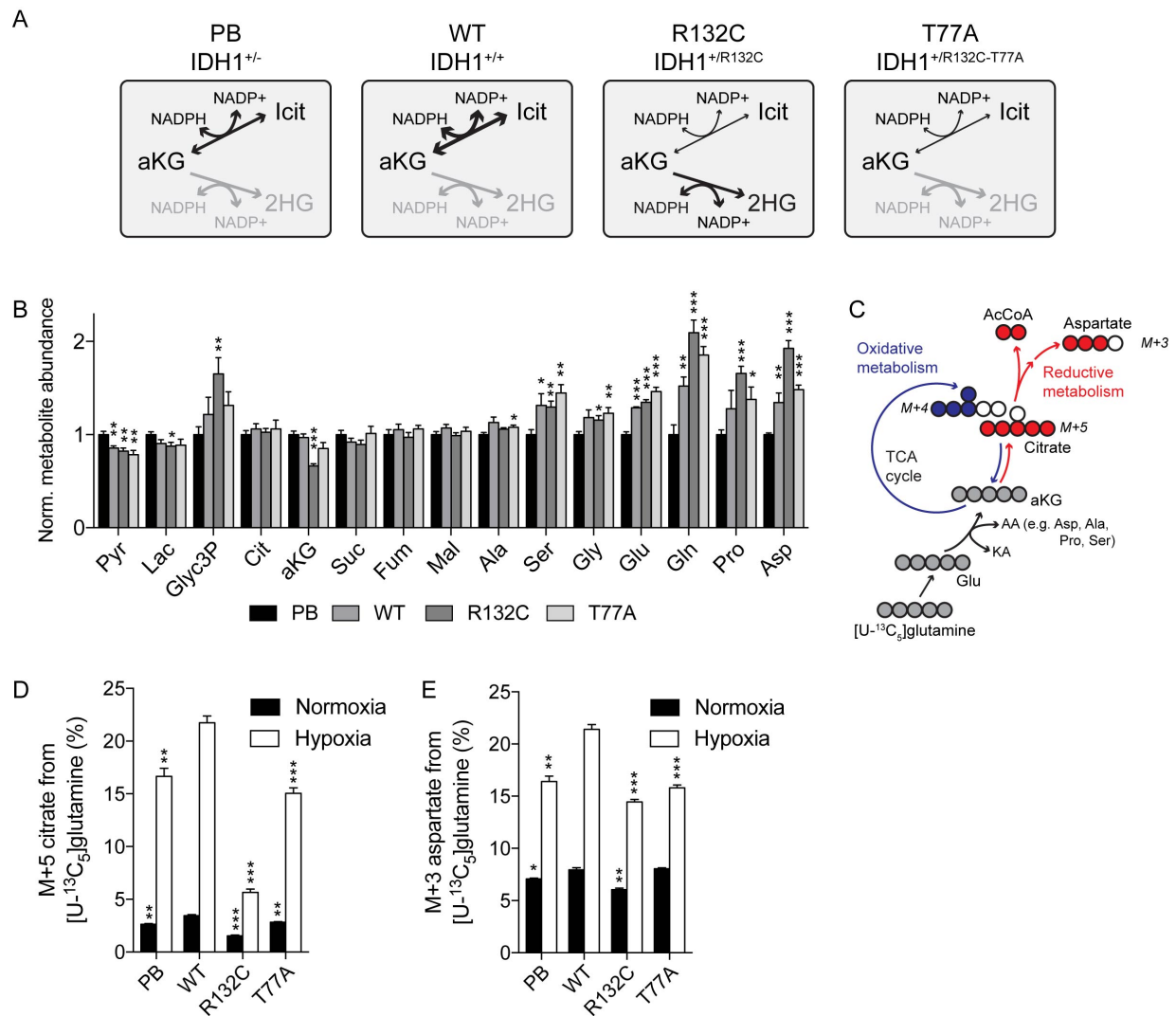


Figure 6.1: Metabolic characterization of isogenic IDH1-expressing HT1080 cell lines. (A) Depiction of enzymatic activity present in each cell line. (B) Relative intracellular abundance of glycolytic intermediates, TCA cycle metabolites, and amino acids (n=6). Normalized to PB. (C) Atom transition map of $[U-^{13}C_5]$ glutamine for reductive and oxidative metabolism. Glutaminase and transamination of glutamate to aKG requires concomitant amination of keto-acids (KA) to amino acids (AA) (e.g. Asp, Ala, Pro, Ser). Oxidative TCA flux leads to M+4 citrate. Reductive carboxylation of aKG leads to the M+5 citrate and subsequently M+3 aspartate. (D) Percentage of M+5 citrate from $[U-^{13}C_5]$ glutamine in normoxia and hypoxia. (E) Percentage of M+3 aspartate from $[U-^{13}C_5]$ glutamine in normoxia and hypoxia.

for generating cytosolic AcCoA (Figure 6.1E and S6.1C). This isogenic panel of HT1080 cells therefore recapitulates hallmarks of cancer cells expressing oncogenic IDH1 mutations. Notably, WT *IDH1* cells had the highest abundance of M+5 citrate and M+3 aspartate isotopologues, while PB and T77A cells (which have only one WT *IDH1* allele) had intermediate levels of these isotopologues (Figure 6.1D-E).

6.4.2 Cytosolic NADPH contributes to D2HG production from *IDH1*^{+/R132C} cells

Basal *IDH1* enzymatic function can facilitate both production and consumption of NADPH and is decreased in *IDH1* mutant cells [6, 29, 30], suggesting cellular redox may be perturbed in these cells. To this end, we also observed elevated levels of Gly3P in R132C cells (Figure 6.1B). To investigate how redox metabolism is altered by *IDH1* mutation, we cultured cells in the presence of [4-²H]glucose and quantified enrichment on downstream metabolites (Figure 6.2A). This tracer specifically labels cytosolic NADH via GAPDH, and these deuterons are subsequently transferred to lactate, malate, and Gly3P by downstream oxidoreductases [25]. We observed similar labeling in all cells tested (Figure 6.2B), indicating that no gross changes in NAD⁺ regeneration occurred upon perturbation of IDH1 activity.

We next examined how NADPH metabolism is altered in these cell lines, as D2HG production by R132C IDH1 relies on the NADPH-dependent reduction of αKG. As NADPH and NADH pools are interconnected through transhydrogenase shuttles and enzymes [31], the redox pathways that support 2HG production are not well understood. Indeed, D2HG accumulates to high millimolar intracellular concentrations in IDH mutant cells [5], and we observed a drastic increase in intracellular 2HG only in R132C cells (Figure 6.2C). However, we also detected low levels of 2HG in cell lines expressing only WT IDH1 or enzymatically-dead R132C-T77A IDH1 and hypothesized that L2HG was endogenously produced in these cells. To investigate the enantiomer of 2HG and source of reducing equivalents used for 2HG production in these

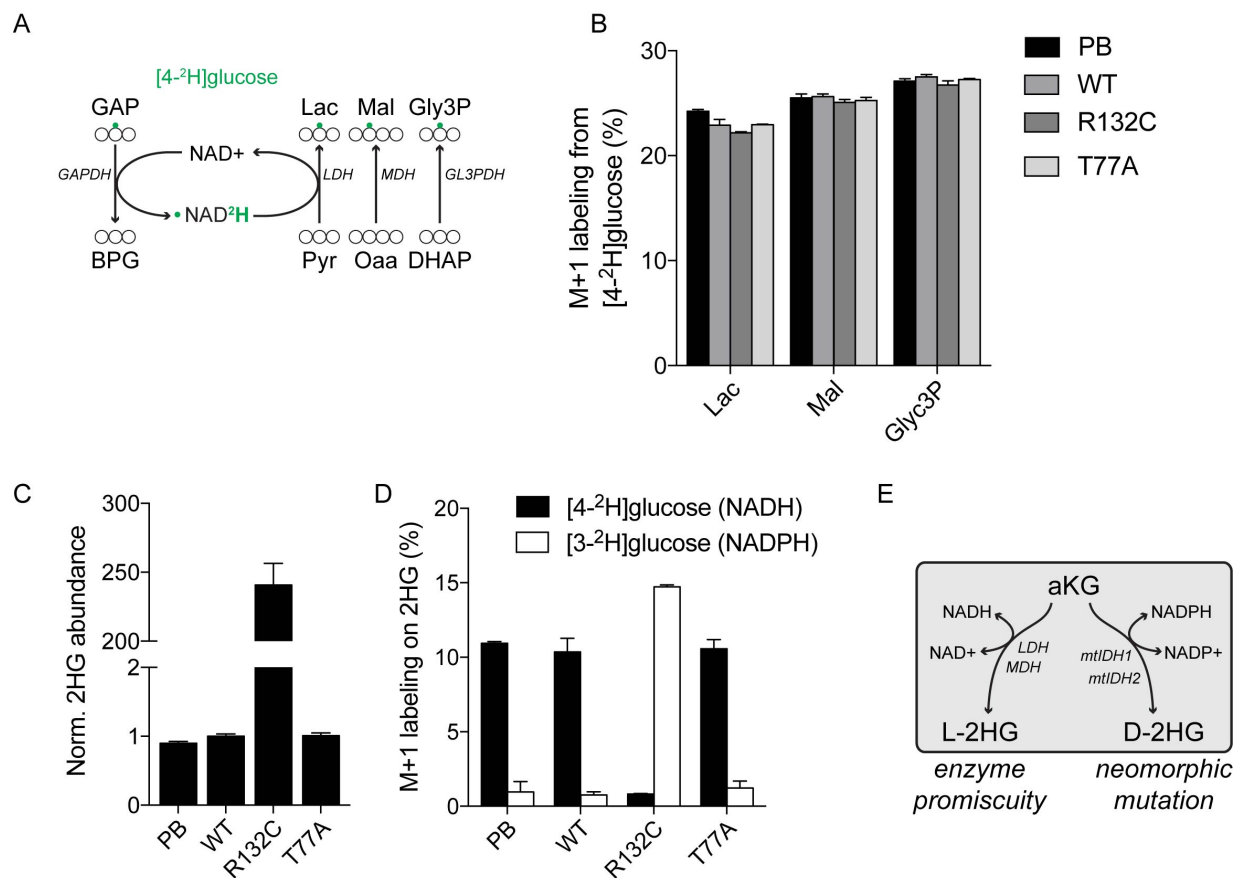


Figure 6.2: Tracing NAD(P)H regeneration and 2HG production in HT1080-IDH1 cell lines. (A) Atom transition map of [4-²H]glucose. The tracer labels cytosolic NADH through GAPDH, leading to downstream labeling through lactate dehydrogenase (LDH), malate dehydrogenase (MDH), and glycerol-3-phosphate dehydrogenase (Gly3PDH). (B) Percentage M+1 label from [4-²H]glucose is not altered by IDH1 status. (C) Relative intracellular abundance of 2-hydroxyglutarate is increased in R132C cells. (D) Percentage M+1 2HG label from [4-²H]glucose and [3-²H]glucose. (E) Depiction of L2HG and D2HG production by NAD(P)H.

cell lines, we cultured each cell type with [4-²H]glucose or [3-²H]glucose, which label NADH and NADPH respectively, and quantified 2HG labeling via GC-MS [25]. Results were distinct in that [4-²H]glucose labeled approximately 10% of 2HG in PB, WT, and T77A cells while [3-²H]glucose labeled 15% of 2HG in R132C cells (Figure 6.2D). These data suggest that L2HG is the predominant enantiomer present in cells expressing only WT IDH1, which has been demonstrated to be a byproduct of lactate dehydrogenase (LDH) or malate dehydrogenase (MDH) in cancer cells (Figure 6.2E) [32, 33]. Notably, 2HG enrichment from [3-²H]glucose was similar to the expected enrichment of cytosolic NADPH calculated from fatty acid labeling (Figure 6.3C) [25]. L2HG enrichment was significantly lower than that observed for lactate, malate, and Gly3P, suggesting that some 2HG is present in cells with WT *IDH1*. Ultimately, these results highlight the utility of deuterium-tracing in assessing redox metabolism associated with altered IDH1 metabolism.

6.4.3 2HG production contributes significantly to cellular NADPH demands

We next attempted to estimate how D2HG production and other pathways contribute to NADPH demands within cells by quantifying 2HG secretion flux. *de novo* lipogenesis (DNL) has been estimated to be the largest consumer of NADPH in cultured cells [14]. We measured DNL flux for fatty acid synthesis using [U-¹³C₆]glucose and isotopomer spectral analysis and compared the NADPH requirements for DNL and 2HG (Figure 6.3A). Strikingly, we found that the NADPH demand for D2HG production was relatively similar to that required for DNL (Figure 6.3A). Importantly, most D2HG-associated NADPH consumption was from the efflux of D2HG, consistent with significant demand of carbon associated with efflux [7].

We then asked if the consumption of NADPH by D2HG production reprogrammed the redox metabolic network. The largest source of cytosolic NADPH in cells is the oxPPP [21]. To probe any alterations in oxPPP redox function, we utilized a modeling approach to estimate the

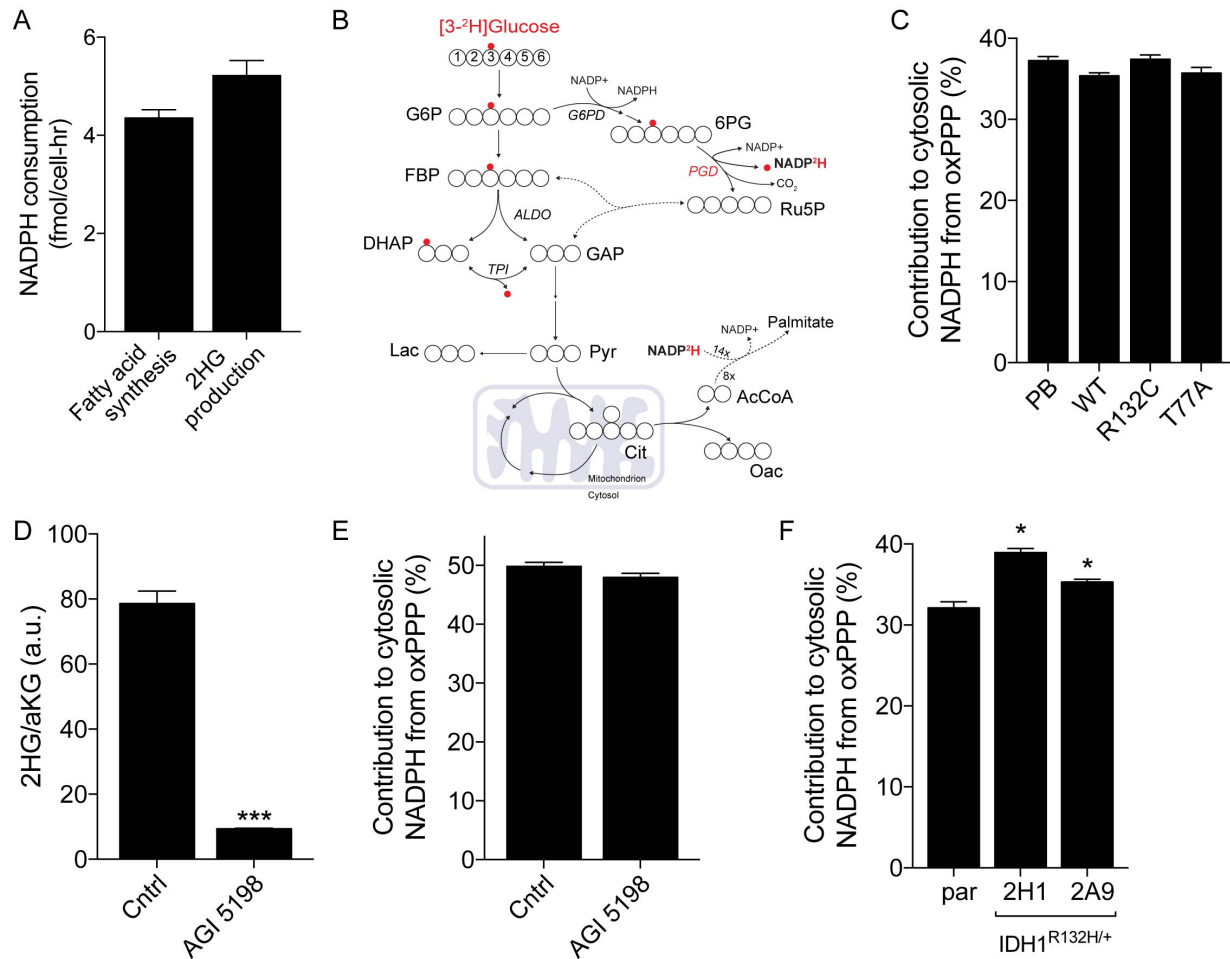


Figure 6.3: D2HG production and secretion increases NADPH demands in IDH1^{+/R132C} cells. (A) NADPH consumption fluxes by lipid synthesis and 2HG production in R132C cells. (B) Atom transition map of [3-²H]glucose. (C) Contribution of oxPPP to cytosolic NADPH in fibrosarcoma panel. (D) 2HG abundance in parental HT1080 cells upon treatment with 10 μ M AGI-5198. (E) Contribution of oxPPP to cytosolic NADPH in parental HT1080 cells with 10 μ M AGI-5198. (F) Contribution of oxPPP to cytosolic NADPH in non-native IDH1-R132H engineered HCT116 cells. (C,E-F) Data plotted as mean \pm 95% CI. * indicates statistical significance by non-overlapping confidence intervals.

fraction of NADPH supplied by oxPPP (Figure 6.3B) [25]. Despite the increased R132C-specific consumption of NADPH by D2HG production, we found no change in the relative proportion of NADPH supplied by the oxPPP across these cell lines (Figure 6.3C). To control for any clonal effects associated with production of the cell line panel, we then inhibited D2HG production in the parental HT1080 cell line using AGI-5198, a pharmacological inhibitor of mutant IDH1 [34]. We observed a 90% reduction in 2HG/aKG levels with AGI-5198 addition, implying a reduction in NADPH consumption by D2HG production (Figure 6.3D). However, inhibition of NADPH consumption did not alter NADPH supplied by oxPPP (Figure 6.3E). Taken together our data indicate that D2HG production does not alter the contribution of oxPPP flux to redox homeostasis, as cells are able to sufficiently rewire pathways to compensate for the increased NADPH demand. Indeed, we also quantified the contribution of oxPPP flux to lipogenic NADPH using engineered HCT116 cells with knock-in of mutant IDH1. IDH1^{+R132H} HCT116 cells exhibited increased contributions of oxPPP to lipogenic NADPH pools (Figure 6.3F), highlighting the ability of cells to reprogram redox pathways to meet the increased demands for NADPH caused by oncogenic D2HG production.

6.4.4 *De novo* lipogenesis competes with D2HG production for NADPH

Our results suggest that R132C cells are able to compensate for NADPH consumed by D2HG production under normal growth conditions. However, this metabolic defect could become a liability in the context of altered nutrient conditions. Recent work has demonstrated the utility in altering extracellular nutrient conditions to understand cancer-specific metabolic liabilities and sparked an interest in engineering more physiologic media [35]. The tumor microenvironment is generally considered to be nutrient-deficient, and tumor cells upregulate DNL to synthesize lipids necessary for growth [36]. Indeed, lipogenesis is necessary for *in vitro* and *in vivo* tumor growth, and limitations in this pathway renders tumor cells more susceptible to chemotherapeutics [37]. To this end, we hypothesized that removal of exogenous lipids from cell culture media could alter

R132C-specific growth by limiting the NADPH available for DNL flux. We observed that R132C cell growth was specifically decreased in delipidated culture conditions (Figure 6.4A). We also confirmed that R132C cells exhibited decreased molar palmitate synthesis flux, suggesting the observed growth defect was mediated by an inability to synthesize enough lipids (due to limited NADPH) (Figure 6.4B).

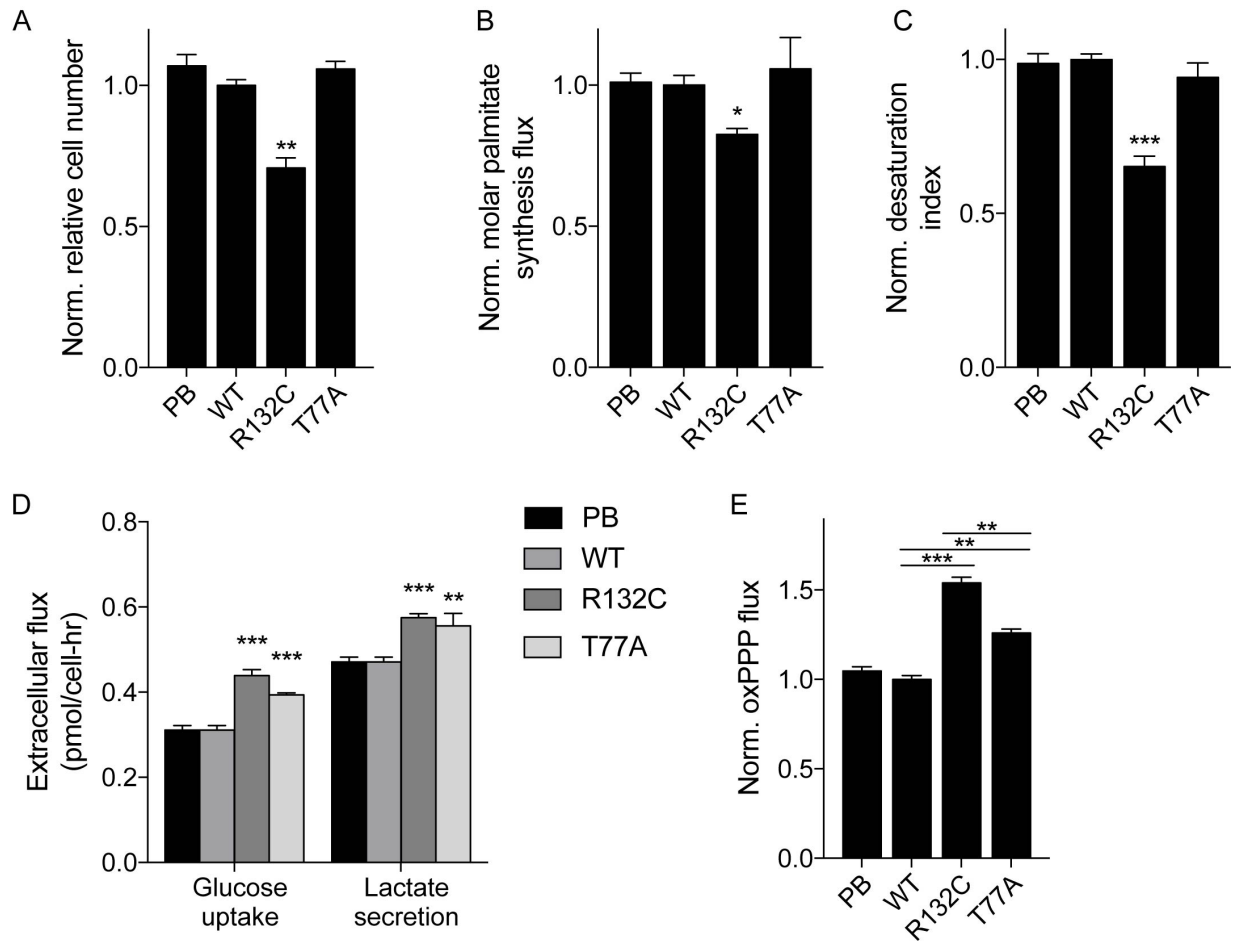


Figure 6.4: D2HG production limits NADPH for DNL in lipid-deficient conditions. (A) Relative cell number after 48 hrs of cell growth in delipidated conditions. (B) Normalized molar palmitate synthesis flux. (C) Normalized desaturation index (C18:1/C18:0). (D) Extracellular glucose uptake and lactate efflux. (E) Normalized oxPPP flux in delipidated conditions.

We then asked what specific metabolic liability could be causing DNL-defect in R132C cells. DNL is critical biosynthetic process that requires the coordination of many enzymes

and sufficient anabolic substrates (i.e. AcCoA and NADPH). As many possible factors could decrease DNL, we investigated potential drivers of this observed growth defect (Figure 6.4A). We observed no alteration in the contribution of oxPPP flux to lipogenic NADPH, indicating that other pathways were not distinctly compensating (Figure S6.2A). 2HG has been widely characterized as an inhibitor of aKG-dependent dioxygenase class enzymes that include important epigenetic modifiers [38–41]. We also observed that expression of genes associated with fatty acid synthesis was not altered in R132C cells, implying that the production of D2HG, rather than a downstream epigenetic modification, was causing defect (Figure S6.2B). We detected a slight increase in glucose contribution to lipogenic AcCoA, consistent with 2HG production shunting glutamine carbon away from DNL (Figure S6.2C). We also observed a concomitant increase in net glutamine anaplerosis in R132C cells cultured under delipidated conditions that could support 2HG production without limiting carbon for DNL (Figure S6.2D). However, these changes are unlikely to account for the increased NADPH demand in R132C cells.

On the other hand, the desaturation index (C18:1/C18:0) quantified from total fatty acids in each cell line was significantly decreased in R132C cells (Figure 6.4B). Production of desaturated fatty acid species requires SCD activity, molecular oxygen, and NADPH [42, 43]. Since we did not detect changes in SCD expression (Figure S6.2B) and molecular oxygen is not limiting under normoxic conditions, this result suggests that NADPH was limiting R132C cells and could explain the decreased palmitate synthesis observed in R132C cells (Figure 6.4B).

Finally, to better understand how NADPH regeneration fluxes were altered, flux through glycolysis and the oxPPP were quantified across the cell panel. We observed increased glycolytic fluxes in both R132C and T77A cells as compared to WT (Figure 6.4D). Increased glycolytic flux is generally associated with altered mitochondrial state, but our data suggests that mitochondrial pathways are maintained by reprogramming of glutamine metabolism [7]. However, increased glucose uptake can also result in elevated oxPPP flux if branching is unchanged. We cultured cells in the presence of [1,2-¹³C]glucose tracer to understand the relative shunting of glucose

carbon through glycolysis and the oxPPP [44]. We observed no difference in relative shunting to the oxPPP across the cell lines (Figure S6.2E). However, when combined with the increased glucose uptake and lactate efflux detected in R132C cells, these data indicate that oxPPP flux is significantly increased to meet the additional NADPH demands for D2HG production (Figure 6.4E). Importantly, R132C cells increase glucose uptake and oxPPP flux to a greater extent than T77A cells, implying that oxPPP flux and NADPH production is further increased to support D2HG production (Figure 6.4E). In turn, the cells are unable to fully compensate for these NADPH demands and growth is reduced in lipid-deficient conditions.

6.5 Discussion

The unique nature of IDH mutant tumors has motivated a large research effort to identify potential targets within their signaling and metabolic networks [45–48]. The dramatic accumulation of 2HG in these tumors has focused much attention on the role of aKG-dependent dioxygenases in driving tumorigenesis [49]. However, as IDH1 and IDH2 play critical roles in TCA metabolism and redox homeostasis, a greater understanding of the metabolic reprogramming required to support this unique liability may yield clues to additional therapeutic opportunities [50].

Maintenance of redox homeostasis is essential for proper cell function, as pyridine nucleotides orthogonally connect bioenergetic and biosynthetic metabolic pathways [51]. Specifically, the regeneration of NADPH is required for anabolism of lipids, DNA, and proline as well as maintenance of reduced glutathione pools [14]. However, the role of *IDH1* in the maintenance of redox homeostasis has been underappreciated. *IDH1* can functionally participate in a redox shuttle that interconnects mitochondrial and cytosolic NAD(P)H pools [52]. Indeed, this shuttle has been demonstrated to be critical for redox homeostasis in anchorage-independent conditions [16]. Upregulation of *IDH1* can promote the survival of pancreatic cancer cell lines under nutrient-

limited conditions [53]. However, the largest source of NADPH in the cell is the oxPPP [14, 21, 25]. Targeting of oxPPP enzymes is particularly deleterious to growth of cancer cell lines [23, 54, 55], and coordinated therapeutic strategies that promote redox stress (e.g. nutrient modulation, radiation) while targeting redox pathway may become attractive options in future [56].

Our work demonstrates the potential for such strategies (albeit in cell culture). We found that D2HG production is a major sink of NADPH, but redox metabolism is reprogrammed to support production. However, when cells are challenged by lipid-deficiency that drives cells to upregulate DNL flux, D2HG production becomes a metabolic liability that limits growth. Similar findings have recently been reported using engineered HCT116 cells [22]. Other pathways have also been described to compensate for such redox defects. For example, *IDH1* mutant glioma cells maintain redox homeostasis by enhancing the mitochondrial production of proline [57]. Metabolic profiling of low grade gliomas has also correlated tumor progression with altered redox state [58]. Our results and others highlight potential therapeutic efficacy in targeting redox metabolism for mutant IDH tumors.

6.6 Acknowledgements

This work was supported by the California Institute of Regenerative Medicine (RB5-07356 to C.M.M.), NIH grant (R01CA188652 to C.M.M.), Camille and Henry Dreyfus Teacher-Scholar (to C.M.M.), NSF CAREER (1454425 to C.M.M.), and NIH grant (R01CA196878 to K.L.G.). M.G.B. is supported by a NSF Graduate Research Fellowship (DGE-1144086).

Chapter 6, in full, has been submitted for publication of the material as it may appear in "Oncogenic R132 IDH1 mutations limit NADPH for *de novo* lipogenesis through (D)2-hydroxyglutarate production in fibrosarcoma cells," *Cell Reports*, 2018. Mehmet G. Badur is the primary author of this publication. Thangaselvam Muthusamy, Seth J. Parker, Shenghong Ma, Thekla Cordes, Jose H. Magana, Kun-Liang Guan are co-authors of this publication. Christian M.

Metallo is the corresponding author of this publication.

6.7 References

1. Mardis, E. R., Ding, L., Dooling, D. J., Larson, D. E., McLellan, M. D., Chen, K., Koboldt, D. C., Fulton, R. S., Delehaunty, K. D., McGrath, S. D., Fulton, L. A., Locke, D. P., Magrini, V. J., Abbott, R. M., Vickery, T. L., Reed, J. S., Robinson, J. S., Wylie, T., Smith, S. M., Carmichael, L., Eldred, J. M., Harris, C. C., Walker, J., Peck, J. B., Du, F., Dukes, A. F., Sanderson, G. E., Brummett, A. M., Clark, E., McMichael, J. F., Meyer, R. J., Schindler, J. K., Pohl, C. S., Wallis, J. W., Shi, X., Lin, L., Schmidt, H., Tang, Y., Haipek, C., Wiechert, M. E., Ivy, J. V., Kalicki, J., Elliott, G., Ries, R. E., Payton, J. E., Westervelt, P., Tomasson, M. H., Watson, M. A., Baty, J., Heath, S., Shannon, W. D., Nagarajan, R., Link, D. C., Walter, M. J., Graubert, T. A., DiPersio, J. F., Wilson, R. K. & Ley, T. J. Recurring mutations found by sequencing an acute myeloid leukemia genome. *N Engl J Med* **361**, 1058–66 (2009).
2. Parsons, D. W., Jones, S., Zhang, X., Lin, J. C., Leary, R. J., Angenendt, P., Mankoo, P., Carter, H., Siu, I. M., Gallia, G. L., Olivi, A., McLendon, R., Rasheed, B. A., Keir, S., Nikolskaya, T., Nikolsky, Y., Busam, D. A., Tekleab, H., Diaz L. A., J., Hartigan, J., Smith, D. R., Strausberg, R. L., Marie, S. K., Shinjo, S. M., Yan, H., Riggins, G. J., Bigner, D. D., Karchin, R., Papadopoulos, N., Parmigiani, G., Vogelstein, B., Velculescu, V. E. & Kinzler, K. W. An integrated genomic analysis of human glioblastoma multiforme. *Science* **321**, 1807–12 (2008).
3. Sjoblom, T., Jones, S., Wood, L. D., Parsons, D. W., Lin, J., Barber, T. D., Mandelker, D., Leary, R. J., Ptak, J., Silliman, N., Szabo, S., Buckhaults, P., Farrell, C., Meeh, P., Markowitz, S. D., Willis, J., Dawson, D., Willson, J. K., Gazdar, A. F., Hartigan, J., Wu, L., Liu, C., Parmigiani, G., Park, B. H., Bachman, K. E., Papadopoulos, N., Vogelstein, B., Kinzler, K. W. & Velculescu, V. E. The consensus coding sequences of human breast and colorectal cancers. *Science* **314**, 268–74 (2006).
4. Yan, H., Parsons, D. W., Jin, G., McLendon, R., Rasheed, B. A., Yuan, W., Kos, I., Batinic-Haberle, I., Jones, S., Riggins, G. J., Friedman, H., Friedman, A., Reardon, D., Herndon, J., Kinzler, K. W., Velculescu, V. E., Vogelstein, B. & Bigner, D. D. IDH1 and IDH2 mutations in gliomas. *N Engl J Med* **360**, 765–73 (2009).
5. Dang, L., White, D. W., Gross, S., Bennett, B. D., Bittinger, M. A., Driggers, E. M., Fantin, V. R., Jang, H. G., Jin, S., Keenan, M. C., Marks, K. M., Prins, R. M., Ward, P. S., Yen, K. E., Liau, L. M., Rabinowitz, J. D., Cantley, L. C., Thompson, C. B., Vander Heiden, M. G. & Su, S. M. Cancer-associated IDH1 mutations produce 2-hydroxyglutarate. *Nature* **462**, 739–44 (2009).

6. Ward, P. S., Patel, J., Wise, D. R., Abdel-Wahab, O., Bennett, B. D., Collier, H. A., Cross, J. R., Fantin, V. R., Hedvat, C. V., Perl, A. E., Rabinowitz, J. D., Carroll, M., Su, S. M., Sharp, K. A., Levine, R. L. & Thompson, C. B. The common feature of leukemia-associated IDH1 and IDH2 mutations is a neomorphic enzyme activity converting alpha-ketoglutarate to 2-hydroxyglutarate. *Cancer Cell* **17**, 225–34 (2010).
7. Grassian, A. R., Parker, S. J., Davidson, S. M., Divakaruni, A. S., Green, C. R., Zhang, X., Slocum, K. L., Pu, M., Lin, F., Vickers, C., Joud-Caldwell, C., Chung, F., Yin, H., Handly, E. D., Straub, C., Growney, J. D., Vander Heiden, M. G., Murphy, A. N., Pagliarini, R. & Metallo, C. M. IDH1 mutations alter citric acid cycle metabolism and increase dependence on oxidative mitochondrial metabolism. *Cancer Res* **74**, 3317–31 (2014).
8. Carbonneau, M., L, M. G., Lalonde, M. E., Germain, M. A., Motorina, A., Guiot, M. C., Secco, B., Vincent, E. E., Tumber, A., Hulea, L., Bergeman, J., Oppermann, U., Jones, R. G., Laplante, M., Topisirovic, I., Petrecca, K., Huot, M. E. & Mallette, F. A. The oncometabolite 2-hydroxyglutarate activates the mTOR signalling pathway. *Nat Commun* **7**, 12700 (2016).
9. Fack, F., Tardito, S., Hochart, G., Oudin, A., Zheng, L., Fritah, S., Golebiewska, A., Nazarov, P. V., Bernard, A., Hau, A. C., Keunen, O., Leenders, W., Lund-Johansen, M., Stauber, J., Gottlieb, E., Bjerkvig, R. & Niclou, S. P. Altered metabolic landscape in IDH-mutant gliomas affects phospholipid, energy, and oxidative stress pathways. *EMBO Mol Med* **9**, 1681–1695 (2017).
10. Chan, S. M., Thomas, D., Corces-Zimmerman, M. R., Xavy, S., Rastogi, S., Hong, W. J., Zhao, F., Medeiros, B. C., Tyvoll, D. A. & Majeti, R. Isocitrate dehydrogenase 1 and 2 mutations induce BCL-2 dependence in acute myeloid leukemia. *Nat Med* **21**, 178–84 (2015).
11. Izquierdo-Garcia, J. L., Viswanath, P., Eriksson, P., Cai, L., Radoul, M., Chaumeil, M. M., Blough, M., Luchman, H. A., Weiss, S., Cairncross, J. G., Phillips, J. J., Pieper, R. O. & Ronen, S. M. IDH1 Mutation Induces Reprogramming of Pyruvate Metabolism. *Cancer Res* **75**, 2999–3009 (2015).
12. Seltzer, M. J., Bennett, B. D., Joshi, A. D., Gao, P., Thomas, A. G., Ferraris, D. V., Tsukamoto, T., Rojas, C. J., Slusher, B. S., Rabinowitz, J. D., Dang, C. V. & Riggins, G. J. Inhibition of glutaminase preferentially slows growth of glioma cells with mutant IDH1. *Cancer Res* **70**, 8981–7 (2010).
13. Tateishi, K., Wakimoto, H., Iafrate, A. J., Tanaka, S., Loebel, F., Lelic, N., Wiederschain, D., Bedel, O., Deng, G., Zhang, B., He, T., Shi, X., Gerszten, R. E., Zhang, Y., Yeh, J. J., Curry, W. T., Zhao, D., Sundaram, S., Nigim, F., Koerner, M. V. A., Ho, Q., Fisher, D. E., Roider, E. M., Kemeny, L. V., Samuels, Y., Flaherty, K. T., Batchelor, T. T., Chi, A. S. &

- Cahill, D. P. Extreme Vulnerability of IDH1 Mutant Cancers to NAD⁺ Depletion. *Cancer Cell* **28**, 773–784 (2015).
14. Fan, J., Ye, J., Kamphorst, J. J., Shlomi, T., Thompson, C. B. & Rabinowitz, J. D. Quantitative flux analysis reveals folate-dependent NADPH production. *Nature* **510**, 298–302 (2014).
 15. Ye, J., Gu, Y., Zhang, F., Zhao, Y., Yuan, Y., Hao, Z., Sheng, Y., Li, W. Y., Wakeham, A., Cairns, R. A. & Mak, T. W. IDH1 deficiency attenuates gluconeogenesis in mouse liver by impairing amino acid utilization. *Proc Natl Acad Sci U S A* **114**, 292–297 (2017).
 16. Jiang, L., Shestov, A. A., Swain, P., Yang, C., Parker, S. J., Wang, Q. A., Terada, L. S., Adams, N. D., McCabe, M. T., Pietrak, B., Schmidt, S., Metallo, C. M., Dranka, B. P., Schwartz, B. & DeBerardinis, R. J. Reductive carboxylation supports redox homeostasis during anchorage-independent growth. *Nature* **532**, 255–8 (2016).
 17. Metallo, C. M., Gameiro, P. A., Bell, E. L., Mattaini, K. R., Yang, J., Hiller, K., Jewell, C. M., Johnson, Z. R., Irvine, D. J., Guarente, L., Kelleher, J. K., Vander Heiden, M. G., Iliopoulos, O. & Stephanopoulos, G. Reductive glutamine metabolism by IDH1 mediates lipogenesis under hypoxia. *Nature* **481**, 380–4 (2011).
 18. Wise, D. R., Ward, P. S., Shay, J. E., Cross, J. R., Gruber, J. J., Sachdeva, U. M., Platt, J. M., DeMatteo, R. G., Simon, M. C. & Thompson, C. B. Hypoxia promotes isocitrate dehydrogenase-dependent carboxylation of alpha-ketoglutarate to citrate to support cell growth and viability. *Proc Natl Acad Sci U S A* **108**, 19611–6 (2011).
 19. Stinccone, A., Prigione, A., Cramer, T., Wamelink, M. M., Campbell, K., Cheung, E., Olin-Sandoval, V., Gruning, N. M., Kruger, A., Tauqeer Alam, M., Keller, M. A., Breitenbach, M., Brindle, K. M., Rabinowitz, J. D. & Ralser, M. The return of metabolism: biochemistry and physiology of the pentose phosphate pathway. *Biol Rev Camb Philos Soc* **90**, 927–63 (2015).
 20. Zhang, H., Badur, M. G., Divakaruni, A. S., Parker, S. J., Jager, C., Hiller, K., Murphy, A. N. & Metallo, C. M. Distinct Metabolic States Can Support Self-Renewal and Lipogenesis in Human Pluripotent Stem Cells under Different Culture Conditions. *Cell Rep* **16**, 1536–1547 (2016).
 21. Zhang, Z., Chen, L., Liu, L., Su, X. & Rabinowitz, J. D. Chemical Basis for Deuterium Labeling of Fat and NADPH. *J Am Chem Soc* **139**, 14368–14371 (2017).
 22. Gelman, S. J., Naser, F., Mahieu, N. G., McKenzie, L. D., Dunn, G. P., Chheda, M. G. & Patti, G. J. Consumption of NADPH for 2-HG Synthesis Increases Pentose Phosphate Pathway Flux and Sensitizes Cells to Oxidative Stress. *Cell Rep* **22**, 512–522 (2018).

23. Zhao, D., Badur, M. G., Luebeck, J., Magana, J. H., Birmingham, A., Sasik, R., Ahn, C. S., Ideker, T., Metallo, C. M. & Mali, P. Combinatorial CRISPR-Cas9 Metabolic Screens Reveal Critical Redox Control Points Dependent on the KEAP1-NRF2 Regulatory Axis. *Mol Cell* **69**, 699–708 e7 (2018).
24. Ma, S., Jiang, B., Deng, W., Gu, Z. K., Wu, F. Z., Li, T., Xia, Y., Yang, H., Ye, D., Xiong, Y. & Guan, K. L. D-2-hydroxyglutarate is essential for maintaining oncogenic property of mutant IDH-containing cancer cells but dispensable for cell growth. *Oncotarget* **6**, 8606–20 (2015).
25. Lewis, C. A., Parker, S. J., Fiske, B. P., McCloskey, D., Gui, D. Y., Green, C. R., Vokes, N. I., Feist, A. M., Vander Heiden, M. G. & Metallo, C. M. Tracing compartmentalized NADPH metabolism in the cytosol and mitochondria of mammalian cells. *Mol Cell* **55**, 253–63 (2014).
26. Young, J. D. INCA: a computational platform for isotopically non-stationary metabolic flux analysis. *Bioinformatics* **30**, 1333–5 (2014).
27. Tritsch, G. L. & Moore, G. E. Spontaneous decomposition of glutamine in cell culture media. *Exp Cell Res* **28**, 360–4 (1962).
28. Wang, X., Spandidos, A., Wang, H. & Seed, B. PrimerBank: a PCR primer database for quantitative gene expression analysis, 2012 update. *Nucleic Acids Res* **40**, D1144–9 (2012).
29. Geisbrecht, B. V. & Gould, S. J. The human PICD gene encodes a cytoplasmic and peroxisomal NADP(+)-dependent isocitrate dehydrogenase. *J Biol Chem* **274**, 30527–33 (1999).
30. Zhao, S., Lin, Y., Xu, W., Jiang, W., Zha, Z., Wang, P., Yu, W., Li, Z., Gong, L., Peng, Y., Ding, J., Lei, Q., Guan, K. L. & Xiong, Y. Glioma-derived mutations in IDH1 dominantly inhibit IDH1 catalytic activity and induce HIF-1 α . *Science* **324**, 261–5 (2009).
31. Cracan, V., Titov, D. V., Shen, H., Grabarek, Z. & Mootha, V. K. A genetically encoded tool for manipulation of NADP(+)/NADPH in living cells. *Nat Chem Biol* **13**, 1088–1095 (2017).
32. Intlekofer, A. M., Dematteo, R. G., Venneti, S., Finley, L. W., Lu, C., Judkins, A. R., Rustenburg, A. S., Grinaway, P. B., Chodera, J. D., Cross, J. R. & Thompson, C. B. Hypoxia Induces Production of L-2-Hydroxyglutarate. *Cell Metab* **22**, 304–11 (2015).
33. Intlekofer, A. M., Wang, B., Liu, H., Shah, H., Carmona-Fontaine, C., Rustenburg, A. S., Salah, S., Gunner, M. R., Chodera, J. D., Cross, J. R. & Thompson, C. B. L-2-Hydroxyglutarate production arises from noncanonical enzyme function at acidic pH. *Nat Chem Biol* **13**, 494–500 (2017).

34. Rohle, D., Popovici-Muller, J., Palaskas, N., Turcan, S., Grommes, C., Campos, C., Tsoi, J., Clark, O., Oldrini, B., Komisopoulou, E., Kunii, K., Pedraza, A., Schalm, S., Silverman, L., Miller, A., Wang, F., Yang, H., Chen, Y., Kernytsky, A., Rosenblum, M. K., Liu, W., Biller, S. A., Su, S. M., Brennan, C. W., Chan, T. A., Graeber, T. G., Yen, K. E. & Mellinghoff, I. K. An inhibitor of mutant IDH1 delays growth and promotes differentiation of glioma cells. *Science* **340**, 626–30 (2013).
35. Cantor, J. R., Abu-Remaileh, M., Kanarek, N., Freinkman, E., Gao, X., Louissaint A., J., Lewis, C. A. & Sabatini, D. M. Physiologic Medium Rewires Cellular Metabolism and Reveals Uric Acid as an Endogenous Inhibitor of UMP Synthase. *Cell* **169**, 258–272 e17 (2017).
36. Ackerman, D. & Simon, M. C. Hypoxia, lipids, and cancer: surviving the harsh tumor microenvironment. *Trends Cell Biol* **24**, 472–8 (2014).
37. Svensson, R. U., Parker, S. J., Eichner, L. J., Kolar, M. J., Wallace, M., Brun, S. N., Lombardo, P. S., Van Nostrand, J. L., Hutchins, A., Vera, L., Gerken, L., Greenwood, J., Bhat, S., Harriman, G., Westlin, W. F., Harwood H. J., J., Saghatelian, A., Kapeller, R., Metallo, C. M. & Shaw, R. J. Inhibition of acetyl-CoA carboxylase suppresses fatty acid synthesis and tumor growth of non-small-cell lung cancer in preclinical models. *Nat Med* **22**, 1108–1119 (2016).
38. Figueroa, M. E., Abdel-Wahab, O., Lu, C., Ward, P. S., Patel, J., Shih, A., Li, Y., Bhagwat, N., Vasanthakumar, A., Fernandez, H. F., Tallman, M. S., Sun, Z., Wolniak, K., Peeters, J. K., Liu, W., Choe, S. E., Fantin, V. R., Paietta, E., Lowenberg, B., Licht, J. D., Godley, L. A., Delwel, R., Valk, P. J., Thompson, C. B., Levine, R. L. & Melnick, A. Leukemic IDH1 and IDH2 mutations result in a hypermethylation phenotype, disrupt TET2 function, and impair hematopoietic differentiation. *Cancer Cell* **18**, 553–67 (2010).
39. Lu, C., Ward, P. S., Kapoor, G. S., Rohle, D., Turcan, S., Abdel-Wahab, O., Edwards, C. R., Khanin, R., Figueroa, M. E., Melnick, A., Wellen, K. E., O'Rourke, D. M., Berger, S. L., Chan, T. A., Levine, R. L., Mellinghoff, I. K. & Thompson, C. B. IDH mutation impairs histone demethylation and results in a block to cell differentiation. *Nature* **483**, 474–8 (2012).
40. Turcan, S., Rohle, D., Goenka, A., Walsh, L. A., Fang, F., Yilmaz, E., Campos, C., Fabius, A. W., Lu, C., Ward, P. S., Thompson, C. B., Kaufman, A., Guryanova, O., Levine, R., Heguy, A., Viale, A., Morris, L. G., Huse, J. T., Mellinghoff, I. K. & Chan, T. A. IDH1 mutation is sufficient to establish the glioma hypermethylator phenotype. *Nature* **483**, 479–83 (2012).
41. Xu, W., Yang, H., Liu, Y., Yang, Y., Wang, P., Kim, S. H., Ito, S., Yang, C., Wang, P., Xiao, M. T., Liu, L. X., Jiang, W. Q., Liu, J., Zhang, J. Y., Wang, B., Frye, S., Zhang, Y., Xu, Y. H., Lei, Q. Y., Guan, K. L., Zhao, S. M. & Xiong, Y. Oncometabolite 2-hydroxyglutarate

- is a competitive inhibitor of alpha-ketoglutarate-dependent dioxygenases. *Cancer Cell* **19**, 17–30 (2011).
42. Kamphorst, J. J., Cross, J. R., Fan, J., de Stanchina, E., Mathew, R., White, E. P., Thompson, C. B. & Rabinowitz, J. D. Hypoxic and Ras-transformed cells support growth by scavenging unsaturated fatty acids from lysophospholipids. *Proc Natl Acad Sci U S A* **110**, 8882–7 (2013).
 43. Young, R. M., Ackerman, D., Quinn, Z. L., Mancuso, A., Gruber, M., Liu, L., Giannoukos, D. N., Bobrovnikova-Marjon, E., Diehl, J. A., Keith, B. & Simon, M. C. Dysregulated mTORC1 renders cells critically dependent on desaturated lipids for survival under tumor-like stress. *Genes Dev* **27**, 1115–31 (2013).
 44. Lee, W. N., Boros, L. G., Puigjaner, J., Bassilian, S., Lim, S. & Cascante, M. Mass isotopomer study of the nonoxidative pathways of the pentose cycle with [1,2-¹³C₂]glucose. *Am J Physiol* **274**, E843–51 (1998).
 45. Chaumeil, M. M., Larson, P. E., Yoshihara, H. A., Danforth, O. M., Vigneron, D. B., Nelson, S. J., Pieper, R. O., Phillips, J. J. & Ronen, S. M. Non-invasive in vivo assessment of IDH1 mutational status in glioma. *Nat Commun* **4**, 2429 (2013).
 46. Salamanca-Cardona, L., Shah, H., Poot, A. J., Correa, F. M., Di Galleonardo, V., Lui, H., Miloushev, V. Z., Granlund, K. L., Tee, S. S., Cross, J. R., Thompson, C. B. & Keshari, K. R. In Vivo Imaging of Glutamine Metabolism to the Oncometabolite 2-Hydroxyglutarate in IDH1/2 Mutant Tumors. *Cell Metab* **26**, 830–841 e3 (2017).
 47. Turcan, S., Makarov, V., Taranda, J., Wang, Y., Fabius, A. W. M., Wu, W., Zheng, Y., El-Amine, N., Haddock, S., Nanjangud, G., LeKaye, H. C., Brennan, C., Cross, J., Huse, J. T., Kelleher, N. L., Osten, P., Thompson, C. B. & Chan, T. A. Mutant-IDH1-dependent chromatin state reprogramming, reversibility, and persistence. *Nat Genet* **50**, 62–72 (2018).
 48. Venteicher, A. S., Tirosh, I., Hebert, C., Yizhak, K., Neftel, C., Filbin, M. G., Hovestadt, V., Escalante, L. E., Shaw, M. L., Rodman, C., Gillespie, S. M., Dionne, D., Luo, C. C., Ravichandran, H., Mylvaganam, R., Mount, C., Onozato, M. L., Nahed, B. V., Wakimoto, H., Curry, W. T., Iafrate, A. J., Rivera, M. N., Frosch, M. P., Golub, T. R., Brastianos, P. K., Getz, G., Patel, A. P., Monje, M., Cahill, D. P., Rozenblatt-Rosen, O., Louis, D. N., Bernstein, B. E., Regev, A. & Suva, M. L. Decoupling genetics, lineages, and microenvironment in IDH-mutant gliomas by single-cell RNA-seq. *Science* **355** (2017).
 49. Losman, J. A. & Kaelin W. G., J. What a difference a hydroxyl makes: mutant IDH, (R)-2-hydroxyglutarate, and cancer. *Genes Dev* **27**, 836–52 (2013).
 50. Parker, S. J. & Metallo, C. M. Metabolic consequences of oncogenic IDH mutations. *Pharmacol Ther* **152**, 54–62 (2015).

51. Badur, M. G. & Metallo, C. M. Reverse engineering the cancer metabolic network using flux analysis to understand drivers of human disease. *Metab Eng* **45**, 95–108 (2018).
52. Sazanov, L. A. & Jackson, J. B. Proton-translocating transhydrogenase and NAD- and NADP-linked isocitrate dehydrogenases operate in a substrate cycle which contributes to fine regulation of the tricarboxylic acid cycle activity in mitochondria. *FEBS Lett* **344**, 109–116 (1994).
53. Zarei, M., Lal, S., Parker, S. J., Nevler, A., Vaziri-Gohar, A., Dukleska, K., Mambelli-Lisboa, N. C., Moffat, C., Blanco, F. F., Chand, S. N., Jimbo, M., Cozzitorto, J. A., Jiang, W., Yeo, C. J., Londin, E. R., Seifert, E. L., Metallo, C. M., Brody, J. R. & Winter, J. M. Posttranscriptional Upregulation of IDH1 by HuR Establishes a Powerful Survival Phenotype in Pancreatic Cancer Cells. *Cancer Res* **77**, 4460–4471 (2017).
54. Lin, R., Elf, S., Shan, C., Kang, H. B., Ji, Q., Zhou, L., Hitosugi, T., Zhang, L., Zhang, S., Seo, J. H., Xie, J., Tucker, M., Gu, T. L., Sudderth, J., Jiang, L., Mitsche, M., DeBerardinis, R. J., Wu, S., Li, Y., Mao, H., Chen, P. R., Wang, D., Chen, G. Z., Hurwitz, S. J., Lonial, S., Arellano, M. L., Khoury, H. J., Khuri, F. R., Lee, B. H., Lei, Q., Brat, D. J., Ye, K., Boggon, T. J., He, C., Kang, S., Fan, J. & Chen, J. 6-Phosphogluconate dehydrogenase links oxidative PPP, lipogenesis and tumour growth by inhibiting LKB1-AMPK signalling. *Nat Cell Biol* **17**, 1484–96 (2015).
55. Rao, X., Duan, X., Mao, W., Li, X., Li, Z., Li, Q., Zheng, Z., Xu, H., Chen, M., Wang, P. G., Wang, Y., Shen, B. & Yi, W. O-GlcNAcylation of G6PD promotes the pentose phosphate pathway and tumor growth. *Nat Commun* **6**, 8468 (2015).
56. Conklin, K. A. Chemotherapy-associated oxidative stress: impact on chemotherapeutic effectiveness. *Integr Cancer Ther* **3**, 294–300 (2004).
57. Hollinshead, K. E. R., Munford, H., Eales, K. L., Bardella, C., Li, C., Escribano-Gonzalez, C., Thakker, A., Nonnenmacher, Y., Kluckova, K., Jeeves, M., Murren, R., Cuzzo, F., Ye, D., Laurenti, G., Zhu, W., Hiller, K., Hodson, D. J., Hua, W., Tomlinson, I. P., Ludwig, C., Mao, Y. & Tennant, D. A. Oncogenic IDH1 Mutations Promote Enhanced Proline Synthesis through PYCR1 to Support the Maintenance of Mitochondrial Redox Homeostasis. *Cell Rep* **22**, 3107–3114 (2018).
58. Jalbert, L. E., Elkhaled, A., Phillips, J. J., Neill, E., Williams, A., Crane, J. C., Olson, M. P., Molinaro, A. M., Berger, M. S., Kurhanewicz, J., Ronen, S. M., Chang, S. M. & Nelson, S. J. Metabolic Profiling of IDH Mutation and Malignant Progression in Infiltrating Glioma. *Sci Rep* **7**, 44792 (2017).

Chapter 7

Conclusions

The works presented in this thesis highlight the complex regulation of metabolic pathways that support redox homeostasis. Cells must maintain the proper balance of oxidized and reduced forms of pyridine nucleotides [NAD(P)+] for biosynthetic and bioenergetic needs. However, the pathways that supply reducing equivalents also supply critical metabolic intermediates for other processes. Moreover, altered consumption of compartment-specific reducing equivalents or metabolic intermediates can reprogram metabolic pathways at a network-level. These phenomena demonstrate the critical need to understand how microenvironment and genotype affect redox-specific cell behavior.

The first chapter, "Reverse engineering the cancer metabolic network using flux analysis to understand drivers of human disease," examines the emerging field of cancer metabolism. This work introduces the theoretical frameworks and technological advancements that have enabled the development of metabolic flux analysis for biomedical studies. Then the work reviews the recent developments in the field that have required this technique. Probing metabolic network function will further elucidate phenotypes that are found in cancer subsets and hopefully generate new therapeutic windows.

The second chapter, "Enzymatic passaging of human embryonic stem cells alters central

carbon metabolism and glycan abundance,” explores how routine passage methods alter the metabolism of human pluripotent stem cells. Enzymatic passaging was found to perturb glucose metabolism in the period immediately after passaging. Detailed tracing and mass spectrometry revealed that high rates of hexosamine biosynthesis supports repair of the cleaved glycolayx. This illustrates a repeated insult to stem cell cultures that could drive drift *in vitro*. Future work will be to engineer better passaging conditions that can supply requisite nutrients while maintaining proper performance for stem cell-applications.

The third chapter, “Distinct metabolic states can support self-renewal and lipogenesis in human pluripotent stem cells under different culture conditions,” investigates the metabolic reprogramming of human pluripotent stem cell metabolism due to culture conditions. Chemically-defined medias have largely supplemented more replete, feeder cell-supported conditions in stem cell culture due to ease of use and reduced variability. However, while all commercially available medias can maintain pluripotency, the effect on metabolism and cellular performance remained understudied. We found that these chemically-defined conditions force cells to reside in increased biosynthetic states to support increased *de novo* lipogenesis and reprogram the metabolic network. These results demonstrate that human pluripotent stem cells can maintain pluripotency in distinct metabolic states. Future work will be to understand how these distinct states affect stem cell function and ability to differentiate into useful cell products.

The fourth chapter, “Lipid availability influences the metabolic maturation of hPSC-derived cardiomyocytes,” extends the work from Chapter 3 to stem cell-derived cardiomyocytes. Stem cell-derived cardiomyocytes are characterized by an immature phenotype presenting an obstacle to their utility in drug toxicity and regenerative medicine applications. Metabolic flux analysis revealed that stem cell-derived cardiomyocytes can oxidize some expected cardiac substrates but lack the ability to activate fatty acid oxidation - demonstrating their immaturity. Tracing throughout differentiation revealed that these cardiomyocytes acquire the correct metabolic “program” during lineage specification but have abnormal lipid metabolism. Reminiscent of the stem

cell work, nutrient-poor media conditions force cardiomyocytes into abnormal lipid biosynthetic state that prevents fatty acid oxidation. By supplying complex sources of fat, cardiomyocytes can undergo metabolic maturation while maintaining proper electrophysiology. Development of more defined fat sources and cardiac-specific nutrient cocktails will be necessary to further this work.

The fifth chapter, "Combinatorial CRISPR-Cas9 metabolic screens reveal critical redox control points dependent on the KEAP1-NRF2 regulatory axis," investigates how the oncogenic status of a cell controls the dispensability and interaction of metabolic enzymes. Metabolic networks are highly redundant with many genes catalyzing the same reaction and many parallel pathways. To probe glucose metabolism in a unbiased, network-level, we utilized combinatorial CRISPR screening technology to rapidly assess the growth defects associated with single- and dual-gene knockouts. While gene expression mainly drove the essentiality of a gene, the oxidative pentose phosphate genes were more highly expressed but less essential in A549 cells as compared to HeLa cells. We hypothesized that this differential sensitivity could be driven by a mutation in *KEAP1*, a key tumor suppressor that controls redox metabolism. Modulation of *KEAP1* altered the oxidative pentose phosphate pathway function and sensitivity to targeting by reprogramming the cellular antioxidant response. These results suggest that *KEAP1* tumors status must be considered when targeting redox-associated pathways. Future work will be to utilize this platform technology on other metabolic sets to understand how metabolic genes work together to drive cancer survival.

The sixth chapter, "Oncogenic R132 IDH1 mutations limit NADPH for de novo lipogenesis through (D)2-hydroxyglutarate production in fibrosarcoma cells," interrogates how mutations in *IDH1* alter redox metabolism and NADPH availability. These neomorphic mutations modify the activity of isocitrate dehydrogenase to favor the NADPH-dependant reduction of alpha-ketoglutarate to 2-hydroxyglutarate, the latter reaching millimolar concentrations in the cell. We found that NADPH consumption for 2-hydroxyglutrate synthesis approached similar levels to that for *de novo* lipogenesis. Surprisingly the IDH mutant cells were generally found to tolerate this NADPH sink by reprogramming the oxidative pentose phosphate pathway. IDH mutation

only represented a redox liability when removing exogenous sources of fat and forcing the cell to maximize *de novo* lipogenesis. These results demonstrate that IDH mutant is a considerable redox liability in the cell only when the redox metabolic network is stressed. Future work will be to connect these *in vitro* findings to preclinical models by modulating availability of fat through dietary modulation or pharmacological inhibition of *de novo* lipogenesis.

Cellular metabolism is one of the highest levels of phenotypic function, dynamically integrating microenvironmental and genetic cues. However probing these deep cellular phenotypes require systems-level analysis and network-level integration of orthogonal data types. Taken together these chapters demonstrate the utility in studying functional metabolic networks and suitable methodologies (i.e. CRISPR screening and metabolic flux analysis) for this kind of work. Understanding the key metabolic and genetic regulators of compartment-specific redox metabolism should enable discovery of mechanistic drivers of disease and allow researchers exploit these redox liabilities for novel treatment modalities.

Chapter S1

Supplement to Chapter 1

S1.1 Abbreviations

BCAA - branched-chain amino acid; ETC - electron transport chain; FOCM - folate-mediated one carbon metabolism; HIFs - hypoxia-induced factors; ISA - isotopomer spectral analysis; ODE - ordinary differential equation; oxPPP - oxidative pentose phosphate pathway; 2HG - 2-hydroxyglutarate; 3PG - 3-phosphoglycerate; 6PG - 6-phosphogluconate; AcCoA - acetyl coenzyme A; aKG - alpha-ketoglutarate; Asp - aspartate; CH₂-THF - 5,10-methylenetetrahydrofolate; Cit - citrate; For - formate; Fum - fumarate; G6P - glucose 6-phosphate; GAP - glyceraldehyde 3-phosphate; Glc - glucose; Glu - glutamate; Gln - glutamine; Gly - glycine; Lac - lactate; Mal - malate; Oac - oxaloacetate; Pro - proline; Pyr - pyruvate; Ru5P - ribulose 5-phosphate; Ser - serine; Suc - succinate;

Chapter S2

Supplement to Chapter 2

S2.1 Abbreviations

AcCoA - Acetyl coenzyme A; GC/MS - Gas chromatography/Mass spectrometry; MID - mass isotopomer distribution; hESC - human embryonic stem cell; ISA - isotopomer spectral analysis; MFA - metabolic flux analysis; UGlc - [U-¹³C₆]glucose;

Table S2.1: MIDs for unlabeled hydrosylate fragments. Avg denotes average and SD denotes standard deviation of three independent hydrosylates.

MID	Glucose		Galactose		Glucosamine		Mannosamine		Ribose		Adenine		Guanine	
	Avg	SD	Avg	SD	Avg	SD	Avg	SD	Avg	SD	Avg	SD	Avg	SD
M+0	100.22	0.15	100.26	0.18	101.37	0.98	97.25	1.91	100.53	0.27	99.34	0.10	100.06	0.28
M+1	-0.15	0.16	-0.09	0.26	-0.73	0.86	1.58	2.48	-0.46	0.32	0.09	0.08	-0.40	0.09
M+2	-0.20	0.04	-0.11	0.46	-0.44	0.30	0.65	0.56	-0.16	0.23	0.04	0.06	0.14	0.14
M+3	0.04	0.04	-0.02	0.01	-0.06	0.26	1.70	2.03	0.09	0.07	0.37	0.02	0.08	0.10
M+4	0.06	0.03	0.05	0.05	-0.12	0.13	-1.26	0.56	0.07	0.04	0.06	0.01	0.16	0.13
M+5	0.02	0.01	-0.11	0.01	-0.05	0.06	-0.04	0.14	-0.06	0.03	0.05	0.01	-0.02	0.04
M+6	0.01	0.01	0.00	0.01	0.02	0.01	0.11	0.06	-	-	-	-	-	-

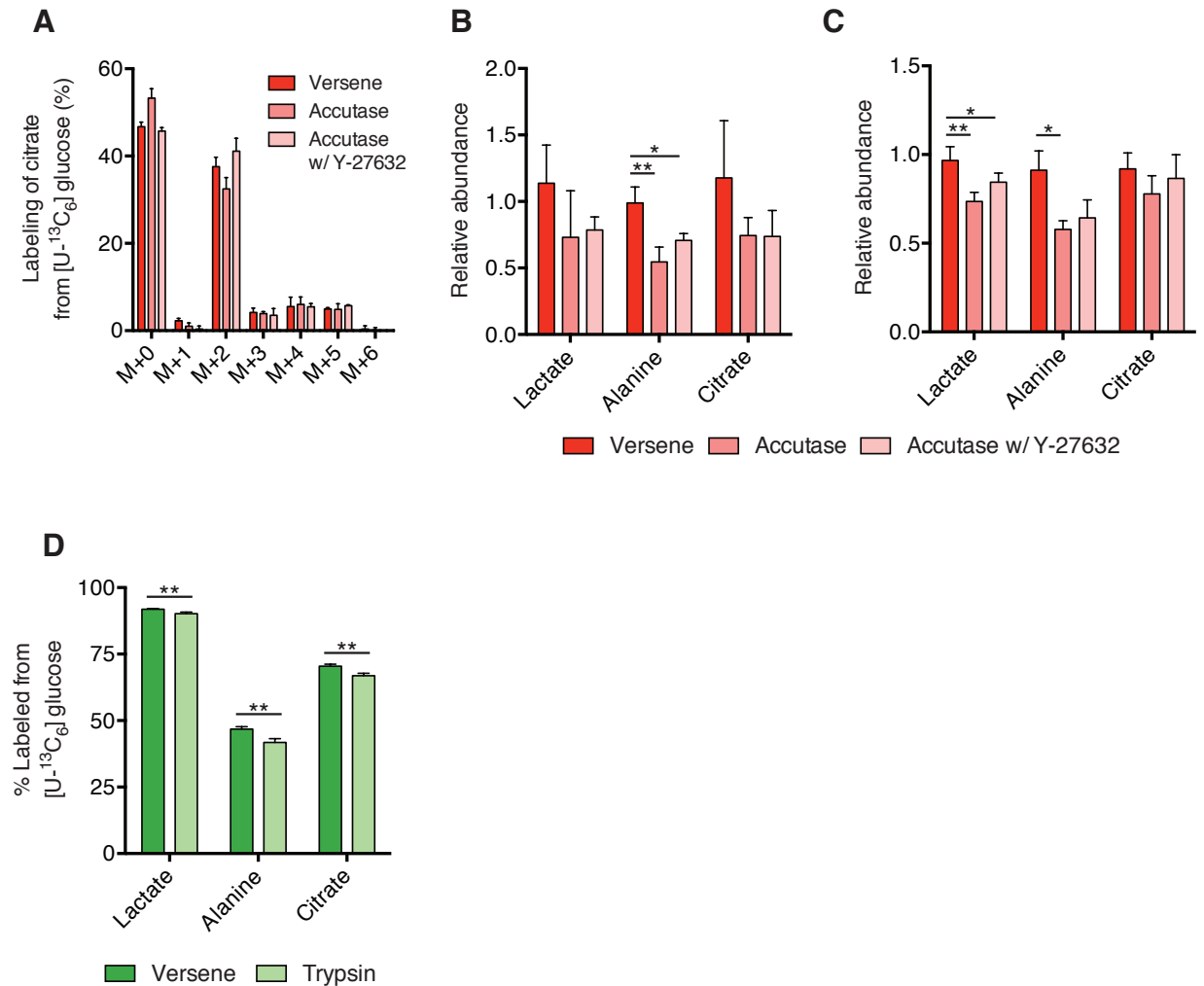


Figure S2.1: Polar metabolite labeling and abundances. (A) Mass isotopomer distribution (MID) of citrate from [U-¹³C₆]glucose (UGlc). (B) Relative abundances of lactate, alanine, and citrate 4 hours after passaging. (C) Relative abundances of lactate, alanine, and citrate one day after passaging (i.e., labeled from 24-28 hours after passaging). (D) Percentage of labeled metabolites from UGlc 0-4 hours after passaging with Versene or trypsin. Error bars represent SD (A-D) for three replicates. *, P value between 0.01 and 0.05; **, P value between 0.001 and 0.01; ***, P value <0.001 by Student's two-tailed t test.

Table S2.2: MIDs for labeled hydrosylate fragments. Avg denotes average and SD denotes standard deviation of three independent hydrosylates.

MID	Glucose		Galactose		Glucosamine		Mannosamine		Ribose	
	Avg	SD	Avg	SD	Avg	SD	Avg	SD	Avg	SD
M+0	74.25	0.13	76.41	0.46	87.60	0.25	87.55	0.33	89.74	0.08
M+1	0.38	0.13	0.21	0.23	-0.07	0.28	0.44	1.34	-0.16	0.12
M+2	0.06	0.01	-0.01	0.07	0.01	0.13	-0.41	1.09	0.41	0.08
M+3	1.32	0.03	1.17	0.23	0.83	0.10	1.54	0.11	10.19	0.11
M+4	24.09	0.13	21.58	0.29	11.83	0.11	11.96	0.80	0.02	0.02
M+5	-0.11	0.03	0.01	0.15	-0.13	0.15	-0.84	0.55	0.04	0.07
M+6	0.01	0.01	0.21	0.07	0.24	0.11	-0.10	0.21	-	-

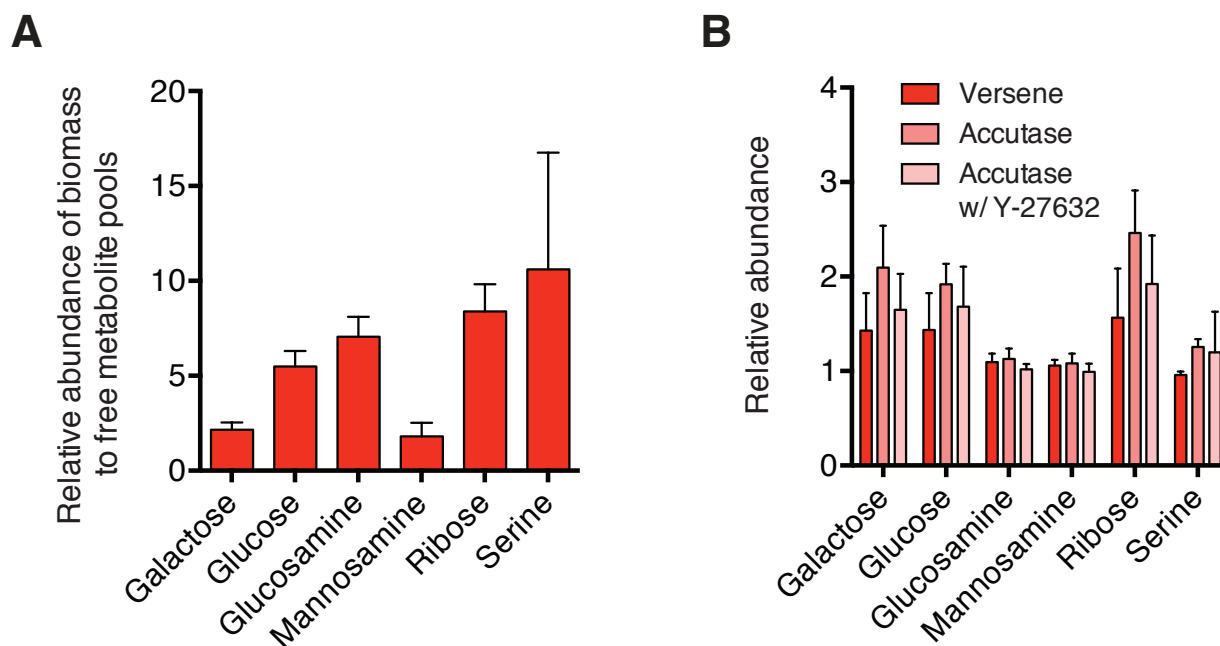


Figure S2.2: Biomass metabolite abundances. (A) Relative abundances of biomass-derived versus free metabolites measured in hydrolyzed interface versus aqueous (polar) extracts, respectively. (B) Relative abundance of biomass metabolites 4 hours after passaging. Error bars represent SD (A-B) for three replicates. *, P value between 0.01 and 0.05; **, P value between 0.001 and 0.01; ***, P value <0.001 by Student's two-tailed t test.

Chapter S3

Supplement to Chapter 3

S3.1 Abbreviations

AcCoA - acetyl-CoA; ÎšKG - Îš-ketoglutarate; Ala - alanine; Asp - aspartate; Asn - asparagine; Lac - lactate; Cit - citrate; Fum - fumarate; Glc - glucose; Glu - glutamate; Gln - glutamine; Gly - glycine; 2HG - 2-hydroxyglutarate; Mal - malate; Oac - oxaloacetate; Olea - oleate; Palm - palmitate; 3PG - 3-phosphoglyceric acid; Pro - proline; Pyr - pyruvate; Ru5P - ribulose-5-phosphate; Ser - serine; Suc - succinate

S3.2 Supplemental Methods

S3.2.1 Cell culture and media

Human embryonic stem cell lines HUES9 and WA09 (H9) were provided by Prof. Shyni Varghese (University of California, San Diego) and Prof. Sean Palecek (University of Wisconsin-Madison), respectively. HESCs were originally maintained on a layer of irradiated CF-1 murine embryonic fibroblasts (P3, MEFs) (MTI-GlobalStem) in DMEM/F12 medium with 20% knockout serum replacement (KSR), 1X MEM non-essential amino acid solution (NEAA), 1 mM L-

glutamine, 1X 2-mercaptoethanol (2-ME), and 4 ng/mL basic fibroblast growth factor recombinant human protein (bFGF). All components were purchased from Life Technologies. Induced pluripotent stem cell line iPS(IMR90)-c4 was also provided by Prof. Sean Palecek. iPSCs were originally cultured in mTeSR1 medium (Stem Cell Technologies). All hPSCs experiments were conducted with cells ranging from 30 and 70 passages.

MEF-conditioned medium was produced by culturing 1 million P3 irradiated CF-1 MEF (MTI-GlobalStem) in 10 mL DMEM/F12 medium with 20% KSR, 1X NEAA, 1 mM L-Glutamine and 1X 2-ME. The conditioned medium was collected every 24 hours from day 2 to day 7 and pooled. Before culturing hESC, the conditioned medium was supplemented with fresh 10 ng/mL bFGF. All components were purchased from Life Technologies.

AlbuMAX media was made by dissolving AlbuMAX I Lipid-Rich BSA (Life Technologies; 1-1.6% w/v) and ultra-fatty acid free BSA (Roche; 1% w/v) into E8 basal media or tracer E8 basal media. E8 supplement was then freshly added to lipid-containing basal media.

In [$U\text{-}^{13}\text{C}_{16}$]palmitate tracer experiments, [$U\text{-}^{13}\text{C}_{16}$]palmitate was first non-covalently conjugated to ultra-fatty acid free BSA (Roche) by dissolving [$U\text{-}^{13}\text{C}_{16}$]sodium palmitate (Cambridge Isotopes) to a concentration of 2.5 mM in 150 mM sodium chloride solution at 70°C and adding 40 mL palmitate solution into 50 mL of 0.34 mM BSA solution at 37°C. A 1 mM working BSA-conjugated [$U\text{-}^{13}\text{C}_{16}$]palmitate solution was prepared by adjusting the pH to 7.4 and diluting to a final volume of 100 mL with 150 mM sodium chloride. In experiments, 50 μM BSA-conjugated [$U\text{-}^{13}\text{C}_{16}$] palmitate and 1 mM carnitine were added to culture medium.

Human cancer cell lines, H1299, HCT116, 143B, SW1353, H358, Hep3b, Huh7 and A549, were maintained in DMEM supplemented with 10% fetal bovine serum (FBS). For measurement of oxidative PPP contribution to lipogenic NADPH, tracer media consisted of either glucose free DMEM medium with 10% dialyzed FBS or glucose free E8 medium, supplemented with [$3\text{-}^2\text{H}$]glucose (Cambridge Isotopes). All components were purchased from Life Technologies.

For tracer experiments, culture medium was removed, cells were rinsed with PBS, and

tracer media were added to wells. Cells were maintained in tracer media for 24 hours before metabolite extraction.

All cells were maintained in a humidified, 37°C incubator at 5% CO₂.

S3.2.2 Detection of 2-hydroxyglutarate isoforms

Derivatization of 2-hydroxyglutarate (2HG) with methanol/methyl chloroformate (Sigma-Aldrich) was performed following essentially the protocol described previously [1]. The derivatives were extracted by the addition of 70 μ L of chloroform. To check the enantiomer separation and to evaluate retention times, standard solutions of both R- α -hydroxyglutaric acid disodium salt and S- α -hydroxyglutaric acid disodium salt (Sigma-Aldrich) were prepared and derivatized in the same way.

A sample volume of 2 μ L was injected into a split/splitless inlet, operating in pulsed splitless mode at 230°C. The injection pulse pressure was set to 15 psi until 1 minute. The gas chromatograph was equipped with a Rt-Î§DEXsa (length: 30 m, I.D.: 0.25 mm, film: 0.25 μ m) capillary column (Restek). The GC oven temperature was held at 70°C for 1 minute and increased at 4°C/min to 150°C. After 5 minutes, the temperature was increased at 3°C/min to 190°C, then held at that temperature for 5 minutes. The total run time for each sample was about 40 minutes [2]. The transfer line temperature was set constantly to 280°C. Full-scan mass spectra were acquired from m/z 70 to 500. Other conditions are same as for other metabolite detection. For quantification, measurements of the derivatives were performed in SIM mode using the following masses: m/z 159, m/z 175.1 (quantification ion) and m/z 202.1. The dwell time for each ion was set to 150 ms. All GC-MS chromatograms were processed using MetaboliteDetector [3].

S3.3 Supplemental Tables and Figures

Table S3.1: Metabolite fragments used for GC/MS analysis.

Metabolite	Carbons	Derivatization	m/z	Fragments for integration
α -Ketoglutarate	1,2,3,4,5	tBDMS	346	C ₁₄ H ₂₈ O ₅ NSi ₂
Alanine	1,2,3	tBDMS	260	C ₁₁ H ₂₆ O ₂ NSi ₂
Aspartate	1,2,3,4	tBDMS	418	C ₁₈ H ₄₀ O ₄ NSi ₃
Lactate	1,2,3	tBDMS	261	C ₁₁ H ₂₅ O ₃ Si ₂
	2,3		233	C ₁₀ H ₂₅ O ₂ Si ₂
Citrate	1,2,3,4,5,6	tBDMS	459	C ₂₀ H ₃₉ O ₆ Si ₃
Fumarate	1,2,3,4	tBDMS	287	C ₁₂ H ₂₃ O ₄ Si ₂
Glutamate	1,2,3,4,5	tBDMS	432	C ₁₉ H ₄₂ O ₄ NSi ₃
Glycine	1,2	tBDMS	246	C ₁₀ H ₂₄ O ₂ NSi ₂
2-Hydroxyglutarate	1,2,3,4,5	tBDMS	433	C ₁₉ H ₄₁ O ₅ Si ₃
Malate	1,2,3,4	tBDMS	419	C ₁₈ H ₃₉ O ₅ Si ₃
Norvaline	1,2,3,4,5	tBDMS	288	C ₁₃ H ₃₀ O ₂ NSi ₂
Proline	1,2,3,4,5	tBDMS	330	C ₁₆ H ₃₆ O ₂ NSi ₂
Pyruvate	1,2,3	tBDMS	174	C ₆ H ₁₂ O ₃ NSi
Serine	1,2,3	tBDMS	390	C ₁₇ H ₄₀ O ₃ NSi ₃
Succinate	1,2,3,4	tBDMS	289	C ₁₂ H ₂₅ O ₄ Si ₂
Cholesterol	1-27	TMS	458	C ₃₀ H ₅₄ OSi
Coprostan-3-ol	1-27	TMS	370	C ₂₇ H ₄₅
Heptadecanoate	1-17	FAME	284	C ₁₈ H ₃₆ O ₂
Oleate	1-18	FAME	296	C ₁₉ H ₃₆ O ₂
Palmitate	1-16	FAME	270	C ₁₇ H ₃₄ O ₂
Stearate	1-18	FAME	298	C ₁₉ H ₃₈ O ₂

Table S3.2: Primers used for gene expression analysis.

Gene	Forward Primer	Reverse Primer	Primerbank ID
<i>ACACA</i>	TCACACCTGAAGACCTTAAAGCC	AGCCACACTGCTTGTACTG	38679973c3
<i>ACLY</i>	ATCGGTTCAAGTATGCTCGGG	GACCAAGTTTTCCACGACGTT	38569422c2
<i>FASN</i>	AAGGACCTGTCTAGGTTTGATGC	TGGCTTCATAGGTGACTTCCA	41872630c1
<i>GAPDH</i>	CTGGGCTACTGAGCACC	AAGTGGTTCGTTGAGGGCAATG	378404907c3
<i>G6PD</i>	ACCGCATCGACCACTACCT	TGGGGCCGAAGATCCTGTT	108773794c2
<i>GLS2</i>	GGCCATGTGGATCGCATCTT	ACAGGTCTGGGTTTGACTTGG	20336213c3
<i>OCT4</i>	CTTGAATCCCGAATGGAAAGGG	CCTTCCCAAATAGAACCCCA	4505967a3
<i>SCD</i>	TTCCTACCTGCAAGTTCTACACC	CCGAGCTTTGTAAGAGCGGT	53759150c3

Figure S3.1: Atom transition maps of labeled glutamine species. Metabolite abbreviations described in Supplemental Text. (A) Schematic of atom transitions in the presence of [U- $^{13}\text{C}_5$]glutamine. ^{12}C carbons depicted with open circles. ^{13}C carbons depicted with filled circles. Dashed lines indicate multi-step atom transitions. M+(n) indicates the number (n) of ^{13}C atoms incorporated into the metabolite. M+5 citrate and M+3 oxaloacetate, aspartate, fumarate, and malate indicative of reductive glutamine flux. M+3 a-ketoglutarate and M+2 succinate, fumarate, and malate indicative of oxidative glutaminolysis. (B) Schematic of atom transitions in the presence of [1- ^{13}C]glutamine. Labeled carbon lost in oxidative TCA flux. M+1 labeling indicative of reductive TCA flux.

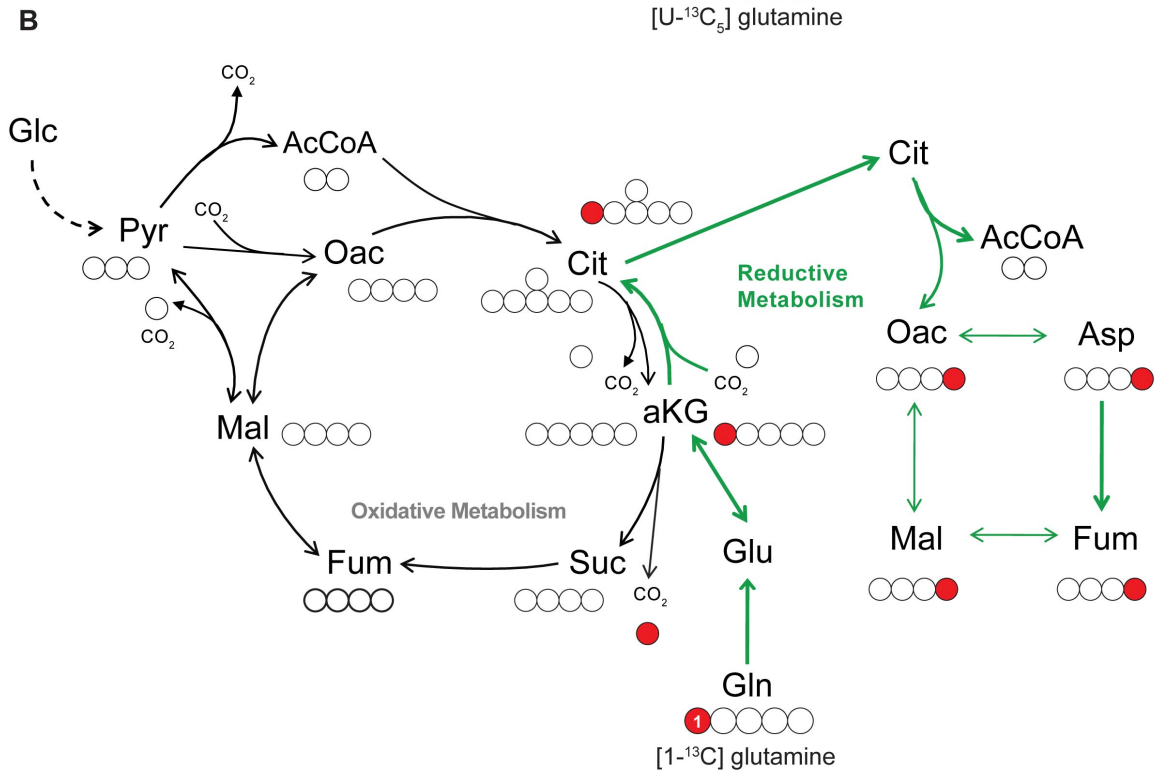
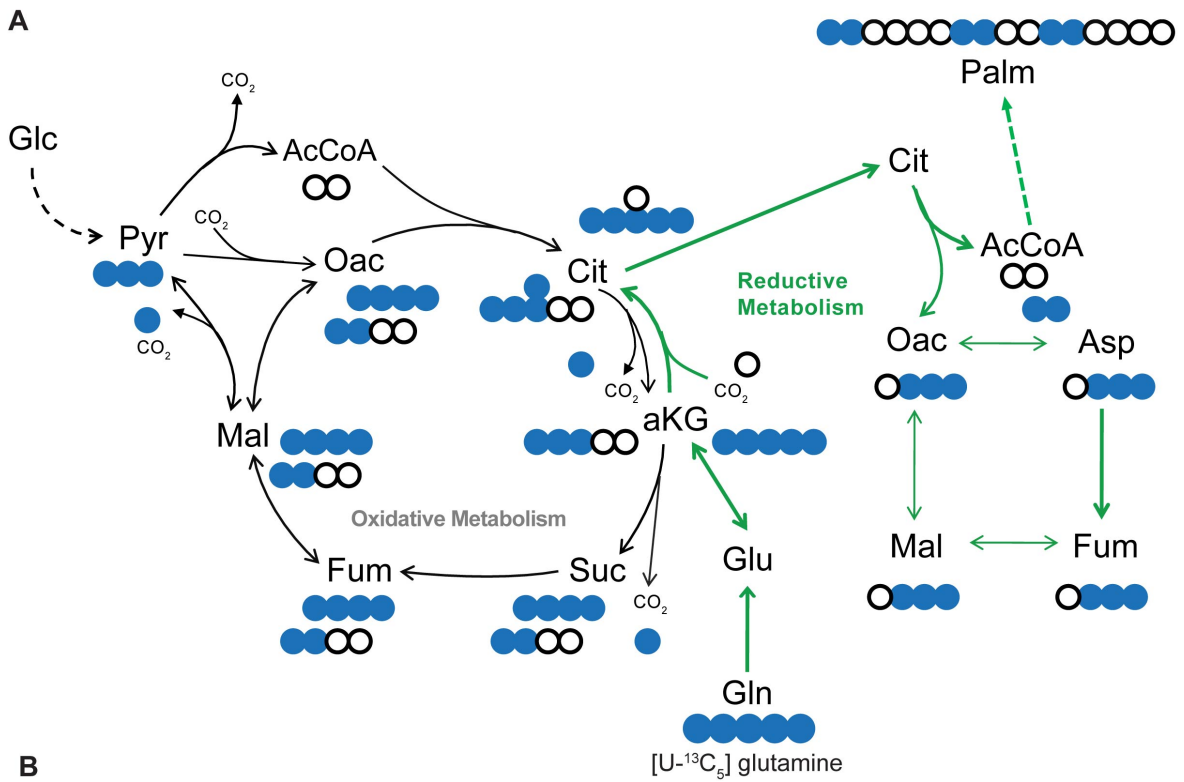


Figure S3.2: Metabolic alterations in hESCs adapted to MEF-CM versus chemically defined media. HESCs were adapted to MEF-CM and chemically defined media for at least 3 passages. (A) Dry cell weight per million H9 hESCs. (B) Relative intracellular metabolite abundance of H9 hESCs normalized by cell number and MEF-CM sample. (C) Percentage of oxidative PPP contribution to lipogenic NADPH in A549 cells cultured in DMEM with 10% FBS or E8 as determined by ISA using [3-²H]glucose. (D) Mole percent enrichment from [U-¹³C₅]glutamine in H9 hESCs throughout intermediary metabolism. (E) Relative percentage of 2-HG isoforms in hESCs grown in E8. (A-B, D-E) All results shown as mean ± SEM. P values were calculated using a Student's two-tailed t test relative to MEF-CM condition; *, P value between 0.01 and 0.05; **, P value between 0.001 and 0.01; ***, P value <0.001. (C) Results shown as mean and 95% CI. *, Significance indicated by non-overlapping 95% confidence intervals.

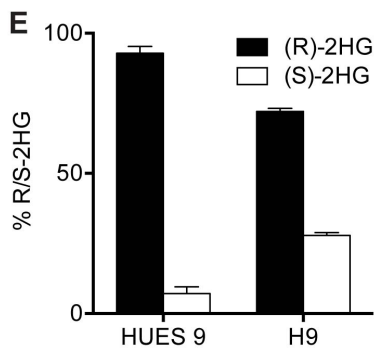
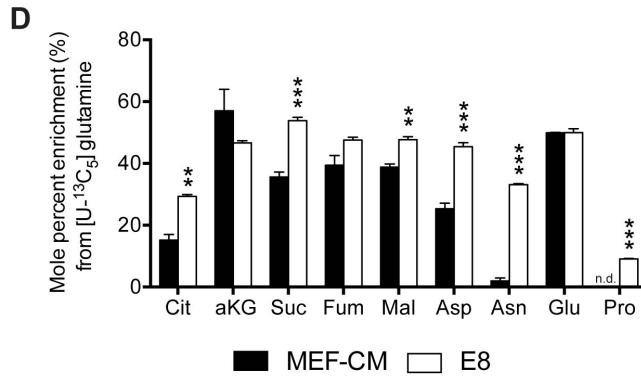
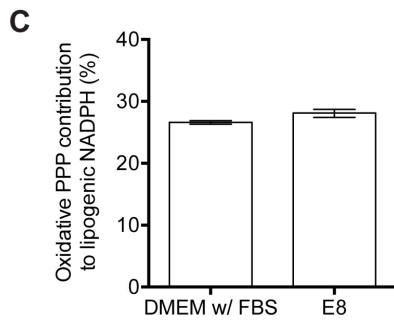
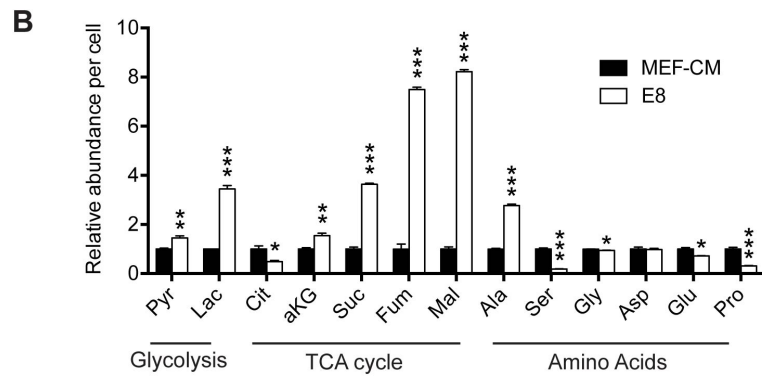
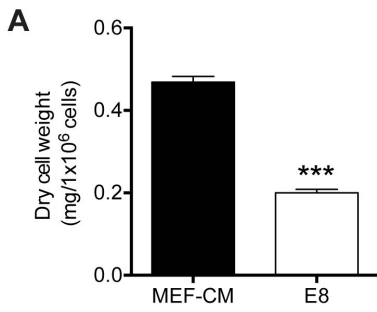


Figure S3.3: Mass isotopomer distributions from [1,2-¹³C]glucose. HUES 9 cells were adapted to MEF-CM and chemically defined media for at least 3 passages. Steady state mass isotopomer distributions (labeling) of metabolites throughout central carbon metabolism in cells cultured with a 1:1 mixture of unlabeled glucose and [1,2-¹³C]glucose over 24 hours. All results shown as mean \pm SEM. M+(n) indicates the number (n) of ¹³C atoms incorporated into the metabolite. Metabolite abbreviations described in Supplemental Text.

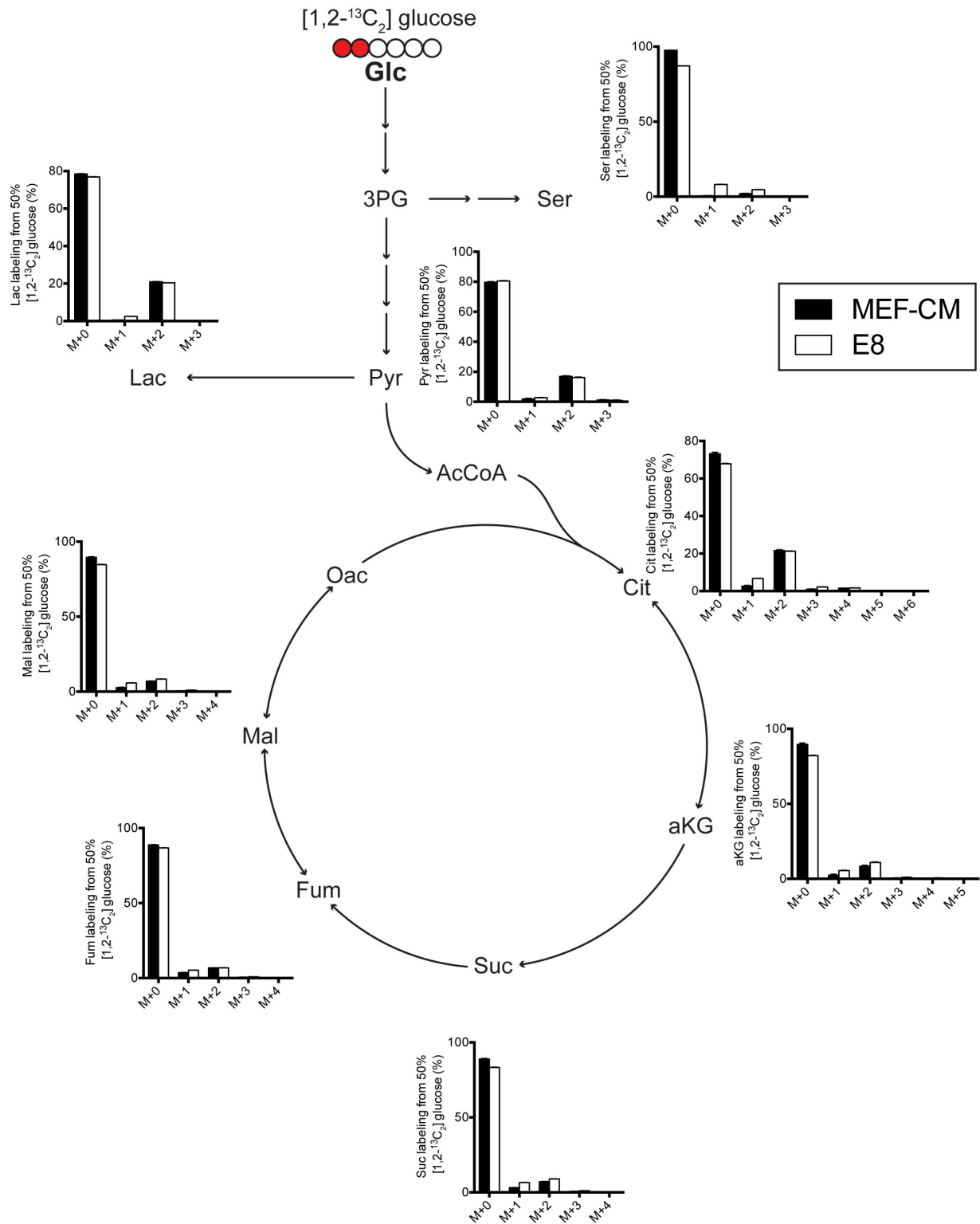


Figure S3.4: Mass isotopomer distributions from [U-¹³C₅]glutamine. HUES 9 cells were adapted to MEF-CM and chemically defined media for at least 3 passages. Steady state mass isotopomer distributions (labeling) of TCA metabolites and amino acids from [U-¹³C₅]glutamine after 24 hours. All results shown as mean ± SEM. M+(n) indicates the number (n) of ¹³C atoms incorporated into the metabolite. Metabolite abbreviations described in Supplemental Text.

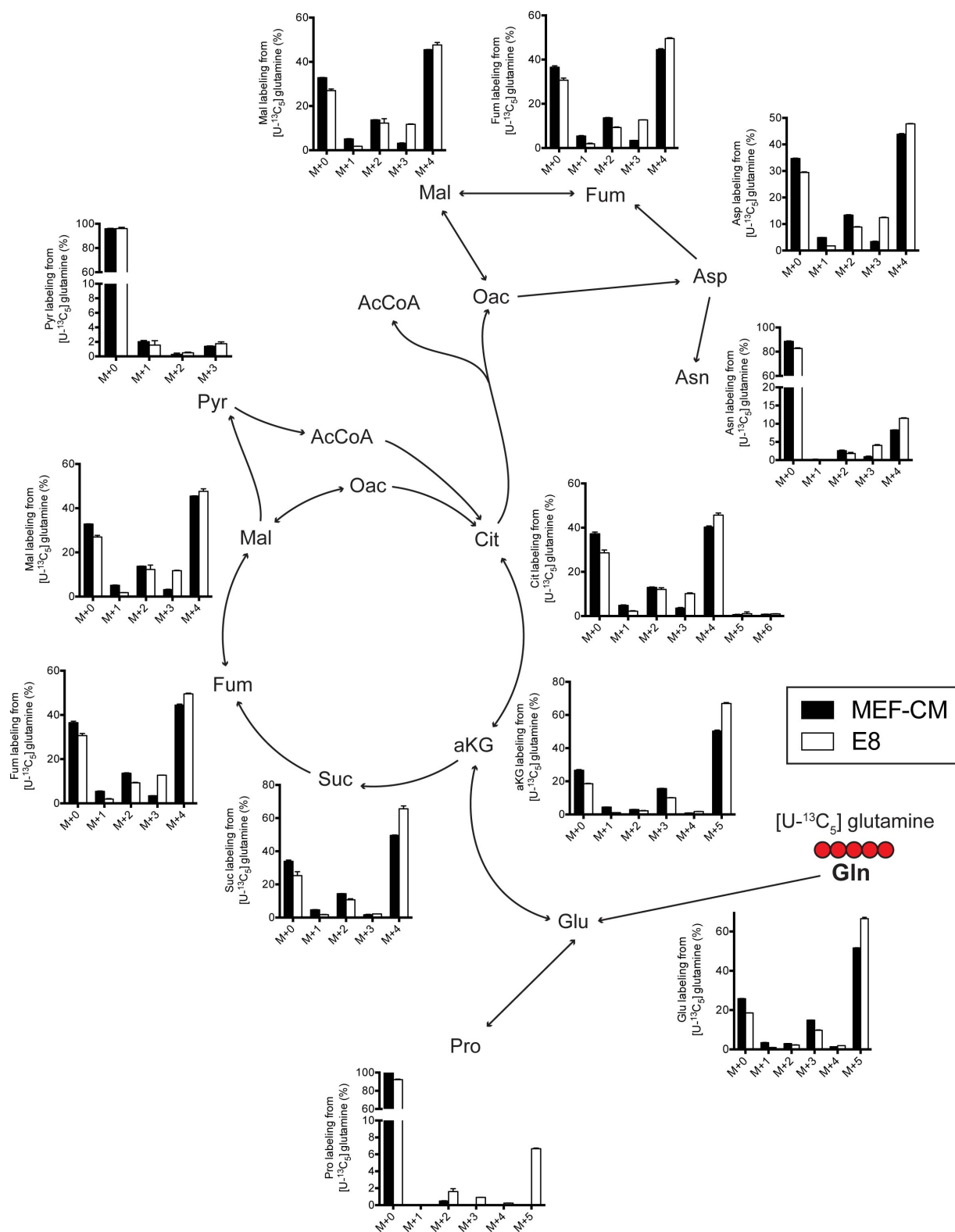
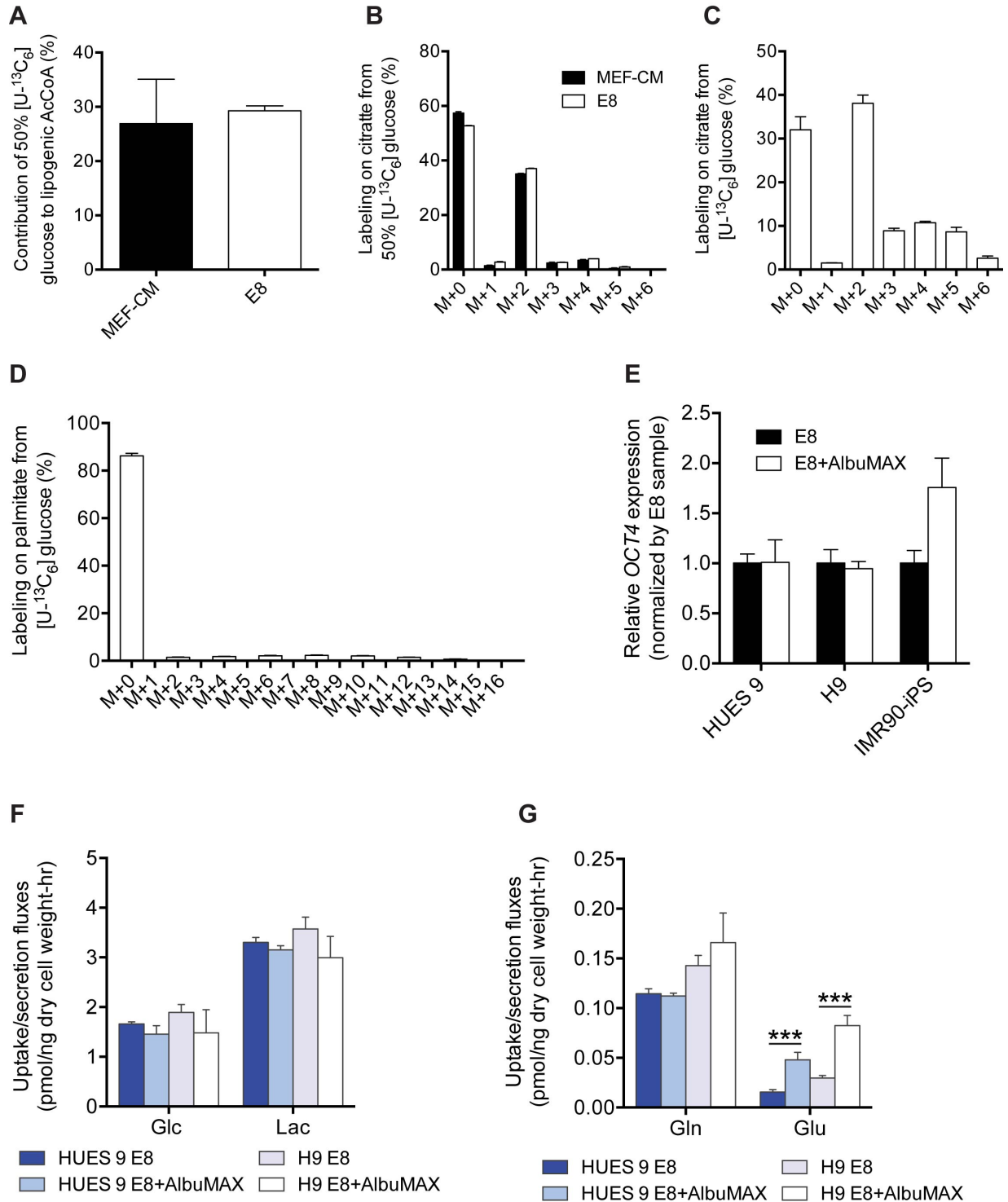


Figure S3.5: HESCs adapted to chemically defined media upregulate lipid biosynthesis. (A) Glucose contribution to lipogenic AcCoA in HUES 9 hESCs in the presence 50% enriched [U-¹³C₆]glucose. (B) Mass isotopomer distribution (labeling) of citrate in HUES 9 hESCs in the presence of 50% enriched [U-¹³C₆]glucose over 24 hours. (C) Mass isotopomer distribution of citrate in irradiated CF-1 MEFs in the presence of 50% enriched [U-¹³C₆]glucose after 24 hours of media conditioning. (D) Mass isotopomer distribution of palmitate in irradiated CF-1 MEFs in the presence of 50% enriched [U-¹³C₆]glucose over 24 hours. (E) Expression of *OCT4* in hPSCs adapted to E8+AlbuMAX relative to cells in E8. (F-G) Glucose uptake, lactate secretion, glutamine uptake and glutamate secretion fluxes of hESCs adapted to E8 or E8+AlbuMAX. Cells were adapted to E8 and E8+AlbuMAX for at least 3 passages. (A) Results shown as mean with 95% CI. *, significance determined by non-overlapping confidence intervals. (B-G) All results shown as mean ± SEM. P values were calculated using a Student's two-tailed t test relative to MEF-CM condition; *, P value between 0.01 and 0.05; **, P value between 0.001 and 0.01; ***, P value <0.001.



S3.4 Supplementary References

1. Villas-Boas, S. G., Delicado, D. G., Akesson, M. & Nielsen, J. Simultaneous analysis of amino and nonamino organic acids as methyl chloroformate derivatives using gas chromatography-mass spectrometry. *Anal Biochem* **322**, 134–8 (2003).
2. Waldhier, M. C., Dettmer, K., Gruber, M. A. & Oefner, P. J. Comparison of derivatization and chromatographic methods for GC-MS analysis of amino acid enantiomers in physiological samples. *J Chromatogr B Analyt Technol Biomed Life Sci* **878**, 1103–12 (2010).
3. Hiller, K., Hangebrauk, J., Jager, C., Spura, J., Schreiber, K. & Schomburg, D. MetaboliteDetector: comprehensive analysis tool for targeted and nontargeted GC/MS based metabolome analysis. *Anal Chem* **81**, 3429–39 (2009).

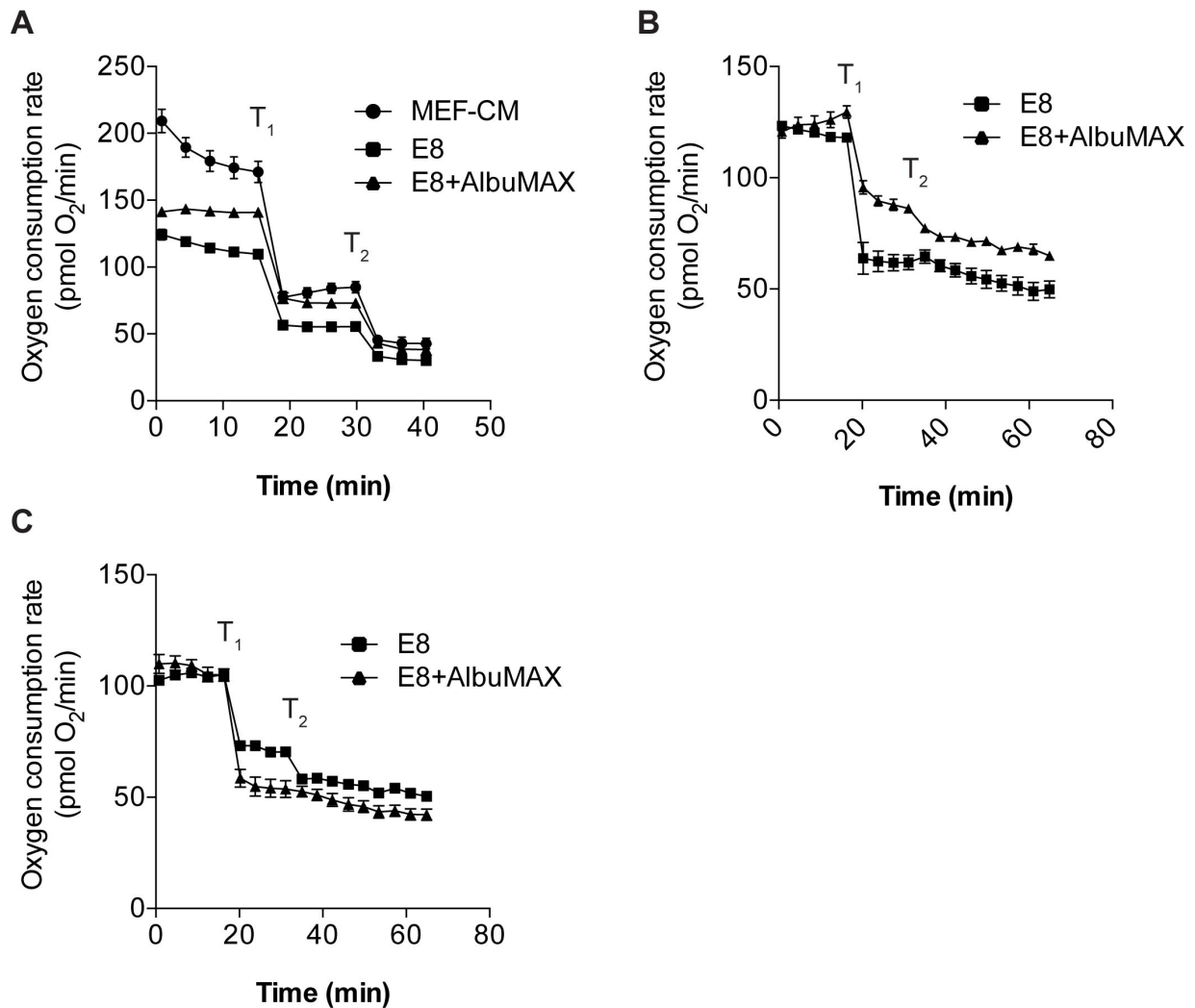


Figure S3.6: Oxygen consumption traces of hPSCs in different culture conditions. (A) Representative traces of HUES 9 hESC oxygen consumption rate (OCR). Oligomycin is added at time T₁ and rotenone/antimycin A is added at time T₂. (B) Representative traces of H9 hESC oxygen consumption rate (OCR). Oligomycin is added at time T₁ and rotenone/antimycin A is added at time T₂. (C) Representative traces of IMR90-iPS hPSC oxygen consumption rate (OCR). Oligomycin is added at time T₁ and rotenone/antimycin A is added at time T₂. (A-C) All results shown as mean \pm SEM.

Chapter S5

Supplement to Chapter 5

S5.1 Supplemental Figures

Figure S5.1: Schematic of dual-gRNA-library construction and quality control of screens.

(A) Oligonucleotides bearing two sgRNA spacers were synthesized, amplified, and cloned into a lentiviral gRNA cloning vector. Next, a fragment containing a sgRNA scaffold and the mouse U6 promoter was inserted between the two spacers to yield the final dual-gRNA expression construct. A pair of primer matching sites labeled in blue were designed for enrichment of the two spacer regions prior to deep sequencing analysis. (B) Frequency distribution of the metabolism dual-gRNA plasmid library. (C) Principle component analysis (PCA) of the dual-gRNA read count distributions. (D) Cumulative frequency of dual-gRNA constructs by deep sequencing. Shift in the curves at days 14, 21, and 28 represents the depletion of dual-gRNA constructs. Each time point was measured in duplicates.

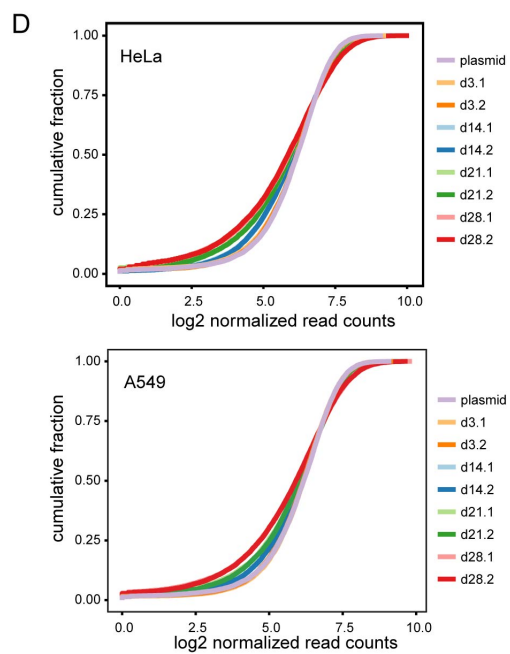
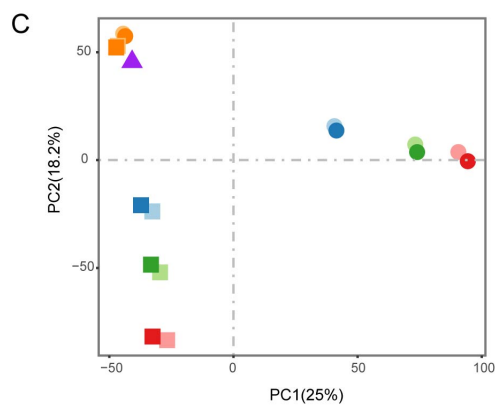
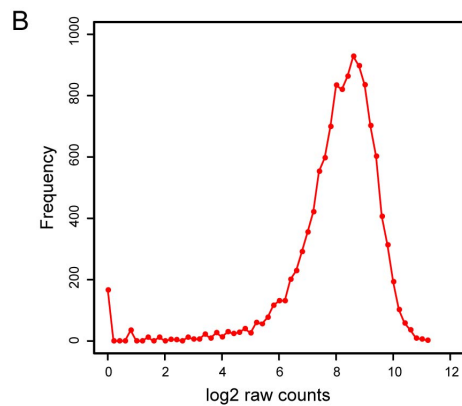
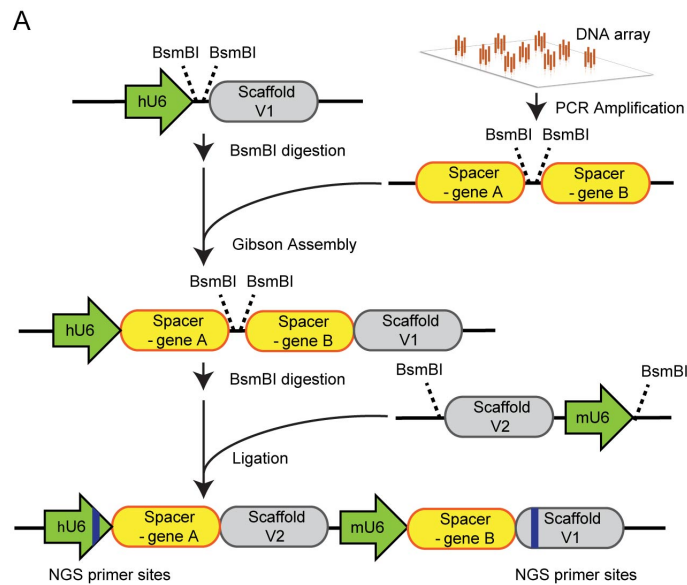


Figure S5.2: CRISPR screening results reveal metabolic network dependencies. (A) SKO fitness scores for A549 cells, plotted as f_g (day^{-1}), with a more negative score representing a decrease in fitness with SKO. Plotted as mean \pm SD. (B) Gene pairs with significant genetic interaction scores (z-score < -3) are shown. Conserved interactions cross HeLa and A549 are indicated in blue. Previously reported interactions are indicated in red. Purple indicates the conserved interactions which have been previously reported.

Figure S5.3: Screening results validated through metabolic flux measurements and fitness assays. (A, B) Metabolic validation of DKO interaction in *ENO1/ENO3*. DKO significantly lowered flux through glycolysis over control or SKOs. A, measurement of labeled Lactate. B, measurement of labeled Alanine. † indicates statistical significance ($p < 0.05$) for all conditions as compared to DKO. (C) SKO competition assay of oxPPP genes in HeLa (left) and A549 (right) cells. HeLa data replicated from Figure 4.3L and log transformed for comparison. (D) Deep sequencing analysis of indels (insertions and deletions) introduced by CRISPR-Cas9 at 10 days after transduction of *G6PD* or *PGD* gRNA constructs. (E) Deep sequencing analysis of indels introduced by CRISPR-Cas9 at two weeks after transduction of *KEAP1* gRNA constructs in HeLa cells. Ordinate shows the read counts of indels at each corresponding location. Most cells were successfully targeted after transduction of gRNAs, while only a background level of mutagenesis was observed in the cells transduced with non-targeting control gRNAs. These experiments suggest high targeting efficiency in both the A549 and HeLa Cas9-stable cell lines.

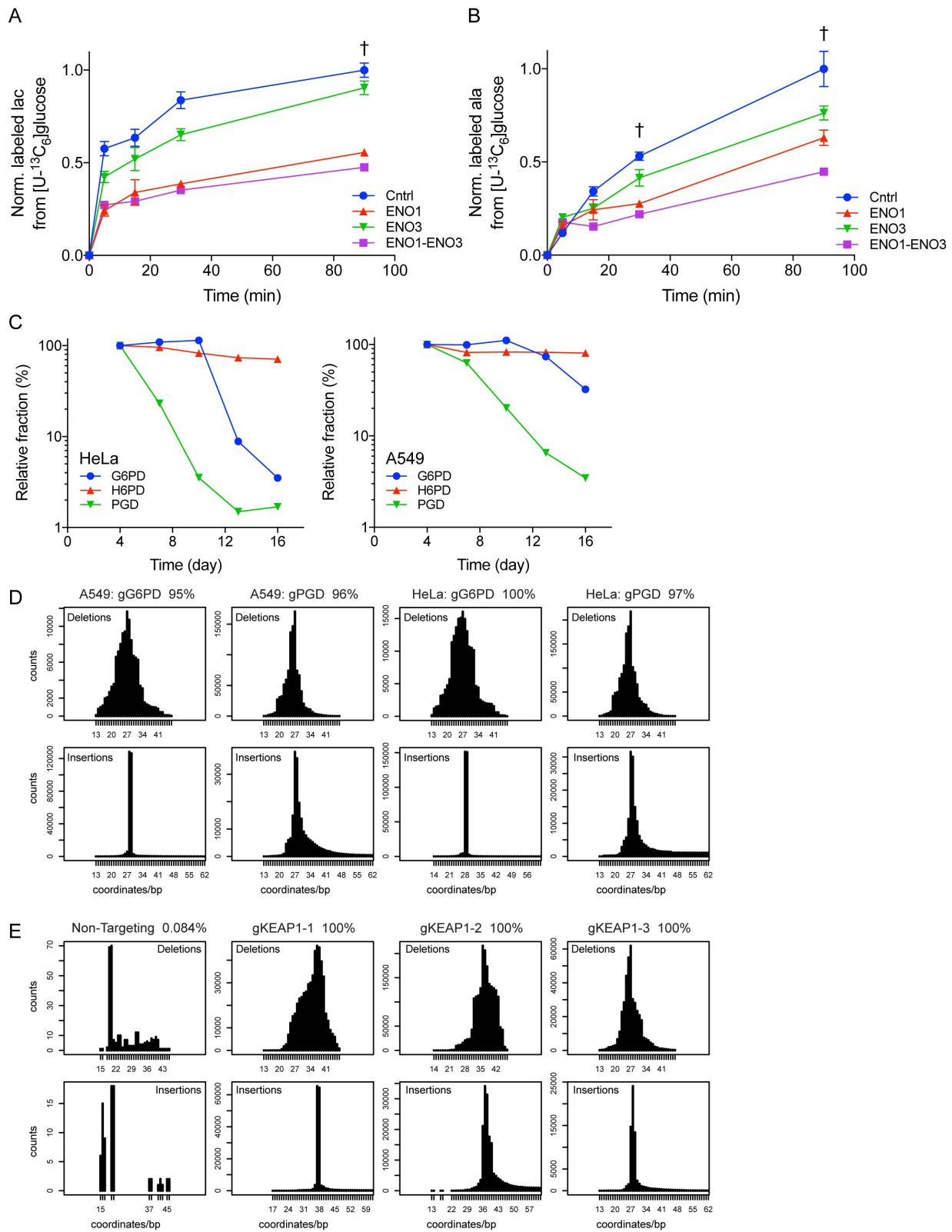
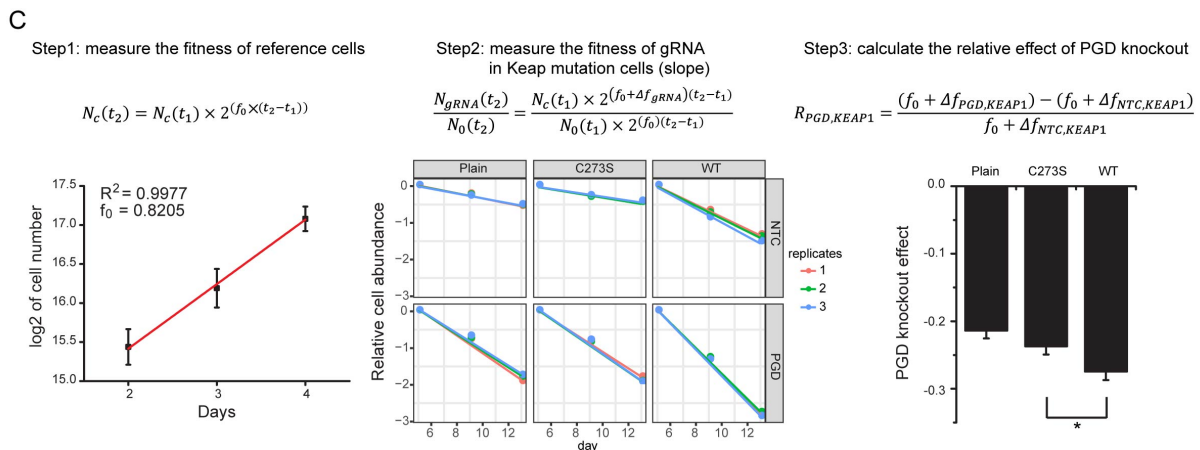
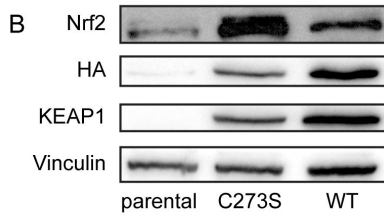
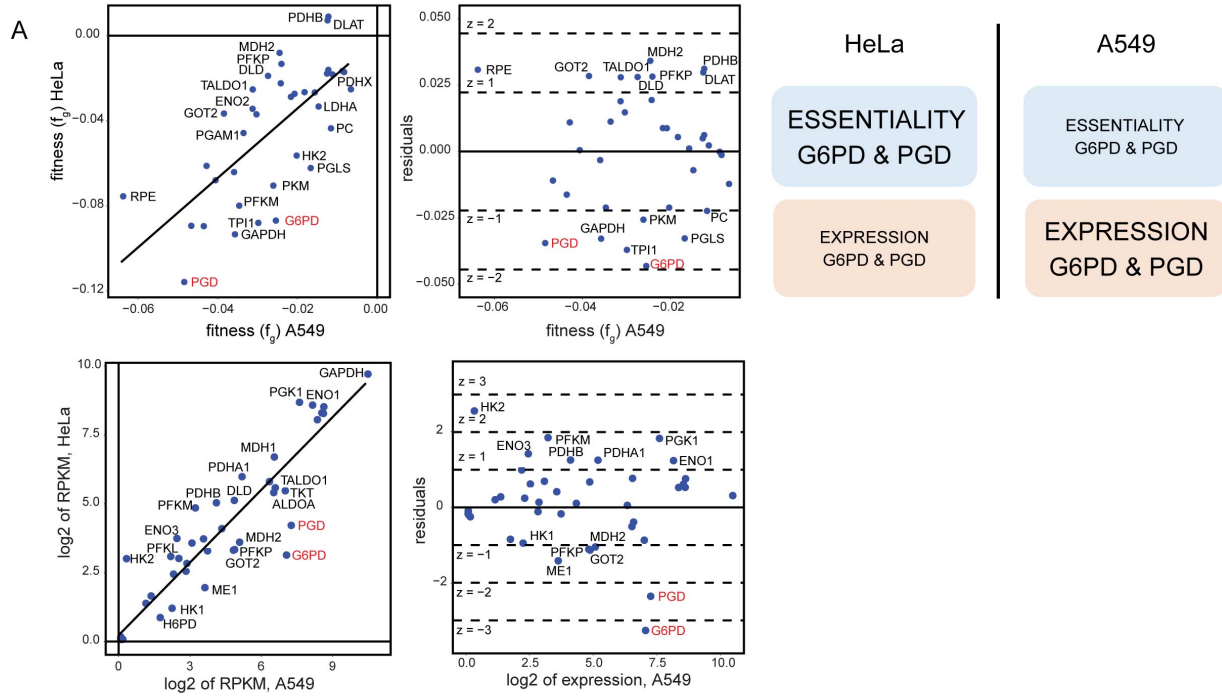


Figure S5.4: *KEAP1* mutational status alters redox metabolism and impact of oxPPP gene knockouts on cellular fitness. (A) Scatter plots (left) of SKO fitness and gene expression in HeLa versus A549. Residual plots (right) of linear regressions showing the outliers between HeLa and A549. oxPPP genes (*G6PD* and *PGD*) showed more essentiality in HeLa cells versus A549, while their mRNA expression levels are lower in HeLa cells versus A549. (B) Immunoblot of A549s with *KEAP1* mutant panel. (C) Measurement of relative *PGD* perturbation effect in A549 cells across *KEAP1* mutant panel. Growth curve of the reference cells, which is tdtomato+ cells in this case, and its absolute fitness (f_0) was extracted by counting average cell numbers in three independent experiments for three days. The fitness of *PGD* perturbation ($\Delta f_{PGD,KEAP1}$) relative to non-targeting controls (NTC) in *KEAP1* mutation cells were measured by competitive assay. Finally, by incorporating also the absolute fitness of reference cells, the relative effects of *PGD* perturbation ($R_{PGD,KEAP1}$) in *KEAP1* mutant cells was calculated.



Chapter S6

Supplement to Chapter 6

S6.1 Supplemental Tables and Figures

Table S6.1: Metabolite fragments.

Metabolite	m/z	Fragments for integration
α -Ketoglutarate	346	C ₁₄ H ₂₈ O ₅ NSi ₂
Alanine	260	C ₁₁ H ₂₆ O ₂ NSi ₂
Aspartate	418	C ₁₈ H ₄₀ O ₄ NSi ₃
Lactate	261	C ₁₁ H ₂₅ O ₃ Si ₂
	233	C ₁₀ H ₂₅ O ₂ Si ₂
Citrate	459	C ₂₀ H ₃₉ O ₆ Si ₃
Fumarate	287	C ₁₂ H ₂₃ O ₄ Si ₂
Glutamate	432	C ₁₉ H ₄₂ O ₄ NSi ₃
Glutamine	431	C ₁₉ H ₄₃ O ₃ N ₂ Si ₃
Glycerol-3-phosphate	571	C ₂₃ H ₅₆ O ₆ Si ₄ P
Glycine	246	C ₁₀ H ₂₄ O ₂ NSi ₂
2-Hydroxyglutarate	433	C ₁₉ H ₄₁ O ₅ Si ₃
Malate	419	C ₁₈ H ₃₉ O ₅ Si ₃
Norvaline	288	C ₁₃ H ₃₀ O ₂ NSi ₂
Proline	330	C ₁₆ H ₃₆ O ₂ NSi ₂
Pyruvate	174	C ₆ H ₁₂ O ₃ NSi
Serine	390	C ₁₇ H ₄₀ O ₃ NSi ₃
Succinate	289	C ₁₂ H ₂₅ O ₄ Si ₂
Myristate	242	C ₁₅ H ₃₀ O ₂
Palmitate	270	C ₁₇ H ₃₄ O ₂
Stearate	298	C ₁₉ H ₃₈ O ₂
Oleate	296	C ₁₉ H ₃₆ O ₂

Table S6.2: RT-PCR primers.

Gene	Forward	Reverse	Primerbank ID
<i>G6PD</i>	ACCGCATCGACCACTACCT	TGGGGCCGAAGATCCTGTT	108773794c2
<i>PGD</i>	ATGGCCCAAGCTGACATCG	AAAGCCGTGGTCATTCATGTT	40068517c1
<i>FAS</i>	AAGGACCTGTCTAGGTTTGATGC	TGGCTTCATAGGTGACTTCCA	41872630c1
<i>SCD</i>	TTCCTACCTGCAAGTTCTACACC	CCGAGCTTTGTAAGAGCGGT	53759150c3
<i>ACACA</i>	TCACACCTGAAGACCTTAAAGCC	AGCCACACTGCTTGACTG	38679973c3
<i>ACLY</i>	ATCGGTTCAAGTATGCTCGGG	GACCAAGTTTTCCACGACGTT	38569422c2
<i>ELOVL6</i>	AACGAGCAAAGTTTGAAGTGGAGG	TCGAAGAGCACCGAATATACTGA	195539341c1
<i>GAPDH</i>	CTGGGCTACACTGAGCACC	AAGTGGTCGTTGAGGGCAATG	378404907c3

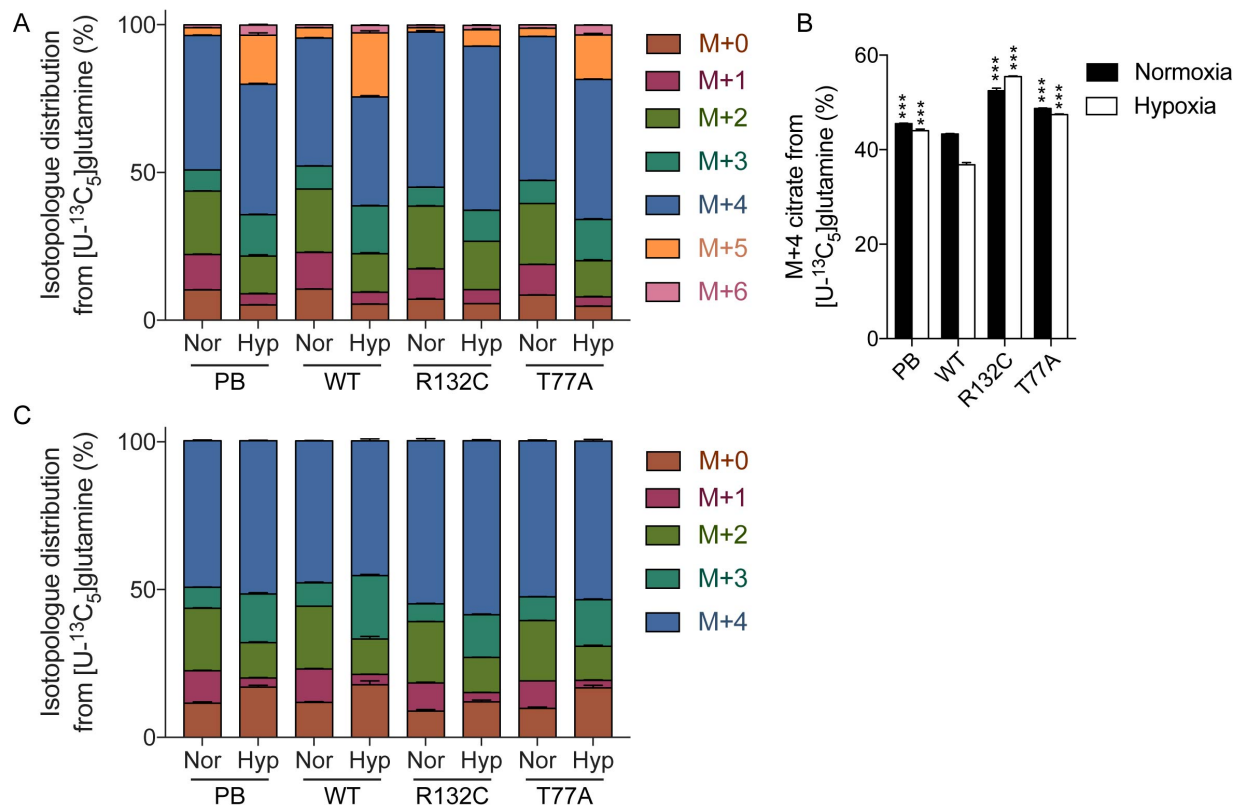


Figure S6.1: Central carbon isotopologue distribution in mtIDH cells. (A) Isotopologue distribution of citrate from [U-¹³C₅]glutamine. (B) Percentage of M+4 citrate isotopologue from [U-¹³C₅]glutamine in normoxia and hypoxia. (C) Isotopologue distribution of aspartate from [U-¹³C₅]glutamine.

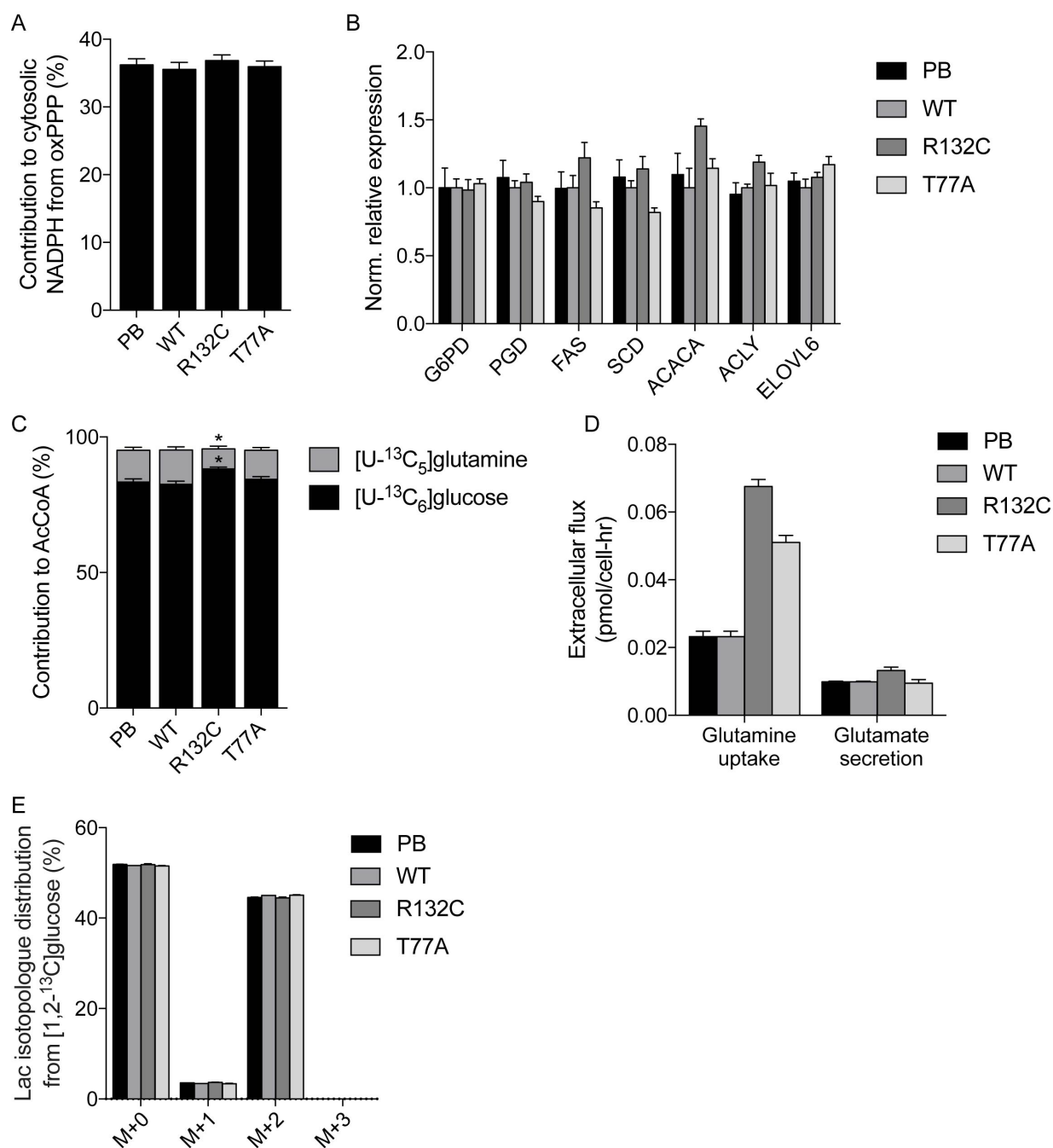


Figure S6.2: Metabolic alterations induced by lipid deficiency. (A) Contribution of oxPPP to cytosolic NADPH in fibrosarcoma panel under delipidated conditions. (B) Normalized relative expression of DNL genes. (C) Contribution of [U-¹³C₆]glucose and [U-¹³C₅]glutamine to lipogenic AcCoA. (D) Extracellular glutamine uptake and glutamate efflux. (E) Normalized oxPPP flux calculated as described in Methods. (A, C) Data plotted as mean \pm 95% CI. * indicates statistical significance by non-overlapping confidence intervals.